CORA Cork Open Research Archive
Cartlann Taighde Oscailte Chorcaí

Title	Electromagnetic tracking methods and magnetic modelling for distortion compensation
Authors	Cavaliere, Marco
Publication date	2023
Original Citation	Cavaliere, M. 2023. Electromagnetic tracking methods and magnetic modelling for distortion compensation. PhD Thesis, University College Cork.
Type of publication	Doctoral thesis
Rights	© 2023, Marco Cavaliere. - https://creativecommons.org/licenses/by-nc-nd/4.0/
Download date	2026-11-06 10:33:03
Item downloaded from	https://hdl.handle.net/10468/15000



UCC
University College Cork, Ireland
Coláiste na hOllscoile Corcaigh



Electromagnetic tracking methods and magnetic modelling for distortion compensation

Marco Cavaliere

Supervisor: Dr. Pádraig Cantillon-Murphy
Advisor: Dr. John G. Hayes

School of Engineering
University College Cork

This dissertation is submitted for the degree of
Doctor of Philosophy

May 2023

Electromagnetic tracking methods and magnetic modelling for distortion compensation

Marco Cavaliere

May 2023

https://orcid.org/0000-0003-1901-0041

Funding

This work was supported by the Science Foundation Ireland under grant TIDA17/4897 and by the European Research Council [ERC-2020-COG] under award number 101002225.

The research was completed at University College Cork and Tyndall National Institute, Cork, Ireland.



Colophon

This thesis was typeset using LaTeX and the `PhDThesisPSnPDF` document class template[1]. All graphics and plots were edited and processed in Inkscape[2]. Palatino from `mathpazo` package[3] acts as both the text and display typeface. Monospaced text uses Courier.

[1] Available at https://github.com/kks32/phd-thesis-template
[2] Available at https://inkscape.org/
[3] Available at https://ctan.org/pkg/mathpazo

Declaration

This is to certify that the work I am submitting is my own and has not been submitted for another degree, either at University College Cork or elsewhere. All external references and sources are clearly acknowledged and identified within the contents. I have read and understood the regulations of University College Cork concerning plagiarism and intellectual property.

Marco Cavaliere
May 2023

Acknowledgements

I would like to express my sincere gratitude to everyone who supported me during my research journey. First and foremost, I want to thank my supervisor, Dr. Pádraig Cantillon-Murphy, for his invaluable guidance, support, and encouragement throughout my research. Dr. Herman Alexander Jaeger and Dr. Kilian O'Donoghue also deserve a huge thank you for their help and assistance. Special thanks go to Michael O'Shea and Tim Power for all their work in constructing and designing the mechanical components required for my research projects.

I would like to extend my thanks to all members of my research group: Aleksandr, Alessandro, Charu, Christian, Daragh, Eoin, Hellen, Irene, and Manish. I could always count on their collaboration and friendship. Many thanks to the postgraduate community in the electrical engineering building. The extensive lunch breaks, fair card games, and passionate ping-pong matches helped make the PhD journey an enjoyable experience.

I wish to express my gratitude to Dr. Lee Swanstrom for giving me the opportunity to spend a research period at IHU, Strasbourg. There, I found an optimal working environment and friendly colleagues that welcomed me and made me feel at home. I would especially like to thank Dr. Juan Manuel Verde for his help and collaboration and Prof. Monique Dannhauser for finding the time and patience to teach me French.

I am grateful to Buvana for her friendship and support, being always ready to help and advise me. A heartfelt thank you to Mariana for her unwavering patience, encouragement, and understanding.

I would like to express my sincere appreciation to all friends and loved ones who have always been there for me, whether they were near or far. Finally, I wish to thank my parents for all their support, love and belief in me throughout my studies.

Abstract

The thesis presents a comprehensive study of electromagnetic tracking (EMT), focusing on developing methods and techniques to reduce and compensate for distortions in the magnetic field through improved modelling and real-time correction methods. To this end, the research-oriented ANSER EMT system is employed. *Anser* is the Latin name of the greylag goose, which uses the geomagnetic field for navigation. In this work, a general method for modelling magnetic fields is developed to significantly improve the ANSER EMT magnetic model by correcting systematic errors and including magnetic shielding. Moreover, real-time compensation techniques for dynamic distortion are proposed using external reference sensors. Further improvements are demonstrated for dynamic tracking by optimising the EMT model and algorithm. Finally, the effectiveness of the ANSER EMT system for developing novel EMT applications is demonstrated by introducing alternative tracking techniques based on the magnetic *scalar potential* formulation, particularly suited for tracking the elongated sensor coils used in medical applications, and on the magnetic *vector potential* formulation, for tracking large-area PCB coils. Overall, this work provides the theoretical and experimental basis for a new approach to distortion rejection in EMT systems with significant potential for future clinical benefit in the years to come.

Table of contents

List of publications xiii

List of figures xvi

List of tables xix

Nomenclature xxi

1 Introduction 1
- 1.1 Electromagnetic tracking in medicine . . . 1
- 1.2 The ANSER EMT platform . . . 2
- 1.3 Thesis assumptions . . . 3
- 1.4 Thesis objectives . . . 3
- 1.5 Thesis structure . . . 5
- References . . . 6

2 Review on electromagnetic tracking systems and methods 9
- 2.1 Object tracking . . . 9
- 2.2 Fundamentals of EMT . . . 12
  - 2.2.1 Magnetic models . . . 14
  - 2.2.2 Tracking methods . . . 16
  - 2.2.3 Field generation . . . 21
  - 2.2.4 Sensor technology . . . 24
- 2.3 EMT for computer-assisted interventions . . . 25
  - 2.3.1 Commercial systems . . . 27
  - 2.3.2 Limitations . . . 29
- 2.4 Magnetic field distortion . . . 29
  - 2.4.1 Eddy currents reduction . . . 31

2.4.2 Volume characterisation . . . 35
2.4.3 Passive shielding . . . 37
2.4.4 Online compensation . . . 38
2.5 Conclusions . . . 40
References . . . 40

3 ANSER EMT system and accuracy assessment methods 73
3.1 ANSER EMT . . . 73
3.1.1 Functional subsystems . . . 74
3.2 Modular software framework . . . 82
3.2.1 Data acquisition . . . 83
3.2.2 Signal extraction . . . 84
3.2.3 Analytical magnetic model . . . 91
3.2.4 Tracking algorithm . . . 97
3.3 Sensors for characterisation and tracking . . . 98
3.3.1 Registration between tracking systems . . . 100
3.3.2 Concurrent magnetic and mechanical calibration . . . 101
3.3.3 Magnetic calibration without optical reference . . . 102
3.4 Robotic two-axial actuator . . . 107
3.4.1 Mechanical oscillations . . . 108
3.4.2 Acquisition time . . . 109
3.5 Performance analysis of ANSER EMT . . . 111
3.5.1 Sources of error . . . 111
3.5.2 Noise and measurement sensitivity . . . 113
3.5.3 System resolution . . . 116
3.6 Experimental performance . . . 120
3.6.1 Accuracy evaluation . . . 121
3.6.2 Computation time and memory requirements . . . 123
3.6.3 Results . . . 124
3.6.4 Discussion . . . 126
3.7 Conclusions . . . 128
References . . . 129

4 Magnetic distortion detection and compensation techniques 141
4.1 Model based on virtual dipole sources . . . 142

4.2 Compensated model for ANSER EMT 146
4.2.1 Methods 146
4.2.2 Static tracking results 149
4.2.3 Freehand trajectory results 151
4.2.4 Discussion 151
4.3 Magnetic shielding 153
4.3.1 Shielded magnetic field generator model 156
4.3.2 Shielding performance in a clinical environment . . 159
4.3.3 Discussion 165
4.4 Distortion detection techniques 166
4.4.1 Multiple sensors rigidly connected 166
4.4.2 Residual of the tracking algorithm 167
4.4.3 Signal phase shift 168
4.4.4 Distortion detection in a clinical environment 168
4.5 Real-time distortion compensation 173
4.5.1 Intraoperative magnetic modelling 174
4.5.2 Interpolation between pre-trained models 181
4.6 Conclusions 186
References 188

5 Tracking algorithm with increased update rate 195
5.1 Improvements to the algorithm and to the magnetic model 196
5.1.1 Algorithm for a faster pose update 196
5.1.2 Increased-speed magnetic model 199
5.2 Random noise reduction 200
5.2.1 Sliding window DFT 200
5.2.2 Exponential moving average 203
5.2.3 EMA with speed estimation 204
5.3 Kalman Filtering 205
5.3.1 Kalman filter 206
5.3.2 Extended Kalman filter 211
5.4 Dynamic test 212
5.4.1 Results 213
5.5 Conclusions 217

References 218

6 Magnetic models for elongated sensors 223
6.1 Introduction 224
6.2 Magnetic models 224
6.2.1 Magnetic field of the ANSER EMT field generator . 226
6.2.2 Scalar potential formulation 226
6.3 Solid angle subtended by a planar spiral 228
6.4 Materials and methods 230
6.4.1 Performance metrics 231
6.4.2 Model interpolation 231
6.4.3 Simulated tracking test 232
6.4.4 Experimental tracking test 233
6.4.5 Long flexible inductive sensors 235
6.5 Results 237
6.5.1 Model interpolation 237
6.5.2 Simulated tracking test 239
6.5.3 Experimental tracking test 240
6.5.4 Long flexible inductive sensors 242
6.6 Discussion 244
6.6.1 Model interpolation 244
6.6.2 Simulated and experimental tracking tests 245
6.6.3 Long flexible inductive sensors 245
6.7 Conclusions 246
References 246

7 Magnetic models for planar sensors 249
7.1 Introduction 250
7.2 Mutual inductance between large-area planar coils 250
7.2.1 Partial mutual inductance between straight wires . 253
7.2.2 Novel implementation of the formula 256
7.3 Sensor manufacturing 258
7.3.1 Planar sensor coil design 258
7.3.2 Coil design optimisation 262
7.3.3 Coil measured parameters 264

7.4 System simulation 266
7.4.1 Simplified magnetic models 266
7.4.2 Dependence on distance 267
7.4.3 Static tracking simulation 268
7.5 Experimental tests 271
7.5.1 Mutual inductance measurement 273
7.5.2 Static tracking accuracy 276
7.6 Discussion 278
7.7 Conclusions 279
References 279

8 Summary and future work **283**
8.1 Thesis summary 283
8.2 Thesis contributions 286
8.3 Perspectives for future work 287
8.3.1 Radiation exposure reduction in a clinical study . . 287
8.3.2 Self-shielded field generator 288
8.3.3 Fusion with complementary imaging systems . . . 289
8.3.4 Reversed magnetic model 291
References 292

List of publications

Peer-reviewed journal papers

1. **Cavaliere, M.**, McVeigh, O., Jaeger, H. A., Hinds, S., O'Donoghue, K., Cantillon-Murphy, P., "Inductive Sensor Design for Electromagnetic Tracking in Image Guided Interventions," *IEEE Sensors Journal*, vol. 20, no. 15, pp. 8623–8630, 2020

2. **Cavaliere, M.**, Jaeger, H. A., O'Donoghue, K., Cantillon-Murphy, P., "Planar Body-Mounted Sensors for Electromagnetic Tracking," *Sensors*, vol. 21, no. 8, p. 2822, 2021

3. **Cavaliere, M.**, Cantillon-Murphy, P., "Electromagnetic Tracking of Elongated Sensors for Endoscopic Navigation," *Magnetism*, vol. 2, no. 3, pp. 271–287, 2022

4. **Cavaliere, M.**, Crowley, D., Jaeger, H. A., O'Donoghue, K., Cantillon-Murphy, P., "Magnetic Model Calibration and Distortion Compensation for Electromagnetic Tracking in a Clinical Environment," *IEEE Transactions on Magnetics*, vol. 59, no. 7, pp. 1–12, 2023

5. Sidun, A., Srivastava, M., O'Donoghue, K., Jaeger, H. A., **Cavaliere, M.**, O'Hare, D., Van den Bosch, C., Cantillon-Murphy, P., "Planar On-Silicon Inductor Design for Electromagnetic Tracking," *IEEE Sensors Journal*, pp. 1–1, 2023

Peer-reviewed conference papers

1. **Cavaliere, M.**, Walsh, C., Jaeger, H. A., O'Donoghue, K., Cantillon-Murphy, P., "Magnetic tracking using a modular C++ environment for image-guided interventions," *Computer Methods in Biomechanics and Biomedical Engineering: Imaging & Visualization*, vol. 10, no. 4, pp. 383–389, 2021

2. **Cavaliere, M.**, Cantillon-Murphy, P., "Intraoperative compensation of magnetic field distortions for fluoroscopic and electromagnetic hybrid navigation," *International Journal of Computer Assisted Radiology and Surgery*, vol. 17, pp. 1717–1721, 2022

3. **Cavaliere, M.**, Cantillon-Murphy, P., "Enhancing electromagnetic tracking accuracy in medical applications using pre-trained witness sensor distortion models," *International Journal of Computer Assisted Radiology and Surgery*, 2023

4. Crowley, D., **Cavaliere, M.**, Cantillon-Murphy, P., "A novel approach to wireless electromagnetic tracking using frequency modulation radio communication," *International Journal of Computer Assisted Radiology and Surgery*, 2023

Conferences

1. **Cavaliere, M.**, McVeigh, O., Jaeger, H.A., Hinds, S., O'Donoghue, K., Cantillon-Murphy, P., "Sensor design for electromagnetic tracking in image guided interventions", *31st International Conference of the international Society for Medical Innovation and Technology*, October 9-11 2019, Heilbronn, Germany (oral presentation)

2. **Cavaliere, M.**, Cantillon-Murphy, P., "Planar coil design for external tracking and magnetic distortion compensation", *32nd International Conference of the international Society for Medical Innovation and Technology*, December 4-10 2020, Virtual Congress (oral presentation)

3. **Cavaliere, M.**, Cantillon-Murphy, P., "Magnetic tracking using a modular C++ environment for image-guided interventions", *24th International Conference on Medical Image Computing and Computer Assisted Intervention 2021*, September 27 2021, Strasbourg, France (oral presentation)

4. **Cavaliere, M.**, Cantillon-Murphy, P., "Data-driven model for magnetic tracking in the presence of static field distortions", *33rd International Conference of the international Society for Medical Innovation and Technology*, June 17-19 2022, Oslo, Norway (poster presentation)

5. **Cavaliere, M.**, Cantillon-Murphy, P., "Challenges of electromagnetic tracking in biomedical navigation", *3rd URSI Atlantic / Asia-Pacific Radio Science Meeting 2022*, May 30 - June 3 2022, Gran Canaria, Spain (oral presentation)

6. **Cavaliere, M.**, Cantillon-Murphy, P., "Intraoperative compensation of magnetic field distortions for fluoroscopic and electromagnetic hybrid navigation", *26th Annual Conference of the International Society for Computer Aided Surgery 2022*, June 7-11 2022, Tokyo, Japan (poster presentation)

7. **Cavaliere, M.**, Jaeger, H.A., O'Donoghue, K., Cantillon-Murphy, P., "A novel method to correct EMT errors for an unseen C-arm distortion", *28th Annual Conference of the Section of Bioengineering of the Royal Academy of Medicine in Ireland*, 27-28 January 2023, Enfield, Ireland (oral presentation)

8. **Cavaliere, M.**, Cantillon-Murphy, P., "Enhancing electromagnetic tracking accuracy in medical applications using pre-trained witness sensor distortion models", *Computer Assisted Radiology and Surgery Congress 2023*, June 7-11 2023, Munich, Germany (poster presentation)

List of figures

1.1 The MONARCH™ robotic endoscopy platform. 2

2.1 EMT basic principle of operation. 10
2.2 Magnetic models for spatially extended transmitting and receiving antennas. 15
2.3 Typical topologies for uniaxial tracking. 19
2.4 Examples of EMT clinical applications. 28
2.5 Metallic distorter: Equivalent RL circuit model. 31

3.1 Data flow in the ANSER EMT system. 75
3.2 Planar field generators the ANSER EMT system. 76
3.3 Full CT scan of an animal model placed above ANSER EMT field generators. 79
3.4 EMT sensors and ANSER EMT control unit. 81
3.5 Signal acquisition window. 85
3.6 Noise level for different numbers of samples at 40 kHz. . . 87
3.7 Effect of the sensor motion on the FFT. 89
3.8 Computation time of the DFT sum and the FFT algorithm. 90
3.9 Analytical model for the magnetic flux crossing an inductive sensor located at **r** with orientation **n**. 92
3.10 Flowchart of the EMT algorithm 97
3.11 Sensors for characterisation and tracking. 99
3.12 Linear transformations between tracking systems. 100
3.13 Model calibration with mechanical constraints. 104
3.14 Robotic two-axial actuator. 107
3.15 Position error due to mechanical oscillations. 109
3.16 EMT solutions showing the effect of mechanical oscillations. 110

3.17 Noise reduction by averaging consecutive measurements. . 112
3.18 Position and orientation random errors distribution. 115
3.19 Clouds of EMT solution points due to jitter noise. 117
3.20 ANSER EMT resolution for two field generators. 119
3.21 ANSER EMT static test. 121
3.22 ANSER EMT experimental performance, cumulative distribution function. 124
3.23 ANSER EMT experimental performance, scatter plot. . . . 125

4.1 Experimental setup used to build a data-driven magnetic field model for ANSER EMT field generator. 147
4.2 Data-driven magnetic field model, fit results. 148
4.3 Freehand tests at the centre, above, and below the training grid. 149
4.4 Novel data-driven model, cumulative distribution error, static test. 150
4.5 Novel data-driven model, cumulative distribution error, freehand test. 152
4.6 Effect of different shielding materials. 154
4.7 Modelling of the shielded magnetic field generator. 157
4.8 Effect of shielding on the magnetic field. 158
4.9 Experimental setup to evaluate the C-arm distortion effect. 161
4.10 Unshielded and uncompensated EMT errors caused by the C-arm at different distances. 162
4.11 EMT error grids with the C-arm at 2 cm below the FG. . . . 163
4.12 EMT accuracy using magnetic shielding. 164
4.13 Experiment to characterise the distortion from the CT scanner table and gantry. 169
4.14 Snapshots of the EMT poses in the three distortion scenarios. 171
4.15 EMT errors and distortion detection techniques. 172
4.16 Online distortion compensation technique. 177
4.17 EMT error grids before and after applying the compensation technique. 178
4.18 EMT accuracy using real-time distortion compensation. . . 179
4.19 Witness sensor and US probe moved on a line. 182

4.20 Distortion tracking with one degree of freedom. 183
4.21 Witness sensor and X-ray detector moved to different distances. 184
4.22 EMT accuracy with the X-ray detector placed 28 cm above the field generator. 186

5.1 Sliding window technique for increased update-rate. . . . 201
5.2 Dynamic EMT test. 213
5.3 Profile of the tracked y coordinate of a horizontal sensor. . 216

6.1 Calculation of the magnetic flux crossing an elongated inductive sensor. 228
6.2 Magnetic field and associated scalar potential. 229
6.3 Experimental setup for an EMT test with elongated sensors. 234
6.4 Simulated EMT test for a 128 mm-long flexible sensor. . . . 236
6.5 Interpolation and position EMT errors versus the table size. 238
6.6 Position error obtained with alternative magnetic models for elongated sensors. 241
6.7 Simulated position error for the end-points of a flexible coil. 243

7.1 Mutual inductance between coils Tx and Rx. 252
7.2 Partial inductance between two straight wires at any angle. 255
7.3 Cross-sectional area and total length of a hexagonal coil. . 259
7.4 SNR for circular, hexagonal, and square planar coil shapes. 263
7.5 Footprints of PCB planar coils. 264
7.6 Three hexagonal sensors manufactured on a 4-layer PCB. . 265
7.7 Mutual inductance using different model approximations. 269
7.8 Static accuracy test simulation with no added noise. 270
7.9 EMT accuracy dependence on model approximations and noise magnitude. 272
7.10 Experimental setup for mutual inductance measurements. 273
7.11 Calculated and measured mutual inductance between the hexagonal sensor coil and the square emitter coil. 275
7.12 Static accuracy tests for large-area planar sensors. 277

8.1 Self-shielded transmitting and shielding coils. 290

List of tables

3.1 ANSER EMT accuracy and precision assessment. 125
3.2 Computation time and memory requirements. 126

4.1 Novel data-driven model, summary table. 151
4.2 Shielding effectiveness of different shielding materials. . . 155
4.3 Aluminium and mu-metal planar shields. 156
4.4 Distorted field interpolation performance. 160
4.5 EMT error metrics with the C-arm at 2 cm below the shielded field generator. 164
4.6 Proposed real-time distortion compensation techniques. . . 175
4.7 EMT error metrics with the field generator placed on top of the X-ray collimator. 179
4.8 EMT error metrics using the witness sensor to localise the X-ray detector. 187

5.1 Speed of different tracking algorithms and filtering techniques. 214

6.1 Speed and accuracy of magnetic models compared. 240
6.2 EMT error metrics obtained with alternative magnetic models for elongated sensors. 241

7.1 Calculated and measured coil resistance and self inductance. 266
7.2 Simulated speed and accuracy of the *6-filaments* and *single-point* models. 271
7.3 Calculated and measured mutual inductance values. 274
7.4 Experimental speed and accuracy of the *6-filaments* and *single-point* models. 276

Nomenclature

Roman Symbols

$\mathbf{A}$	Magnetic vector potential $[\mathrm{Tm}]$
$\widetilde{\mathbf{B}}$	Magnetic flux density vector (measurement) $[\mathrm{T}]$
$\mathbf{B}$	Magnetic flux density vector (model), $\mathbf{B} = \mu\mathbf{H}$
$\mathbf{H}$	Magnetic field vector $\left[\mathrm{Am}^{-1}\right]$
$\mathbf{J}$	Electric current density $\left[\mathrm{Am}^{-2}\right]$
$\mathbf{n}$	Orientation unit vector
$\mathbf{p}$	Pose vector, $\mathbf{p} = [x\, y\, z\, \theta\, \varphi]^T$
$\widetilde{\mathbf{p}}$	Pose vector estimated by the EMT algorithm
$\mathbf{r}$	Position vector
$\mathbf{t}$	Tangential unit vector
$x\, y\, z$	Cartesian coordinates (in mm, unless otherwise specified)

Greek Symbols

Γ	Electric current path, or wire center-line
Φ	Magnetic flux (model) enclosed by an inductive coil $[\mathrm{Wb}]$
$\widetilde{\Phi}$	Magnetic flux (measurement) enclosed by an inductive coil $[\mathrm{Wb}]$
$\overline{\Phi}$	The overline is used to indicate a phasor

$\mathbf{\Phi}$	Array of magnetic fluxes from different emitter coils (model)
$\widetilde{\mathbf{\Phi}}$	Array of magnetic fluxes from different emitter coils (measurement)
ψ	Magnetic scalar potential $[\mathrm{A}]$
ρ	Roll angle (in rad, unless otherwise specified)
θ	Pitch angle (in rad, unless otherwise specified)
φ	Yaw angle (in rad, unless otherwise specified)
μ	Magnetic permeability, $\mu = \mu_r \mu_0$
μ_0	Vacuum magnetic permeability, $\mu_0 \simeq 1.2566e^{-6}$ $\left[\mathrm{NA}^{-2}\right]$
μ_r	Relative magnetic permeability

Acronyms / Abbreviations

ADC	Analog-to-Digital Converter
AMR	Anisotropic Magneto-Resistance
BLE	Bluetooth Low Energy
CDF	Cumulative Distribution Function
CI	Confidence Interval
DAQ	Data Acquisition
DDS	Direct Digital Synthesis
DFT	Discrete Fourier Transform
DOF	Degrees Of Freedom
DRF	Dynamic Reference Frame
EC	Emitter Coil
EMT	Electromagnetic Tracking

ENT Ear, Nose and Throat

EP Electrophysiology

FDM Frequency Domain Multiplexing

FFT Fast Fourier Transform

FG Field Generator

GMR Giant Magneto-Resistance

INA Instrumentation Amplifier

LUT Look-Up Table

MRI Magnetic Resonance Imaging

NMAE Normalised Mean Absolute Error

PRC50, PRC95 50^{th} and 95^{th} percentiles, respectively

PMT Permanent Magnet Tracking

RMSE Root-Mean-Square Error

ROI Region Of Interest

SNR Signal to Noise Ratio

SQUID Superconducting Quantum Interference Device

TDM Time Domain Multiplexing

TMR Tunnelling Magneto-Resistance

Chapter 1

Introduction

This chapter provides an overview of the research work presented in this thesis. Relevant background information is initially presented, followed by the motivation for the work and the objectives of the thesis. Finally, the thesis structure and key contributions are outlined.

1.1 Electromagnetic tracking in medicine

Electromagnetic tracking (EMT) enables instrument positioning and navigation during image-guided interventions [1, 2]. The technology uses magnetic fields to determine the position and orientation of a target, allowing for object tracking without a line of sight or harmful X-rays [3].

Traditional imaging techniques such as cameras, X-ray fluoroscopy, and ultrasound can only provide local guidance, posing some limitations to image-guided interventions. Moreover, fluoroscopy creates a significant health risk to patients and medical staff [4, 5]. Conversely, EMT provides global positioning in relation to the patient anatomy and does not pose additional health risks. It can be used in multi-modal imaging applications to improve clinical outcomes [6].

For these reasons, EMT is currently used for intra-operative tool tracking in minimally-invasive and endoscopic interventions, such as cardiovascular navigation [7], endoscopy [8], and robotic surgery [9]. Figure 1.1 shows a typical clinical use of EMT in robotic bronchoscopy.



Figure 1.1: The MONARCH™ robotic endoscopy platform (Auris Health Inc., Redwood City, CA) [10], as an example of EMT-guided medical intervention.

While EMT has shown great promise in enabling minimally invasive procedures, current technology still faces significant challenges that prevent it from becoming widely adopted in more general clinical use. The main shortcomings include the need for wired sensors, model errors due to tissue deformation and organ internal motion, and accuracy degradation due to magnetic field distortion. This thesis specifically examines the shortcomings due to magnetic field distortion.

1.2 The ANSER EMT platform

The ANSER EMT project originated at University College Cork, Ireland, with the primary objective of establishing an open platform to conduct research investigations, focusing on the challenges associated with EMT technology [11]. The system is named after the greylag goose, *Anser anser*, which relies on the Earth's magnetic field for navigation during migrations. The ANSER EMT system provided a foundation for the research presented in this thesis and served as the basis of the experimental setup.

In particular, the work introduced hardware and software innovations to the system. Additionally, novel calibration, characterisation, magnetic field modelling, and distortion compensation techniques were tested and evaluated using the ANSER EMT platform. These methods could equally be applied to other EMT systems where developer tools are enabled.

1.3 Thesis assumptions

As said, the thesis builds upon the existing ANSER EMT system. Therefore, it is important to clarify that the hardware components presented in Section 3.1.1 are only introduced to provide the background information necessary to understand the following work. All other sections presented in Chapter 3 are novel contributions.

The experiments conducted in this study use five-degrees-of-freedom (5 DOF) EMT sensors. These sensors measure the magnetic field vector along their axis and are not sensitive to axial rotations. However, all findings and methodologies developed also apply to six-degrees-of-freedom (6 DOF) sensors, which essentially combine two 5 DOF sensing elements to enable the measurement of two field components and detect rotations around the sensor axis.

The scope of the work is limited to compensating for external magnetic distortion, i.e. occurring outside the region of interest, because they represent the primary concern in EMT applications. This includes both static distortion, which remains unchanged during the EMT procedure, and dynamic distortion, which manifests with unpredictable impact. Possible sources of distortion inside the patient, such as surgical instruments and other medical devices, are not considered.

While the developed application and tested improvements have practical relevance for the ANSER EMT system, the primary objective of the thesis is to propose novel methods and advance the theory of EMT. Therefore, the emphasis is on academic contributions and not focused on commercial product development or solutions to specific medical procedures.

1.4 Thesis objectives

This thesis aims to address some of the challenges encountered in EMT technology by proposing improvements to the existing ANSER EMT system and testing novel solutions. To achieve this goal, the following specific objectives were pursued:

Literature review. Conduct a comprehensive review of the literature on EMT technology, with a particular focus on EMT systems, methods, and techniques used to reduce and compensate for distortion in the magnetic field. Present and evaluate the ANSER EMT system and its current limitations.

Distortion detection and compensation. Develop a general method for data-driven magnetic modelling. Test for the distortion introduced by medical equipment and propose new techniques for detecting and correcting it. These methods aim to improve the reliability and accuracy of the tracking results by accounting for the impact of magnetic field distortion on the sensor measurements.

Tracking algorithm speed and performance. Improve the speed of the tracking algorithm used in the ANSER EMT system while minimising the jitter noise. Investigations include optimising the ANSER EMT model and algorithm to achieve faster update rates and incorporating Kalman filtering to reduce noise and latency.

Model for elongated sensors. Propose a new model for EMT sensors that accounts for the impact of their elongated shape and does not approximate them as single points. The model is based on a magnetic scalar potential formulation to automatically calculate the integral of the magnetic field vector along the measurement axis.

Redundant body-mounted sensors. Investigate the use of redundant body-mounted sensors in EMT systems. This work studies the design of PCB planar coils and explores the tracking of such coils. To this end, a novel, more accurate magnetic model is introduced to account for the coil spatial extension.

1.5 Thesis structure

The thesis is structured into eight main chapters, including this introductory chapter.

Chapter 2 outlines the results of a literature survey on electromagnetic tracking (EMT) systems, methods, applications, and magnetic distortion compensation techniques. The review helps clarify the state of the art of the research topics that are the focus of this thesis.

Chapter 3 introduces the ANSER EMT system. The working principle, the main hardware components, and the software implementations are presented. The theoretical accuracy and noise sensitivity of the system are analysed. The chapter also covers the design and implementation of a 2D actuator for field mapping and accuracy testing. A detailed experimental test is performed to assess the precision, trueness, and speed of the ANSER EMT system under ideal laboratory conditions.

Chapter 4 is focused on testing for distortions introduced by medical equipment and developing novel techniques to increase EMT robustness. A new method for modelling magnetic fields is presented and used to improve the ANSER EMT magnetic model by correcting for systematic errors. The technique is also used to model the static distortions introduced by planar magnetic shields. The effectiveness of shielding is then demonstrated in reducing the effect of surrounding metallic materials. Novel real-time distortion detection techniques are presented, and methods are discussed for real-time correction using external reference sensors, identification of the distortion source using a witness sensor, and dynamic distortion compensation by interpolation of static field maps.

Chapter 5 presents improved signal processing and tracking algorithms for ANSER EMT to achieve faster update-rates using multiple sensors. Kalman filtering is applied to reduce measurement noise, improve precision, and minimise latency. A dynamic tracking test is performed to analyse the performance of the new methods and compare them with the previous implementation.

Chapter 6 describes tracking of long sensors and introduces a novel, more accurate model that takes into account the sensor length. Moreover,

the new model results in faster performance, reduced memory usage, and can potentially be used to track the endpoints of flexible coil sensors. Tracking tests are included to demonstrate the effectiveness of the new model.

Chapter 7 explores tracking of planar sensors printed on PCB, introducing a novel, more accurate model that accounts for the sensor cross-sectional extension. A new procedure is presented for calculating the mutual coupling between filament-based sensors and filament-based transmitter coils, such as those of the ANSER EMT field generator. Planar coils are designed with an optimised signal-to-noise ratio, and higher EMT accuracy is obtained with the proposed model. Such coils can be used as reference sensors to implement the methods described in Chapter 4.

Chapter 8 summarises the main findings and results of the thesis, and their implications are discussed. The chapter also provides recommendations for future work.

References

[1] T. Peters and K. Cleary, Eds., *Image-Guided Interventions: Technology and Applications*. New York, NY: Springer Science+Business Media, 2008, ISBN: 978-0-387-73858-1 978-0-387-73856-7.

[2] K. Cleary and T. M. Peters, "Image-Guided Interventions: Technology Review and Clinical Applications," *Annual Review of Biomedical Engineering*, vol. 12, no. 1, pp. 119–142, 2010, ISSN: 1523-9829. DOI: 10.1146/annurev-bioeng-070909-105249.

[3] A. Sorriento *et al.*, "Optical and Electromagnetic Tracking Systems for Biomedical Applications: A Critical Review on Potentialities and Limitations," *IEEE Reviews in Biomedical Engineering*, vol. 13, pp. 212–232, 2020, ISSN: 1941-1189. DOI: 10.1109/RBME.2019.2939091.

[4] IAEA, *Preventing unnecessary exposure in fluoroscopy*, Text, 2017. [Online]. Available: https://www.iaea.org/resources/rpop/health-professionals/radiology/fluoroscopy/unnecessary-exposure (visited on 03/01/2023).

[5] Center for Devices and Radiological Health, "White Paper: Initiative to Reduce Unnecessary Radiation Exposure from Medical Imaging," *FDA*, Fri, 06/14/2019 - 10:41. [Online]. Available: https://www.fda.gov/radiation-emitting-products/initiative-reduce-unnecessary-radiation-exposure-medical-imaging/white-paper-initiative-reduce-unnecessary-radiation-exposure-medical-imaging (visited on 02/10/2023).

[6] A. M. Franz, H. A. Jaeger, A. Seitel, P. Cantillon-Murphy, and L. Maier-Hein, "Open-Source Tracked Ultrasound with Anser Electromagnetic Tracking," in *Bildverarbeitung für die Medizin 2019*, H. Handels, T. M. Deserno, A. Maier, K. H. Maier-Hein, C. Palm, and T. Tolxdorff, Eds., ser. Informatik aktuell, Wiesbaden: Springer Fachmedien, 2019, pp. 232–237, ISBN: 978-3-658-25326-4. DOI: 10.1007/978-3-658-25326-4_52.

[7] F. Gaita, P. G. Guerra, A. Battaglia, and M. Anselmino, "The dream of near-zero X-rays ablation comes true," *European Heart Journal*, vol. 37, no. 36, pp. 2749–2755, 2016, ISSN: 0195-668X. DOI: 10.1093/eurheartj/ehw223.

[8] X. Duan, "Chapter 10 - Magnetic tracking and positioning in endoscopy," in *Magnetic Materials and Technologies for Medical Applications*, ser. Woodhead Publishing Series in Electronic and Optical Materials, A. M. Tishin, Ed., Woodhead Publishing, 2022, pp. 287–338, ISBN: 978-0-12-822532-5. DOI: 10.1016/B978-0-12-822532-5.00013-3.

[9] A. Agrawal, D. K. Hogarth, and S. Murgu, "Robotic bronchoscopy for pulmonary lesions: A review of existing technologies and clinical data," *Journal of Thoracic Disease*, vol. 12, no. 6, pp. 3279–3286, 2020, ISSN: 2072-1439. DOI: 10.21037/jtd.2020.03.35.

[10] Ethicon Inc. - Johnson & Johnson, *MONARCH™ Bronchoscopy*. [Online]. Available: https://www.jnjmedtech.com/en-US/product/monarch-bronchoscopy (visited on 12/21/2022).

[11] H. A. Jaeger *et al.*, "Anser EMT: The first open-source electromagnetic tracking platform for image-guided interventions," *International Journal of Computer Assisted Radiology and Surgery*, vol. 12, pp. 1059–1067, 2017. DOI: 10.1007/s11548-017-1568-7.

Chapter 2

Review on electromagnetic tracking systems and methods

This chapter outlines the results of a literature review on electromagnetic tracking (EMT). The review provides an overview of the current state of research on the topics that are the focus of this thesis.

After introducing general concepts on object tracking, the operation principles of EMT are presented in Section 2.2, where alternative tracking solutions are reviewed with focus on magnetic modelling and topology configurations.

Section 2.3 explains the requirement of EMT systems for medical applications and lists several procedures where EMT is already in use for computer-assisted interventions. Finally, magnetic distortion compensation techniques are reviewed in Section 2.4.

2.1 Object tracking

The position and orientation of an object are totally defined by six coordinates in a reference system for a total of six degrees of freedom (6 DOF), as shown in Figure 2.1. Three DOFs account for the position, e.g. x, y, and z in a Cartesian coordinate system, and three for the orientation, ρ, θ, and φ in a spherical coordinate system. Therefore, at least six independent equations are required to track an object in a constraint-free environment.

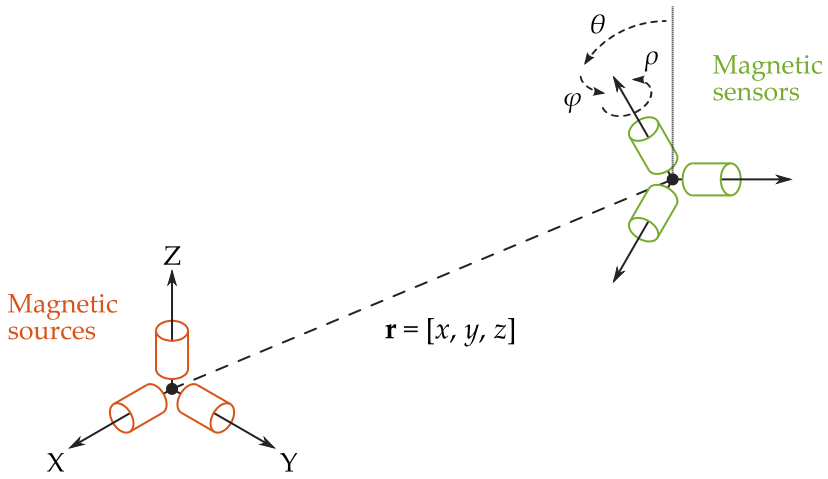


Figure 2.1: The magnetic sources generate a magnetic reference frame where unique magnetic field vectors characterise each position. The signal measured by the magnetic sensors is used to determine the relative pose, $[x, y, z, \rho, \theta, \varphi]$, between the sources and the sensors.

For an example solution, the two cameras of an optical tracking system can recognise the position of a marker within the field of vision in two dimensions and calculate the distance by triangulation, the third dimension. The presence of more than three markers, rigidly connected, allows for retrieval of the three-dimensional orientation. Note that a total of twelve constraints, two per marker per camera, was used to resolve the complete pose of the object (6 DOF). Redundancy in information makes the system more resilient to errors and noise.

Magnetic positioning includes all the techniques that use magnetic fields to find the position and orientation of an object. The geomagnetic field, magnets, electric currents, or any combination can be used as a magnetic field source. Magnetic tracking refers to the continuous magnetic positioning of an object in motion.

Electromagnetic tracking (EMT) is the magnetic tracking technique that involves magnetic fields generated by electric currents circulating in coils. The term *electromagnetic* can be misleading because EMT methods are not based on electric fields or electromagnetic waves, and effectively only static or quasistatic magnetic field physics applies. EMT is by far the most popular magnetic tracking method used in medical applications for reasons that will be discussed in this chapter.

In EMT, one uniaxial magnetic field measurement at a point in space provides one constraint to the position of that point. The presence of more magnetic fields, more sensors, or both, as long as they are arranged so that the measurements are independent, introduces additional spatial constraints and allows the collection of more information about the local magnetic field.

The basic principle of operation behind EMT is illustrated in Figure 2.1 and can be expressed as follows. The magnetic field is used as a reference frame for the free space, where each position is characterised by unique field vectors. The field effectively acts as a system of coordinates defined by the magnetic field map, which is the transformation from a rectangular coordinate system to the respective field values. The process of inferring the position of a point starting from the measured values of the field corresponds to an inversion of the transformation between the two coordinate systems.

For example, Figure 2.1 shows three orthogonal dipole-sources that define a X, Y, and Z Cartesian reference system. Each dipole is characterised by a magnetic moment, $\mathbf{m} = \mathbf{u_m} M$, where $\mathbf{u_m}$ is the unit vector that defines the dipole orientation, and $M\,[\mathrm{A} \cdot \mathrm{m}^2]$ is the moment magnitude.

Three orthogonal sensors are located at $\mathbf{r} = \mathbf{u_r} R$, where $\mathbf{u_r}$ is the unit vector in the direction from the dipole to the evaluation point, and R is the distance in metres. At the point in space $\mathbf{r}$, the magnetic flux density generated by a magnetic dipole source is [1]:

$$\mathbf{B}(\mathbf{r}) = \frac{\mu_0 M}{4\pi} \frac{3\mathbf{u_r}(\mathbf{u_m} \cdot \mathbf{u_r}) - \mathbf{u_m}}{R^3} \tag{2.1}$$

where μ_0 is the vacuum magnetic permeability.

The three dipole-sources, with magnetic moment magnitudes M_1, M_2, and M_3, generate three independent magnetic flux density vectors that can be organised in the columns of a matrix, $\mathbf{B_3}$, each calculated as per Equation 2.1. At a point located on the X axis, $\mathbf{u_r} = [1\,0\,0]^T$ and $\mathbf{B_3}$

simplifies to:

$$\mathbf{B_3} = \frac{\mu_0}{4\pi} \begin{bmatrix} \frac{2M_1}{R^3} & 0 & 0 \\ 0 & -\frac{M_2}{R^3} & 0 \\ 0 & 0 & -\frac{M_3}{R^3} \end{bmatrix} \tag{2.2}$$

Similarly, the three measured vectors obtained by a three-axis sensor form the rows of matrix $\mathbf{S_3}$. If the sensor is located on the X axis and is oriented along the main axes, the measurements correspond to the X, Y, and Z components of the three generated field vectors and, therefore, $\mathbf{S_3} = \mathbf{B_3}$.

In general, the sensor can be located in any direction from the origin, $\mathbf{u_r}$, that is identified by two angles, α and β. A rotation of $\mathbf{S_3}$ and $\mathbf{B_3}$ matrices, $R_{\alpha\beta}$, allows to express the equations in the same convenient reference system used in Equation 2.2:

$$R_{\alpha\beta}\mathbf{S_3} = \mathbf{B_3}R_{\alpha\beta} \rightarrow \mathbf{S_3} = R_{\alpha\beta}^{-1}\mathbf{B_3}R_{\alpha\beta} \tag{2.3}$$

Finally, the sensor can assume any roll, pitch, and yaw angles, with a rotation defined by the matrix $R_{\rho\theta\varphi}$, and the sensor measurement matrix is modelled by the following vector equation:

$$\mathbf{S_3} = R_{\rho\theta\varphi}R_{\alpha\beta}^{-1}\mathbf{B_3}R_{\alpha\beta} \tag{2.4}$$

Therefore, the nine measurements in $\mathbf{S_3}$ can be used to estimate the total of six degrees of freedom of the sensor relative to the source, three for the orientation in $R_{\rho\theta\varphi}$, and three for the position, the two direction angles in $R_{\alpha\beta}$ and the distance R in $\mathbf{B_3}$.

2.2 Fundamentals of EMT

The total freedom left to the realisation of a working EMT solution explains why there exist several EMT techniques which have been proposed. They mostly differ in the following aspects:

- System topology: how the field sources and magnetic sensors are arranged in space to generate independent constraints that depend on their reciprocal pose.
- Magnetic model: how the coupling between the source(s) and the sensor(s) is modelled to obtain the mathematical equations.
- Search algorithm: how the information captured by the magnetic sensor(s) is used to find the source-sensor reciprocal pose.
- Field generation: what technique is used to generate the magnetic flux density in the tracking region and what is its time dependence.
- Magnetic sensing: which sensor technology is used to measure the magnetic field.
- Signal multiplexing: how the magnetic fields from different sources are distinguished.
- Signal acquisition: how the signal is acquired, filtered, amplified, digitalised, and transmitted to the central computation unit.
- Final application: how the tracked pose is visualised or used by the system.

In principle, the solutions above are ideally independent as long as unique magnetic field components distinguish every pose in space. Then the magnetic flux density could assume any waveform, amplitude, geometrical shape, and spatial variation, and any sensor technology could be used to receive the signal, while the search method could be solved using any algorithm.

In reality, calculation methods depend on the sources and sensors' configuration as well as on the magnetic model used to describe their interaction, which in turn needs to be a good approximation of real physics. Some methods of signal multiplexing, like frequency domain multiplexing (FDM), are only available with AC magnetic fields. The acquisition chain must be optimised for the signal to be processed and for the sensor technology, which needs to be compatible with the field waveform and

amplitude range. The final tracking application and the environment where the system operates are essential factors in the choice of the field waveform, and the source and sensor dimensions and power consumption need to meet the limits imposed by the specific application.

Technical reviews on EMT systems typically focus on specific solutions for the system architectures, governing equations, and tracking methods [2–4], or they describe the EMT general principles on a high-level [5–7].

The following sections present a comprehensive review of varied EMT techniques found in the literature. In Sections 2.2.1 and 2.2.2, the methods are categorised based on the system topology and governing equations, whereas in Sections 2.2.3 and 2.2.4, magnetic sensing technologies commonly used in EMT applications are presented.

2.2.1 Magnetic models

The equations governing an EMT system describe the physical principle upon which the tracking method is based.

A first important consideration is that the mutual magnetic coupling between a source and a sensor is symmetric, i.e. in the mathematical model, the field generation and measurement stages do not need to correspond to reality. For example, the interaction between a single-axis sensor and a transmitting antenna could also be modelled as the magnetic field generated by a dipole source and received by a pick-up coil. We will refer as *marker* to the object tracked, regardless if it is a field source or a sensing element. With this in mind, in the following discussion, considerations made for magnetic sensors and transmitting coils are also valid for magnetic sources and receiving coils.

Typically, the sensor is sufficiently small that the gradient of the magnetic field can be considered locally uniform. In this case, the sensor measurement corresponds to the field *at* the sensor position and the magnetic coupling is completely modelled by the vector field component in the direction of the sensing axis.

An exact understanding of the real magnetic field is essential for accurate tracking. If the transmitting antenna is small relative to the sensor

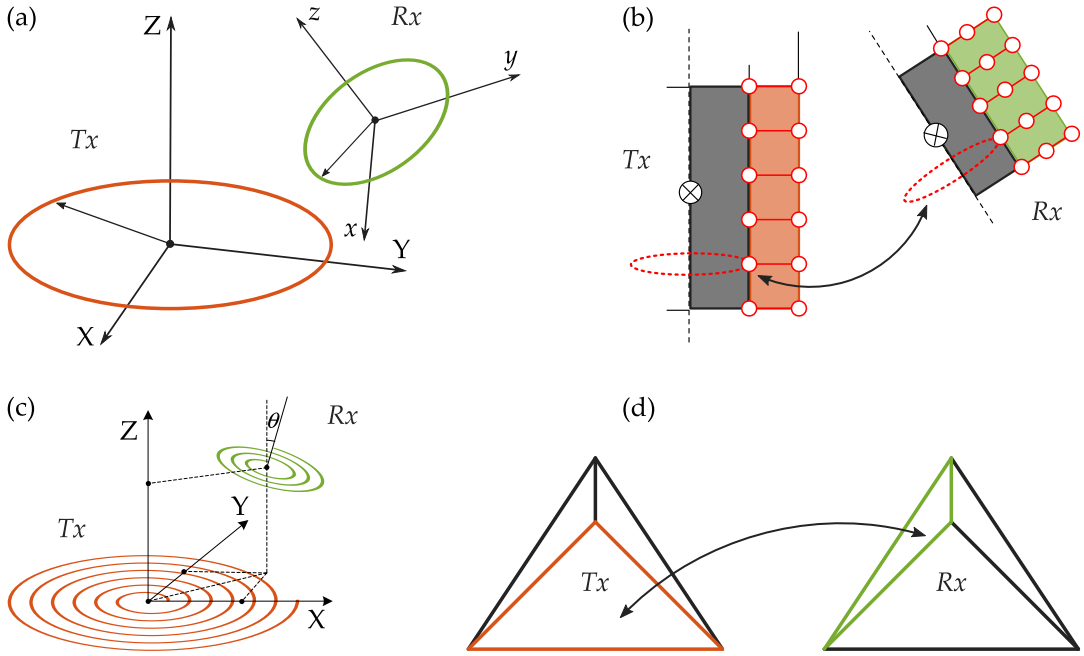


Figure 2.2: Magnetic models for spatially extended transmitting, Tx, and receiving, Rx, antennas. The mutual inductance is calculated using approximations such as (a) circular loops [18], (b) distributed loops [19], (c) spiral coils [20], and (d) straight-line conductors [21].

or far enough from it, it can be treated as a point dipole source. Otherwise, the field must be described using quadrupole or higher multipole expansion.

To minimise the complexity of the model, field generator coils are usually designed with shapes for which simple analytical formulations for the near magnetic field exist, such as elliptic integrals for circular or rectangular loops [8–10], low-order polynomials [11], or simple analytical expressions for magnetic dipoles [12, 13], current filaments [14], and current sheets [15].

In the case of spatially extended transmitting and receiving antennas, the magnetic field at one point is not enough to accurately model the magnetic coupling between the coils. The mutual inductance can be calculated using approximations like circular loops [16–18], distributed circular loops [19], spiral coils [20], or straight-line conductors [21–23]. Some of these models are illustrated in Figure 2.2 for reference.

The limits imposed by an analytical model can be overcome by volume characterisation, where the magnetic field values are measured at predefined locations [24–27]. This solution also effectively compensates for the presence of static magnetic distortions, such as passive shields or nearby electronics. Data-driven field models can be obtained from multi-variable function interpolation of look-up tables (LUT) [28–31], using neural networks trained on the data sampled [32–34], or fitting an underlying analytical physics-based model to the data [35, 36].

The field's spatial variation also plays an important role in increasing the resolution and precision of the tracking and ensuring fast and global convergence if the gradient is monotonic [27]. The system topology determines the reliability of the tracking method against noise and interference, and the arrangement of redundant coils can help in this regard [37, 38].

The shape of the magnetic field can be modified based on the sensor position to guarantee optimal tracking everywhere within the region of interest or to increase the tracking volume. Solutions include mechanical servoing [39–41], or methods where the emitter coils are rotated to point towards the sensor and deliver the maximum signal [42, 43]. However, these techniques might be of limited value if multiple sensors need to be tracked.

2.2.2 Tracking methods

The tracking methods available for a particular sources-sensors arrangement are mainly determined by the possibility of measuring the complete field vector or just one or two components of the field. The main solutions available for every configuration are reviewed in the following paragraphs.

2.2.2.1 Triaxial tracking

As seen in the example of Section 2.1, three-axis generation and measurement provide a total of nine non-independent equations, sufficient to determine the pose of a sensor relative to the source [44–46]. After initialisation, which involves solving for multiple trigonometric products

and sums, the equations can be linearised if small changes in the position and orientation are considered.

For the single source and single sensor case, each with three orthogonal axes, equation-based algorithms are available that might be used to increase the speed of the initialisation [47]. Multiple sources can be included in a second moment using a non-linear optimisation method to improve accuracy. The three-axis generation and sensing problem is further explored in [48], where a closed-form formulation was presented for linearly independent, but not necessarily orthogonal, magnetic dipoles.

To the best of our knowledge, solutions based on closed-form equations have only been proposed using the simple magnetic dipole model. Although other analytical field models might also accept closed-form solutions for the positioning algorithm, it is not certain that they would guarantee a lower computational cost relative to iterative algorithms with proper initial conditions.

Non-model-based EMT methods can make use of the mechanical rotation of the transmitting coil, accounting for two degrees of freedom [42, 43]. The same effect can be reproduced using three orthogonal coils to electrically rotate a virtual coil in any desired direction. The method does not use a magnetic model, the only assumption being that the maximum field magnitude is generated on the coil axis. The search algorithm stops when the two source-coils point towards the three-axis sensor and the maximum magnetic flux density vector is detected. The location and orientation can therefore be determined by triangulation. Similarly, a reference sensor at a known position can be included to reduce the effect of metallic distortions by measuring the time difference between the instants when the maximum field magnitude is detected by the known reference and by the tracking sensor in the presence of a rotating magnetic field [49].

Using the same configuration, a faster, direct, non-iterative algorithm was proposed, which does not involve mechanical or electrical rotation of the sources [50]. A further improved method with excellent anti-noise ability is based on the phase difference between the square of the excitation current of the magnetic sources and the square of the signal measured, allowing to directly triangulate the sensor location [51].

The same method applies to the reversed configuration, where a three-axis source is tracked using a uniaxial sensor rotated using two stepper-motors to control the horizontal and vertical rotation or using triaxial sensing to simulate a virtual electrical rotation [52, 53].

Spinning of a transmitting coil, of a permanent magnet [54, 55], or equivalently two orthogonal coils with quadrature currents, can be used to generate an elliptically rotating magnetic field vector at any point in space. In this case, the fast non-iterative tracking algorithm is based on the aspect ratio, size, phase, and orientation of the ellipse, which can be determined in a single period of excitation [56]. Based on the same topology, a simplified algorithm was proposed where only the amplitude and phase of the 3-axis sensing signals are required [57].

For closer range tracking, the dipole model can be improved if the coils are made of current sheets with constant current density [15]. Planar antennas with adequate shape can reproduce field generation in independent directions [58–60], and planar coupled coils can generate monotonic field gradients to quickly find the position [27, 61]. Similarly, three planar receiving coils can be designed to occupy the same volume without losing their linear independence [62].

If the field sources and sensors are not designed in shapes that can be modelled by simple analytical expressions, magnetic models may require considering a high number of contributions and have high computational cost, so discretised numerical field models [63] or data-driven neural network models [34] are preferred.

2.2.2.2 Biaxial tracking

An early application of EMT was used to determine the distance and angle between two vehicles [64]. Two perpendicular emitter coils are driven with quadrature currents to generate a rotating magnetic field, and two identical coils act as a receiver. The transmitter and receiver coils are assumed to be on the same plane, so only two degrees of freedom are involved. The phase difference between the two received signals provides information on the angular displacement, while the measured field magnitude indicates the distance.

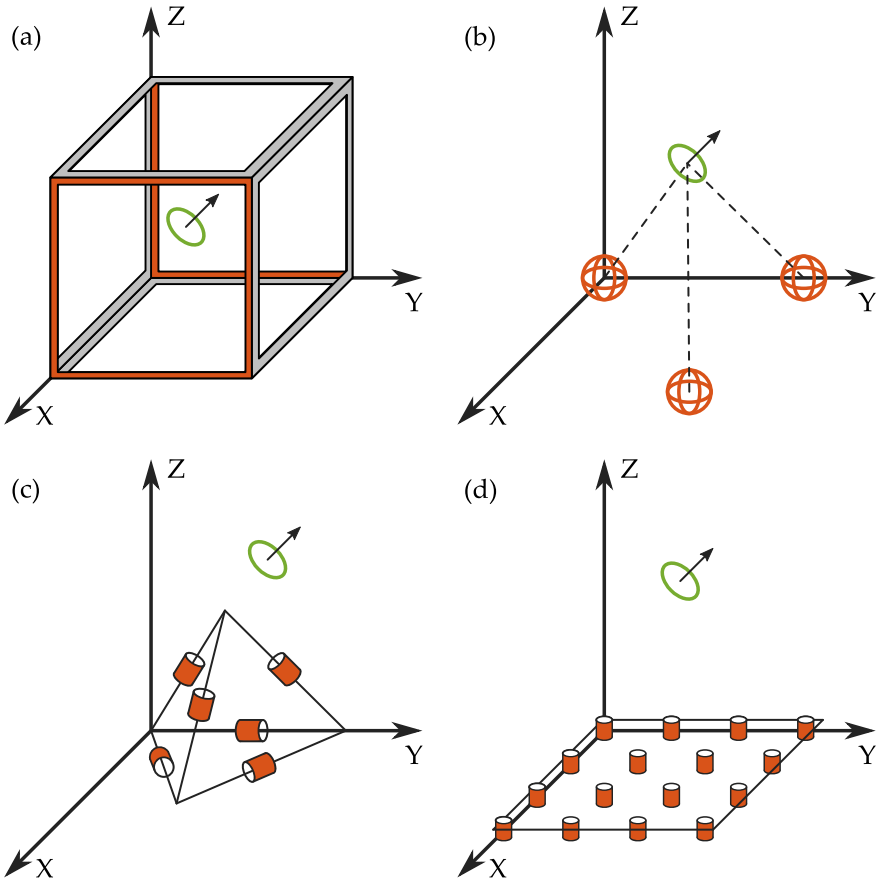


Figure 2.3: Alternative topologies for uniaxial tracking. (a) Rectangular cube transmitter [37]. (b) Triaxial sources or sensors [68]. (c) Tetrahedron configuration [69]. (d) Coplanar array of emitter coils [70].

Three-axis generation and biaxial sensing provide enough information to resolve the 6 DOF of the sensor [65–67]. Once again, additional sources can be included for redundancy and noise mitigation.

In general, all the methods presented in the next paragraph for uniaxial tracking can also be applied to the two axes of a biaxial sensor separately, where the two orientations allow for determining the roll angle, ρ.

2.2.2.3 Uniaxial tracking

Uniaxial sources or sensors are commonly used in EMT applications where the dimensions of the target marker must be limited. Typical topologies for uniaxial tracking are shown in Figure 2.3.

A small permanent magnet is a magnetic dipole that can be tracked by multiple external sensors. Alternatively, miniature transmitter coils can be used, powered from wires [68, 71], using resonance [41, 72–74], or with wireless power transfer [75, 76]. An unusual technique is based on the harmonics generated by a marker of high-permeability material operated on the saturation knee in the presence of an external AC field [77].

Using the configuration with internal magnetic field generation and external sensing, limitations on the dimension of the sensor are less strict and allow to have three sensing axes. Sensors can be arranged on a planar array [72, 78] or on a cube surrounding the tracking volume [52, 79], and the positioning algorithm is typically an iterative method, such as Levenberg–Marquardt, trust region, genetic algorithms, or particle swarm optimisation [80]. The layout should be optimised to maximise the SNR in the region of interest and reduce the number of sensing units. Nine sensors were found to be optimal [81, 82].

A fast Newton method was proposed for two triaxial sensors [68, 83], and an efficient linear algorithm exists when there are at least five three-axis sensors [84–86]. These fast methods can be used in conjunction with non-iterative methods to guarantee faster convergence to the global minimum.

Methods based on artificial neural networks (ANN) are particularly beneficial to low-power processors because, while training the network is computationally demanding, running a trained model is fast if the number of layers and nodes is limited. A closed-form approximation to the tracking problem was obtained using an ANN model to regress the transmitter pose directly from the measurements of three triaxial sensors [87]. ANNs can also be used to find the transmitter pose using four [88] or more [89] sensing units.

To extend the magnetic tracking range, a particle swarm optimisation method based on the magnetic dipole model was applied in the near-source zone. An ANN was adopted in the far field region, and an adaptive sigmoid function was used to fuse the two algorithms in the transition zone [90].

By measuring the magnetic field gradient tensor, a closed-form formula was proposed to localise a magnetic dipole [91]. Gradiometer-based methods can also be used to compensate for magnetic distortions, assuming that the error part of the magnetic field has smaller spatial derivatives than the dipole part, which is true if the interfering sources are much larger or are located further away [92].

From the mathematical point of view, the same methods presented above could be applied to the case of external triaxial sources and a uniaxial sensor marker, thanks to the reciprocity of the mutual magnetic coupling. However, it is more problematic to scale the number of sources rather than sensors because of the higher power requirements and the need to multiplex the signal. In contrast, multiple sensors can acquire measurements in parallel.

A rectangular cube transmitter configuration generates orthogonal fields with constant gradients for a simple analytical tracking algorithm [93]. However, in most cases, enclosing the tracking volume within the field generator is impossible.

Transmitting coils arranged on the edges of a tetrahedron are a good design solution for a compact field generator [69]. Alternatively, planar field generators can be realised comprising a large coplanar array of transmitting coils [70, 94], or eight coils arranged in an optimised layout [10, 14, 37, 95].

All these examples rely on iterative tracking methods because closed-form solutions are unavailable in the absence of triaxial generation or sensing.

2.2.3 Field generation

The hardware used to generate and measure the magnetic field must guarantee a stable, reproducible, and noise-free signal at every point within the region of interest.

2.2.3.1 Uniaxial sources

The main advantages of using a permanent magnet as the source of a DC magnetic field include a simplified system architecture, inherent safety due to the absence of electrical power, and the fact that no wires are required to connect the marker. However, the signal decays as the third power of the distance, as seen in Equation 2.1, limiting the maximum tracking range, which is typically between 10 to 20 centimetres [90]. Moreover, it becomes challenging to distinguish the pose of multiple markers and remove the contribution due to Earth's magnetic field.

A miniature transmitting coil can overcome all these disadvantages [68] but requires wires and electrical power delivery to the marker location, which may be unsafe in many EMT medical applications.

LC oscillators are a suitable option due to their passive nature and ability to be activated by an external magnetic field [41, 72–74]. The drawback is that they usually operate with a resonance frequency in the range of hundreds of kHz. Such frequencies can easily induce eddy currents in nearby conductive materials, and it becomes impossible to distinguish the oscillation due to the current in the marker from the field generated by undesired currents.

One possible workaround is using a lower frequency AC field to shift a magnetic core in and out of the saturation region [77]. Alternatively, electronic circuits can be included in the marker to analogically shift the response frequency in order to recognise it from interfering fields [75], or to convert the signal and transmit it over Bluetooth [27], binary frequency-shift keying [76], or other RF communication techniques [96].

2.2.3.2 DC and AC generation

Some magnetic navigation systems use external DC magnetic fields to steer tools wirelessly [97]. Localisation of the target is possible, for example, by using gradiometer-based methods [98] or an external array of sensors [99]. Similarly, the magnetic fields generated during magnetic resonance imaging (MRI) can be measured for tracking [100–102]. In these

examples, the advantage is a single system that provides both tracking and actuation or tracking and imaging.

One way to reduce the number of field generation elements is by measuring and leveraging the local geomagnetic field [103]. An efficient way to generate AC magnetic fields is by inducing a spin on spherical permanent magnets within enclosures [54, 55]. The main disadvantage is the presence of moving elements that can deteriorate faster.

When multiple field sources are present, it is essential to recognise the contribution given by each of them [3]. For DC magnetic fields, the only possibility is to activate the generating coils sequentially [104]. This technique could be slow, especially for topologies comprising many transmitting coils, for example, when uniaxial sensors are used. However, waiting for the complete excitation cycle to run the tracking algorithm is not required, as the pose can be updated after every new field measurement [105].

AC field-based EMT systems operate from 1 kHz [106] to 400 kHz [107]. AC magnetic fields are commonly employed because they allow for higher SNR, faster frequency-based demodulation techniques, resilience to low-frequency noise, or in general minimal interference ability from frequencies different from the transmitting channels. All these benefits enable higher dynamic response and larger tracking volumes, typically up to 60 centimetres [7].

2.2.3.3 Multiplexing techniques

Several signal multiplexing techniques are available for AC fields, including frequency division multiplexing (FDM), amplitude or frequency modulation [108], and spread spectrum or phase multiplexing [109]. Time division multiplexing (TDM) is also a possibility, but not convenient in this case [110], because with FDM, it is possible to achieve higher update rates, reduced latency, and lower noise. Moreover, FDM enables multiple sensor tracking, compatibility between different EMT systems working next to each other on a continuous basis [31], as well as modular configurations where multiple field generators can be used in conjunction [111, 112].

Although it is easier to generate and demodulate sinusoidal waveforms, in many environments, the use of AC fields is significantly limited by surrounding conductive materials and eddy currents distortion. Alternative excitations can be used in this case, such as DC pulsed [113, 114], quadratic [115], or linear ramps [116]. For these methods, FDM is not possible.

Ideally, a system could employ two excitation patterns, an eddy-current-free method with TDM, which is slower and more affected by random noise, and an AC signal with FDM, which is faster and more precise but suffers from systematic errors due to distortions. The two solutions can then be fused using a Kalman filter approach [117]. Combining lower and higher frequencies is also possible [118, 119].

2.2.4 Sensor technology

A variety of magnetic sensors are available for EMT systems [120, 121]. Typically, in the presence of time-varying magnetic fields, search coils are used to measure the time derivative of the magnetic flux density component in the direction of the coil axis [122]. This method offers an inexpensive and passive solution for high-sensitivity sensing, especially when the field frequency is high or the waveform has a steep slope.

For low-frequency AC fields, fluxgate sensors are better-suited [123], whereas superconducting quantum interference devices (SQUIDs) [83] and Hall-Effect sensors [124] are commonly used to measure static magnetic fields [125, 126].

For DC fields, another promising technology is based on magneto-resistive sensing elements, or xMR effect sensors [127], e.g. anisotropic magneto-resistance (AMR), giant magneto-resistance (GMR), tunnelling effect (TMR) [90]. The use of novel magnetoelectric sensors for EMT was recently proposed [128–130].

The main advantage of DC sensors is that they usually provide triaxial measurements in digital form. However, this comes at the cost of needing a power supply, larger dimensions compared to miniature inductive coils,

and the same disadvantages discussed for EMT systems with DC magnetic fields.

2.3 EMT for computer-assisted interventions

EMT systems can be used in various industrial, military, and biomedical applications [131].

Examples include body motion tracking [132, 133], tracking of hand controllers or head-mounted devices for augmented and virtual reality [34], automated guided vehicles [134], indoor positioning [135–137]. In military applications, the use of EMT was demonstrated in flying object tracking, helmet-mounted sight (HMS), and head trackers for armoured vehicles [108].

Typically, the applications mentioned above require a lightweight system, battery-powered, with low computational requirements, and capable of tracking fast movements. For these reasons, these systems are usually based on EMT methods involving triaxial sensing and closed-form analytical solutions.

Conversely, intra-body navigation systems for medical applications usually require much smaller marker sizes. However, they are less concerned with the system cost, power consumption, and dimension and weight of external components [138, 139]. In this case, the typical architecture consists of an external field generator and a small magnetic sensor used as a marker attached to the tracked instrument.

Magnetic sensors used in endoscopic applications are generally inductive pick-up coils, which are passive and therefore reduce the risk to the patient in the event of a malfunctioning medical device, compared to active devices [140]. Such coils can be manufactured to miniature sizes of less than 0.3 mm in diameter, and they provide high sensitivities in the presence of time-varying magnetic fields [141, 142]. However, recent improvements in miniaturisation and sensitivity of Hall sensors might enable new applications for tracking surgical tools with integrated magnetometers [143, 144].

As opposed to optical navigation systems, EMT enables tracking and navigation during image-guided interventions with no line-of-sight limitation [145, 146]. The goal is to provide the surgeon with real-time information about the position and orientation of surgical instruments, allowing them to perform more precise and accurate procedures [147].

Applications of EMT in medicine include: clinical diagnosis or therapy with flexible bronchoscopy [148, 149], orthopaedic procedures [150, 151], percutaneous hepatic interventions [152, 153], percutaneous vascular access and catheterisation [154, 155], EP navigation and mapping [156], ENT needle navigation [157], and neuronavigation in pediatric neurosurgery [158].

The technology also finds application for guidance in flexible robotic surgical devices [159, 160], e.g. for catheter tracking for atrial fibrillation treatment and ablation [161–163]. A multitude of magnetic sensors can be used for the real-time shape estimation of curvilinear flexible surgical robots in minimally invasive surgery [164–166].

Multi-modal imaging applications combine EMT with traditional interventional radiology imaging [167, 168], ultrasound [169], or other local imaging modalities, and the output can be visualised in the form of virtual or augmented reality [170].

All EMT biomedical applications mentioned above operate in a wired manner, meaning that they require a physical connection to transmit sensor readout data. Wireless products require larger markers due to the need to include a battery and electronic circuitry.

For this reason, the only solutions can be found for wireless robotic capsule endoscopy [4, 171, 172] or for tumour tracking [173], where the operational space is larger, and capsule sizes of several millimetres are acceptable. Medical capsule robots are used for diagnostics, drug delivery and surgical treatment [174], where external magnets can be present for manipulation and actuation [6].

Wireless methods are made possible by introducing permanent magnets [84] or three-axis sensors and battery-powered electronics [76, 175–177] inside the capsule. Battery-less methods include resonant antennas with a divide-by-3 circuit to separate the transmitting and receiving fre-

quencies [75] or a wireless power transfer link and digital transmission [27, 76].

There is ongoing research and development in the field of EMT to improve the capabilities of wireless systems and to reduce the size and weight of the sensors. Solutions may involve the development of new wireless communication technologies or using more energy-efficient sensors and energy-harvesting techniques.

2.3.1 Commercial systems

Several magnetic tracking systems are commercially available for medical applications in the market. They can either be sold alone or in the form of integrated surgical navigation systems.

NDI (Northern Digital Inc., Waterloo, Canada) [178] offers two medically approved EMT systems, Aurora and 3D Guidance, which are the most popular commercial solutions. Other original equipment manufacturers (OEM) of EMT systems available in the market are Radwave (Radwave Technologies Inc., MN, USA) [179] and DeepTrack (Quadrant Scientific, Cork, Ireland) [180].

Systems that integrate the OEM Aurora system include, among others:

- SCOPEPILOT (PENTAX Medical, Hamburg, Germany), which provides intuitive navigation in colonoscopy [181];
- MediGuide Technology (Abbott Laboratories, Chicago, IL, USA) [182] and Rhythmia™ (Boston Scientific Corporation, Marlborough, MA, USA) [183], to facilitate cardiovascular procedures in the electrophysiology (EP) mapping and navigation;
- the SPiN System™ (Veran Medical Technologies, St. Louis, MO, USA), used in image-guided bronchoscopy [184];
- the MONARCH™ Platform (Ethicon Inc., Johnson & Johnson, Raritan, NJ, USA), which enables robotic endoscopy [185];
- the EMT platforms proposed by Brainlab (Munich, Germany), for neurosurgery and ENT navigation [186];



(a) (b) (c) (d)

Figure 2.4: Examples of clinical applications for magnetic tracking technology: (a) Pentax ScopePilot, colonoscopy; (b) Boston Scientific Rhythmia, EP navigation; (c) Veran SPiN, thoracic navigation; (d) Auris Monarch, robotic bronchoscopy.

- the Fiagon ENT Navigation System (Fiagon GmbH, Hennigsdorf, Germany) [187].

Some of these systems are shown in Figure 2.4.

In addition, commercial EMT systems based on proprietary technology other than NDI are:

- ScopeGuide (Olympus Corporation, Shinjuku, Tokyo, Japan), for colonoscopy and enteroscopy [188];
- the CARTO©3 System (Biosense Webster, Irvine, CA, USA), for catheter-based applications in current clinical environments [189];
- superDimension™ (Medtronic, Minneapolis, MN, USA), for airway navigation [190];
- the Sirio navigation system (Masmec Biomed, Bari, Italy), for interventional radiology [191];
- EndoScout Tracking System (Robin Medical Inc., Baltimore, MD, USA), for MRI applications [192];
- the tracking solutions proposed by Polhemus (VT, USA) [193].

Depending on the application, such systems offer EMT sensors in a variety of sizes, with diameters as small as 0.3 mm up to 10 mm, and configurations which are stand-alone or integrated inside surgical instruments. They typically have a tracking range of 50 cm to 60 cm where a resolution of about one millimetre and about one degree is guaranteed [7].

2.3.2 Limitations

Although available EMT systems might work well for the application for which they are designed, they lack the flexibility required for research investigations.

The black-box nature of these systems limits the users to a few possible settings and configurations and leaves little or no space for modifications in the software or hardware required for technology improvement.

Another relevant factor is the prohibitive price of such products, even in the most basic configurations, which typically is on the order of 10k euros for a complete functioning system. Smaller institutes or research groups with fewer resources and laboratories in poorer regions of the world may not have the budget to afford these expenses and start doing fundamental research to improve the current EMT solutions.

These considerations led to the development of the ANSER EMT project that is presented in the next Chapter 3. The platform design files and software algorithms are made available for free under Creative Commons license, and it is estimated that the hardware components necessary to assemble a fully operating system can be sourced in Europe for less than 300 euros.

2.4 Magnetic field distortion

EMT systems for computer-assisted interventions are applied in the highly variable environment of the operative room. They are surrounded by other instrumentation that generates magnetic fields interfering with the accuracy of position measurements or by equipment containing metallic materials that may modify the ideal magnetic field [194, 195].

The wires connecting the sensor might also be a source of undesired signals where small gaps in the twisted pair pick up stray fields produced by nearby electronic devices, including the internal electronic components of the EMT system, power lines, or the field generator [196]. Foils of aluminium or copper might be used for signal shielding. However, such shields increase the wire diameter and are more effective at higher frequencies, whereas this kind of interference particularly affects smaller sensors and lower frequencies because of the lower sensitivity. One solution is to use a polarity inverter to periodically reverse the coil terminals and cancel the signal coming from the wires [197].

Assuming that the magnetic coupling between the transmitters and the sensors is modelled correctly and that the measurements are reliable and clean, tracking errors can occur if the real magnetic field is modified in a way that is not accounted for in the model.

Different materials might have opposite distortion effects [198]. Ferromagnetic materials provide an alternative low-reluctance path and therefore alter the shape of the reference magnetic fields, both for DC and AC-based EMT systems. The error is reduced with increasing frequency because the magnetic permeability of the distorting material decreases. In general, the signal is amplified, causing the sensor to appear nearer to the excitation source. AC magnetic fields induce eddy currents in nearby conductive materials, which generate secondary fields at the same frequency as the excitation field. Eddy currents are proportional to frequency and tend to oppose the field variation, making the sensor appear further from the field generator.

Figure 2.5 shows the equivalent circuit for the mutual coupling between a transmitting coil, a conductive distorter, and an inductive sensor coil. It can be noticed that the distortion effect is minimal if the metal is either far from the field generator, in which case the mutual inductance M_{DT} is low and the eddy currents are reduced, or far from the receiving coil, when M_{SD} and then the interfering field are low. Similar considerations apply to ferromagnetic materials, where the magnetisation strength is proportional to the received magnetic field.

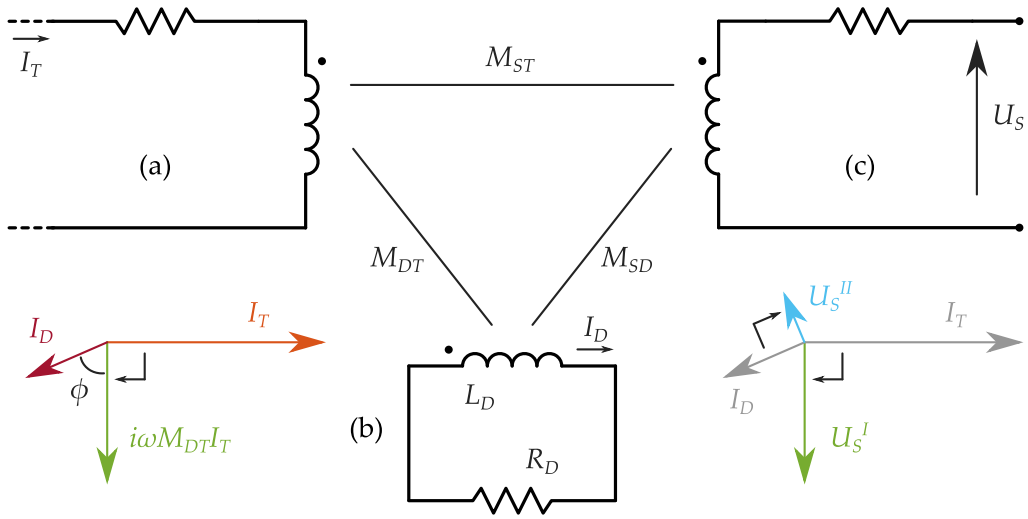


Figure 2.5: Equivalent RL circuit model for (a) one transmitting coil, (b) one conductive distorter, and (c) the inductive sensor coil.

The following sections review the main solutions for distortion compensation employed by EMT systems, with a focus on tracking with uniaxial sensors for biomedical applications.

2.4.1 Eddy currents reduction

Eddy currents generation could be entirely avoided by using DC [113] or quasi-DC magnetic fields [199]. However, to date, only inductive pick-up coils can be manufactured to the miniaturised dimensions required by many medical applications. Such sensors measure the magnetic flux variation and, therefore, can achieve high sensitivities even with low-magnitude magnetic fields if the field time variation is fast. In this way, higher SNR and a larger tracking range are guaranteed. The use of AC signals allows for a narrow bandwidth, further reducing the susceptibility to interference and low-frequency noise.

With reference to Figure 2.5, using the complex notation with $i = \sqrt{-1}$, if the current I_T is a sine-wave at angular frequency ω, the voltage induced on the sensor coil by the magnetic flux generated by the transmitter coil is:

$$U_S^I = i\omega M_{ST} I_T \tag{2.5}$$

In the presence of a conductive material, the contribution given by the eddy-current field is:

$$U_S^{II} = i\omega M_{SD} I_D = -\omega^2 \frac{M_{SD} M_{DT} (R_D - i\omega L_D)}{|Z_D|^2} I_T \tag{2.6}$$

where the current I_D was calculated as:

$$I_D = \frac{i\omega M_{DT} I_T}{R_D + i\omega L_D} = \frac{i\omega M_{DT} I_T}{|Z_D|} e^{-i\phi} \tag{2.7}$$

with $|Z_D| = \sqrt{R_D^2 + \omega^2 L_D^2}$ and $\phi = \arctan {}^{\omega L_D}/_{R_D}$.

The total normalised voltage measured by the sensor is given by:

$$\frac{U_S}{i\omega I_T} = \frac{U_S^I + U_S^{II}}{i\omega I_T} = M_{ST} + \omega \frac{M_{SD} M_{DT} \omega L_D}{|Z_D|^2} + i\omega \frac{M_{SD} M_{DT} R_D}{|Z_D|^2} \tag{2.8}$$

which has a component in phase with the original undistorted signal, $U_d = \mathfrak{Re}\left(\frac{U_S}{i\omega I_T}\right)$, and a component in quadrature, $U_q = \mathfrak{Im}\left(\frac{U_S}{i\omega I_T}\right)$.

From Equation 2.8, it can be noticed that:

$$M_{ST} = U_d - U_q \frac{\omega L_D}{R_D} = U_d - U_q \frac{\omega}{\omega_D} \tag{2.9}$$

where $\omega_D = {}^{R_D}/_{L_D} = {}^{1}/_{\tau_D}$ is the characteristic frequency of the conductive distorter.

In other words, it is possible to calculate the contribution given by the distortion by adequately scaling the quadrature component of the measurement, U_q, and then recover the undistorted signal by removing the distortion from the direct component, U_d.

The unknown ω_D can be included in the tracking algorithm as an additional degree of freedom or can be calculated using redundant measurements at fixed, known points, assuming that it does not change for different transmitter coils and different sensors [200]. However, R_D and L_D depend on the path followed by the magnetic flux density lines and, therefore, they are likely to change for sources and sensors at different relative positions [201].

To overcome this problem, every coil might generate two AC fields at different frequencies, ω_1 and ω_2, if the two frequencies are similar so that R_D and L_D can be considered to not change [202]. In this way, two equations like Equation 2.9 are obtained which can be solved for ω_D:

$$\omega_D = \frac{U_{q1}\omega_1 - U_{q2}\omega_2}{U_{d1} - U_{d2}} \tag{2.10}$$

One way to generate multiple frequencies on the same coil is to frequency modulate the current. For example, if $I_T = \cos(\omega t + \alpha \sin(\omega_m t))$, the signal contains satellite harmonics at $\omega \pm n\omega_m$ with amplitude ${}^{(0.5\alpha)^2}/_{n!}$. Using the symmetry of the first two satellite components, $\omega + \omega_m$ and $\omega - \omega_m$, an alternative closed-form formula was proposed to compensate for the distortion [108].

Multiple frequencies per coil can also be generated through harmonically rich waveforms, such as square or triangular waves. With more than two frequencies, it is possible to resolve multiple distortion sources. For instance, in the presence of j distorters, the total normalised voltage on the sensor may be written as:

$$U_S = k \sum_j \frac{z_j + i\omega}{p_j + i\omega} \tag{2.11}$$

and the eddy currents reduction is obtained by collecting sufficient data to estimate the parameters k, z_j, and p_j [203].

All methods presented above become unstable when $\omega_D \ll \omega$, which is the case if the distorting material is mainly inductive, $R_D \ll L_D$, or for higher signal frequencies, ω. In both cases, the distortion mainly acts on the direct component of the field and becomes difficult to recognise and correct if the magnitude of the out-of-phase signal is small.

Alternative non-sinusoidal excitation methods take advantage of the fact that the signal induced by the magnetic flux density coming from the field generator is proportional to the first derivative of the current in the transmitter coil, whereas the eddy currents distortion follows the second derivative.

With reference to Figure 2.5, the total sensed voltage, U_S, is given by Equation 2.12 in the Laplace domain:

$$U_S = sM_{ST}I_T + s^2\frac{M_{SD}M_{DT}}{R_D + sL_D}I_T \tag{2.12}$$

If I_T is a ramp function, $I_T(s) = s^{-2}$, the first term of Equation 2.12 becomes a constant step, and the second term exponentially decays to zero. In the time domain:

$$U_S(t) = M_{ST} + \frac{M_{SD}M_{DT}}{L_D}e^{-\frac{t}{\tau_D}} \tag{2.13}$$

where $\tau_D = {}^{L_D}/_{R_D}$ is the time constant of the current path in the distorter.

The time constant depends on the material's conductivity, permeability, shape, and position relative to the field generator. For an aluminium disk, a brass disk and a neurological reflex hammer, τ_D was measured to be in general below 5 ms [116].

The necessity to wait for the transient to fade out increases the system latency and reduces the pose refresh rate. Moreover, without changing the maximum magnetic field generated, a longer acquisition time implies a smaller time derivative and a reduction in sensitivity. A workaround is to sample points in a number sufficient to fit an exponential curve to the transient signal and estimate the steady state value [31].

Quadratic excitation was also proposed [115, 204, 205]. In this case, the signal induced directly by the transmitter is a ramp with a constant slope, whereas the distortion adds a DC offset. The system's transient behaviour was characterised by the response to a rectangular waveform and removed from the signal. Linear regression can be used to calculate the signal slope, which only depends on the undistorted magnetic field.

As for DC field-based methods, non-AC excitation techniques need to use time division multiplexing (TDM) and suffer from slower update capabilities and susceptibility to low-frequency noise. On the other hand, they are compatible with inductive sensors and guarantee higher SNR if the field variation is high.

EMT systems can combine two frequency components, where a very low frequency, immune to distortion, is used to correct the measurement at the higher frequency [206, 207]. However, this approach also has some limitations because the lower sensitivity of the low-frequency measurement can result in higher errors and less accuracy.

Possible improvements might be accomplished by combining AC and non-AC methods, such as using adaptive switching between sinusoidal and ramp excitation or characterising the distortion properties during the transient of the step response and then correcting the sinusoidal waveform as per Equation 2.9.

2.4.2 Volume characterisation

Measurement and calibration of static distortion is a fundamental task aimed to compensate for systematic tracking errors due to imperfect modelling or caused by magnetic distortions in a given clinical environment [25, 208, 209].

Volume characterisation can be obtained on two levels: correcting the tracked position and orientation or adjusting the field model to match the field measurements.

In the first case, the EMT error is evaluated within the region of interest, and an error map is created from the distorted EMT pose to the compensated one. In general, the error is also orientation dependent and, therefore, an accurate mapping must include sensor orientation information [30]. In the second case, a characterisation of the real magnetic field is generated based on simulations or experimental measurements at reference positions within the workspace.

Calibration approaches based on the correction of the tracking sensor pose are suitable for low to mild distortion scenarios. However, they cannot be used for highly distorted environments when the mismatch between the model and the real magnetic field is such that the tracking algorithm may converge to local minima or not converge. In these cases, creating a field map rather than an error map is advantageous for the following reasons: the magnetic field is only a function of the location,

not of the sensor orientation, faster convergence of the tracking algorithm is generally attained, and both EMT position and orientation errors are automatically corrected.

Several techniques have been proposed to build the distortion map, which can be classified into an analytical model fit to the collected data, global interpolation of scattered points, and local interpolation methods of regular grids [32, 210]. Calibration techniques include polynomial regression, radial basis function (RBF) interpolation [208], and neural network-based methods [33, 211]. In general, the error correction method must be designed for the specific EMT system and environment configuration [196].

Once the error map is generated, the effect of the magnetic distortion on the position and orientation errors can be visualised through markers of different shapes and styles [25, 30], grid representations [208, 212], or illuminated streamlines [213], among other methods. The error may be displayed to the user [214].

Similarly, methods of building a data-driven magnetic model include fitting of an underlying analytical model [215], interpolation of the field values stored in a look-up table [216], artificial and convolutional [34, 217], and random forests [218], among others.

In both error or field mapping cases, reference positions can be physically defined by a calibration phantom, a robotic system, or obtained using an accurate, undistorted tracking system, such as an optical tracking system [213, 219]. Typical solutions include the use of Lego blocks (The Lego Company, Billund, Denmark) [220, 221], phantoms of polycarbonate [222–224], or other mechanical structures [225].

The characterisation can be performed as a one-time factory calibration, the first time after installing the system in a new environment, any time the tracking accuracy is degraded, or every time before starting a medical procedure. The process can be complex and time-consuming, and using external systems for optical reference or robotised movements is not always feasible inside the environment of the operative room. Solutions have been proposed to make data acquisition simpler and more portable. Some solutions include: using free-hand mapping constrained

on fixed planes [220], building fixtures containing multiple sensors [143, 226], designing Lego-like modular blocks containing magnetometers [227], or using a combination of static and hand-held calibration tools [216].

Characterisation techniques cannot compensate for dynamic distortions originating from distorters that change position relative to the field generator, such as surgical tools or movable imaging machines. One way to revert back to the static distortion problem is to incorporate the EMT system within the medical equipment that may cause distortions, e.g. C-arm fluoroscopy machines [63, 228, 229], surgery and imaging tables [230, 231], or ultrasound probes [232–234]. However, this solution may be challenging to implement on existing equipment and should be included at the design and manufacturing stage instead.

2.4.3 Passive shielding

The error mapping techniques presented in Section 2.4.2 become ineffective if the environment changes and for severe magnetic distortion, in which case different physical spatial points may be determined to be the same position in the EMT domain [235].

For this reason, many surgical navigation systems employ magnetic shielding to prevent the field lines from encountering metallic materials [236]. A standard configuration is a flat field generator placed below the patient, with shielding to avoid distortion from the surgical bed [237].

Magnetic shields might be made of high-permeability materials, effective for DC and AC systems, or conductive material for AC systems [238]. In the first case, the field magnitude increases in the region above the field generator. In the second case, eddy currents in the conductive shield oppose the field variation, therefore reducing the signal. However, conductive aluminium plates are generally cheaper and provide a better shielding effect against higher-frequency interference.

A solution is then the use of two layers, including a non-conductive high-permeability material, such as ferrite or mu-metal, placed on top of a conductive plate [235]. Current loops placed around the periphery of the field generator might also be employed to nullify edge fields [239].

The magnetic shield is a significant source of static distortion that acts in a stable and repeatable manner. Thus, it is possible to accurately characterise the magnetic field vectors in the tracking volume. Methods include the use of finite element analysis to solve the magneto-quasistatic problem and compute the magnetic flux density at mesh nodes, or the use of data-driven approaches such as the mapping techniques presented in Section 2.4.2 [240].

When the EMT device is used in a multi-modal imaging navigation system, the presence of the shield might affect the quality of fluoroscopy images [241, 242]. Solutions have been proposed, including using radio-translucent materials [243–247], or spatial configurations of the transmitting coils to leave an open window in the centre where the X-rays are not absorbed [231, 248].

2.4.4 Online compensation

Online distortion compensation techniques operate in real time during the navigation procedure. These methods can be applied to correct errors caused by dynamic magnetic distortions or to update the registration between the pre-operative image and the EMT reference.

Such methods are typically based on redundant measurements, which can be obtained using multiple field generators [249] or multiple sensors fixed around the region of interest [250]. Fiducial markers can be placed on the patient skin to record the motion and the deformation of the surface of the EMT domain, using anatomical body models to predict how internal organs move and deform [251, 252].

Witness sensors measuring the magnetic field vector at known spatial points close to the volume of interest give information on the amount of distortion if the measurements deviate from the expected values [253]. Different surgery tools might exhibit a specific distortion fingerprint, which can be pre-characterised and recognised during the procedure using an array of sensors [254, 255]. In addition, the contribution due to external distortions can be estimated by measuring the first and second-order derivatives of the magnetic field vector [92]. More advanced methods

might use such reference sensors to enable real-time field mapping and use the updated model to predict and remove distortions [35, 36].

SLAM (Simultaneous Localisation and Mapping) is a technique used in robotics and computer vision to create a map of an unknown environment and, at the same time, locate the position of a device within that environment [256, 257]. By constantly updating the map of the environment and the device location within it, SLAM can help correct any errors in the measurements.

For example, the ambient magnetic distortion was modelled and used as a landmark for tracking, using sensor fusion with IMUs or cameras, for controller tracking [258] or indoor localisation [136, 259]. In clinical applications that include endoscopic or surgical cameras, the camera images can be used to optimise the EMT solution for more robust surgical navigation [260].

Additional information upon which a SLAM method is based might also come from the known reciprocal position of multiple magnetic markers rigidly fixed on the target instrument [261, 262]. Using this approach, an extended Kalman filter simultaneous localisation and mapping (EKF-SLAM) method was proposed for real-time EMT error mapping and compensation [263].

The method was tested in the presence of static field distorting samples that were not previously characterised and allowed the generation of an error map based on a multivariate Gaussian model, which was simultaneously used to correct the EMT position [264]. The distance between the sensors must be larger than the spatial variation of the distortion field. In this way, some sensors provide undistorted measurements and can be used for localisation, whereas the sensors entering a region affected by distortion are used to record and model the error.

The method was subsequently applied for tracking ultrasound probes with application in high-dose-rate prostate brachytherapy [265] and transbronchial needle aspiration [266]. A similar SLAM technique was formulated using particle filtering for compensation of breathing artefacts [267].

2.5 Conclusions

This chapter provided the background to the research topics that are the focus of this thesis. Alternative EMT methods and applications were introduced, and traditional distortion compensation techniques were presented.

In this context, the EMT system used in this thesis work is based on the uniaxial tracking of inductive sensor coils with a planar topology of magnetic sources, which are modelled by straight-line conductors. Further details of this system will be given in the next Chapter 3.

References

[1] D. J. Griffiths, *Introduction to Electrodynamics*. Englewood Cliffs, N.J: Prentice-Hall, 1981, ISBN: 978-0-13-481374-5.

[2] C. Park *et al.*, "Technical Review: Electromagnetic Sensor System for Localization of Medical Devices," in *2018 IEEE International Conference on Consumer Electronics - Asia (ICCE-Asia)*, 2018, pp. 206–212. DOI: 10.1109/ICCE-ASIA.2018.8552100.

[3] H. Ren and J. Sun, Eds., *Electromagnetic Actuation and Sensing in Medical Robotics* (Series in BioEngineering). Singapore: Springer Singapore, 2018, ISBN: 978-981-10-6034-2 978-981-10-6035-9. DOI: 10.1007/978-981-10-6035-9.

[4] X. Duan, "Chapter 10 - Magnetic tracking and positioning in endoscopy," in *Magnetic Materials and Technologies for Medical Applications*, ser. Woodhead Publishing Series in Electronic and Optical Materials, A. M. Tishin, Ed., Woodhead Publishing, 2022, pp. 287–338, ISBN: 978-0-12-822532-5. DOI: 10.1016/B978-0-12-822532-5.00013-3.

[5] A. M. Franz, T. Haidegger, W. Birkfellner, K. Cleary, T. M. Peters, and L. Maier-Hein, "Electromagnetic Tracking in Medicine—A Review of Technology, Validation, and Applications," *IEEE Transactions on Medical Imaging*, vol. 33, no. 8, pp. 1702–1725, 2014, ISSN: 0278-0062. DOI: 10.1109/TMI.2014.2321777.

[6] J. J. Abbott, E. Diller, and A. J. Petruska, "Magnetic Methods in Robotics," *Annual Review of Control, Robotics, and Autonomous Systems*, vol. 3, no. 1, pp. 57–90, 2020. DOI: 10.1146/annurev-control-081219-082713.

[7] A. Sorriento *et al.*, "Optical and Electromagnetic Tracking Systems for Biomedical Applications: A Critical Review on Potentialities and Limitations," *IEEE Reviews in Biomedical Engineering*, vol. 13, pp. 212–232, 2020, ISSN: 1941-1189. DOI: 10.1109/RBME.2019.2939091.

[8] M. R. Schneider, "Electromagnetic tracking for catheter localization," in *Biomedical Diagnostic, Guidance, and Surgical-Assist Systems*, vol. 3595, International Society for Optics and Photonics, 1999, pp. 61–68. DOI: 10.1117/12.351518.

[9] M. Schneider, "Measuring position and orientation using magnetic fields," US6073043A, 2000. [Online]. Available: https://patents.google.com/patent/US6073043A/en (visited on 01/22/2020).

[10] A. Plotkin, O. Shafrir, E. Paperno, and D. M. Kaplan, "Magnetic Eye Tracking: A New Approach Employing a Planar Transmitter," *IEEE Transactions on Biomedical Engineering*, vol. 57, no. 5, pp. 1209–1215, 2010, ISSN: 0018-9294. DOI: 10.1109/TBME.2009.2038495.

[11] P. Gilboa, "Object tracking using a single sensor or a pair of sensors," US6615155B2, 2003. [Online]. Available: https://patents.google.com/patent/US6615155/en (visited on 02/07/2020).

[12] E. Paperno and A. Plotkin, "Cylindrical induction coil to accurately imitate the ideal magnetic dipole," *Sensors and Actuators A: Physical*, vol. 112, no. 2, pp. 248–252, 2004, ISSN: 0924-4247. DOI: 10.1016/j.sna.2004.01.004.

[13] J. Xie *et al.*, "The Simulations and Experiments of the Electromagnetic Tracking System Based on Magnetic Dipole Model," *IEEE Transactions on Applied Superconductivity*, vol. 24, no. 3, pp. 1–4, 2014, ISSN: 2378-7074. DOI: 10.1109/TASC.2013.2283773.

[14] K. O'Donoghue *et al.*, "Catheter Position Tracking System Using Planar Magnetics and Closed Loop Current Control," *IEEE Transactions on Magnetics*, vol. 50, no. 7, pp. 1–9, 2014, ISSN: 0018-9464. DOI: 10.1109/tmag.2014.2304271.

[15] T. Schroeder, "An accurate magnetic field solution for medical electromagnetic tracking coils at close range," *Journal of Applied Physics*, vol. 117, no. 22, p. 224 504, 2015, ISSN: 0021-8979. DOI: 10.1063/1.4922667.

[16] S. I. Babic and C. Akyel, "Calculating Mutual Inductance Between Circular Coils With Inclined Axes in Air," *IEEE Transactions on Magnetics*, vol. 44, no. 7, pp. 1743–1750, 2008, ISSN: 1941-0069. DOI: 10.1109/TMAG.2008.920251.

[17] S. Babic, F. Sirois, C. Akyel, and C. Girardi, "Mutual Inductance Calculation Between Circular Filaments Arbitrarily Positioned in Space: Alternative to Grover's Formula," *IEEE Transactions on Magnetics*, vol. 46, no. 9, pp. 3591–3600, 2010, ISSN: 1941-0069. DOI: 10.1109/TMAG.2010.2047651.

[18] K. V. Poletkin and J. G. Korvink, "Efficient calculation of the mutual inductance of arbitrarily oriented circular filaments via a generalisation of the Kalantarov-Zeitlin method," *Journal of Magnetism and Magnetic Materials*, vol. 483, pp. 10–20, 2019, ISSN: 0304-8853. DOI: 10.1016/j.jmmm.2019.03.078.

[19] C.-Y. Lin, Y.-C. Wu, Z.-H. Kuo, H.-Y. Ma, and M. Teng, "Analytical and Experimental Investigation of Electromagnetic Tracking System for Location and Orientation Estimation," *IEEE Access*, vol. 11, pp. 9931–9941, 2023, ISSN: 2169-3536. DOI: 10.1109/ACCESS.2023.3239262.

[20] S. Liu, J. Su, and J. Lai, "Accurate Expressions of Mutual Inductance and Their Calculation of Archimedean Spiral Coils," *Energies*, vol. 12, no. 10, p. 2017, 2019. DOI: 10.3390/en12102017.

[21] P. T. Anderson, "A source of accurately calculable quasi-static magnetic fields," Ph.D. dissertation, The University of Vermont, Burlington,VT,USA, 2001.

[22] C. L. W. Sonntag, E. A. Lomonova, and J. L. Duarte, "Implementation of the Neumann formula for calculating the mutual inductance between planar PCB inductors," in *2008 18th International Conference on Electrical Machines*, 2008, pp. 1–6. DOI: 10.1109/ICELMACH.2008.4799978.

[23] M. Cavaliere, H. A. Jaeger, K. O'Donoghue, and P. Cantillon-Murphy, "Planar Body-Mounted Sensors for Electromagnetic Tracking," *Sensors*, vol. 21, no. 8, p. 2822, 2021. DOI: 10.3390/s21082822.

[24] W. Briggs, "Magnetic calibration by tetrahedral interpolation," *Proc. NIST-ASME Industrial Virtual Reality Symposium, Nov., 1999*, vol. 5, pp. 27–32, 1999. [Online]. Available: https://ci.nii.ac.jp/naid/10011833091/ (visited on 04/06/2020).

[25] S. T. Bryson, "Measurement and calibration of static distortion of position data from 3D trackers," in *Stereoscopic Displays and Applications III*, vol. 1669, Washington, DC, USA: International Society for Optics and Photonics, 1992, pp. 244–255. DOI: 10.1117/12.60417.

[26] F. Attivissimo, A. M. L. Lanzolla, S. Carlone, P. Larizza, and G. Brunetti, "A novel electromagnetic tracking system for surgery navigation," *Computer Assisted Surgery*, vol. 23, no. 1, pp. 42–52, 2018, ISSN: null. DOI: 10.1080/24699322.2018.1529199.

[27] S. Sharma *et al.*, "Wireless 3D Surgical Navigation and Tracking System with 100μm Accuracy Using Magnetic-Field Gradient-Based Localization," *IEEE Transactions on Medical Imaging*, pp. 2066–2079, 2021, ISSN: 0278-0062, 1558-254X. DOI: 10.1109/TMI.2021.3071120.

[28] M. Czernuszenko, D. Sandin, and T. DeFanti, "Line of sight method for tracker calibration in projection-based VR systems," in *Proceedings of 2nd International Immersive Projection Technology Workshop*, University Park, PA, USA: Citeseer, 1998, pp. 11–12.

[29] M. Ghazisaedy, D. Adamczyk, D. Sandin, R. Kenyon, and T. DeFanti, "Ultrasonic calibration of a magnetic tracker in a virtual reality space," in *Proceedings Virtual Reality Annual International Symposium '95*, 1995, pp. 179–188. DOI: 10.1109/VRAIS.1995.512494.

[30] M. A. Livingston and A. State, "Magnetic Tracker Calibration for Improved Augmented Reality Registration," *Presence: Teleoperators and Virtual Environments*, vol. 6, no. 5, pp. 532–546, 1997. DOI: 10.1162/pres.1997.6.5.532.

[31] M. R. Schneider and C. D. Conover, "Position and orientation measuring with magnetic fields," US6427079B1, 2002. [Online]. Available: https://patents.google.com/patent/US6427079B1/en (visited on 08/21/2021).

[32] V. Kindratenko and A. Bennett, "Evaluation of Rotation Correction Techniques for Electromagnetic Position Tracking Systems," in *Virtual Environments 2000*, J. Mulder and R. van Liere, Eds., ser. Eurographics, Vienna: Springer, 2000, pp. 13–22, ISBN: 978-3-7091-6785-4. DOI: 10.1007/978-3-7091-6785-4_3.

[33] V. V. Kindratenko and W. R. Sherman, "Neural network-based calibration of electromagnetic tracking systems," *Virtual Reality*, vol. 9, no. 1, pp. 70–78, 2005, ISSN: 1434-9957. DOI: 10.1007/s10055-005-0005-3.

[34] E. Whitmire, F. Salemi Parizi, and S. Patel, "Aura: Inside-out Electromagnetic Controller Tracking," in *Proceedings of the 17th Annual International Conference on Mobile Systems, Applications, and Services - MobiSys '19*, Seoul, Republic of Korea: ACM Press, 2019, pp. 300–312, ISBN: 978-1-4503-6661-8. DOI: 10.1145/3307334.3326090.

[35] M. R. Schneider and K. Fujioka, "Compensating for Distortion in an Electromagnetic Tracking System," US20190242952A1, 2019. [Online]. Available: https://patents.google.com/patent/US20190242952A1/en (visited on 05/12/2020).

[36] M. Cavaliere and P. Cantillon-Murphy, "Intraoperative compensation of magnetic field distortions for fluoroscopic and electromagnetic hybrid navigation," *International Journal of Computer Assisted Radiology and Surgery*, vol. 17, pp. 1717–1721, 2022, ISSN: 1861-6429. DOI: 10.1007/s11548-022-02663-7.

[37] O. Shafrir, E. Paperno, and A. Plotkin, *Magnetic Tracking with a Flat Transmitter*. LAP LAMBERT Academic Publishing, 2010, ISBN: 978-3-8383-4436-2. [Online]. Available: https://www.morebooks.shop/store/gb/book/magnetic-tracking-with-a-flat-transmitter/isbn/978-3-8383-4436-2 (visited on 02/10/2020).

[38] P. T. Anderson, "Coil arrangement for an electromagnetic tracking system," US8391952B2, 2013. [Online]. Available: https://patents.google.com/patent/US8391952B2/en (visited on 05/12/2020).

[39] T. Reichl, J. Gardiazabal, and N. Navab, "Electromagnetic Servoing—A New Tracking Paradigm," *IEEE Transactions on Medical Imaging*, vol. 32, no. 8, pp. 1526–1535, 2013, ISSN: 1558-254X. DOI: 10.1109/TMI.2013.2259636.

[40] M. Wang, Q. Shi, S. Song, and M. Q.-H. Meng, "A Novel Magnetic Tracking Approach for Intrabody Objects," *IEEE Sensors Journal*, vol. 20, no. 9, pp. 4976–4984, 2020, ISSN: 1558-1748. DOI: 10.1109/JSEN.2020.2965144.

[41] P. Chiu, J. Huang, and Y. Kitamura, "Enabling Robot-assisted Motion Capture with Human Scale Tracking Optimization," in *Proceedings of the 27th ACM Symposium on Virtual Reality Software and Technology*, ser. VRST '21, New York, NY, USA: Association for Computing Machinery, 2021, pp. 1–6, ISBN: 978-1-4503-9092-7. DOI: 10.1145/3489849.3489881.

[42] X. Ge, D. Lai, X. Wu, and Z. Fang, "A novel non-model-based 6-DOF electromagnetic tracking method using non-iterative algorithm," in *2009 Annual International Conference of the IEEE Engineering in Medicine and Biology Society*, 2009, pp. 5144–5117. DOI: 10.1109/IEMBS.2009.5332723.

[43] X. Ge, Y. Wang, N. Ding, X. Wu, Y. Wang, and Z. Fang, "An Electromagnetic Tracking Method Using Rotating Orthogonal Coils," *IEEE Transactions on Magnetics*, vol. 48, no. 12, pp. 4802–4810, 2012, ISSN: 1941-0069. DOI: 10.1109/TMAG.2012.2203917.

[44] J. Kuipers, "TWOWAY: A position and orientation measurement system," in *OCEANS '77 Conference Record*, 1977, pp. 510–522. DOI: 10.1109/OCEANS.1977.1154326.

[45] F. H. Raab, E. B. Blood, T. O. Steiner, and H. R. Jones, "Magnetic Position and Orientation Tracking System," *IEEE Transactions on Aerospace and Electronic Systems*, vol. AES-15, no. 5, pp. 709–718, 1979, ISSN: 2371-9877. DOI: 10.1109/TAES.1979.308860.

[46] F. H. Raab, "Remote object position and orientation locator," US4346384A, 1982. [Online]. Available: https://patents.google.com/patent/US4346384A/en (visited on 01/22/2020).

[47] C. Hu, S. Song, X. Wang, M. Q.-H. Meng, and B. Li, "A Novel Positioning and Orientation System Based on Three-Axis Magnetic Coils," *IEEE Transactions on Magnetics*, vol. 48, no. 7, pp. 2211–2219, 2012, ISSN: 0018-9464, 1941-0069. DOI: 10.1109/TMAG.2012.2188537.

[48] W. Kim, J. Song, and F. C. Park, "Closed-Form Position and Orientation Estimation for a Three-Axis Electromagnetic Tracking System," *IEEE Transactions on Industrial Electronics*, vol. 65, no. 5, pp. 4331–4337, 2018, ISSN: 0278-0046, 1557-9948. DOI: 10.1109/TIE.2017.2760244.

[49] S. T. Elhardt, "Method and device for measuring the position and orientation of objects in the presence of interfering metals," US5347289A, 1994. [Online]. Available: https://patents.google.com/patent/US5347289A/en (visited on 03/30/2021).

[50] M. Sha, Y. Wang, N. Ding, X. Wu, and Z. Fang, "An electromagnetic tracking method based on fast determination of the maximum magnetic flux density vector represented by two azimuth angles," *Measurement*, vol. 109, pp. 160–167, 2017, ISSN: 0263-2241. DOI: 10.1016/j.measurement.2017.04.027.

[51] X. Huang and X. Wu, "An Electromagnetic Tracking Method Based on Phase Difference Detection," *IEEE Transactions on Magnetics*, vol. 55, no. 9, pp. 1–8, 2019, ISSN: 1941-0069. DOI: 10.1109/TMAG.2019.2915264.

[52] S. Song, H. Ren, and H. Yu, "An Improved Magnetic Tracking Method Using Rotating Uniaxial Coil With Sparse Points and Closed Form Analytic Solution," *IEEE Sensors Journal*, vol. 14, no. 10, pp. 3585–3592, 2014, ISSN: 1558-1748. DOI: 10.1109/JSEN.2014.2329186.

[53] S. Song, W. Qiao, B. Li, C. Hu, H. Ren, and M. Q.-H. Meng, "An Efficient Magnetic Tracking Method Using Uniaxial Sensing Coil," *IEEE Transactions on Magnetics*, vol. 50, no. 1, pp. 1–7, 2014, ISSN: 1941-0069. DOI: 10.1109/TMAG.2013.2273061.

[54] K. M. Popek, A. W. Mahoney, and J. J. Abbott, "Localization method for a magnetic capsule endoscope propelled by a rotating magnetic dipole field," in *2013 IEEE International Conference on Robotics and Automation*, 2013, pp. 5348–5353. DOI: 10.1109/ICRA.2013.6631343.

[55] D. J. Foster, R. N. Hastings, D. R. Wulfman, M. A. Felling, M. Hein, and C. D. Rousemiller, "Electromagnetic tracking system using rotating permanent magnets for field generation," US20190056243A1, 2019. [Online]. Available: https://patents.google.com/patent/US20190056243A1/en (visited on 01/22/2020).

[56] E. Paperno, I. Sasada, and E. Leonovich, "A new method for magnetic position and orientation tracking," *IEEE Transactions on Magnetics*, vol. 37, no. 4, pp. 1938–1940, 2001, ISSN: 1941-0069. DOI: 10.1109/20.951014.

[57] S. Song, C. Hu, B. Li, X. Li, and M. Q.-H. Meng, "An Electromagnetic Localization and Orientation Method Based on Rotating Magnetic Dipole," *IEEE Transactions on Magnetics*, vol. 49, no. 3, pp. 1274–1277, 2013, ISSN: 1941-0069. DOI: 10.1109/TMAG.2012.2211375.

[58] P. Gilboa, "Wireless six-degree-of-freedom locator," US6188355B1, 2001. [Online]. Available: https://patents.google.com/patent/US6188355B1/en (visited on 02/07/2020).

[59] P. T. Anderson, "Electromagnetic tracking method and system," US7782046B2, 2010. [Online]. Available: https://patents.google.com/patent/US7782046B2/en (visited on 09/06/2020).

[60] S. M. Morgan and L. A. Koyrakh, "Electromagnetic navigation antenna assembly and electromagnetic navigation system including the same," US10446931B2, 2019. [Online]. Available: https://patents.google.com/patent/US10446931B2/en (visited on 12/20/2022).

[61] A. Sharma, G. Singh, D. Bhatnagar, I. J. Garcia Zuazola, and A. Perallos, "Magnetic field forming Using Planar Multicoil Antenna to Generate Orthogonal H-Field Components," *IEEE Transactions on Antennas and Propagation*, vol. 65, no. 6, pp. 2906–2915, 2017, ISSN: 0018-926X, 1558-2221. DOI: 10.1109/TAP.2017.2695009.

[62] P. Gilboa and D. Zur, "Wireless six-degree-of-freedom locator," EP0922966A2, 1999. [Online]. Available: https://patents.google.com/patent/EP0922966A2/en (visited on 02/07/2020).

[63] D. A. Li, P. T. Anderson, and G. L. Beauregard, "Electromagnetic tracking using a discretized numerical field model," US7532997B2, 2009. [Online]. Available: https://patents.google.com/patent/US7532997B2/en (visited on 02/10/2020).

[64] H. P. Kalmus, "A New Guiding and Tracking System," *IRE Transactions on Aerospace and Navigational Electronics*, vol. ANE-9, no. 1, pp. 7–10, 1962, ISSN: 2331-0812. DOI: 10.1109/TANE3.1962.4201833.

[65] E. Paperno and P. Keisar, "Three-dimensional magnetic tracking of biaxial sensors," *IEEE Transactions on Magnetics*, vol. 40, no. 3, pp. 1530–1536, 2004, ISSN: 1941-0069. DOI: 10.1109/TMAG.2004.826615.

[66] M. Li, S. Song, C. Hu, D. Chen, and M. Q.-H. Meng, "A novel method of 6-DoF electromagnetic navigation system for surgical robot," in *2010 8th World Congress on Intelligent Control and Automation*, 2010, pp. 2163–2167. DOI: 10.1109/WCICA.2010.5554348.

[67] J. Tian, S. Song, X. Wang, T. Yan, C. Hu, and M. Q.-H. Meng, "An improved method and algorithm for electromagnetic localization," in *2011 IEEE International Conference on Information and Automation*, 2011, pp. 406–411. DOI: 10.1109/ICINFA.2011.5949026.

[68] R. Jin and B. Jung, "Magnetic Tracking System for Heart Surgery," *IEEE Transactions on Biomedical Circuits and Systems*, vol. 16, no. 2, pp. 275–286, 2022, ISSN: 1940-9990. DOI: 10.1109/TBCAS.2022.3163172.

[69] S. R. Kirsch and C. J. Schilling, "Errors in systems using magnetic fields to locate objects," US6553326B1, 2003. [Online]. Available: https://patents.google.com/patent/US6553326B1/en (visited on 12/17/2022).

[70] A. Plotkin and E. Paperno, "3-D magnetic tracking of a single subminiature coil with a large 2-D array of uniaxial transmitters," *IEEE Transactions on Magnetics*, vol. 39, no. 5, pp. 3295–3297, 2003, ISSN: 0018-9464. DOI: 10.1109/TMAG.2003.816750.

[71] P. T. Anderson, "Electromagnetic tracking system and method using a single-coil transmitter," US7158754B2, 2007. [Online]. Available: https://patents.google.com/patent/US7158754B2/en (visited on 01/27/2020).

[72] S. Hashi *et al.*, "Wireless magnetic motion capture system using multiple LC resonant magnetic markers with high accuracy," *Sensors and Actuators A: Physical*, The Sixth European Magnetic Sensor and Actuator Conference, vol. 142, no. 2, pp. 520–527, 2008, ISSN: 0924-4247. DOI: 10.1016/j.sna.2007.09.011.

[73] C. Silva, D. Mateus, M. Eiras, and S. Vieira, "Calypso® 4D Localization System: A review," *Journal of Radiotherapy in Practice*, vol. 13, no. 4, pp. 473–483, 2014, ISSN: 1460-3969, 1467-1131. DOI: 10.1017/S1460396914000223.

[74] Y. Osaki, S. Hashi, S. Yabukami, H. Kanetaka, and K. Ishiyama, "Wireless Magnetic Position-Detection System With Four Excitation Coils," *IEEE Sensors Journal*, vol. 17, no. 14, pp. 4412–4419, 2017, ISSN: 1558-1748. DOI: 10.1109/JSEN.2017.2707388.

[75] A. Ray, I. Habibagahi, and A. Babakhani, "Fully Wireless and Batteryless Localization and Physiological Motion Detection System for Point-of-care Biomedical Applications," in *2022 IEEE Biomedical Circuits and Systems Conference (BioCAS)*, 2022, pp. 26–30. DOI: 10.1109/BioCAS54905.2022.9948647.

[76] M. Rustom and C. Sideris, "Wireless Frequency-Division Multiplexed 3D Magnetic Localization for Low Power Sub-mm Precision Capsule Endoscopy," in *2022 IEEE Custom Integrated Circuits Conference (CICC)*, 2022, pp. 01–02. DOI: 10.1109/CICC53496.2022.9772802.

[77] W. S. Ashe, "Magnetic sensors," US9360294B2, 2016. [Online]. Available: https://patents.google.com/patent/US9360294/en (visited on 03/29/2021).

[78] V. Schlageter, P. .-. Besse, R. S. Popovic, and P. Kucera, "Tracking system with five degrees of freedom using a 2D-array of Hall sensors and a permanent magnet," *Sensors and Actuators A: Physical*, Selected Papers for Eurosensors XIV, vol. 92, no. 1, pp. 37–42, 2001, ISSN: 0924-4247. DOI: 10.1016/S0924-4247(01)00537-4.

[79] C. Hu, M. Li, S. Song, W. Yang, R. Zhang, and M. Q. .-. Meng, "A Cubic 3-Axis Magnetic Sensor Array for Wirelessly Tracking Magnet Position and Orientation," *IEEE Sensors Journal*, vol. 10, no. 5, pp. 903–913, 2010, ISSN: 2379-9153. DOI: 10.1109/JSEN.2009.2035711.

[80] S. Song *et al.*, "6-D Magnetic Localization and Orientation Method for an Annular Magnet Based on a Closed-Form Analytical Model," *IEEE Transactions on Magnetics*, vol. 50, no. 9, pp. 1–11, 2014, ISSN: 0018-9464, 1941-0069. DOI: 10.1109/TMAG.2014.2315592.

[81] L. Maréchal *et al.*, "Optimal spatial design of non-invasive magnetic field-based localization systems," in *2014 IEEE International Conference on Robotics and Automation (ICRA)*, 2014, pp. 3510–3516. DOI: 10.1109/ICRA.2014.6907365.

[82] S. Song, X. Qiu, J. Wang, and M. Q. H. Meng, "Design and Optimization Strategy of Sensor Array Layout for Magnetic Localization System," *IEEE Sensors Journal*, vol. 17, no. 6, pp. 1849–1857, 2017, ISSN: 1530437X. DOI: 10.1109/JSEN.2017.2652470.

[83] J. E. McGary, "Real-Time Tumor Tracking for Four-Dimensional Computed Tomography Using SQUID Magnetometers," *IEEE Transactions on Magnetics*, vol. 45, no. 9, pp. 3351–3361, 2009, ISSN: 1941-0069. DOI: 10.1109/TMAG.2009.2020430.

[84] C. Hu, M. Q.-H. Meng, and M. Mandal, "Efficient magnetic localization and orientation technique for capsule endoscopy," *International Journal of Information Acquisition*, vol. 02, no. 01, pp. 23–36, 2005, ISSN: 0219-8789. DOI: 10.1142/S0219878905000398.

[85] C. Hu, M.-H. Meng, and M. Mandal, "Efficient Linear Algorithm for Magnetic Localization and Orientation in Capsule Endoscopy," in *2005 IEEE Engineering in Medicine and Biology 27th Annual Conference*, 2005, pp. 7143–7146. DOI: 10.1109/IEMBS.2005.1616154.

[86] C. Hu, M. Q.-H. Meng, and M. Mandal, "A Linear Algorithm for Tracing Magnet Position and Orientation by Using Three-Axis Magnetic Sensors," *IEEE Transactions on Magnetics*, vol. 43, no. 12, pp. 4096–4101, 2007, ISSN: 1941-0069. DOI: 10.1109/TMAG.2007.907581.

[87] F. S. Parizi, E. Whitmire, and S. Patel, "AuraRing: Precise Electromagnetic Finger Tracking," *Proceedings of the ACM on Interactive, Mobile, Wearable and Ubiquitous Technologies*, vol. 3, no. 4, 150:1–150:28, 2019. DOI: 10.1145/3369831.

[88] A.-I. Sasaki, "Effectiveness of Artificial Neural Networks for Solving Inverse Problems in Magnetic Field-Based Localization," *Sensors (Basel, Switzerland)*, vol. 22, no. 6, p. 2240, 2022, ISSN: 1424-8220. DOI: 10.3390/s22062240.

[89] Z. Sun, L. Maréchal, and S. Foong, "Passive magnetic-based localization for precise untethered medical instrument tracking," *Computer Methods and Programs in Biomedicine*, vol. 156, pp. 151–161, 2018, ISSN: 0169-2607. DOI: 10.1016/j.cmpb.2017.12.018.

[90] B. Lv, Y. Chen, H. Dai, S. Su, and M. Lin, "PKBPNN-Based Tracking Range Extending Approach for TMR Magnetic Tracking System," *IEEE Access*, vol. 7, pp. 63 123–63 132, 2019, ISSN: 2169-3536. DOI: 10.1109/ACCESS.2019.2917140.

[91] T. Nara, S. Suzuki, and S. Ando, "A Closed-Form Formula for Magnetic Dipole Localization by Measurement of Its Magnetic Field and Spatial Gradients," *IEEE Transactions on Magnetics*, vol. 42, no. 10, pp. 3291–3293, 2006, ISSN: 1941-0069. DOI: 10.1109/TMAG.2006.879151.

[92] Z. Xiong, J. E. McGary, and J. Chen, "Self-Correcting Magnetic Tracking in Dynamic Medical Environments," *IEEE Transactions on Magnetics*, vol. 51, no. 2, pp. 1–9, 2015, ISSN: 1941-0069. DOI: 10.1109/TMAG.2014.2345333.

[93] D. A. Robinson, "A Method of Measuring Eye Movemnent Using a Scieral Search Coil in a Magnetic Field," *IEEE Transactions on Bio-medical Electronics*, vol. 10, no. 4, pp. 137–145, 1963, ISSN: 2168-1600. DOI: 10.1109/TBMEL.1963.4322822.

[94] A. Plotkin, V. Kucher, Y. Horen, and E. Paperno, "A New Calibration Procedure for Magnetic Tracking Systems," *IEEE Transactions on Magnetics*, vol. 44, no. 11, pp. 4525–4528, 2008, ISSN: 1941-0069. DOI: 10.1109/TMAG.2008.2003056.

[95] A. Plotkin, E. Paperno, G. Vasserman, and R. Segev, "Magnetic Tracking of Eye Motion in Small, Fast-Moving Animals," *IEEE Transactions on Magnetics*, vol. 44, no. 11, pp. 4492–4495, 2008, ISSN: 1941-0069. DOI: 10.1109/TMAG.2008.2002187.

[96] N. Sun, Y. Liu, H. Lee, R. Weissleder, and D. Ham, "CMOS RF Biosensor Utilizing Nuclear Magnetic Resonance," *IEEE Journal of Solid-State Circuits*, vol. 44, no. 5, pp. 1629–1643, 2009, ISSN: 0018-9200, 1558-173X. DOI: 10.1109/JSSC.2009.2017007.

[97] C. Chautems and B. J. Nelson, "The tethered magnet: Force and 5-DOF pose control for cardiac ablation," in *2017 IEEE International Conference on Robotics and Automation (ICRA)*, 2017, pp. 4837–4842. DOI: 10.1109/ICRA.2017.7989562.

[98] C. Fischer, T. Quirin, C. Chautems, Q. Boehler, J. Pascal, and B. J. Nelson, "Gradiometer-based magnetic localization for medical tools," *IEEE Transactions on Magnetics*, pp. 1–1, 2022, ISSN: 1941-0069. DOI: 10.1109/TMAG.2022.3206590.

[99] D. Son, S. Yim, and M. Sitti, "A 5-D Localization Method for a Magnetically Manipulated Untethered Robot Using a 2-D Array of Hall-Effect Sensors," *IEEE/ASME Transactions on Mechatronics*, vol. 21, no. 2, pp. 708–716, 2016, ISSN: 1941-014X. DOI: 10.1109/TMECH.2015.2488361.

[100] S. P. Souza, C. L. Dumoulin, and R. D. Darrow, "Tracking system to monitor the position of a device using multiplexed magnetic resonance detection," US5353795A, 1994. [Online]. Available: https://patents.google.com/patent/US5353795A/en (visited on 11/11/2022).

[101] P. D. Jakab, "Magnetic resonance scanner with electromagnetic position and orientation tracking device," US6879160B2, 2005. [Online]. Available: https://patents.google.com/patent/US6879160B2/en (visited on 11/11/2022).

[102] J.-B. Schell *et al.*, "Towards a Hall effect magnetic tracking device for MRI," in *2013 35th Annual International Conference of the IEEE Engineering in Medicine and Biology Society (EMBC)*, 2013, pp. 2964–2967. DOI: 10.1109/EMBC.2013.6610162.

[103] H. Dai, S. Song, X. Zeng, S. Su, M. Lin, and M. Q. H. Meng, "6-D Electromagnetic Tracking Approach Using Uniaxial Transmitting Coil and Tri-Axial Magneto-Resistive Sensor," *IEEE Sensors Journal*, vol. 18, no. 3, pp. 1178–1186, 2018, ISSN: 1530437X. DOI: 10.1109/JSEN.2017.2779560.

[104] J. T. Scully and M. R. Schneider, "DC magnetic-based position and orientation monitoring system for tracking medical instruments," US7835785B2, 2010. [Online]. Available: https://patents.google.com/patent/US7835785B2/en (visited on 09/11/2020).

[105] G. Welch and G. Bishop, "SCAAT: Incremental tracking with incomplete information," in *Proceedings of the 24th Annual Conference on Computer Graphics and Interactive Techniques - SIGGRAPH '97*, Not Known: ACM Press, 1997, pp. 333–344, ISBN: 978-0-89791-896-1. DOI: 10.1145/258734.258876.

[106] M. Li, T. Bien, and G. Rose, "FPGA based electromagnetic tracking system for fast catheter navigation," *International Journal of Scientific and Engineering Research*, vol. 4, no. 9, IJSER, Ed., pp. 2566–2570, 2013, ISSN: 22295518. DOI: 10.14299/ijser.2013.09.001.

[107] A. M. Franz *et al.*, "Standardized accuracy assessment of the calypso wireless transponder tracking system," *Physics in Medicine & Biology*, vol. 59, no. 22, p. 6797, 2014, ISSN: 0031-9155. DOI: 10.1088/0031-9155/59/22/6797.

[108] I. Khalfin, "Method and apparatus for electromagnetic position and orientation tracking with distortion compensation employing modulated signal," US6624626B2, 2003. [Online]. Available: https://patents.google.com/patent/US6624626B2/en (visited on 12/12/2022).

[109] H. R. Jones, "Method and apparatus for determining remote object orientation and position," US4737794A, 1988. [Online]. Available: https://patents.google.com/patent/US4737794A/en (visited on 03/31/2020).

[110] F. Attivissimo, A. M. L. Lanzolla, S. Carlone, P. Larizza, and G. Brunetti, "TDM-FDM configuration of electromagnetic tracking system for image-guided surgery devices," in *2017 IEEE International Instrumentation and Measurement Technology Conference (I2MTC)*, 2017, pp. 1–6. DOI: 10.1109/I2MTC.2017.7969719.

[111] H. A. Jaeger and P. Cantillon-Murphy, "Electromagnetic Tracking Using Modular, Tiled Field Generators," *IEEE Transactions on Instrumentation and Measurement*, vol. 68, no. 12, pp. 4845–4852, 2019, ISSN: 1557-9662. DOI: 10.1109/TIM.2019.2900884.

[112] L. Koyrakh, S. Morgan, and A. Brown, "Modular reconfigurable magnetic navigation system and method," US20220037085A1, 2022. [Online]. Available: https://patents.google.com/patent/US20220037085A1/en (visited on 12/20/2022).

[113] E. B. Blood, "Device for quantitatively measuring the relative position and orientation of two bodies in the presence of metals utilizing direct current magnetic fields," US4945305A, 1990. [Online]. Available: https://patents.google.com/patent/US4945305A/en (visited on 01/30/2020).

[114] W. Ashe, "Method of measuring position and orientation with improved signal to noise ratio," US20040088136A1, 2004. [Online]. Available: https://patents.google.com/patent/US20040088136A1/en (visited on 03/31/2021).

[115] T. Bien, M. Li, Z. Salah, and G. Rose, "Electromagnetic tracking system with reduced distortion using quadratic excitation," *International Journal of Computer Assisted Radiology and Surgery*, vol. 9, no. 2, pp. 323–332, 2014, ISSN: 1861-6429. DOI: 10.1007/s11548-013-0925-4.

[116] M. Li, C. Hansen, and G. Rose, "A software solution to dynamically reduce metallic distortions of electromagnetic tracking systems for image-guided surgery," *International Journal of Computer Assisted Radiology and Surgery*, vol. 12, no. 9, pp. 1621–1633, 2017, ISSN: 1861-6429. DOI: 10.1007/s11548-017-1546-0.

[117] R. A. MacLachlan, R. L. Hollis, B. Jaramaz, C. N. Riviere, J. N. Martel, and K. L. Urish, "Multirate Kalman filter rejects impulse noise in frequency-domain-multiplexed tracker measurements," in *2017 IEEE SENSORS*, 2017, pp. 1–3. DOI: 10.1109/ICSENS.2017.8234073.

[118] R. A. MacLachlan, N. Parody, S. Mukherjee, R. Hollis, and C. N. Riviere, "Electromagnetic Tracker for Active Handheld Robotic Systems," *Proceedings of IEEE Sensors. IEEE International Conference on Sensors*, vol. 2016, 2016, ISSN: 1930-0395. [Online]. Available: https://www.ncbi.nlm.nih.gov/pmc/articles/PMC5891151/ (visited on 11/16/2019).

[119] M. N. Islam and A. J. Fleming, "Resonance-Enhanced Coupling for Range Extension of Electromagnetic Tracking Systems," *IEEE Transactions on Magnetics*, vol. 54, no. 4, pp. 1–9, 2018, ISSN: 1941-0069. DOI: 10.1109/TMAG.2017.2784384.

[120] H. Heidari and V. Nabaei, "Magnetic Sensors for Biomedical Applications," 2019, ISSN: 1119552176. [Online]. Available: https://onlinelibrary.wiley.com/doi/book/10.1002/9781119552215.

[121] P. Ripka, M. Mirzaei, and J. Blažek, "Magnetic position sensors," *Measurement Science and Technology*, vol. 33, no. 2, p. 022 002, 2021, ISSN: 0957-0233. DOI: 10.1088/1361-6501/ac32eb.

[122] G. Dehmel, "Magnetic Field Sensors: Induction Coil (Search Coil) Sensors," in *Sensors*, R. Boll and K. J. Overshott, Eds., Weinheim, Germany: Wiley-VCH Verlag GmbH, 2008, pp. 205–253, ISBN: 978-3-527-62016-6 978-3-527-26771-2. DOI: 10.1002/9783527620166.ch6.

[123] P. Ripka, "Advances in fluxgate sensors," in *Sensors and Actuators, A: Physical*, vol. 106, Elsevier, 2003, pp. 8–14. DOI: 10.1016/S0924-4247(03)00094-3.

[124] P. K. Hansen, "Magnetic position and orientation measurement system," US4622644A, 1986. [Online]. Available: https://patents.google.com/patent/US4622644A/en (visited on 01/28/2020).

[125] "Induction Sensors," in *Magnetic Sensors and Magnetometers*, ser. Artech House Remote Sensing Library, P. Ripka, Ed., Boston: Artech House, 2001, ISBN: 978-1-58053-057-6.

[126] P. Ripka and M. Janošek, "Advances in magnetic field sensors," *IEEE Sensors Journal*, vol. 10, no. 6, pp. 1108–1116, 2010, ISSN: 1530437X. DOI: 10.1109/JSEN.2010.2043429.

[127] S. Tumanski, "Thin Film Magnetoresistive Sensors," in *Thin Film Magnetoresistive Sensors*, IOP Publishing Ltd, 2001, ISBN: 0-7503-0702-1. DOI: 10.1887/0750307021.

[128] J. Hoffmann, E. Elzenheimer, C. Bald, C. Hansen, W. Maetzler, and G. Schmidt, "Active Magnetoelectric Motion Sensing: Examining Performance Metrics with an Experimental Setup," *Sensors*, vol. 21, no. 23, p. 8000, 2021, ISSN: 1424-8220. DOI: 10.3390/s21238000.

[129] J. Gao, Z. Jiang, S. Zhang, Z. Mao, Y. Shen, and Z. Chu, "Review of Magnetoelectric Sensors," *Actuators*, vol. 10, no. 6, p. 109, 2021, ISSN: 2076-0825. DOI: 10.3390/act10060109.

[130] M. Bichurin *et al.*, "Magnetoelectric Magnetic Field Sensors: A Review," *Sensors (Basel, Switzerland)*, vol. 21, no. 18, p. 6232, 2021, ISSN: 1424-8220. DOI: 10.3390/s21186232.

[131] A. Bernieri, G. Cerro, L. Ferrigno, M. Laracca, and F. Milano, "Use of Magnetic Positioning Systems in Industrial and Biomedical Applications," *IEEE Instrumentation & Measurement Magazine*, vol. 25, no. 6, pp. 4–10, 2022, ISSN: 1941-0123. DOI: 10.1109/MIM.2022.9847191.

[132] D. Roetenberg, P. Slycke, A. Ventevogel, and P. H. Veltink, "A portable magnetic position and orientation tracker," *Sensors and Actuators A: Physical*, vol. 135, no. 2, pp. 426–432, 2007, ISSN: 0924-4247. DOI: 10.1016/j.sna.2006.08.020.

[133] M. Schepers, M. Giuberti, and G. Bellusci, "Xsens MVN: Consistent Tracking of Human Motion Using Inertial Sensing," 2018. DOI: 10.13140/RG.2.2.22099.07205.

[134] S.-W. LUO, S.-H. Hsieh, and J.-S. Hu, "Localization and attitude estimation method using magnetic field and system thereof," US20200149862A1, 2020. [Online]. Available: https://patents.google.com/patent/US20200149862A1/en (visited on 06/30/2020).

[135] G. De Angelis *et al.*, "An Indoor AC Magnetic Positioning System," *IEEE Transactions on Instrumentation and Measurement*, vol. 64, no. 5, pp. 1267–1275, 2015, ISSN: 1557-9662. DOI: 10.1109/TIM.2014.2381353.

[136] A. Solin, M. Kok, N. Wahlström, T. B. Schön, and S. Särkkä, "Modeling and interpolation of the ambient magnetic field by Gaussian processes," *arXiv:1509.04634 [cs, stat]*, 2018. arXiv: 1509.04634 [cs, stat]. [Online]. Available: http://arxiv.org/abs/1509.04634 (visited on 12/02/2020).

[137] M. Hehn, E. Sippel, C. Carlowitz, and M. Vossiek, "High-Accuracy Localization and Calibration for 5-DoF Indoor Magnetic Positioning Systems," *IEEE Transactions on Instrumentation and Measurement*, vol. 68, no. 10, pp. 4135–4145, 2019, ISSN: 1557-9662. DOI: 10.1109/TIM.2018.2884040.

[138] P. Gilboa and D. Blecher, "Intrabody navigation system for medical applications," US6593884B1, 2003. [Online]. Available: https://patents.google.com/patent/US6593884B1/en (visited on 02/07/2020).

[139] I. Umay, B. Fidan, and B. Barshan, "Localization and Tracking of Implantable Biomedical Sensors," *Sensors (Basel, Switzerland)*, vol. 17, no. 3, 2017, ISSN: 1424-8220. DOI: 10.3390/s17030583.

[140] W. S. Ashe, "Magnetically tracked sensor," US8994366B2, 2015. [Online]. Available: https://patents.google.com/patent/US8994366B2/en (visited on 03/29/2021).

[141] M. Cavaliere, O. McVeigh, H. A. Jaeger, S. Hinds, K. O'Donoghue, and P. Cantillon-Murphy, "Inductive Sensor Design for Electromagnetic Tracking in Image Guided Interventions," *IEEE Sensors Journal*, vol. 20, no. 15, pp. 8623–8630, 2020, ISSN: 1558-1748. DOI: 10.1109/JSEN.2020.2984323.

[142] H. Jaeger, K. O'Donoghue, and P. Cantillon-Murphy, "Induction sensor characterisation for electromagnetic tracking systems," in *IEEE I2MTC 16-19 May 2022*, Ottawa, ON, Canada, 2022.

[143] T. Quirin *et al.*, "Towards Tracking of Deep Brain Stimulation Electrodes Using an Integrated Magnetometer," *Sensors*, vol. 21, no. 8, p. 2670, 2021, ISSN: 1424-8220. DOI: 10.3390/s21082670.

[144] C. Vergne *et al.*, "Low-field electromagnetic tracking using 3D magnetometer for assisted surgery," *IEEE Transactions on Magnetics*, pp. 1–1, 2022, ISSN: 1941-0069. DOI: 10.1109/TMAG.2022.3204918.

[145] T. Peters and K. Cleary, Eds., *Image-Guided Interventions: Technology and Applications*. New York, NY: Springer Science+Business Media, 2008, ISBN: 978-0-387-73858-1 978-0-387-73856-7.

[146] K. Cleary and T. M. Peters, "Image-Guided Interventions: Technology Review and Clinical Applications," *Annual Review of Biomedical Engineering*, vol. 12, no. 1, pp. 119–142, 2010, ISSN: 1523-9829. DOI: 10.1146/annurev-bioeng-070909-105249.

[147] C. A. Linte, J. T. Moore, E. C. S. Chen, and T. M. Peters, "Chapter 4 - Image-Guided Procedures: Tools, Techniques, and Clinical Applications," in *Bioengineering for Surgery*, W. A. Farhat and J. Drake, Eds., Chandos Publishing, 2016, pp. 59–90, ISBN: 978-0-08-100123-3. DOI: 10.1016/B978-0-08-100123-3.00004-X.

[148] Y. Schwarz, J. Greif, H. D. Becker, A. Ernst, and A. Mehta, "Real-Time Electromagnetic Navigation Bronchoscopy to Peripheral Lung Lesions Using Overlaid CT Images: The First Human Study," *Chest*, vol. 129, no. 4, pp. 988–994, 2006, ISSN: 0012-3692. DOI: 10.1378/chest.129.4.988.

[149] H. A. Jaeger *et al.*, "Peripheral tumour targeting using open-source virtual bronchoscopy with electromagnetic tracking: A multi-user pre-clinical study," *Minimally Invasive Therapy & Allied Technologies*, vol. 28, no. 6, pp. 363–372, 2019, ISSN: 1364-5706. DOI: 10.1080/13645706.2018.1544911.

[150] B. Martins, G. Dagnino, and S. Dogramadzi, "Real-time electromagnetic tracking of orthopaedic pins for robot-assisted fracture surgery," in *Computer and Robot Assisted Surgery (CRAS)*, London, UK, 2018. [Online]. Available: https://uwe-repository.worktribe.com/output/860731/real-time-electromagnetic-tracking-of-orthopaedic-pins-for-robot-assisted-fracture-surgery (visited on 01/12/2021).

[151] Y. Luo and E. Badreddin, "Survey of Navigation Guided Robotics for Orthopedic Surgical Assistance–Concept and Components," in *2022 6th International Conference on Robotics and Automation Sciences (ICRAS)*, 2022, pp. 92–99. DOI: 10.1109/ICRAS55217.2022.9842146.

[152] M. W. Lee, "Fusion imaging of real-time ultrasonography with CT or MRI for hepatic intervention," *Ultrasonography*, vol. 33, no. 4, pp. 227–239, 2014, ISSN: 2288-5919, 2288-5943. DOI: 10.14366/usg.14021.

[153] Y. Akhtar *et al.*, "Risk Assessment of Computer-Aided Diagnostic Software for Hepatic Resection," *IEEE Transactions on Radiation and Plasma Medical Sciences*, vol. 6, no. 6, pp. 667–677, 2022, ISSN: 2469-7303. DOI: 10.1109/TRPMS.2021.3071148.

[154] G. Placidi, D. Franchi, A. Maurizi, and A. Sotgiu, "Review on Patents about Magnetic Localisation Systems for in vivo Catheterizations," *Recent Patents on Biomedical Engineering*, vol. 2, no. 1, pp. 58–64, 2009.

[155] E. Lima *et al.*, "Ureteroscopy-assisted Percutaneous Kidney Access Made Easy: First Clinical Experience with a Novel Navigation System Using Electromagnetic Guidance (IDEAL Stage 1)," *European Urology*, vol. 72, no. 4, pp. 610–616, 2017, ISSN: 03022838. DOI: 10.1016/j.eururo.2017.03.011.

[156] E. González Torrecilla, "Navigation Systems in Current Electrophysiology," *Revista Española de Cardiología (English Edition)*, vol. 57, no. 8, pp. 722–724, 2004, ISSN: 1885-5857. DOI: 10.1016/S1885-5857(06)60304-6.

[157] M. Nagel, M. Hoheisel, R. Petzold, W. A. Kalender, and U. H. W. Krause, "Needle and catheter navigation using electromagnetic tracking for computer-assisted C-arm CT interventions," in *Medical Imaging 2007: Visualization and Image-Guided Procedures*, vol. 6509, International Society for Optics and Photonics, 2007, 65090J. DOI: 10.1117/12.709435.

[158] E. J. Hermann, H.-H. Capelle, C. A. Tschan, and J. K. Krauss, "Electromagnetic-guided neuronavigation for safe placement of intraventricular catheters in pediatric neurosurgery," *Journal of Neurosurgery: Pediatrics*, vol. 10, no. 4, pp. 327–333, 2012, ISSN: 1933-0707. DOI: 10.3171/2012.7.PEDS11369.

[159] A. Schwein *et al.*, "Flexible robotics with electromagnetic tracking improves safety and efficiency during in vitro endovascular navigation," *Journal of Vascular Surgery*, vol. 65, no. 2, pp. 530–537, 2017, ISSN: 0741-5214. DOI: 10.1016/j.jvs.2016.01.045.

[160] A. Schwein *et al.*, "Electromagnetic tracking of flexible robotic catheters enables "assisted navigation" and brings automation to endovascular navigation in an in vitro study," *Journal of Vascular Surgery*, vol. 67, no. 4, pp. 1274–1281, 2018, ISSN: 10976809. DOI: 10.1016/j.jvs.2017.01.072.

[161] J. Kim, "Non-fluoroscopic Catheter Tracking System for Atrial Fibrillation Ablation," *Korean Circulation Journal*, vol. 49, no. 1, pp. 97–98, 2018, ISSN: 1738-5520. DOI: 10.4070/kcj.2018.0319.

[162] S. Yamada *et al.*, "The Accuracy and Clinical Applicability of a Sensor Based Electromagnetic Non-fluoroscopic Catheter Tracking System," *Korean Circulation Journal*, vol. 49, no. 1, pp. 84–96, 2019, ISSN: 1738-5520. DOI: 10.4070/kcj.2018.0195.

[163] A. Ramadani, M. Bui, T. Wendler, H. Schunkert, P. Ewert, and N. Navab, "A survey of catheter tracking concepts and methodologies," *Medical Image Analysis*, vol. 82, 2022, ISSN: 1361-8415. DOI: 10.1016/j.media.2022.102584.

[164] C. Shi *et al.*, "Shape Sensing Techniques for Continuum Robots in Minimally Invasive Surgery: A Survey," *IEEE Transactions on Biomedical Engineering*, vol. 64, no. 8, pp. 1665–1678, 2017, ISSN: 1558-2531. DOI: 10.1109/TBME.2016.2622361.

[165] S. Song, C. Zhang, J. Wang, H. Ren, and M. Q. H. Meng, "Real-time shape estimation of curvilinear flexible surgical robots: Methods, experiments and analysis," *International Journal of Robotics and Automation*, vol. 33, no. 5, pp. 559–568, 2018, ISSN: 08268185. DOI: 10.2316/Journal.206.2018.5.206-5329.

[166] M. Oda *et al.*, "Colonoscope tracking method based on shape estimation network," in *Medical Imaging 2019: Image-Guided Procedures, Robotic Interventions, and Modeling*, B. Fei and C. A. Linte, Eds., San Diego, United States: SPIE, 2019, p. 25, ISBN: 978-1-5106-2549-5 978-1-5106-2550-1. DOI: 10.1117/12.2512729.

[167] B. J. Wood *et al.*, "Navigation with Electromagnetic Tracking for Interventional Radiology Procedures: A Feasibility Study," *Journal of Vascular and Interventional Radiology*, vol. 16, no. 4, pp. 493–505, 2005, ISSN: 1051-0443. DOI: 10.1097/01.RVI.0000148827.62296.B4.

[168] O. V. Ivashchenko *et al.*, "CBCT-based navigation system for open liver surgery: Accurate guidance toward mobile and deformable targets with a semi-rigid organ approximation and electromagnetic tracking of the liver," *Medical Physics*, vol. 48, no. 5, pp. 2145–2159, 2021, ISSN: 2473-4209. DOI: 10.1002/mp.14825.

[169] A. M. Franz, H. A. Jaeger, A. Seitel, P. Cantillon-Murphy, and L. Maier-Hein, "Open-Source Tracked Ultrasound with Anser Electromagnetic Tracking," in *Bildverarbeitung für die Medizin 2019*, H. Handels, T. M. Deserno, A. Maier, K. H. Maier-Hein, C. Palm, and T. Tolxdorff, Eds., ser. Informatik aktuell, Wiesbaden: Springer Fachmedien, 2019, pp. 232–237, ISBN: 978-3-658-25326-4. DOI: 10.1007/978-3-658-25326-4_52.

[170] O. Halabi, S. Balakrishnan, S. P. Dakua, N. Navab, and M. Warfa, "Virtual and Augmented Reality in Surgery," in *The Disruptive Fourth Industrial Revolution: Technology, Society and Beyond*, ser. Lecture Notes in Electrical Engineering, W. Doorsamy, B. S. Paul, and T. Marwala, Eds., Cham: Springer International Publishing, 2020, pp. 257–285, ISBN: 978-3-030-48230-5. DOI: 10.1007/978-3-030-48230-5_11.

[171] M. Q. Meng, Tao Mei, Jiexin Pu, Chao Hu, Xiaona Wang, and Yawen Chan, "Wireless robotic capsule endoscopy: State-of-the-art and challenges," in *Fifth World Congress on Intelligent Control and Automation (IEEE Cat. No.04EX788)*, vol. 6, 2004, 5561–555a Vol.6. DOI: 10.1109/WCICA.2004.1343799.

[172] T. D. Than, G. Alici, H. Zhou, and W. Li, "A Review of Localization Systems for Robotic Endoscopic Capsules," *IEEE Transactions on Biomedical Engineering*, vol. 59, no. 9, pp. 2387–2399, 2012, ISSN: 1558-2531. DOI: 10.1109/TBME.2012.2201715.

[173] E. Kok *et al.*, "Accurate surgical navigation with real-time tumor tracking in cancer surgery," *npj Precision Oncology*, vol. 4, 2020. DOI: 10.1038/s41698-020-0115-0.

[174] S. S. Mapara and V. B. Patravale, "Medical capsule robots: A renaissance for diagnostics, drug delivery and surgical treatment," *Journal of Controlled Release*, vol. 261, pp. 337–351, 2017, ISSN: 0168-3659. DOI: 10.1016/j.jconrel.2017.07.005.

[175] M. N. Islam and A. J. Fleming, "A novel and compatible sensing coil for a capsule in Wireless Capsule Endoscopy for real time localization," in *2014 IEEE SENSORS*, 2014, pp. 1607–1610. DOI: 10.1109/ICSENS.2014.6985326.

[176] H. Park, C. Park, S.-J. Kweon, J.-H. Suh, J. Choi, and M. Je, "Miniature Electromagnetic Sensor Nodes for Wireless Surgical Navigation Systems," in *2020 IEEE International Symposium on Circuits and Systems (ISCAS)*, 2020, pp. 1–5. DOI: 10.1109/ISCAS45731.2020.9180508.

[177] S. Sharma *et al.*, "Location-aware ingestible microdevices for wireless monitoring of gastrointestinal dynamics," *Nature Electronics*, vol. 6, no. 3, pp. 242–256, 3 Mar. 2023, ISSN: 2520-1131. DOI: 10.1038/s41928-023-00916-0.

[178] NDI, *Aurora - NDI's premier electromagnetic tracking solution.* [Online]. Available: https://www.ndigital.com/electromagnetic-tracking-technology/aurora/ (visited on 10/07/2022).

[179] Radwave Technologies Inc., *Accurate tracking tailored for your purpose.* [Online]. Available: https://radwavetech.com/ (visited on 10/07/2022).

[180] Quadrant Scientific, *Deep Track System*. [Online]. Available: https://quadrant.ie/deep-track-system/ (visited on 12/21/2022).

[181] PENTAX Medical, *SCOPEPILOT*. [Online]. Available: http://www.scopepilot.com/ (visited on 12/21/2022).

[182] F. Bourier *et al.*, "Sensor-Based Electromagnetic Navigation (Mediguide®): How Accurate Is It? A Phantom Model Study," *Journal of Cardiovascular Electrophysiology*, vol. 26, no. 10, pp. 1140–1145, 2015, ISSN: 1540-8167. DOI: 10.1111/jce.12741.

[183] Boston Scientific, *RHYTHMIA HDx™ Mapping System*. [Online]. Available: https://www.bostonscientific.com/en-US/products/capital-equipment--mapping-and-navigation/rhythmia-mapping-system.html (visited on 12/21/2022).

[184] Olympus America, *Peripheral Bronchoscopy with the SPiN System™*. [Online]. Available: https://medical.olympusamerica.com/procedure/peripheral-bronchoscopy-spin-thoracic-navigation-system (visited on 02/23/2023).

[185] Ethicon Inc. - Johnson & Johnson, *MONARCH™ Bronchoscopy*. [Online]. Available: https://www.jnjmedtech.com/en-US/product/monarch-bronchoscopy (visited on 12/21/2022).

[186] Brainlab, *Kick EM - Electromagnetic Surgical Navigation*. [Online]. Available: https://www.brainlab.com/surgery-products/overview-platform-products/kick-em/ (visited on 12/21/2022).

[187] Fiagon, *ENT Series*. [Online]. Available: https://www.fiagon.com/ous/ent-solutions (visited on 12/21/2022).

[188] Olympus Medical Systems, *ScopeGuide*. [Online]. Available: https://www.olympus-europa.com/medical/en/Products-and-Solutions/Medical-Solutions/ScopeGuide/ (visited on 12/21/2022).

[189] Biosense Webster, *Carto® 3 System*. [Online]. Available: https://www.jnjmedtech.com/en-US/product/carto-3-system (visited on 02/23/2023).

[190] Medtronic, *superDimension™ Navigation System*. [Online]. Available: https://www.medtronic.com/covidien/en-us/products/interventional-lung-solutions/superdimension-navigation-system.html (visited on 12/21/2022).

[191] Masmec Biomed, *Sirio*. [Online]. Available: https://masmecbiomed.com/en/navigation/sirio/ (visited on 12/21/2022).

[192] Robin Medical Inc., *The EndoScout Tracking System*. [Online]. Available: https://www.robinmedical.com/endoscout.html (visited on 12/21/2022).

[193] Polhemus, *Polhemus is the premier precision motion tracking company*. [Online]. Available: https://polhemus.com/ (visited on 12/21/2022).

[194] M. A. Nixon, B. C. McCallum, W. R. Fright, and N. B. Price, "The Effects of Metals and Interfering Fields on Electromagnetic Trackers," *Presence: Teleoperators and Virtual Environments*, vol. 7, no. 2, pp. 204–218, 1998, ISSN: 1054-7460, 1531-3263. DOI: 10.1162/105474698565587.

[195] F. Poulin and L. .-. Amiot, "Interference during the use of an electromagnetic tracking system under OR conditions," *Journal of Biomechanics*, vol. 35, no. 6, pp. 733–737, 2002, ISSN: 0021-9290. DOI: 10.1016/S0021-9290(02)00036-2.

[196] J. Traub, S. Kaur, P. Kneschaurek, and N. Navab, "Evaluation of Electromagnetic Error Correction Methods," in *Bildverarbeitung Für Die Medizin 2007*, A. Horsch, T. M. Deserno, H. Handels, H.-P. Meinzer, and T. Tolxdorff, Eds., ser. Informatik Aktuell, Berlin, Heidelberg: Springer, 2007, pp. 363–367, ISBN: 978-3-540-71091-2. DOI: 10.1007/978-3-540-71091-2_73.

[197] W. Ashe, "System and method for magnetic position tracking," US9474465B2, 2016. [Online]. Available: https://patents.google.com/patent/US9474465B2/en (visited on 03/30/2021).

[198] S. LaScalza, J. Arico, and R. Hughes, "Effect of metal and sampling rate on accuracy of Flock of Birds electromagnetic tracking system," *Journal of Biomechanics*, vol. 36, no. 1, pp. 141–144, 2003, ISSN: 0021-9290. DOI: 10.1016/S0021-9290(02)00322-6.

[199] A. Govari, A. C. Altmann, and Y. Ephrath, "Position tracking using quasi-DC magnetic fields," US9295529B2, 2016. [Online]. Available: https://patents.google.com/patent/US9295529B2/en (visited on 03/31/2021).

[200] H. R. J. Jr, R. F. Higgins, and H. E. Himberg, "Magnetic position and orientation measurement system with eddy current distortion compensation," US7292948B2, 2007. [Online]. Available: https://patents.google.com/patent/US7292948/en (visited on 11/29/2022).

[201] J. M. Nieminen and S. R. Kirsch, "Eddy current detection and compensation," US7353125B2, 2008. [Online]. Available: https://patents.google.com/patent/US7353125B2/en (visited on 12/30/2022).

[202] W. Ashe, "Eddy current error-reduced AC magnetic position measurement system," US6172499B1, 2001. [Online]. Available: https://patents.google.com/patent/US6172499/en (visited on 03/30/2021).

[203] M. R. Schneider, "System and method for measuring position and orientation using distortion-compensated magnetic fields," US7373271B1, 2008. [Online]. Available: https://patents.google.com/patent/US7373271B1/en (visited on 03/30/2021).

[204] M. Li, T. Bien, and G. Rose, "Construction of a conductive distortion reduced electromagnetic tracking system for computer assisted image-guided interventions," *Medical Engineering & Physics*, vol. 36, no. 11, pp. 1496–1501, 2014, ISSN: 1350-4533. DOI: 10.1016/j.medengphy.2014.07.018.

[205] M. Li, C. Hansen, and G. Rose, "A robust electromagnetic tracking system for clinical applications," in *CURAC 2015*, Tagungsband: Digitaldruck Bremen, 2015, pp. 31–36.

[206] R. J. Lewandowski and E. J. Wier, "Metal immune magnetic tracker," US6154024A, 2000. [Online]. Available: https://patents.google.com/patent/US6154024A/en (visited on 12/30/2022).

[207] R. A. MacLachlan, R. L. Hollis, J. N. Martel, L. A. Lobes, and C. N. Riviere, "Toward Improved Electromagnetic Tracking for Handheld Robotics," in *Proceedings of the 3rd International Conference on Mechatronics and Robotics Engineering*, ser. ICMRE 2017, Paris, France: Association for Computing Machinery, 2017, pp. 75–80, ISBN: 978-1-4503-5280-2. DOI: 10.1145/3068796.3068823.

[208] G. Zachmann, "Distortion Correction of Magnetic Fields for Position Tracking," in *Proc. Computer Graphics International*, Society Press, 1997, pp. 213–220.

[209] W. Birkfellner, F. Watzinger, F. Wanschitz, R. Ewers, and H. Bergmann, "Calibration of tracking systems in a surgical environment," *IEEE Transactions on Medical Imaging*, vol. 17, no. 5, pp. 737–742, 1998, ISSN: 1558-254X. DOI: 10.1109/42.736028.

[210] V. V. Kindratenko, "A survey of electromagnetic position tracker calibration techniques," *Virtual Reality*, vol. 5, no. 3, pp. 169–182, 2000, ISSN: 1434-9957. DOI: 10.1007/BF01409422.

[211] H. Krumb, D. Das, R. Chadda, and A. Mukhopadhyay, "CycleGAN for interpretable online EMT compensation," *International Journal of Computer Assisted Radiology and Surgery*, vol. 16, no. 5, pp. 757–765, 2021, ISSN: 1861-6410, 1861-6429. DOI: 10.1007/s11548-021-02324-1.

[212] V. Harish, T. Ungi, A. Lasso, A. MacDonald, S. Nanji, and G. Fichtinger, "Intraoperative visualization and assessment of electromagnetic tracking error," in *Medical Imaging 2015: Image-Guided Procedures, Robotic Interventions, and Modeling*, vol. 9415, International Society for Optics and Photonics, 2015, 94152H. DOI: 10.1117/12.2082330.

[213] M. Ikits, J. Brederson, C. Hansen, and J. Hollerbach, "An improved calibration framework for electromagnetic tracking devices," in *Proceedings IEEE Virtual Reality 2001*, 2001, pp. 63–70. DOI: 10.1109/VR.2001.913771.

[214] A. K. Jain, M. B. Matinfar, R. Chan, V. Parthasarthy, and D. A. Stanton, "Method and system for characterizing and visualizing electromagnetic tracking errors," US9165114B2, 2015. [Online]. Available: https://patents.google.com/patent/US9165114B2/en (visited on 05/21/2020).

[215] M. Cavaliere, D. Crowley, H. A. Jaeger, K. O'Donoghue, and P. Cantillon-Murphy, "Magnetic Model Calibration and Distortion Compensation for Electromagnetic Tracking in a Clinical Environment," *IEEE Transactions on Magnetics*, vol. 59, no. 7, pp. 1–12, 2023, ISSN: 1941-0069. DOI: 10.1109/TMAG.2023.3275297.

[216] H. Himberg, Y. Motai, and A. Bradley, "Interpolation Volume Calibration: A Multisensor Calibration Technique for Electromagnetic Trackers," *IEEE Transactions on Robotics*, vol. 28, no. 5, pp. 1120–1130, 2012, ISSN: 1941-0468. DOI: 10.1109/TRO.2012.2198929.

[217] S. L. Charreyron, Q. Boehler, B. Kim, C. Weibel, C. Chautems, and B. J. Nelson, "Modeling Electromagnetic Navigation Systems," *IEEE Transactions on Robotics*, vol. 37, no. 4, pp. 1009–1021, 2021, ISSN: 1552-3098, 1941-0468. DOI: 10.1109/TRO.2020.3047053.

[218] R. Yu *et al.*, "Modeling Electromagnetic Navigation Systems for Medical Applications using Random Forests and Artificial Neural Networks," in *2020 IEEE International Conference on Robotics and Automation (ICRA)*, 2020, pp. 9251–9256. DOI: 10.1109/ICRA40945.2020.9197212.

[219] T. Bien and G. Rose, "Algorithm for calibration of the electromagnetic tracking system," in *Proceedings of 2012 IEEE-EMBS International Conference on Biomedical and Health Informatics*, 2012, pp. 85–88. DOI: 10.1109/BHI.2012.6211512.

[220] C. Nafis, V. Jensen, and R. v. J. M.d, "Method for evaluating compatibility of commercial electromagnetic (EM) microsensor tracking systems with surgical and imaging tables," in *Medical Imaging 2008: Visualization, Image-Guided Procedures, and Modeling*, vol. 6918, International Society for Optics and Photonics, 2008, p. 691 820. DOI: 10.1117/12.769513.

[221] D. Kügler *et al.*, "High-precision evaluation of electromagnetic tracking," *International Journal of Computer Assisted Radiology and Surgery*, vol. 14, no. 7, pp. 1127–1135, 2019, ISSN: 1861-6429. DOI: 10.1007/s11548-019-01959-5.

[222] J. B. Hummel *et al.*, "Design and application of an assessment protocol for electromagnetic tracking systems," *Medical Physics*, vol. 32, no. 7Part1, pp. 2371–2379, 2005, ISSN: 2473-4209. DOI: 10.1118/1.1944327.

[223] E. Wilson *et al.*, "A hardware and software protocol for the evaluation of electromagnetic tracker accuracy in the clinical environment: A multi-center study," in *Medical Imaging 2007: Visualization and Image-Guided Procedures*, vol. 6509, International Society for Optics and Photonics, 2007, 65092T. DOI: 10.1117/12.712701.

[224] L. Maier-Hein *et al.*, "Standardized assessment of new electromagnetic field generators in an interventional radiology setting," *Medical Physics*, vol. 39, no. 6, pp. 3424–3434, 2012, ISSN: 00942405. DOI: 10.1118/1.4712222.

[225] J. Nijkamp *et al.*, "Comparing position and orientation accuracy of different electromagnetic sensors for tracking during interventions," *International Journal of Computer Assisted Radiology and Surgery*, vol. 11, no. 8, pp. 1487–1498, 2016, ISSN: 18616429. DOI: 10.1007/s11548-015-1348-1.

[226] J. Pascal, D. Vogel, S. Knecht, M. Vescovo, and L. Hébrard, "Three-dimensional Magnetic Camera for the Characterization of Magnetic Manipulation Instrumentation Systems for Electrophysiology Procedures," in *EMBEC & NBC 2017*, H. Eskola, O. Väisänen, J. Viik, and J. Hyttinen, Eds., ser. IFMBE Proceedings, Singapore: Springer, 2018, pp. 410–413, ISBN: 978-981-10-5122-7. DOI: 10.1007/978-981-10-5122-7_103.

[227] A. Ahmed, S. A. Abbasi, N. L. Gharamaleki, J.-Y. Kim, and H. Choi, "An economical, Lego-like approach for real-time magnetic field mapping (MagMaps) using commercial magnetic sensors," *IEEE Transactions on Instrumentation and Measurement*, pp. 1–1, 2022, ISSN: 1557-9662. DOI: 10.1109/TIM.2022.3232168.

[228] B. Jascob, D. Simon, P. Kessman, and A. Smith, "Method and apparatus for electromagnetic navigation of a surgical probe near a metal object," US6636757B1, 2003. [Online]. Available: https://patents.google.com/patent/US6636757B1/en (visited on 09/11/2020).

[229] R. Graumann, G. Kleinszig, J. Siewerdsen, and J. Yoo, "C-arm integrated electromagnetic tracking system," US20120289821A1, 2012. [Online]. Available: https://patents.google.com/patent/US20120289821A1/en (visited on 09/11/2020).

[230] V. T. Jensen and W. H. Huber, "Surgical navigation enabled imaging table environment," US8483800B2, 2013. [Online]. Available: https://patents.google.com/patent/US8483800B2/en (visited on 01/03/2023).

[231] J. Yoo, S. Schafer, A. Uneri, Y. Otake, A. J. Khanna, and J. H. Siewerdsen, "An electromagnetic "Tracker-in-Table" configuration for X-ray fluoroscopy and cone-beam CT-guided surgery," *International Journal of Computer Assisted Radiology and Surgery*, vol. 8, no. 1, pp. 1–13, 2013, ISSN: 1861-6429. DOI: 10.1007/s11548-012-0744-z.

[232] A. M. Franz *et al.*, "Electromagnetic tracking for US-guided interventions: Standardized assessment of a new compact field generator," *International Journal of Computer Assisted Radiology and Surgery*, vol. 7, no. 6, pp. 813–818, 2012, ISSN: 1861-6429. DOI: 10.1007/s11548-012-0740-3.

[233] K. März *et al.*, "Interventional real-time ultrasound imaging with an integrated electromagnetic field generator," *International Journal of Computer Assisted Radiology and Surgery*, vol. 9, no. 5, pp. 759–768, 2014, ISSN: 1861-6429. DOI: 10.1007/s11548-014-0990-3.

[234] A. M. Franz *et al.*, "First clinical use of the EchoTrack guidance approach for radiofrequency ablation of thyroid gland nodules," *International Journal of Computer Assisted Radiology and Surgery*, vol. 12, no. 6, pp. 931–940, 2017, ISSN: 1861-6410, 1861-6429. DOI: 10.1007/s11548-017-1560-2.

[235] W. S. Ashe, "Magnetic field permeable barrier for magnetic position measurement system," US6246231B1, 2001. [Online]. Available: https://patents.google.com/patent/US6246231B1/en (visited on 03/31/2021).

[236] P. T. Anderson, "Surgical navigation system with electrostatic shield," US20080287771A1, 2008. [Online]. Available: https://patents.google.com/patent/US20080287771A1/en (visited on 09/11/2020).

[237] J. Scully and M. Schneider, "DC magnetic-based position and orientation monitoring system for tracking medical instruments," US20070078334A1, 2007. [Online]. Available: https://patents.google.com/patent/US20070078334A1/en (visited on 03/30/2021).

[238] K. O'Donoghue and P. Cantillon-Murphy, "Planar Magnetic Shielding for Use With Electromagnetic Tracking Systems," *IEEE Transactions on Magnetics*, vol. 51, no. 2, pp. 1–12, 2015, ISSN: 1941-0069. DOI: 10.1109/TMAG.2014.2352344.

[239] W. Ashe, "Magnetic position and orientation measurement system with magnetic field permeable attenuator," US6784660B2, 2004. [Online]. Available: https://patents.google.com/patent/US6784660B2/en (visited on 03/31/2021).

[240] W. Ashe, "Magnetic position measurement system with field containment means," US6528991B2, 2003. [Online]. Available: https://patents.google.com/patent/US6528991B2/en (visited on 03/31/2021).

[241] Z. Yaniv, E. Wilson, D. Lindisch, and K. Cleary, "Electromagnetic tracking in the clinical environment," *Medical Physics*, vol. 36, no. 3, pp. 876–892, 2009, ISSN: 00942405. DOI: 10.1118/1.3075829.

[242] E. Lugez, H. Sadjadi, D. R. Pichora, R. E. Ellis, S. G. Akl, and G. Fichtinger, "Electromagnetic tracking in surgical and interventional environments: Usability study," *International Journal of Computer Assisted Radiology and Surgery*, vol. 10, no. 3, pp. 253–262, 2015, ISSN: 1861-6410. DOI: 10.1007/s11548-014-1110-0.

[243] W. S. Ashe, "Radiolucent Transmitters for Magnetic Position Measurement Systems," US20150216490A1, 2015. [Online]. Available: https://patents.google.com/patent/US20150216490A1/en (visited on 01/03/2023).

[244] D. J. Foster, D. R. Wulfman, M. Hein, and K. R. Poppe, "Coils and coil assemblies that are radio-translucent," US20170188882A1, 2017. [Online]. Available: https://patents.google.com/patent/US20170188882A1/en (visited on 01/03/2023).

[245] V. Gliner, "Fluoro-invisible location pad structure for cardiac procedures," US20170007155A1, 2017. [Online]. Available: https://patents.google.com/patent/US20170007155A1/en (visited on 01/03/2023).

[246] A. D. Hill, J. Hauck, R. M. Albu, T. G. Curran, and R. Link, "Fluorolucent magnetic field generator," US20200060547A1, 2020. [Online]. Available: https://patents.google.com/patent/US20200060547A1/en (visited on 01/03/2023).

[247] K. O'Donoghue, H. A. Jaeger, and P. Cantillon-Murphy, "A Radiolucent Electromagnetic Tracking System for Use with Intraoperative X-ray Imaging," *Sensors*, vol. 21, no. 10, p. 3357, 2021. DOI: 10.3390/s21103357.

[248] L. E. Bø, H. O. Leira, G. A. Tangen, E. F. Hofstad, T. Amundsen, and T. Langø, "Accuracy of electromagnetic tracking with a prototype field generator in an interventional OR setting," *Medical Physics*, vol. 39, no. 1, pp. 399–406, 2012, ISSN: 2473-4209. DOI: 10.1118/1.3666768.

[249] M. Bar-tal and A. Govari, "Distortion-immune position tracking using redundant measurements," US8536859B2, 2013. [Online]. Available: https://patents.google.com/patent/US8536859B2/en (visited on 05/12/2020).

[250] G. Shechter, "Electromagnetic tracking method and apparatus for compensation of metal artifacts using modular arrays of reference sensors," US7902816B2, 2011. [Online]. Available: https://patents.google.com/patent/US7902816B2/en (visited on 09/20/2021).

[251] E. Shen, "System and method for dynamic metal distortion compensation for electromagnetic tracking systems," US20110270083A1, 2011. [Online]. Available: https://patents.google.com/patent/US20110270083A1/en (visited on 09/20/2021).

[252] E. Shen and J. Kruecker, "System for local error compensation in electromagnetic tracking systems," EP2005208B1, 2017. [Online]. Available: https://patents.google.com/patent/EP2005208B1/en (visited on 09/20/2021).

[253] I. Khalfin and H. S. J. Jr, "Electromagnetic position and orientation tracking system with distortion compensation employing wireless sensors," US6369564B1, 2002. [Online]. Available: https://patents.google.com/patent/US6369564B1/en (visited on 12/13/2022).

[254] B. Ramachandran and A. K. Jain, "Distortion fingerprinting for EM tracking compensation, detection and error correction," US9522045B2, 2016. [Online]. Available: https://patents.google.com/patent/US9522045B2/en.

[255] P. L. Bono, J. D. Lark, and J. S. Scales, "System and method for reducing interference in positional sensors for robotic surgery," US20200337783A1, 2020. [Online]. Available: https://patents.google.com/patent/US20200337783A1/en.

[256] H. Durrant-Whyte and T. Bailey, "Simultaneous localization and mapping: Part I," *IEEE Robotics Automation Magazine*, vol. 13, no. 2, pp. 99–110, 2006, ISSN: 1558-223X. DOI: 10.1109/MRA.2006.1638022.

[257] T. Bailey and H. Durrant-Whyte, "Simultaneous localization and mapping (SLAM): Part II," *IEEE Robotics Automation Magazine*, vol. 13, no. 3, pp. 108–117, 2006, ISSN: 1558-223X. DOI: 10.1109/MRA.2006.1678144.

[258] R. B. Chan, "Ambient electromagnetic distortion correction for electromagnetic tracking," 20 200 133 405, 2020. [Online]. Available: http://www.freepatentsonline.com/y2020/0133405.html.

[259] M. Kok and A. Solin, "Scalable Magnetic Field SLAM in 3D Using Gaussian Process Maps," in *2018 21st International Conference on Information Fusion (FUSION)*, 2018, pp. 1353–1360. DOI: 10.23919/ICIF.2018.8455789.

[260] X. Luo *et al.*, "Evolutionarily Optimized Electromagnetic Sensor Measurements for Robust Surgical Navigation," *IEEE Sensors Journal*, vol. 19, no. 22, pp. 10 859–10 868, 2019, ISSN: 15581748. DOI: 10.1109/JSEN.2019.2928835.

[261] H. Sadjadi, "Electromagnetic instrument tracking in computer-assisted interventions," Thesis, 2014. [Online]. Available: https://qspace.library.queensu.ca/handle/1974/12358 (visited on 05/12/2020).

[262] H. Sadjadi, E. Lugez, K. Hashtrudi-Zaad, and G. Fichtinger, "Methods and apparatus for improved electromagnetic tracking and localization," US10285760B2, 2019. [Online]. Available: https://patents.google.com/patent/US10285760B2/en (visited on 05/12/2020).

[263] H. Sadjadi, K. Hashtrudi-Zaad, and G. Fichtinger, "Simultaneous localization and calibration for electromagnetic tracking systems," *The International Journal of Medical Robotics and Computer Assisted Surgery*, vol. 12, no. 2, pp. 189–198, 2016, ISSN: 1478-596X. DOI: 10.1002/rcs.1670.

[264] H. Sadjadi, K. Hashtrudi-Zaad, and G. Fichtinger, "Simultaneous Electromagnetic Tracking and Calibration for Dynamic Field Distortion Compensation," *IEEE Transactions on Biomedical Engineering*, vol. 63, no. 8, pp. 1771–1781, 2016, ISSN: 1558-2531. DOI: 10.1109/TBME.2015.2502138.

[265] E. Lugez, H. Sadjadi, C. P. Joshi, K. Hashtrudi-Zaad, S. G. Akl, and G. Fichtinger, "Field distortion compensation for electromagnetic tracking of ultrasound probes with application in high-dose-rate prostate brachytherapy," *Biomedical Physics & Engineering Express*, vol. 5, no. 3, p. 035 026, 2019, ISSN: 2057-1976. DOI: 10.1088/2057-1976/ab12b6.

[266] S. N. Lavasani, M. Deevband, P. Farnia, A. Ahmadian, and S. Saghatchi, "Compensation of dynamic electromagnetic field distortion using simultaneous localization and mapping method with application in endobronchial ultrasound-transbronchial needle aspiration (EBUS-TBNA) guidance," *The International Journal of Medical Robotics and Computer Assisted Surgery*, vol. 16, no. 1, e2035, 2020, ISSN: 1478-596X. DOI: 10.1002/rcs.2035.

[267] T. I. Götz *et al.*, "On the use of particle filters for electromagnetic tracking in high dose rate brachytherapy," *Physics in Medicine and Biology*, vol. 62, no. 19, pp. 7617–7640, 2017, ISSN: 1361-6560. DOI: 10.1088/1361-6560/aa8591.

Chapter 3

ANSER EMT system and accuracy assessment methods

This chapter presents the instruments and methods employed in this thesis. Section 3.1 describes the hardware and software components of the ANSER EMT system. Particular emphasis is placed on the methods that lay the groundwork for the following chapters, like signal demodulation in Section 3.2.2 and magnetic modelling and calibration in Section 3.2.3.

Section 3.3 introduces novel tools to host EMT sensors, including the optical system utilised for accurate pose reference, and Section 3.4 describes the 2D robotic actuator designed to help move the sensors consistently and repeatedly.

Section 3.5 presents a theoretical analysis of tracking errors, followed by an examination of the experimental performance in Section 3.6.

3.1 ANSER EMT

The ANSER EMT project aims to provide an open, low-cost research platform for EMT with particular application to image-guided interventions [2].

Parts of this chapter are based on M. Cavaliere *et al.*, "Magnetic tracking using a modular C++ environment for image-guided interventions," *Computer Methods in Biomechanics and Biomedical Engineering: Imaging & Visualization*, vol. 10, no. 4, pp. 383–389, 2021 [1].

The software [3] and hardware [4] are freely released under Creative Commons license, and guides and tutorials are available to support new users and facilitate the first installation [5].

ANSER EMT is application-independent and can potentially integrate with existing hardware and software in any operating environment. The system is compatible with commercially available EMT sensors as well as with any kind of customised magnetic sensor and supports the open network interface for image-guided therapy (OpenIGTLink) [6] for easy communication with other navigation platforms, e.g. MITK [7], CustusX [8], and 3D Slicer [9].

The platform has enabled hardware innovation with bespoke sensor design [10, 11], custom tracking volumes [12], and provided a basis for characterising and compensating for magnetic distortions [13, 14].

The following sections give an overview of the system, whereas more detailed information can be found on the online project repository [15].

3.1.1 Functional subsystems

The working principle of the ANSER EMT system is detailed in Figure 3.1. The position and orientation information is based on the magnetic coupling between the emitter coils in the field generator and the sensor. The magnetic model is the function that maps the position and orientation of the target sensor to the magnetic field measured at that location. By contrasting the field measurement to the model, the map is reversed, and the sensor pose in the working space is determined.

Overall, the tracking process can be summarised in three steps: field generation, signal acquisition, and signal processing. The first two steps are accomplished by the field generator, the magnetic sensor, and the control unit, which are the main hardware components of the ANSER EMT system and will be presented in the following paragraphs. The signal processing step, including the tracking algorithm, is part of the software that runs on a computer connected to the system and will be discussed in Section 3.2.

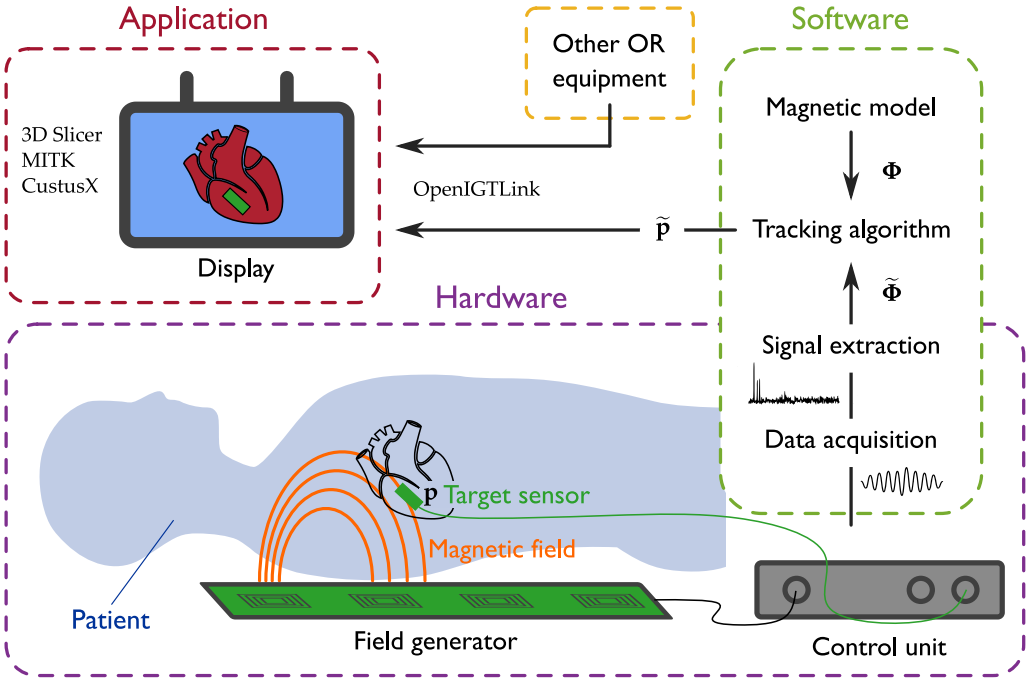


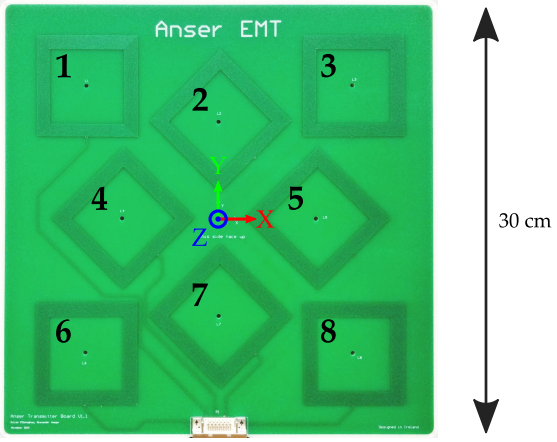
Figure 3.1: A schematic representation of the overall data flow in the ANSER EMT system. The target sensor, typically attached to the instrument tip, measures the magnetic field generated by a set of transmitter coils inside the field generator. The signal is acquired in the control unit and transmitted to a personal computer, where it is processed to determine sensor position and orientation using a known magnetic field model. The instrument can be visualised inside a pre-recorded anatomical image to assist the medical procedure.

3.1.1.1 Field generator

The field generator is a planar two-layer printed circuit board (PCB) comprising a set of eight transmitter coils arranged in a known configuration, following an optimised constellation [16, 17]. In this thesis, the terms *transmitter* and *emitter* coil will be used interchangeably. Several versions of the field generator are available, and the two boards used in the experiments presented in this thesis are shown in Figure 3.2.

The smaller board has a dimension of $30 \times 30\,\text{cm}^2$ and PCB depth of 1.6 mm. It hosts planar coils of 25 turns and square shape with an external edge of 70 mm. The coils have a DC resistance of $4.7\,\Omega$ measured on the coil, which varies from $5.2\,\Omega$ to $5.6\,\Omega$ if measured at the board connector, depending on the position of the coil in the board and the length of

(a) Field generator, 30 cm board



(b) Field generator, 42 cm board

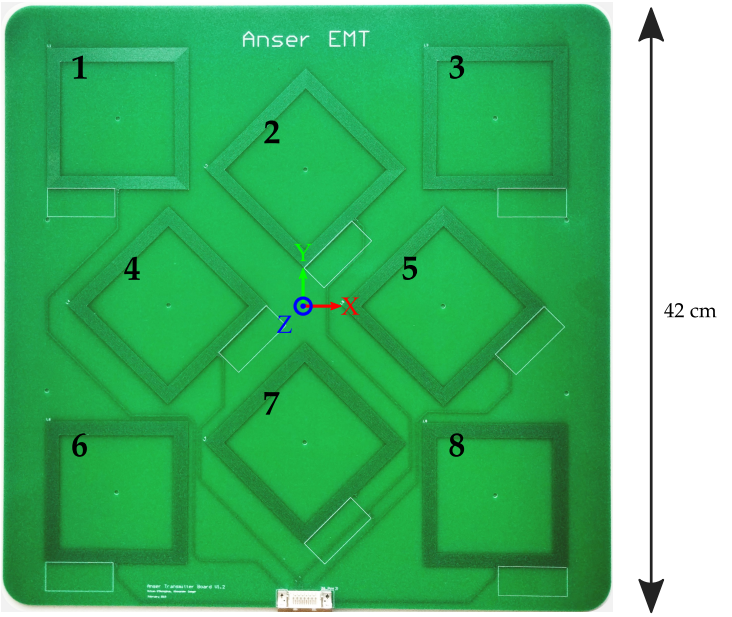


Figure 3.2: Two of the field generators available for the ANSER EMT system, with board dimensions of (a) 30 cm and (b) 42 cm, respectively. The eight emitter coils embedded in the field generators are visible and are numbered from 1 to 8.

the PCB traces connecting it. The values did not change substantially if the measurement was taken at 10 kHz. The coils' self-inductance was measured to be approximately 75 μH at 10 kHz, and 74 μH at 1 kHz. The same values were obtained if the measurement was taken at the board connector because the paired traces have a limited contribution to the inductance.

The larger board has a dimension of $42 \times 42\,\text{cm}^2$ and PCB depth of 2 mm. The square coils of 25 turns have an external edge of 98 mm. The DC resistance was measured as 6.3 Ω on the coil and ranging from 7.0 Ω to 7.8 Ω at the connector. The self-inductance resulted in 125.5 μH at 10 kHz, and 124.5 μH at 1 kHz.

Each emitter coil is driven with a sinusoidal current, with the frequency selected in software between 1 kHz and 50 kHz, and a current amplitude that can be configured up to 300 mA. It is worth noting that within the operating range of the system, which is typically 5 to 40 cm from the field generator, electromagnetic radiation can be neglected, and the magnetic field can be treated as quasi-static. For comparison, a 100 kHz wave has a wavelength of approximately 3 km in vacuum.

Such low-frequency magnetic fields are safe [18], where the only undesired effect might be tissue heating at sufficiently high field amplitude and exposure time. The human body has minimal absorption of AC magnetic fields below 100 kHz [19–21], which becomes relevant only in cases of prolonged exposure to high-magnitude fields.

For this reason, the International Commission on Non-Ionizing Radiation Protection (ICNIRP) and the IEEE International Committee on Electromagnetic Safety provide safety levels to limit human exposure to magnetic fields [22, 23]. In restricted environments, which is the case for EMT applications in the operative room, and in the frequency range 1–50 kHz, the maximum recommended magnetic flux density is 0.615 mT for head and torso, and above 75 mT for limbs exposure. For multi-frequency exposure, the limit is calculated as the sum of the ratios between the amplitude of each harmonic and the reference level calculated for the same frequency.

For the ANSER EMT system, considering a minimum distance of 5 cm from the field generator, the highest value of the magnetic flux density is found on the axis of each emitter coil, and it results in approximately 0.025 mT peak flux density when the maximum drive current of 300 mA is used. The eight coils are in different positions, but even applying a conservative calculation and considering eight times the value of the maximum field, the resulting 0.200 mT magnitude falls well below the limit levels allowed.

The PCB base material in flame retardant epoxy resin (FR4) is partially transparent to X-rays, which makes the board compatible with intraoperative fluoroscopy imaging. On the contrary, the copper coils can cause X-ray attenuation and imaging artefacts. The use of low-density aluminium coils is a viable solution to significantly reduce the impact on X-ray imaging systems [24].

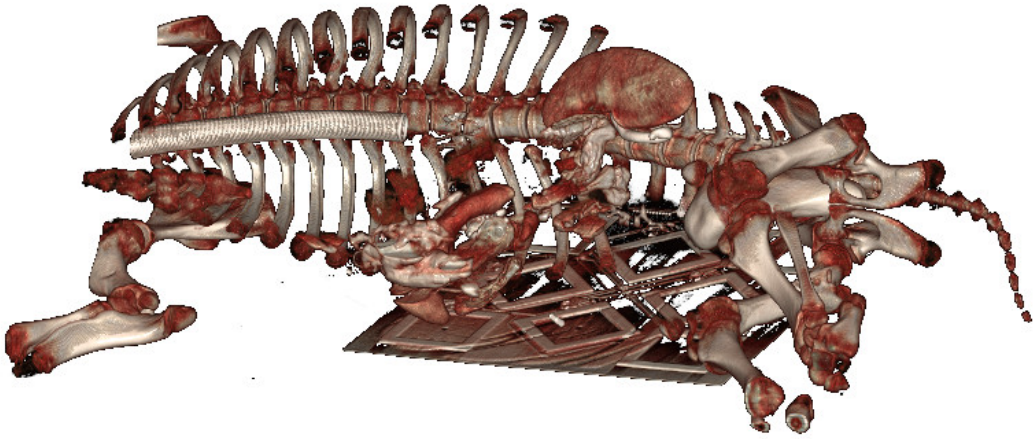
This issue is less relevant for computed tomography (CT) scans because, in this case, the 3D volume reconstruction allows localising the field generator, and its presence has minimal impact on the 3D image of objects located elsewhere. Figure 3.3 shows the full CT scan of an animal model placed above the two ANSER EMT field generators introduced above. In these images, the emitter coils and the planar boards are visible, but they do not introduce significant artefacts in the 3D reconstruction of the animal's internal organs.

3.1.1.2 Magnetic sensor

In the ANSER EMT system, the magnetic sensor is the marker whose position and orientation are tracked. The most efficient way to measure AC magnetic fields is by using induction pick-up coils [25]. Such sensors are relatively inexpensive, inherently safe since they are passive by nature, and can be fabricated to less than 0.3 mm in diameter [26], as shown in Figure 3.4a. For these reasons, they can be made biocompatible and disposable at a reasonable cost, and they are the preferred solution for biomedical applications.

Induction coil sensors work on the principle of magnetic induction, described by Faraday's law, which states that the electromotive force,

(a) Field generator, 30 cm board



(b) Field generator, 42 cm board

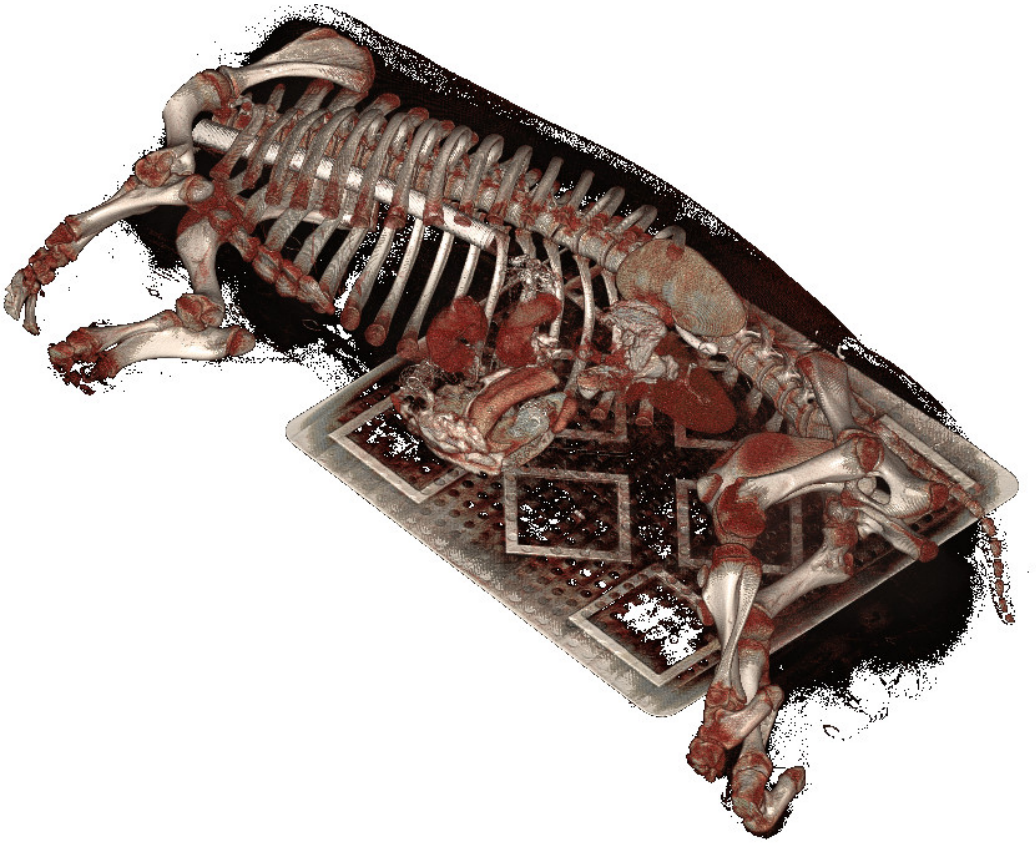


Figure 3.3: Full CT scan of an animal model placed above the two ANSER EMT field generators introduced in Section 3.1.1.1.

$v(t)$, on a static loop is equal to the negative of the time derivative of the magnetic flux, Φ, crossing that loop:

$$v(t) = -\frac{\partial \Phi(t)}{\partial t} \quad [\mathrm{V}] \tag{3.1}$$

The magnetic flux Φ is calculated as the surface integral of the magnetic flux density, $\mathbf{B}$, over the loop's area, A_l:

$$\Phi_l(t) = \oint_{A_l} \mathbf{B} \cdot \mathbf{n}\, dA_l \quad [\mathrm{Wb}] \tag{3.2}$$

where $\mathbf{n}$ is the unit vector normal to the area element dA_l.

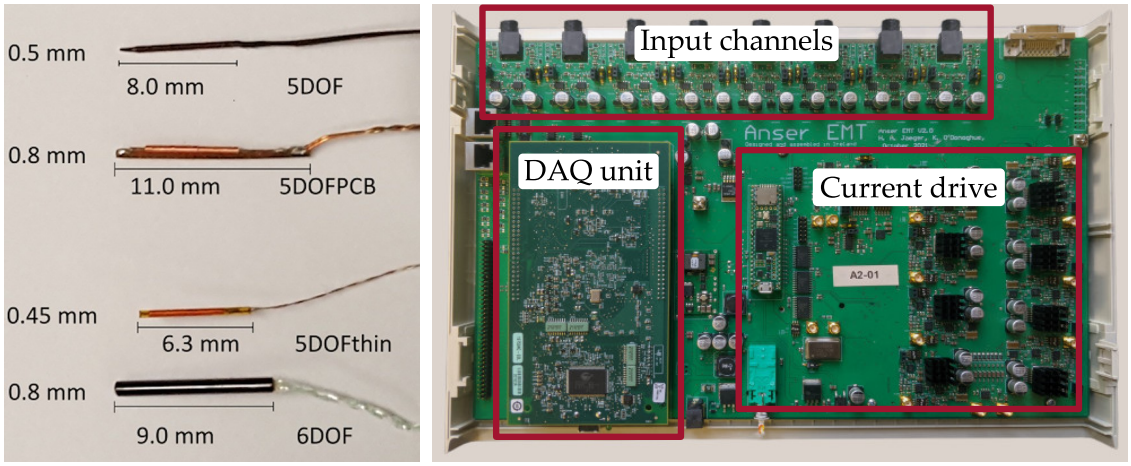
An inductive coil comprises N consecutive loops forming the winding turns. Each loop experiences a magnetic flux calculated according to Equation 3.2, and because they are connected in series, the total voltage appearing at the coil terminals is given by:

$$v(t) = -\frac{\partial}{\partial t} \sum_{n=1}^{N} \oint_{A_l} \mathbf{B} \cdot \mathbf{n}\, dA_l \quad [\mathrm{V}] \tag{3.3}$$

Simplifications of Equation 3.3 are possible when the coil is small relative to the spatial variation of the magnetic flux density and will be discussed in Section 3.2.3.

From Equation 3.3, it is evident that the smaller the sensor cross-sectional area, the smaller the magnetic flux enclosed by it and thus the signal. The addition of a ferromagnetic core can significantly increase the received sensor voltage [11]. However, all ferromagnetic materials are inherently non-linear. Hence, the sensor output will exhibit some non-linear behaviour, which can depend on many factors, such as frequency, temperature, and field strength [27]. Typically, the temperature can be considered constant inside the human body, but ANSER EMT field frequencies and magnitudes may be taken into account for the choice of the sensor core material [28].

The magnetic flux through the coil area depends on the ferrite core's relative permeability and the ratio between the core length and diameter [29, 30]. A higher demagnetising factor affects shorter cores, where



(a) EMT sensors (b) Control unit

Figure 3.4: (a) Four EMT sensors available in the market [26]. Image adapted from [33]. (b) ANSER EMT control unit.

magnetic flux lines find a closed path inside the core itself due to the low reluctance, adding a negative contribution to the flux linked to the coil [31, 32]. This reason and the necessity to include a high number of turns forces the EMT sensor design towards elongated shapes at the centimetre scale to guarantee satisfactory sensitivity.

3.1.1.3 Control unit

The ANSER EMT control unit comprises the hardware necessary for field generation, signal acquisition, and communication with the computer, as shown in Figure 3.4b.

For every emitter coil, the field generation chain includes a direct digital synthesiser (DDS) that outputs a reference signal with an amplitude of 0.6 V, 2× amplification, passive passband filtering between 820 Hz and 30 kHz, a fast, AC-coupled, closed-loop current control, and a final boosting stage to power the coil up to a maximum electric current of 300 mA in amplitude. A small-footprint microcontroller development system (Teensy 4.1, PJRC, OR, USA) is also present to configure the DDS with sinusoidal waveform generation at the frequency required.

For every sensor, the acquisition chain includes an instrumentation amplifier (INA) and high-pass filtering to remove frequencies above the

Nyquist–Shannon band limit before analogue-to-digital conversion (ADC). Signal digitalisation is carried out by a data acquisition (DAQ) unit (NI-USB-6212, National Instruments, TX, USA), which supports USB communication with a computer using the NI-DAQmx companion drivers.

The DAQ unit features sixteen analogue inputs, fifteen of which are used to sample and track up to fifteen 5 DOF sensors concurrently. A 6 DOF EMT sensor is typically obtained by fixing two 5 DOF sensors at a relative angle [34], so the fifteen inputs could also be used to connect up to seven 6 DOF and one 5 DOF sensors.

The last input is used to sample the current of each emitter coil. The currents are sampled after being summed together using a current-summing amplifier. This step is required to obtain a time reference and efficiently demodulate the composite signal, as will be explained in Section 3.2.2.

3.2 Modular software framework

The ANSER EMT software framework has previously been implemented in MATLAB [2], Python [35, 36], and C++ [1].

MATLAB requires a license to use and has limited support for operating systems other than Microsoft© Windows©. On the other hand, Python is free and well-supported by open-source libraries. However, either implementation is based on an interpreted language and may require an increased amount of computation time and memory compared to lower-level programming languages like C++ . Despite these limitations, both environments are well-suited for prototyping, debugging, and data manipulation and visualisation, which is why MATLAB was primarily used for the novel work presented in this thesis.

The framework has recently been extended to create a modular open-source C++ environment [1]. This represents an important step in the effort to develop open-source platforms for navigated image-guided interventions [37]. C++ code is translated into machine code by a compiler before it is executed and can be optimised for the specific hardware it is running on, making the C++ framework more efficient and faster.

Regardless of the programming environment, the software system of ANSER EMT can be described as having four main components:

- Signal acquisition: the first step in solving for the sensor position and orientation is to acquire the measurement from the magnetic sensor. The coil experiences an induced voltage from the set of eight sinusoidal magnetic sources of the field generator.
- Signal extraction or demodulation: the sampled signal is digitally filtered to extract the magnetic flux due to each transmitter coil.
- Magnetic modelling: a physical model of the mutual inductance between the magnetic sources and tracking coil is calculated.
- Solver or tracking algorithm: the difference between the field measurements from the tracking coil and physical model is the base of an objective function which is minimised to estimate the sensor pose.

These steps are illustrated in the schematic representation of Figure 3.1, showing the information flow in the ANSER EMT system.

As previously mentioned, the framework currently requires a computer to operate. However, the C++ implementation is the first step towards integrating it into a microcontroller.

The following sections provide a more detailed explanation of the four main modules of the software framework.

3.2.1 Data acquisition

After analogue amplification and filtering, the differential voltage from the magnetic sensor is sampled. Analogue-to-digital conversion and USB transmission are carried out by the NI-USB-6212 unit presented in Section 3.1.1.3.

The NI-DAQmx is a cross-platform driver compatible with different programming languages and provides an application programming interface (API) for configuring the DAQ hardware and reading/writing data from/to DAQ analogue and digital output channels. In particular, the Data Acquisition Toolbox [38] is required in MATLAB to enable NI-DAQmx

support, while the *nidaqmx* package [39] and PyDAQmx [40] provide user-friendly interfaces between the NI-DAQmx driver and Python. External compiler support files for C/C++ are automatically included in the installation directory when installing the NI-DAQmx APIs and driver [41].

Typically, the DAQ is configured to run continuously in the background to parallelise the sampling and solving stages. The sampling rate, F_s, and the number of samples, N_s, can be selected, and when a signal window of N_s samples is available, it is stored in a buffer variable. The foreground program is then free to read the last signal window whenever required and proceed with the demodulation and solving stages presented in the following sections.

The DAQ can also be configured as an external clock source for the waveform generators that provide reference to the current in the emitter coils. In this way, the same clock is used for generation and sampling, guaranteeing coherence between the signal and the sampling frequencies, which is essential to reduce spectral leakage, as will be discussed in Section 3.2.2.3.

3.2.2 Signal extraction

In its typical configuration, the ANSER EMT system uses frequency division multiplexing (FDM) to transmit the eight independent magnetic fields at the same time. Each emitter coil is driven with a sinusoidal current at a specific frequency, F_{ec}, where $1 \leq ec \leq 8$ identifies the emitter coil. The signal picked up by the magnetic sensor is the superposition of the eight frequency components, as shown in Figure 3.5.

The measurement of the signal magnitude and phase can be obtained by several analogue or digital means [42], such as filtering, phase-lock amplification, digital lock-in detection [43], function fitting [42], discrete Fourier transform (DFT) or discrete Hartley transform (DHT) [44], and sliding DFT [45]. A sliding window method will be discussed in Section 5.2.1 to increase the refresh rate of the measured signal.

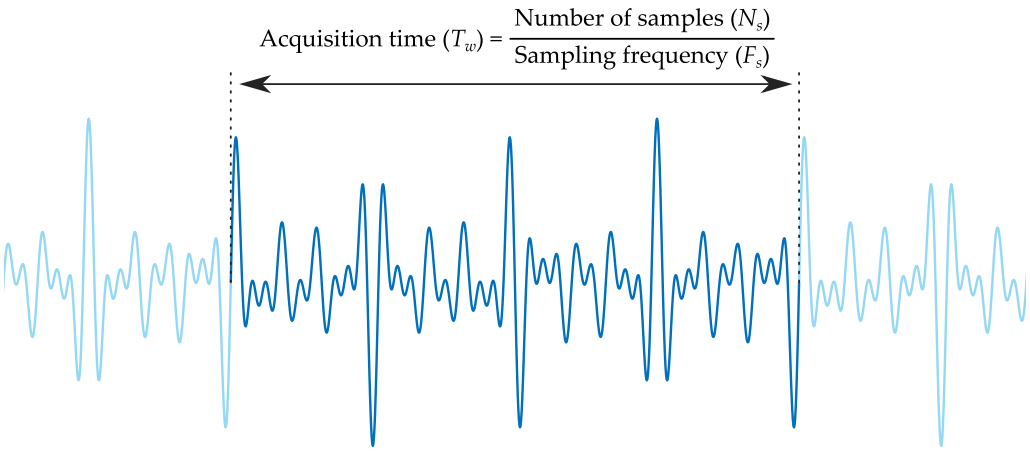


Figure 3.5: The sampled signal window is the superposition of the eight magnetic field frequency components.

3.2.2.1 Discrete Fourier transform

In ANSER EMT, the demodulation is performed after digitalisation, and a DFT approach is used [46]. A signal window sampled at a constant rate is a train of equally spaced samples, $s[n]$, and it is characterised by the sampling frequency, F_s, and the number of samples, N_s.

The acquisition time, or the duration of the sampling window, T_w, is the reciprocal of the bin width, F_b, which is the minimum frequency that can be resolved or the difference between consecutive DFT bins.

$$T_w = \frac{1}{F_s} N_s; \quad F_b = \frac{F_s}{N_s} \tag{3.4}$$

Using the usual complex notation with $i = \sqrt{-1}$, a weighted average is performed to calculate the DFT bins of interest [47] and recover, or demodulate, the magnetic flux due to emitter coil ec:

$$\overline{\Phi_{ec}} = \Phi_{ec} e^{i\alpha_{ec}} = \frac{1}{N_s} \sum_{n=0}^{N_s-1} s[n] \cdot e^{-i2\pi F_{ec} \frac{nT_w}{N_s}} = \frac{1}{N_s} \sum_{n=0}^{N_s-1} s[n] \cdot e^{-i\frac{2\pi n}{N_s} m_{ec}} \tag{3.5}$$

where $m_{ec} = F_{ec} T_w = F_{ec} {}^{N_s}/_{F_s} = {}^{F_{ec}}/_{F_b}$ is the frequency index and indicates how many cycles of the signal at frequency F_{ec} are contained in the acquisition time T_w. Considering all DFT bins contained in the signal, m ranges

from 0 to $N_s - 1$, like the sample index n. The overline is used to indicate that $\overline{\Phi_{ec}}$ is a complex number or phasor.

For the frequency component at $m = 0$, or DC component, it is clear that Equation 3.5 simply becomes the average of $s[n]$ calculated across the N_s samples. The same is true for a signal expressed as $A_m e^{i2\pi F_m nT_w/N_s}$, for which the sum of Equation 3.5 returns the amplitude A_m, whereas any other frequency component at $F_p \neq F_m$ is cancelled out after the sum, because $\sum A_p e^{i2\pi(F_p - F_m)nT_w/N_s} = 0$.

3.2.2.2 Noise level

The acquisition time affects the standard deviation of the demodulated signal, $\overline{\Phi_{ec}}$. Intuitively, a longer sum in Equation 3.5 allows taking an average across more samples and getting a cleaner estimate. This is a direct consequence of Parseval's identity and the fact that the total energy of a signal does not change from the time to the frequency domain [48], and therefore the standard deviation of Gaussian noise in the time domain equals the RMS of the white noise in the frequency domain. The noise power distributes evenly over the frequency bins, so a wider bin width contains more noise [49].

Figure 3.6 shows the demodulated signal for a vertical sensor placed at [0, 0, 150] mm. The magnetic field values, in A/m, are around the unity, and Gaussian noise with a standard deviation of 10 mA/m was added to the simulated signal.

It is evident that the noise level in the spectrum depends on the number of samples, N_s, if the constant sampling frequency is not changed. In particular, when N_s is doubled, the noise power per bin is halved, and the amplitude is $\sqrt{2}$ times smaller, lowering the RMS level by 3 dB.

The standard deviation of the signal extracted can be estimated from the RMS level of the DFT bins around the frequency of interest. This technique is helpful to estimate the precision of the measurement in real time, which can be transferred to the EMT jitter as explained in Section 3.5.2, to dynamically optimise the acquisition time, the amplifier gain, or the magnetic field power in order to maintain the required precision.

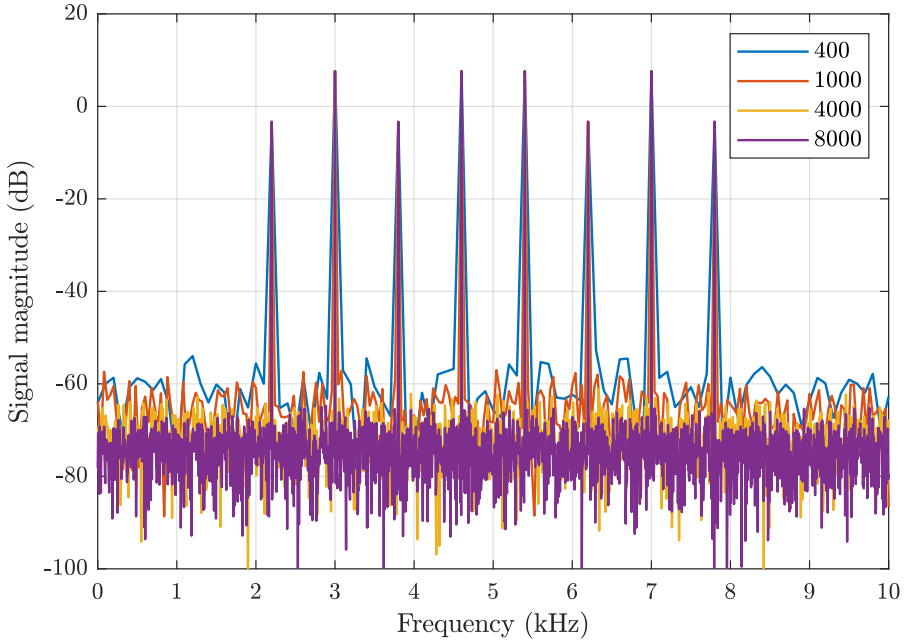


Figure 3.6: Noise level for different numbers of samples at 40 kHz. The shortest window (400 samples) has a bin resolution of 100 Hz, while the longest window (8000 samples) has a bin resolution of 5 Hz.

3.2.2.3 Spectral leakage

It is important to notice that the sampling frequency and the total number of samples must be selected so that the eight frequencies of interest fall into a frequency bin of the DFT. In other words, each field frequency, F_{ec}, must be a multiple of the bin resolution F_b to guarantee that an integer number of periods, m_{ec}, is contained within the acquisition time.

Failure to coherently sample the waveform leads to leakage in the DFT spectrum, with the power of the signal of interest being spread onto the nearby frequency bins, causing a *scalloping loss* [50, 51].

Incoherent sampling might also be caused by different speeds of the clocks used for magnetic field generation and sensing. Different crystal oscillators do not count time at the same exact rate because the crystal's frequency is influenced by temperature, mechanical stress, and ageing in a way that depends on the oscillator quality.

For this reason, the same clock source is used in ANSER EMT to generate the reference for the currents in the emitter coils and to sample the input signal. However, there are applications where coherent sampling cannot be attained, for example, if the signal is digitalised remotely and transmitted wirelessly. In these cases, window functions can be used to spectrally distribute the leakage in a way that reduces the scalloping loss [52, 53].

Another cause of spectral leakage is the time variation of the frequency component measured. In real tracking applications, the sensor is not static, but the position and orientation may change during the time that a signal window is sampled. Figure 3.7 shows how the signal is affected if the sensor moves during the acquisition time.

It can be observed that the leakage due to motion does not depend on the sampling window dimension or period if the speed of the sensor is not changed. The leakage between the frequencies of interest can be used to estimate the sensor's linear and angular velocity.

The demodulated flux values always fall between the values at the start and end points. However, they do not correspond precisely to the values obtained at the middle of the sensor trajectory, as would be the case if the flux gradients were constant. In general, the assumption of a constant gradient is correct for shorter window periods and, therefore, minor position and angular displacements.

3.2.2.4 Phase offset

Phase information is essential to resolve the sensor orientation because a phase difference of 180 degrees corresponds to a sensor flip in orientation. The phase of a DFT bin depends on the instant in time when the window was sampled relative to the period of the sinusoid. Accurate knowledge of the phase is also essential to recognise eddy currents distortion, as will be presented in Section 4.4.

According to Faraday's law, reported in Equation 3.1, the voltage induced on the sensor has a phase which is 90 degrees delayed relative to the AC magnetic flux that generates it. Additional phase offset is introduced by the acquisition chain presented in Section 3.2.1. However,

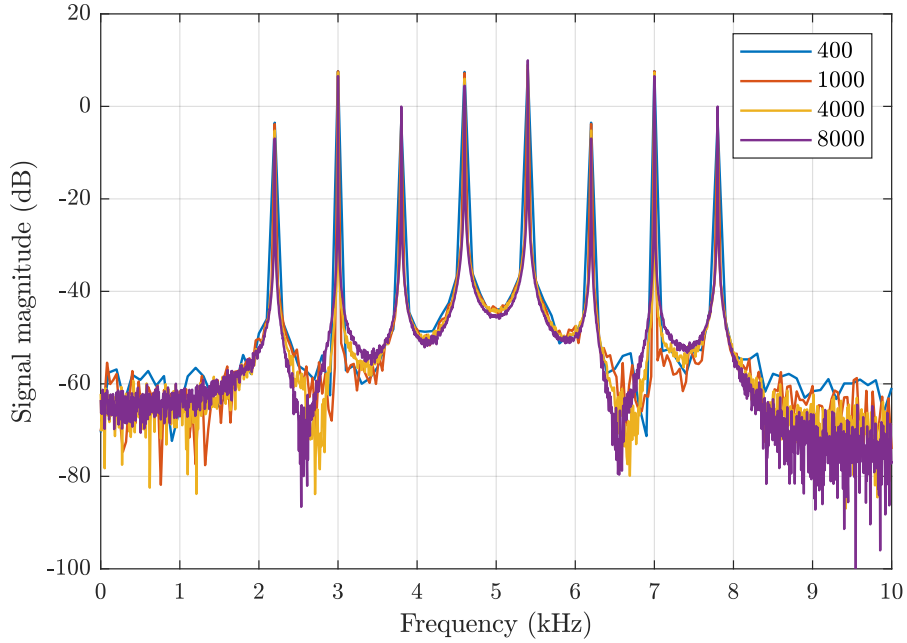


Figure 3.7: Effect of sensor linear motion in the X direction starting from $\mathbf{p} = [0, 0, 150, 0, 0]$, for different numbers of samples at 40 kHz. The sensor was moved at the unrealistic speed of 25 cm/s, for visualisation purposes, corresponding to a displacement of 2.5 mm in the shortest window case (400 samples) and 50 mm for the longest window (8000 samples).

acquisition chain delays can be characterised once for every frequency of interest and may be considered constant thereafter.

In the magnetic quasistatic approximation, when radiating effects can be neglected, as is the case inside the tracking volume for the frequencies used, the AC magnetic field and the current that generates it are synchronised. For this reason, the eight electric currents in the emitter coils are summed together, as mentioned in Section 3.1.1.3, and the composite signal is sampled and demodulated in an identical manner to the sensor signal. After that, the magnetic field phase is subtracted from the signal phase to get the absolute reference. It should be noticed that if consecutive demodulated values, $\overline{\Phi_{ec}}$, are averaged to reduce the noise level, the phase must be referred to the current before averaging because the sum of non-aligned complex numbers would lead to an incorrect result.

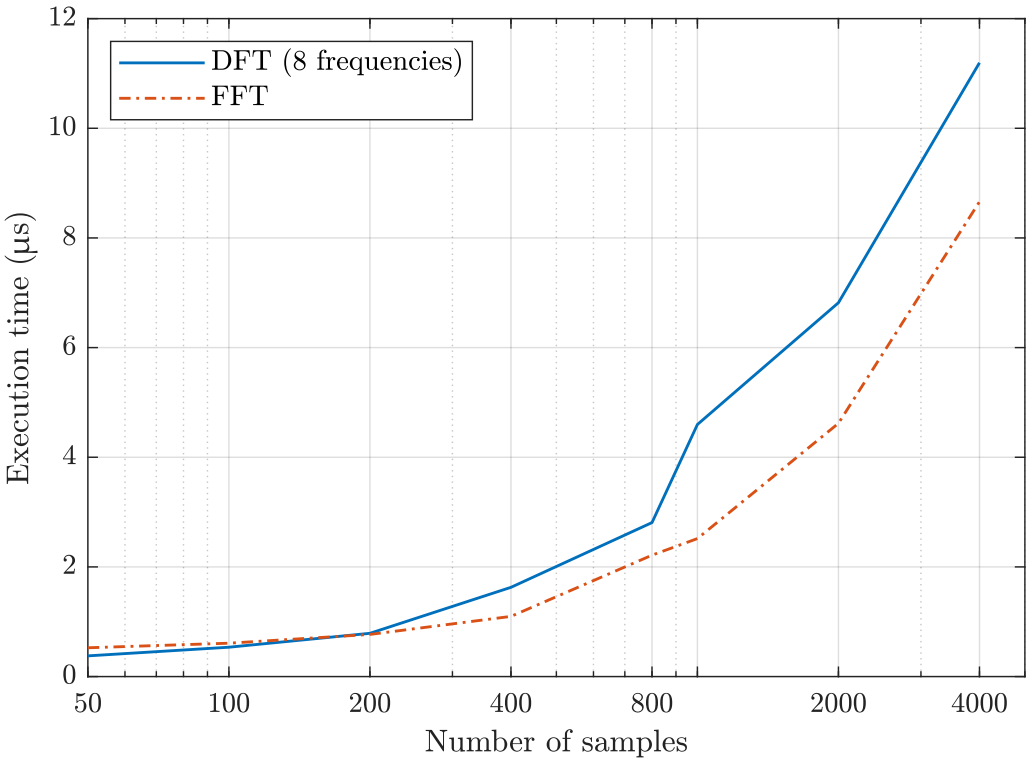


Figure 3.8: Average computation time of the DFT sum for the eight frequencies of interest and the *fft* MATLAB function for an increasing number of samples.

3.2.2.5 Software implementation

Equation 3.5 can be implemented in the form of a DFT matrix to extract only the eight values at the frequencies of interest. This approach involves a number of $8 \times N_s$ multiplications and additions. Alternatively, optimised fast Fourier transform (FFT) algorithms can be used to compute the full DFT spectrum with complexity $O(N_s \log N_s)$ [54].

FFT routines can be implemented in C or C++ using the FFTW library [55, 56], which is also the basis for the *fft* function in MATLAB [57]. In Python, *scipy.fft* [58] and pyFFTW [59] are available.

An experiment was performed to compare the computation time of the direct DTF matrix multiplication and the *fft* function in MATLAB on a Windows 10 laptop with i5-11th Gen. Intel Core Processor. The results are shown in Figure 3.8 for different sizes of the sampled window.

Similar speeds were obtained for the DFT matrix multiplication versus the *fft* function. However, the FFT has the advantage of returning all frequency bins, enabling estimation of the noise level or sensor speed using the techniques described in the previous subsections.

Although the FFT demodulation algorithm is already highly efficient, further solutions exist to reduce the computational power. These can be helpful for embedded system applications [60]. The Goertzel's filter returns the frequency bins of interest using half of the number of operations if compared to the DFT sum [61]. Similarly, the sparse fast Fourier transform (SFFT) is an optimised FFT implementation when only a limited number of frequencies are present in the signal, as is the case for FDM [62]. Finally, the zoom FFT method returns the frequencies in the bandwidth of interest with the same resolution that would be achieved using a full-size FFT on the original signal but, using this method, a smaller-size FFT is computed on a shorter signal [63].

3.2.3 Analytical magnetic model

As seen in Section 3.1.1.1, the two field generators investigated in this work are two-layer PCBs comprising eight equal planar emitter coils. In either case, the emitter coils can be modelled as one-dimensional current filaments if the trace width and thickness are neglected.

At the evaluation point identified by the position vector $\mathbf{r}$, the magnetic field $\mathbf{H_{ec}}(\mathbf{r})$ generated by each emitter coil can be calculated using the Biot-Savart's law [64]:

$$\mathbf{H_{ec}}(\mathbf{r}) = \frac{I_{ec}}{4\pi} \int_{\Gamma_{ec}} \frac{\mathbf{t} \times \mathbf{r}}{R^3} \, d\Gamma_{ec} \quad \left[\frac{\mathrm{A}}{\mathrm{m}}\right] \tag{3.6}$$

where I_{ec} is the electric current in the coil, Γ_{ec} is the current path along the coil winding, $\mathbf{t}$ is the tangential unit vector and $R = |\mathbf{r}|$ is the distance between the evaluation and the integration points, as shown in Figure 3.9. The subscript *ec* is hereafter neglected for brevity.

Because Equation 3.6 is linear, Γ can be split into the contributions given by straight wires, which can be solved in closed form as expressed

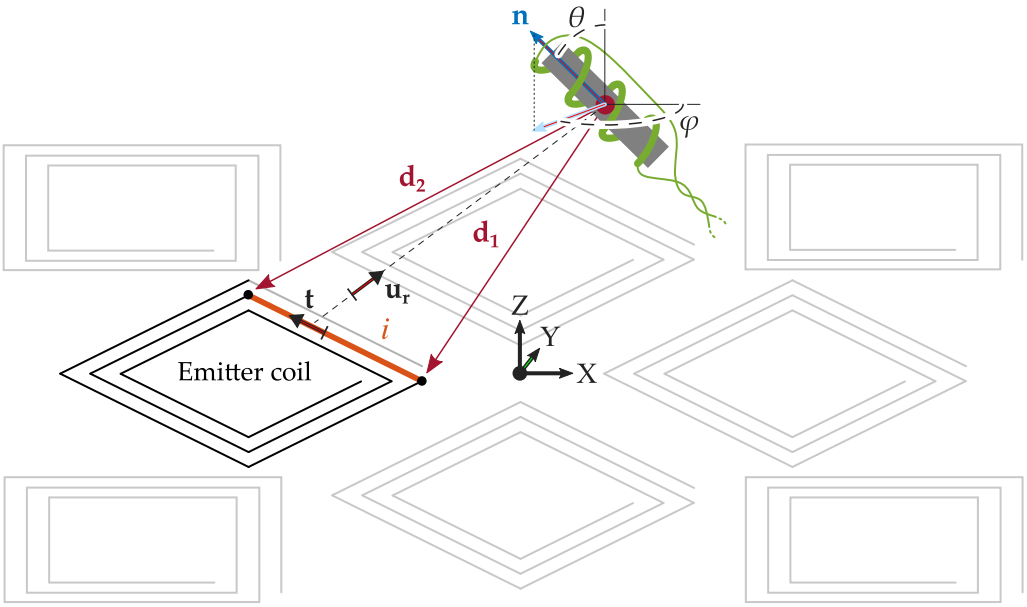


Figure 3.9: Analytical model for the magnetic flux crossing an inductive sensor located at **r** with orientation **n**. For every emitter coil, the field is split into the sum of the contributions due to the individual filaments forming the coil, each calculated as per Equation 3.7.

by Equation 3.7 [65]:

$$\mathbf{H_i}(\mathbf{r}) = \frac{I}{4\pi}\left(\frac{\mathbf{d_2}\times\mathbf{d_{12}}}{\|\mathbf{d_2}\times\mathbf{d_{12}}\|^2}\right)\left(\frac{\mathbf{d_{12}}\cdot\mathbf{d_2}}{\|\mathbf{d_2}\|}-\frac{\mathbf{d_{12}}\cdot\mathbf{d_1}}{\|\mathbf{d_1}\|}\right)\quad\left[\frac{\mathrm{A}}{\mathrm{m}}\right] \tag{3.7}$$

where $\mathbf{d_1}$ and $\mathbf{d_2}$ are the vectors from the evaluation point, $\mathbf{r}$, to the end-points of the i^{th} straight filament, and $\mathbf{d_{12}} = \mathbf{d_2} - \mathbf{d_1}$, as defined in Figure 3.9.

Each emitter coil in the field generator has 25 square turns, for a total of 100 straight PCB tracks that compose that coil. For every emitter coil, the total magnetic field is given by the superposition of 100 straight wires:

$$\mathbf{H}(\mathbf{r}) = \sum_{i=1}^{100}\mathbf{H_i}(\mathbf{r}) \tag{3.8}$$

where the contributions $\mathbf{H_i}(\mathbf{r})$, calculated as per Equation 3.7, can be summed together in a linear and homogeneous medium like free space.

The field measurement is sensitive to the negative time-derivative of the magnetic flux density enclosed by the sensor coil, as stated by Equation 3.3. The magnetic flux density, **B**, is proportional to the magnetic field, **H**, through the permeability of the material, μ:

$$\mathbf{B} = \mu\mathbf{H} \quad [\mathrm{T}] \tag{3.9}$$

Biological tissues have magnetic permeability that is effectively equivalent to the permeability of vacuum, μ_0 [66]. Moreover, experiments have shown that other effects, such as electric parasitic capacitances and eddy currents induced in the human tissues, are not significant below 1 MHz [67, 68]. Therefore, it can be assumed that the magnetic field generated by the ANSER EMT system is not altered in the patient body. This is a significant aspect because it enables the evaluation and characterisation of the system in free space, ensuring that its performance remains consistent in the final application.

As seen in Section 3.1.1.2, the total magnetic flux enclosed by the sensor coil is given by:

$$\Phi = \sum_{n=1}^{N} \oint_{A_l} \mathbf{B} \cdot \mathbf{n}\, dA_l \quad [\mathrm{Wb}] \tag{3.10}$$

For miniature coils, such as those typically used in EMT for biomedical applications, some reasonable assumptions can be made, e.g. the increment in sensitivity due to the ferromagnetic core is the same for every coil-turn, and a constant apparent magnetic permeability, μ_a, can be used to account for the core effect; every coil-turn is planar and parallel, with the central axis oriented along the unit vector **n**; every coil-turn has the same area, equal to the cross-sectional area of the coil, A_c; **B** has a constant gradient throughout the coil's length and across the coil's cross-sectional area.

Under these assumptions, Equation 3.10 can be simplified to:

$$\Phi(\mathbf{r}, \mathbf{n}) = \mu_a N\, A_c \mathbf{B}(\mathbf{r}) \cdot \mathbf{n} \quad [\mathrm{Wb}] \tag{3.11}$$

which gives the magnetic flux crossing the sensor winding of a tracking sensor at position **r** and oriented along **n**, and has to be calculated for every emitter coil in the field generator.

The inductive sensor measurement is proportional to the negative time derivative of Equation 3.11. ANSER EMT magnetic fields have a sinusoidal waveform. Therefore, their time derivative is another sinusoidal signal at the same frequency, where the amplitude is scaled by the constant factor $2\pi F_{ec}$. Moreover, the acquisition chain described in Section 3.1.1.3 introduces other constant scaling factors to the signal coming from the sensor. By taking the derivative of Equation 3.11, and grouping together all the constant terms in the factor C, the measured voltage in response to a sinusoidal field is obtained as follows:

$$v(t) = C\,\mu_0 \mathbf{H}(\mathbf{r}) \cdot \mathbf{n} = C\,\Phi(\mathbf{r}, \mathbf{n}) \quad [\mathrm{V}] \tag{3.12}$$

where $\mathbf{H}(\mathbf{r})$ is calculated from Equation 3.8.

The analytical magnetic flux model described in this section, $\Phi(\mathbf{r}, \mathbf{n})$, returns the values predicted for the flux enclosed by a coil at *position* $\mathbf{r}$ with *orientation* defined by the unit vector $\mathbf{n}$. We define $\mathbf{p} \in \mathbb{R}^{5\times 1}$ as the *pose* vector of the uni-axial sensor coil, as per Equation 3.13:

$$\begin{aligned} \mathbf{r} &= [x\, y\, z] \\ \mathbf{n} &= [\sin(\theta)\cos(\varphi),\ \sin(\theta)\sin(\varphi),\ \cos(\theta)] \\ \mathbf{p} &= [x\, y\, z\, \theta\, \varphi]^T \end{aligned} \tag{3.13}$$

where x, y, and z are the Cartesian coordinates of the sensor position, and θ and φ are the pitch and yaw angles defined in spherical coordinates, as shown in Figure 3.9.

We define the *flux* vector $\mathbf{\Phi} \in \mathbb{R}^{8\times 1}$, $\mathbf{\Phi} = f(\mathbf{p})$, as the array of the eight values from the magnetic flux *model* of the eight emitter coils.

3.2.3.1 Jacobian calculation

The Jacobian matrix is the 8×5 matrix containing the partial derivatives of the eight dependent variables of $\mathbf{\Phi}$ with respect to the five independent variables of $\mathbf{p}$.

The Jacobian is a function of $\mathbf{p}$ and indicates how a variation in $\mathbf{p}$ is reflected into a variation in $\mathbf{\Phi}$ at a specific sensor position and orientation.

The analytical formulation for the Jacobian was obtained by differentiation of the model presented in Section 3.2.3. The result was verified using the Symbolic Math Toolbox [69] in MATLAB.

Alternatively, the partial derivatives in the Jacobian matrix can be approximated as a finite difference of the magnetic flux model. In this case, it was found that the result is typically correct up to the ninth digit after the decimal point.

In the remainder of the thesis, the numerical approximation is typically used because it can be calculated faster. Furthermore, it can be extended to magnetic flux models that do not have an analytical expression, such as data-driven tabulated or neural network models.

3.2.3.2 Model calibration

As seen before, the magnetic coupling between the inductive sensor and the field generator can be effectively modelled up to a constant scaling factor, C. Factors that determine C include the sensor's sensitivity, the gain introduced by the acquisition chain, and the field frequency. Typical values are indicated as 0.05 to 0.5 $\mathrm{VT^{-1}Hz^{-1}}$ for the sensitivity, 1 to 1000 for the amplifier gain, and 1 to 50 kHz for the frequency.

Calibration is an important step aimed at precisely determining the scaling coefficient from the raw voltage signal measurement to the corresponding value in terms of magnetic flux density or magnetic field, which in the human body differ by the constant factor μ_0.

We define the flux vector $\widetilde{\mathbf{\Phi}} \in \mathbb{R}^{8\times 1}$, that contains the eight values of the magnetic flux *measurement* from the eight emitter coils, and the calibration vector $\mathbf{C} \in \mathbb{R}^{8\times 1}$, that contains the eight scaling coefficients.

The calibration process aims to find $\mathbf{C}$ that minimises the two-norm of the difference between the fluxes measured and modelled within the region of interest (ROI):

$$\arg\min_{\mathbf{C}} \|\mathbf{C} \odot \widetilde{\mathbf{\Phi}} - \mathbf{\Phi}\|_2 \tag{3.14}$$

where $\odot$ indicates the element-wise multiplication.

Equation 3.14 may employ normalisation or weighting functions to prioritise tracking points deemed more critical or to adjust for the decline in field magnitude with distance, which would otherwise give more weight to points closer to the field generator [17].

Minimising Equation 3.14 over every possible pose $\mathbf{p}$ in the ROI is unfeasible. For this reason, the calibration points must be sampled with suitable distribution and density. Reference can be provided by slides or mechanical supports [70], optical tracking [71], calibration fixtures [72], or robotic systems [73].

If the reference poses are known, meaning that $\mathbf{\Phi}(\mathbf{p})$ can be calculated for every calibration point, Equation 3.14 can be formulated as a linear least-squares problem, and the solution for $\mathbf{C}$ can be found in closed-form as follows. Considering N_c calibration points, a fast formula can be found by setting the derivative to 0 and solving for C:

$$\frac{d}{dC}\sum_{n=1}^{N_c}(\mathbf{C}\odot\widetilde{\mathbf{\Phi}}_\mathbf{n}-\mathbf{\Phi}_\mathbf{n})^2 = 2\sum_{n=1}^{N_c}\widetilde{\mathbf{\Phi}}_\mathbf{n}\odot(\mathbf{C}\odot\widetilde{\mathbf{\Phi}}_\mathbf{n}-\mathbf{\Phi}_\mathbf{n}) = 0 \tag{3.15}$$

$$\mathbf{C} = \frac{\sum_{n=1}^{N_c}\mathbf{\Phi}_\mathbf{n}\odot\widetilde{\mathbf{\Phi}}_\mathbf{n}}{\sum_{n=1}^{N_c}\widetilde{\mathbf{\Phi}}_\mathbf{n}\odot\widetilde{\mathbf{\Phi}}_\mathbf{n}} \tag{3.16}$$

where the fraction must also be considered an element-wise operation.

As mentioned in Section 3.2.2.4, correcting for constant phase offsets introduced during the acquisition process might also be necessary. In this case, Equation 3.14 can be extended by considering $\mathbf{C}$ and $\widetilde{\mathbf{\Phi}}$ as arrays of complex numbers, which encode both the magnitude and the phase of the calibration coefficients and the demodulated signal, respectively. After that, the product $\mathbf{C}\odot\widetilde{\mathbf{\Phi}}$ automatically applies magnitude scaling and phase offset correction.

By appropriately redefining the cost-function of Equation 3.14, extended calibration methods might solve for additional degrees of freedom. For example, the calibration points could be collected free-hand without a ground-truth reference, and the five DOFs per point become $5\times N_c$ additional unknown parameters to be estimated. Variations include constraining some degrees of freedom, e.g. by using a fixed horizontal plate

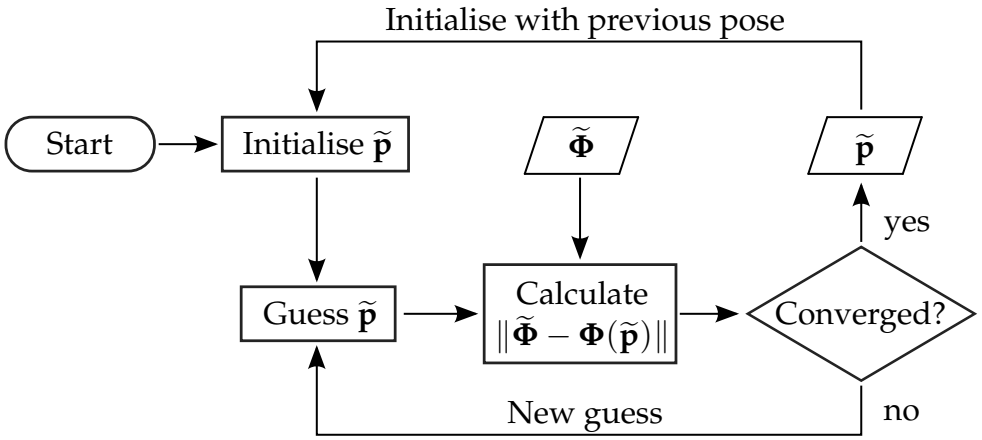


Figure 3.10: A schematic representation of the iterative algorithm used to estimate the EMT pose.

as a support or placing the sensor at fixed grid points with known relative distances. These calibration procedures require non-linear optimisation techniques similar to those used for the tracking algorithm, which will be presented in Section 3.2.4.

Unless otherwise specified, in the remainder of the thesis, we will assume that $\widetilde{\mathbf{\Phi}}$ has been previously calibrated, so that $\widetilde{\mathbf{\Phi}} = \mathbf{C} \odot \widetilde{\mathbf{\Phi}}$.

3.2.4 Tracking algorithm

The core function of the tracking algorithm aims to resolve the sensor pose, $\mathbf{p}$, based on the set of field measurements, $\widetilde{\mathbf{\Phi}}$. The problem is typically formulated as a non-linear optimisation in which the two-norm of vector $\widetilde{\mathbf{\Phi}} - \mathbf{\Phi}$ is minimised:

$$\widetilde{\mathbf{p}} = \arg\min_{\mathbf{p}} \|\widetilde{\mathbf{\Phi}} - \mathbf{\Phi}(\mathbf{p})\|_2 \tag{3.17}$$

where $\widetilde{\mathbf{p}}$ is the estimated pose. Figure 3.10 shows the flowchart that summarises the main steps of the iterative EMT algorithm.

In the standard form presented in Equation 3.17, the cost-function automatically weights the terms relative to the eight emitter coils so that higher signals, which are less affected by random noise because of the higher SNR, contribute more to the difference. In this way, the solver

is biased toward the coils nearer to the sensor position or generating a magnetic field vector aligned to the sensor direction.

Variations to Equation 3.17 are possible by introducing normalisation or weighting functions or using other vector norms or other cost-functions depending on the difference $\widetilde{\mathbf{\Phi}} - \mathbf{\Phi}$. In these cases, the best-fit pose $\widetilde{\mathbf{p}}$ might change.

Equation 3.17 is minimised using iterative methods, as shown in Figure 3.10 [74, 75]. The Levenberg–Marquardt (LM) and the Trust-region (TR) algorithms were proven optimal for EMT with a planar field generator [16]. When the algorithm is started for the first time or if the EMT sensor is moved outside the volume range, the estimated pose is initialised to the centre of the region of interest. Afterwards, as the sensor moves following a continuous trajectory, the pose to which the solver has converged is used as an initial estimate for the subsequent pose.

Non-linear least-squares solvers support LM and TR methods in MATLAB. In particular, the *lsqnonlin* function is used in this work [76]. In the Python implementation, solving operations are performed using NumPy [77] and SciPy [78] libraries. Linear algebra functionality in C++ is enabled by the Eigen 3 library [79]. The convergence time for the three implementations will be compared in Section 3.6.2.

3.3 Sensors for characterisation and tracking

Two commercially available inductive sensor coils were used in part of the work presented in this thesis: a three-axis receiver (3DV11AOI-A-S0600J, Grupo Premo, Malaga, Spain) [80], and a clinical-size micro-coil (610158, Northern Digital Inc., Waterloo, Canada) [26].

The three-axis coil was chosen as a cost-effective solution to collect low-noise data quickly during the volume calibration. However, this sensor has a dimension of $11 \times 11\,\mathrm{mm}^2$, which is incompatible with the requirements for endoscopic applications.

For this reason, the miniature coil with dimensions of 0.45 mm in diameter and 8.2 mm in length was used when evaluating the electromagnetic tracking positional and angular accuracy.

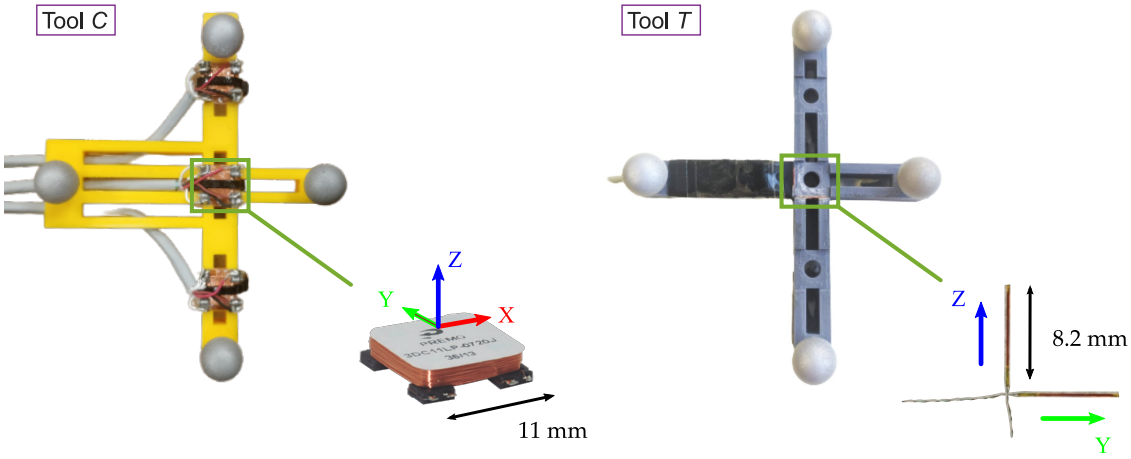


Figure 3.11: (a) Tool *C* includes (b) three triaxial sensor coils. (c) Tool *T* is equipped with (d) two uniaxial clinical-size sensors.

In the case of both sensors, a 3D-printed dynamic reference frame (DRF) [81] was appropriately customised to host the sensors together with passive markers for optical tracking.

One tool included three of the three-axis coils from Grupo Premo, spaced by 3 cm, for a total of nine pick-up coils which were connected to nine separate acquisition channels of the control unit for concurrent measurements. This tool was mainly intended for fast volume characterisation using a multitude of sensors.

A second tool was equipped with two miniature single-axis coils from NDI mounted with orthogonal orientations. This tool was used for testing and EMT accuracy evaluation. In this work, we will refer to the two tools as *tool C* and *tool T*, respectively, as shown in Figure 3.11.

The presence of reflective spheres on the tools enables optical tracking of the DRF position. Other markers were attached to the field generator to give relative reference positioning.

The Polaris Vega system (Northern Digital Inc., Waterloo, Canada) provided ground-truth pose reference of the sensors and the field generator. The system has a volumetric accuracy of 0.15 mm RMS, provided by the manufacturer [82]. Optical reference was used to assign magnetic measurements to the correct point in space when performing volume char-

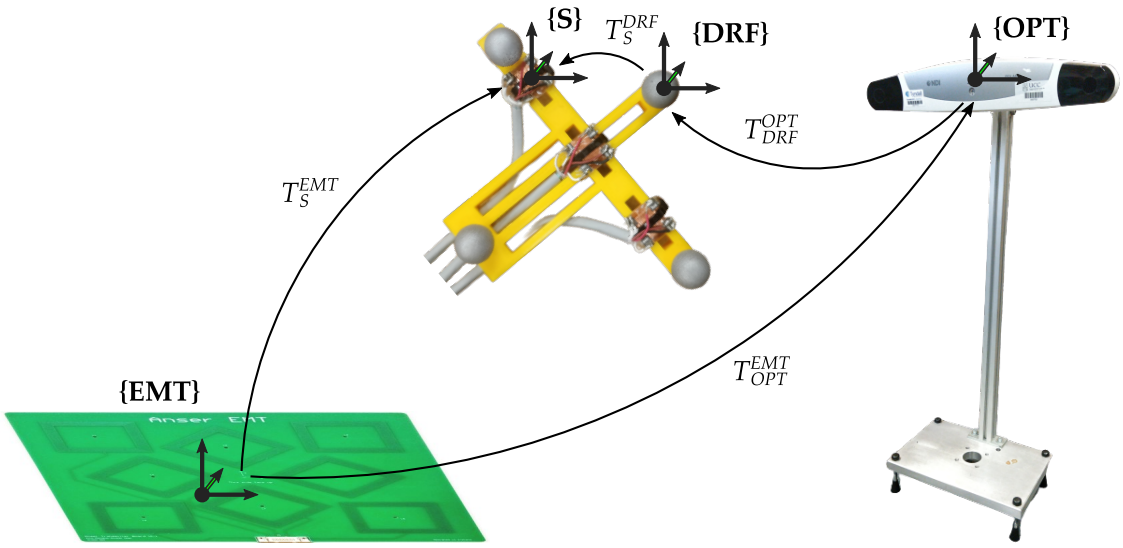


Figure 3.12: Linear transformations between the reference frames of ANSER EMT **{EMT}**, the optical system **{OPT}**, the optical marker **{DRF}**, and the sensor pose within the dynamic reference frame **{S}**.

acterisation and to provide undistorted pose reference when assessing EMT accuracy.

3.3.1 Registration between tracking systems

ANSER EMT and Polaris Vega have different reference systems, **{EMT}** and **{OPT}**, respectively, as shown in Figure 3.12. The linear transformation between the two coordinate frames, T_{OPT}^{EMT}, defines the 6 DOF pose of **{OPT}** in the **{EMT}** reference system. The process of determining T_{OPT}^{EMT} is called *registration*.

The reflective spheres mounted on the optical marker define a dynamic reference frame **{DRF}** which is optically tracked relative to **{OPT}**, T_{DRF}^{OPT}. The position and orientation of the magnetic sensor coil in the DRF, T_S^{DRF}, is defined by the *rigid-body* geometry and must be known with accuracy.

Such linear transformations involve one rigid translation and one rigid rotation, which can be identified by three positional displacements and three rotation angles, respectively. The roto-translation is typically expressed as a 4×4 matrix in homogeneous coordinates [83] because

this allows for fast coordinate transformation by performing one matrix multiplication.

EMT of the magnetic sensor provides the sensor pose in the **{EMT}** reference system, T_S^{EMT}. If T_{OPT}^{EMT} and T_S^{DRF} are known, it is possible to compare the tracking results of the two systems, T_S^{EMT} and T_{DRF}^{OPT}, as given by Equation 3.18:

$$T_S^{EMT} \leftrightarrow T_{OPT}^{EMT} \cdot T_{DRF}^{OPT} \cdot T_S^{DRF} \tag{3.18}$$

Although the tool's mechanical design is known, 3D-printing inaccuracies and the unknown coil geometry might cause errors in the definition of T_S^{DRF}. An external optically-tracked stylus can be used to touch fiducial points on the field generator and find T_{OPT}^{EMT}.

Similarly, the stylus could be used to localise the magnetic sensor. However, this relies on pivoting accuracy and the ability to touch the coil's centre correctly. For larger coils, reaching the centre of the ferromagnetic core is unfeasible, and for miniature coils in the sub-millimetre scale, identification by visual inspection might be unpractical.

The difficulty in determining the exact coil central point and the real magnetic axis requires more accurate calibration routines. In the following sections, novel methods will be described for calibrating tool *C*. Similar methods were applied to tool *T*.

3.3.2 Concurrent magnetic and mechanical calibration

When the ANSER EMT is already calibrated, as seen in Section 3.2.3.2, a number of sensor poses can be collected in the EMT domain, T_S^{EMT}, with the associated optical marker poses collected simultaneously in the optical domain, T_{DRF}^{OPT}. The transformations for registration and for the rigid-body, T_{OPT}^{EMT} and T_S^{DRF}, might then be solved as a hand-eye calibration problem [84]:

$$T_S^{EMT} \cdot T_{DRF}^{S} = T_{OPT}^{EMT} \cdot T_{DRF}^{OPT} \tag{3.19}$$

If the EMT system requires calibration, an external positioning reference is needed for fast and accurate optimisation of the scaling coefficients, as discussed in Section 3.2.3.2.

In this section, the two problems are solved concurrently by introducing a novel calibration technique to find the optimal scaling coefficients and the mechanical transformations described above. The method is an extension of hand-eye calibration routines commonly used for registration between tracking systems [84].

The unknowns are the eight magnetic model calibration coefficients, $\mathbf{C}$, the six degrees of freedom (DOF) of the optical system relative to the EMT reference frame, T_{OPT}^{EMT}, and the 5 DOF pose of every sensor in relation to the dynamic reference frame (DRF), T_S^{DRF}.

The three coils inside each triaxial sensor of tool C are considered independent, each accounting for 5 DOFs for a total of 15 DOFs. Alternatively, if manufacturing tolerances are neglected, they can be assumed coincident and arranged along orthogonal axes, in which case they are localised with a total of 6 DOFs.

The tool is moved free-hand within the region of interest (ROI), and magnetic and optical measurements are acquired. At every sampled point, the matrix T_{DRF}^{OPT} and one vector of eight field measurements per sensor are recorded.

Given an estimate for the calibration coefficients, the flux measurement vector is found as $\widetilde{\mathbf{\Phi}} = \mathbf{C} \odot \widetilde{\mathbf{\Phi}}$. Given an estimate for the registration T_{OPT}^{EMT} and the rigid-body T_S^{DRF}, the flux model vector, $\mathbf{\Phi}$, is calculated at the pose defined by $T_{OPT}^{EMT} \cdot T_{DRF}^{OPT} \cdot T_S^{DRF}$.

The calibration routine involves an iterative algorithm where the cost $\|\widetilde{\mathbf{\Phi}} - \mathbf{\Phi}\|$ is minimised for every sensor and every point sampled. The non-linear least-squares problem was solved using the *lsqnonlin* function in MATLAB.

3.3.3 Magnetic calibration without optical reference

Estimating the scaling coefficients is typically less accurate if an exact reference is unavailable. The nine coils in tool C were calibrated individually without a ground-truth reference. The calibration routine involved sampling a cloud of points in the ROI and solving for the eight coefficients and the 5 DOFs per test point.

Tracking results are visualised in Figure 3.13a and demonstrate small displacements between coils belonging to the same triaxial sensor, which are supposed to be coincident. A new calibration algorithm was designed to include mechanical constraints between the sensors and therefore improve the tracking results, as shown in Figure 3.13b.

The position and orientation of each coil relative to the dynamic reference frame, T_S^{DRF}, is defined by the tool's geometry and is assumed to have been previously characterised using the methods described in Section 3.3.2.

Each sensor axis, i, is tracked individually by the electromagnetic tracking system, with the resulting pose that is identified by the position vector $\mathbf{t_i^{EMT}} = [t_X\, t_Y\, t_Z]^T$ and the orientation unit vector $\mathbf{n_i^{EMT}} = [n_X\, n_Y\, n_Z]^T$, both defined in the global coordinate system **{EMT}**. The position and orientation of the nine sensors can be expressed in homogeneous coordinates and combined in a single 4×18 matrix, T_S^{EMT}:

$$T_S^{EMT} = \begin{bmatrix} \cdots & \begin{pmatrix} \\ \mathbf{n_i^{EMT}} \\ \\ \end{pmatrix} & \begin{pmatrix} \\ \mathbf{t_i^{EMT}} \\ \\ \end{pmatrix} & \cdots \\ \cdots & 0 & 1 & \cdots \end{bmatrix} \tag{3.20}$$

The rigid-body definition gives the position and orientation of every sensor axis in the local coordinate system of the optical marker, **{DRF}**. A 4×18 matrix T_S^{DRF} can be constructed in the same way as Equation 3.20.

The linear transformation between T_S^{DRF} and T_S^{EMT}, i.e. the change of coordinates from the local to the global reference systems, is the 4×4 matrix T_{DRF}^{EMT} that defines the position and orientation of the DRF with respect to the origin of the field generator, as described in Section 3.3.2.

In the proposed calibration routine, the array of sensors is moved free-hand within the ROI. For every point sampled, matrix T_S^{EMT} is given by EMT methods, and matrix T_{DRF}^{EMT}, the position of the sensor array, is estimated by minimising the difference between T_S^{EMT} and $T_{DRF}^{EMT} \cdot T_S^{DRF}$ after normalisation of the nine position vectors $\mathbf{t}$.

Normalisation is required because orientation vectors have a two-norm equal to 1, while position vectors are in the range of hundreds of

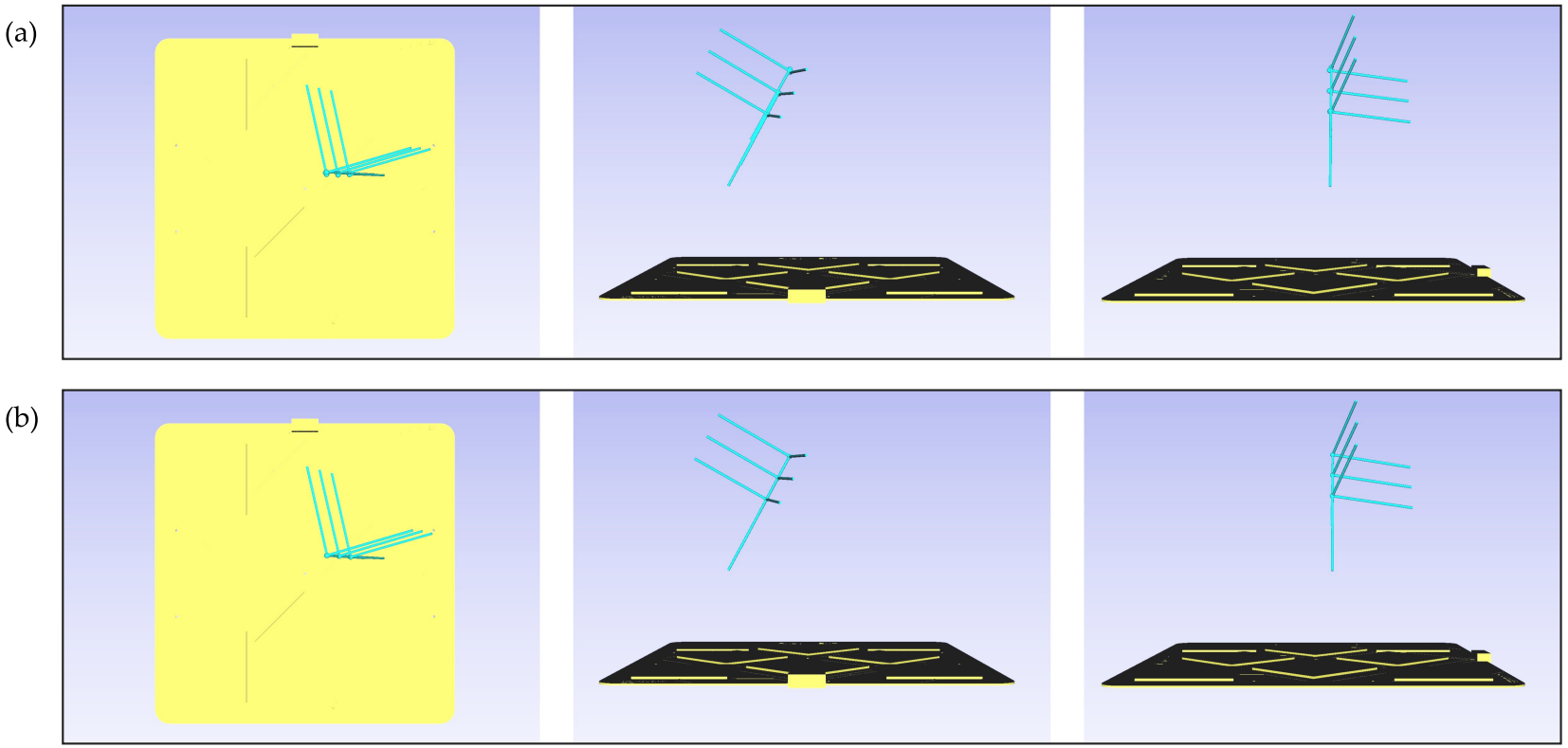


Figure 3.13: (a) Tracking results after individual calibration of the nine pick-up coils of tool *C*. (b) Improvement was obtained using the calibration routine described in this section, accounting for mechanical constraints.

millimetres. This would bias the cost function in favour of the position vectors. The mean value of the two-norm of the nine vectors was used as the normalisation constant.

The equation was solved using the *slash*, /, operator of MATLAB, also called the *mrdivide* function [85], which returns the least-squares solution to the system of equations $T_{DRF}^{EMT} \cdot T_{S}^{DRF} = T_{S}^{EMT}$ by minimising Equation 3.21:

$$\sum_{i=1}^{9} \left\| \mathbf{t_i^{EMT}} - \mathbf{t_i^{DRF}} \right\|^2 + \left\| \mathbf{n_i^{EMT}} - \mathbf{n_i^{DRF}} \right\|^2 \tag{3.21}$$

In general, the 4×4 matrix obtained in this manner is not a valid rigid transformation matrix. The first 3×3 block can be made a valid rotation matrix by taking its singular value decomposition and setting the eigenvalues to 1 [86], the 4^{th} row is set to $[0\,0\,0\,1]$, and the translation vector in the 4^{th} column is re-scaled by the normalisation constant calculated before.

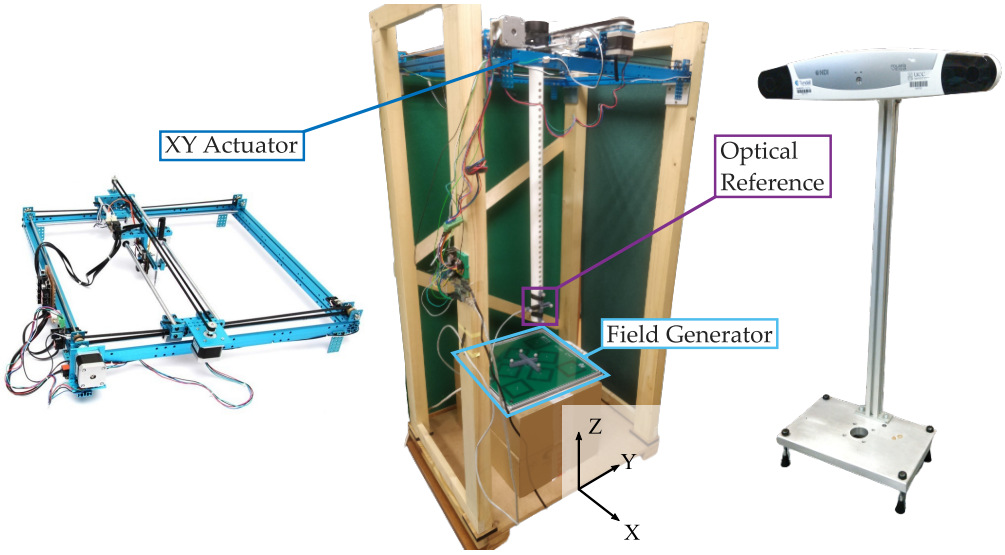
In this way, the expected position of the tool, T_{DRF}^{EMT}, is obtained, and new position and orientation vectors are derived for every sensor according to T_{DRF}^{EMT}. The mismatch between the independent sensor poses given by the EMT system and the new mechanically-constrained poses is quantified as the Euclidean distance in millimetres and the angle difference in degrees for the position and orientation vectors, respectively. The total cost is calculated as the sum of the squared errors of the nine coils at all the sampled points.

For each of the nine coils, eight calibration coefficients are found to give the EMT positions and orientations that minimise the total cost in the least-squares sense. At each iteration of the algorithm, the pose of the sensors is calculated from the magnetic flux measurement as an update to the previous solution using the faster tracking algorithm that will be presented in Section 5.1.1.

The calibration algorithm is summarised in Listing 3.1, and the tracking results obtained with the newly calculated calibration coefficients are visualised in Figure 3.13.

Listing 3.1: Calibration algorithm that includes mechanical constraints between sensors.

```
% PandO is calculated according to the current
    calibration coefficients
...
% PandO := (6 x 9 x numPoints) array of the position and
    orientation of the nine coils at every sampled point
for p = 1:numPoints
    % 3x9 position vector for the nine coils at point p
    t = PandO(1:3,:,p);
    % 3x9 orientation vector for the nine coils at p
    n = PandO(4:6,:,p);
    % normalisation factor
    t_norm = mean(vecnorm(PandO(1:3,:,p)));
    % 4x18 matrix TOA with normalised position vectors
    TOA_norm = [[n;zeros(1,9)] [t/t_norm;ones(1,9)]];
    % 4x18 matrix TPA with normalised position vectors
    TPA_norm = TPA;
    TPA_norm(1:3,10:end) = TPA_norm(1:3,10:end)/t_norm;
    % 4x4 matrix TOP with normalised position vectors
    TOP_norm = TOA_norm / TPA_norm;
    % 3x3 rotation block to orthogonal matrix
    [U,~,V] = svd( TOP_norm(1:3,1:3) );
    % position vector re-scaled to original
    TOP(:,:,p) = [U*V' TOP_norm(1:3,4)*t_norm; 0 0 0 1];
end
% Constrained position of the coils
TOA_rb = TOP*TPA;
% PandO_rb := (6 x 9 x numPoints) PandO array
    constrained to the Rigid Body definition
PandO_rb(1:3,:,:) = TOA_rb(1:3,10:end,:);
PandO_rb(4:6,:,:) = TOA_rb(1:3,1:9,:);
%% error between PandO (independent sensor axes) and
    PandO_rb (mechanically constrained)
% position error in mm, approx. range: -150 to +150
err_p = squeeze(rms(PandO_rb(1:3,:,:)-PandO(1:3,:,:)));
% angle error in degrees, range: -90 to +90
err_a = squeeze(acos(dot(PandO_rb(4:6,:,:) , PandO
    (4:6,:,:))))*180/pi;
% cost to be minimised
cost = [err_p err_a];
% Find new calibration coefficients to minimise the cost
...
```



(a) (b) (c)

Figure 3.14: (a) XY Plotter Robot Kit available in the market [87].
(b) A wooden frame is used to keep the robot far from the ROI and avoid magnetic distortion. The sensor is mounted on a plastic rod.
(c) Accurate pose reference is provided by an external optical system [82].

3.4 Robotic two-axial actuator

When conducting tracking tests or characterising the volume, data collection within the region of interest (ROI) can be time-consuming. To automate this process, a 2D linear actuator was designed to move sensors repeatedly and consistently along pre-planned paths or to predefined test points. The complete experimental setup is illustrated in Figure 3.14.

A cost-effective XY Plotter Robot Kit readily available in the market was utilised for this purpose [87]. The robot was mounted on a wooden frame to keep the aluminium structure and stepper motors at a distance of over one meter from the ROI in order to avoid magnetic field distortion.

The stepper motor drivers were upgraded to the TMC2208 driver (TRINAMIC Motion Control, Hamburg, Germany) [88] to ensure smoother motion. An Arduino© Uno microcontroller was used for communication between MATLAB and the stepper motor drivers using the *AccelStepper* library [89].

Despite the ability of the actuator to be programmed for repeatable positions, the inherent inaccuracies of the motorised system and the plastic rod holding the sensor do not allow for the sub-millimetre accuracy necessary to test or characterise the EMT system. Therefore, when an accurate sensor position and orientation are required, the Polaris Vega optical system presented in Section 3.3 is used.

3.4.1 Mechanical oscillations

When the robot moves to a new test point, the sensor position requires some time to stabilise. Part of the mechanical oscillations is due to the pendulum effect created by the plastic rod holding the sensor.

The 2D actuator was characterised to assess its stability and any undesired motion that may occur after stopping. The sensor was moved to nine test points on a 3×3 grid located approximately 15 cm above the field generator. Positions were recorded using optical methods for nine seconds after reaching the target point.

Figure 3.15 shows the position error calculated in relation to the value at convergence. The final static position was estimated as the average between the measurements taken in the last four seconds of acquisition. Similar plots were obtained for the other test points.

The convergence can be observed within the initial three seconds, with the error dropping to below 40 µm after just one second. This error is well below the 150 µm RMS error of the optical system.

Following a one-second interval to allow for the damping of oscillations, 40 field measurements were collected at every test point, and the corresponding 40 EMT positions were determined. The solutions obtained through EMT are presented in Figure 3.16, where they are compared to the expected cloud distribution obtained by utilising a completely static sensor.

In this way, it is possible to visually determine the proportion of error that can be attributed to random noise in the measurements and the proportion that is due to minor mechanical oscillations. For instance, at test point 9 of Figure 3.16, it is evident that the solution cloud is deformed in

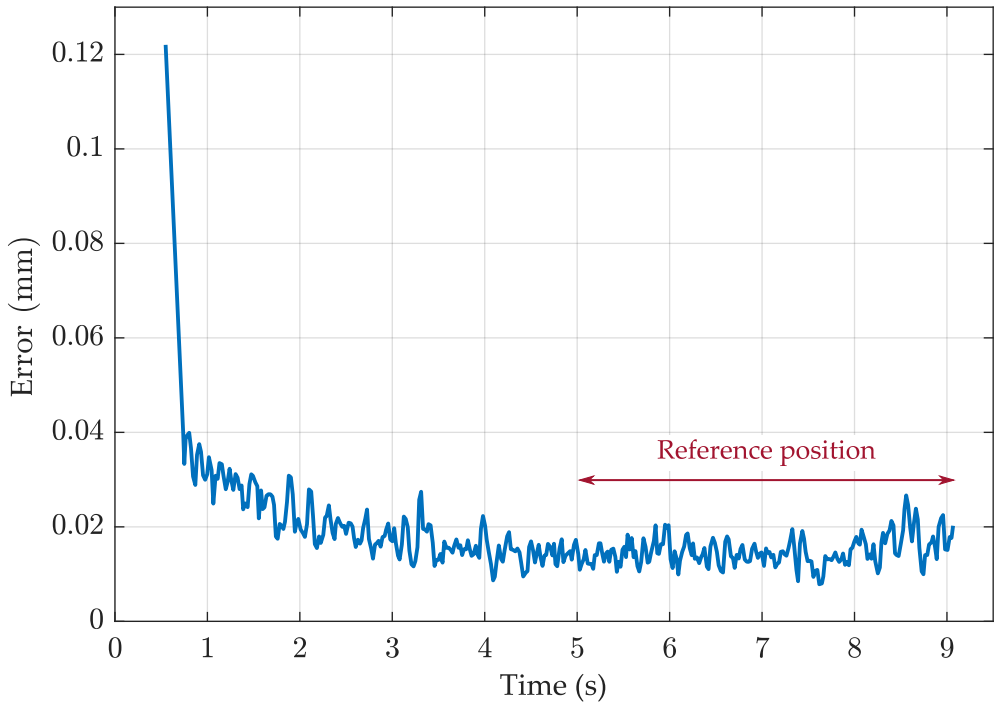


Figure 3.15: Position error due to mechanical oscillations. The error is calculated in relation to the value at convergence.

the direction of motion when compared to the static solution, thus indicating that a measurable portion of the error distribution can be attributed to the physical displacement of the sensor.

In all cases, the difference is on the order of tens of micrometres, and a significant portion of it is eliminated through the averaging of measurements, as will be discussed in Section 3.4.2. Therefore, a one-second interval for oscillation damping was chosen as a trade-off between the oscillation amplitude decay and the time required for sampling. In all experiments presented in this work, the damping interval is utilised prior to collecting magnetic measurements.

3.4.2 Acquisition time

The same field measurements used in the experiment of Figure 3.16 were considered to determine the number of consecutive measurements that must be averaged in order to obtain a stable value. The 40 signals were collected over a two-second interval, and an increasing number of mea-

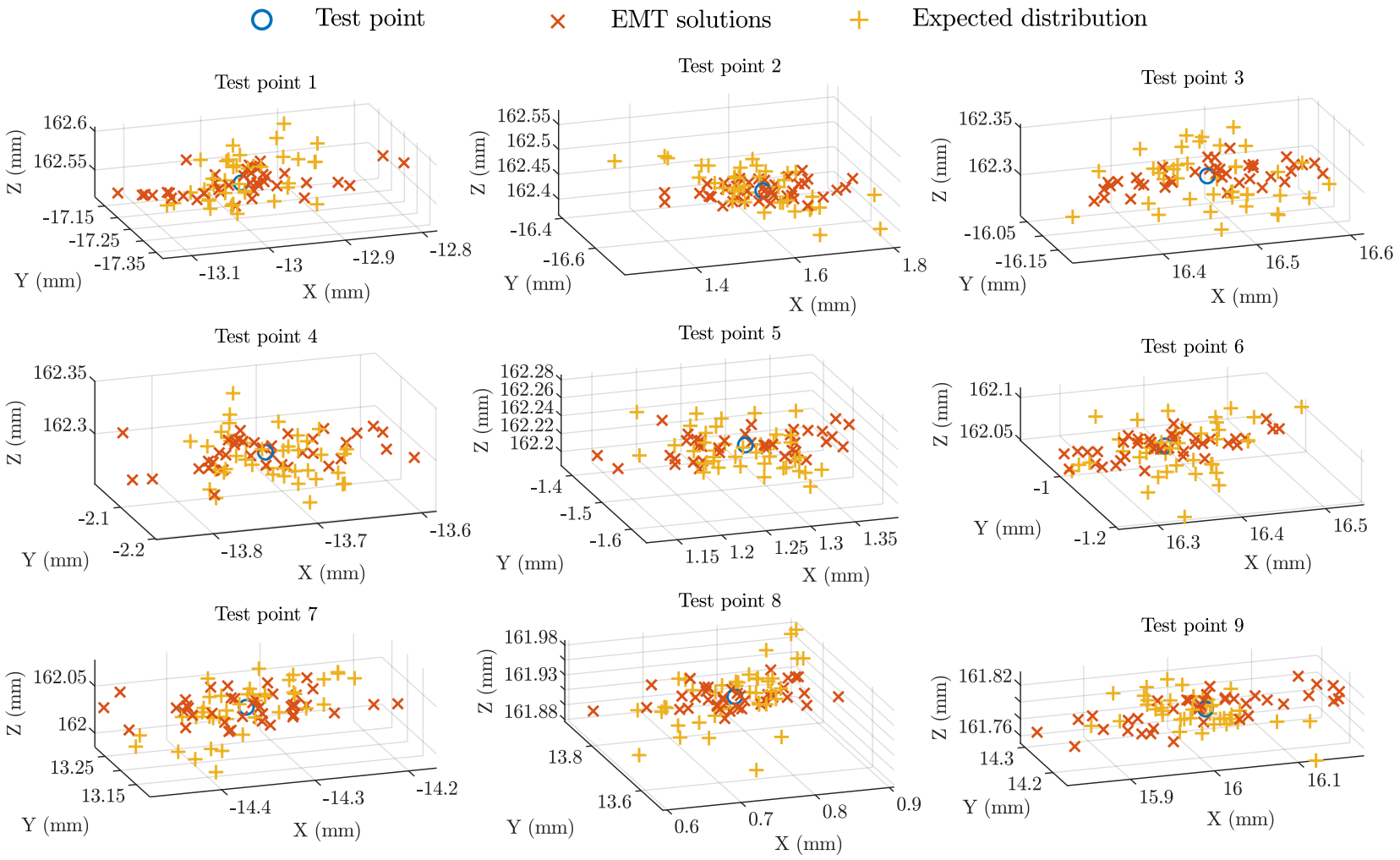


Figure 3.16: EMT solutions showing the effect of mechanical oscillations. At nine test points, 40 EMT poses were obtained following a one-second interval for the damping of oscillations. Solutions obtained with a completely static sensor are shown for comparison to highlight possible error components due to mechanical oscillations in the X direction of motion. The nine plots do not share the same scale because the purpose is to qualitatively compare the two error distributions at each test point.

surements were incorporated into the average. For each value obtained in this manner, the percentage error was calculated in relation to the global average of the 40 measurements. Figure 3.17 shows the results for four emitter coils (EC) at the nine test points used for evaluation.

Through visual inspection, it was determined that 20 values are sufficient to get low-noise field measurements. This is also supported by the fact that the standard deviation of the corresponding EMT solutions obtained for individual measurements is already on the order of tens of micrometres, as previously illustrated in Figure 3.16.

In conclusion, it was found that the 2D actuator can be used to move magnetic sensors to positions that are highly stable after one second, and that an additional second is sufficient to collect field measurements with a minimal level of randomness.

3.5 Performance analysis of ANSER EMT

In this section, the sources of EMT error affecting the ANSER EMT system are discussed, and the theoretical accuracy is evaluated.

This section shows how magnetic flux measurement errors are related to the corresponding EMT errors. Uncertainty propagation from the measurement domain to the EMT pose domain is analysed.

The theoretical tracking resolution of ANSER EMT field generators is presented. The study demonstrates a novel method to perform resolution analyses to evaluate or design EMT systems and topologies.

3.5.1 Sources of error

Errors affecting the accuracy of the ANSER EMT system can be classified into systematic and random errors.

Systematic errors occur consistently and in a predictable manner and cannot be reduced by the average of consecutive measurements or by filtering the EMT poses. These errors can be caused by factors such as the stability and reproducibility in the field generation and measurement, the system calibration accuracy, the mathematical model approximation used

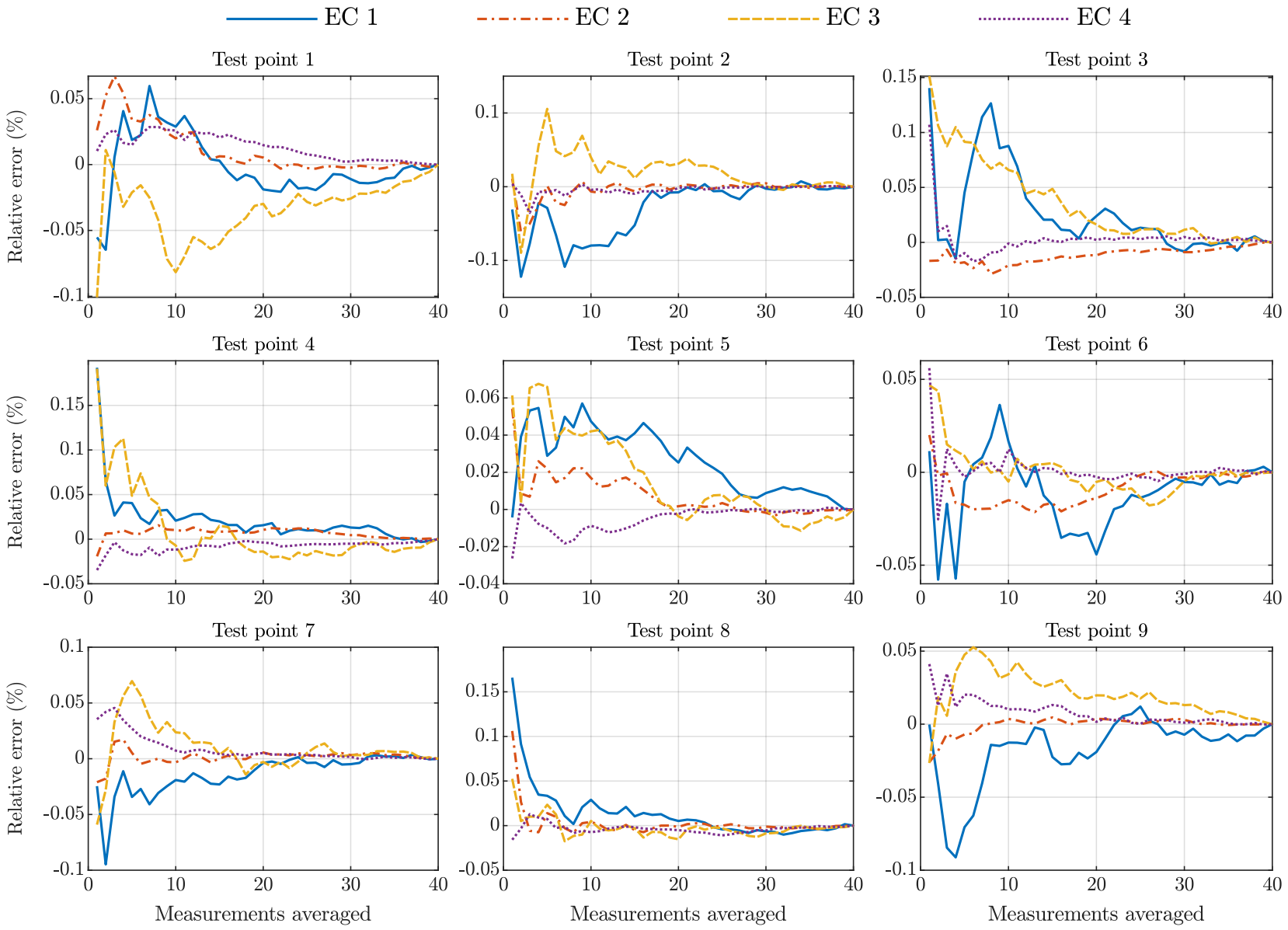


Figure 3.17: Noise reduction by averaging consecutive measurements. At nine test points, a static sensor collected consecutive measurements and an increasing number of measured values, from 1 to 40, were incorporated into the average. The percentage relative error was calculated in relation to the global average of the 40 measurements.

for the magnetic field, and the accuracy of any reference system used to define the real pose of the sensor when calculating the error.

Random errors are mainly caused by the noise in the sensor measurements. They can be reduced by using sensors with higher sensitivity and SNR, increasing the field frequencies to enhance the voltage induced on the pick-up coil, shielding the sensor's wires to minimise undesired signals, and averaging or using filtering techniques, with consequently increased latency.

Other sources of error may include errors caused by field distortion from nearby metallic materials, interference from external sources, and changes in the surrounding equipment, as discussed in Section 2.4. These cannot be pre-determined in a laboratory setting and must be evaluated when installing the system in a new environment.

In general, a tracking error is present every time the field measurements and/or the magnetic model differ from the real magnetic field. For example, unintentional errors could be introduced if the transmitter coils are moved due to the board bending or deformation, or if the shielded wires of a sensor are placed too close to the field generator.

3.5.2 Noise and measurement sensitivity

This section analyses the sensitivity of the EMT solution to a random error in the field measurement to show how the jitter noise of the signal affects the tracking position and orientation. The noise could be intrinsic to the sensor or from an external source, as discussed in Section 3.5.1. In either case, it will change the estimated pose.

Vector $\widetilde{\mathbf{\Phi}}$, defined in Section 3.2.3.2, is the vector of the corrupted magnetic flux values, and $\widetilde{\mathbf{p}}$ is the correspondent sensor pose estimation. A Taylor expansion of the magnetic flux model can be performed around the reference sensor pose, $\mathbf{p}$:

$$\widetilde{\mathbf{\Phi}} \approx \mathbf{\Phi} + \mathbf{J}_{\mathbf{p}} \cdot (\widetilde{\mathbf{p}} - \mathbf{p}), \tag{3.22}$$

where $\mathbf{J}_{\mathbf{p}} \in \mathbb{R}^{8\times5}$ is the Jacobian matrix of the flux model calculated in $\mathbf{p}$.

The pose error, $\Delta\mathbf{p} = (\widetilde{\mathbf{p}} - \mathbf{p})$, can be estimated from the field difference, $\Delta\mathbf{\Phi} = (\widetilde{\mathbf{\Phi}} - \mathbf{\Phi})$, by inverting Equation 3.22:

$$\Delta\mathbf{p} = \mathbf{J}_{\mathbf{p}}^{\dagger} \cdot \Delta\mathbf{\Phi}, \tag{3.23}$$

where $\mathbf{J}_{\mathbf{p}}^{\dagger}$ is the Moore–Penrose inverse of the matrix $\mathbf{J}_{\mathbf{p}}$.

Equation 3.23 shows that the smaller $\mathbf{J}_{\mathbf{p}}^{\dagger}$ is, the smaller the tracking error for a given error in the field measurements. Additional emitter coils would increase the dimension of matrix $\mathbf{J}_{\mathbf{p}}$, further reducing the inverse $\mathbf{J}_{\mathbf{p}}^{\dagger}$. This explains how redundant transmitter coils help reduce the EMT error and why, in general, EMT systems provide more constraints, eight in the ANSER EMT system, than degrees of freedom, five for the pose of a uniaxial sensor.

For every emitter coil, the random noise affecting the measurement at that frequency can be modelled by a Gaussian distribution with variance σ_{ec}^2 on the diagonal of the 8×8 covariance matrix, $\Sigma_{\mathbf{\Phi}}$. When the noise is assumed uncorrelated, the out-of-diagonal elements of $\Sigma_{\mathbf{\Phi}}$ are all zero. If the frequency components are correlated, then $\Sigma_{\mathbf{\Phi}}$ is a full matrix. Error correlation could be caused by spectrum leakage in the demodulation step or cross-talk in the analogue signal path.

Because the magnetic flux and the tracking pose are connected in a local linear dependence, as per Equation 3.23, the error propagates to the pose covariance matrix, $\Sigma_{\mathbf{p}}$, as given by Equation 3.24:

$$\Sigma_{\mathbf{p}} = \mathbf{J}_{\mathbf{p}}^{\dagger} \cdot \Sigma_{\mathbf{\Phi}} \cdot \mathbf{J}_{\mathbf{p}}^{\dagger\,T} \tag{3.24}$$

which is valid as long as the errors are small enough for the linearisation approximation to hold.

In general, $\Sigma_{\mathbf{p}}$ results in a full matrix. This implies intercorrelation between the sensor spatial and angular coordinates. Furthermore, $\Sigma_{\mathbf{p}}$ depends both on the sensor's position and the orientation because $\mathbf{J}_{\mathbf{p}}$ is calculated in $\mathbf{p}$, the complete sensor pose.

The first 3×3 block of $\Sigma_{\mathbf{p}}$ is the covariance matrix that encodes the trivariate Gaussian distribution describing the position uncertainty, $\Sigma_{\mathbf{x}}$. The associated confidence region assumes the shape of an ellipsoid in the

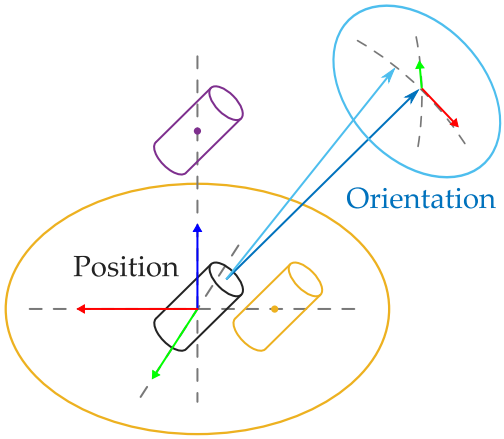


Figure 3.18: The position and orientation random errors are typically distributed as ellipses whose shape and dimension depend both on the sensor pose and noise level.

3D space, with some directions that are more prone to errors than others, as illustrated by the drawing of Figure 3.18.

The three semi-axes of the ellipsoid are obtained from the singular value decomposition (SVD) of the matrix $\Sigma_{\mathbf{x}}$:

$$[U, S, V] = \text{svd}(\Sigma_{\mathbf{x}}) \tag{3.25}$$

The columns of U are the direction vectors of the three semi-axes, and the diagonal entries of S, namely the singular values s_1, s_2, and s_3, indicate the variance associated with that direction. In this case, $V = U^T$ because $\Sigma_{\mathbf{x}}$ is symmetric.

The square root of the largest singular value, $\sigma_1 = \sqrt{s_1}$, is the standard deviation of the Euclidean error along the longest semi-axis of the ellipsoid, which is affected by the highest error. The square root of the sum of the three singular values is the global standard deviation considering all directions, equal to the addition in quadrature of the standard deviation associated with the x, y, and z coordinates:

$$\sqrt{s_1 + s_2 + s_3} = \sqrt{\sigma_x^2 + \sigma_y^2 + \sigma_z^2} \tag{3.26}$$

Similar considerations are valid for the orientation error, for which the last 2×2 block of the matrix $\Sigma_{\mathbf{p}}$ encodes the two directions and the associated standard deviations of the error in the orientation angles.

As an example, Figure 3.19 shows the position and orientation obtained for one hundred EMT solutions for a sensor at $[100, 50, 150]$ mm and three different orientations, in the presence of white noise with $SNR = -60$ dB.

3.5.3 System resolution

As demonstrated in Section 3.5.2 above, error in the magnetic flux measurements propagates to EMT errors in a way that depends on the pose of the sensor, following Equation 3.24.

The system *robustness* against systematic or random errors is attested if significant measurement errors translate into minor EMT errors. From another point of view, this also means that a slight change in the sensor pose causes a considerable variation in the magnetic measurements, which is easier to detect. In this way, higher spatial and angular tracking *resolution* are achieved.

Both of these effects are obtained if the magnetic model gradient is high, that is where the Jacobian matrix, $\mathbf{J_p}$, assumes large values, as demonstrated by Equation 3.23. Differences in the flux vector, $\Delta\mathbf{\Phi}$, might be caused by jitter noise or by approximations of the magnetic model, which could also be due to poor calibration of the scaling coefficients seen in Section 3.2.3.2.

A systematic analysis was performed to characterise the region of interest (ROI) of the ANSER EMT system and determine what poses can be tracked more accurately. The 30 cm and the 42 cm planar field generators shown in Figure 3.2 were included in the analysis.

For the smaller board, the ROI was defined as a $30 \times 30 \times 30\,\text{cm}^3$ cubic volume at a distance of 5 cm. The plane at $Z = 15$ cm was considered for this study. The average absolute value between the three magnetic field components on the plane was calculated as $788\,{}^{mA}/_{\text{m}}$, considering a unitary current in the emitter coils.

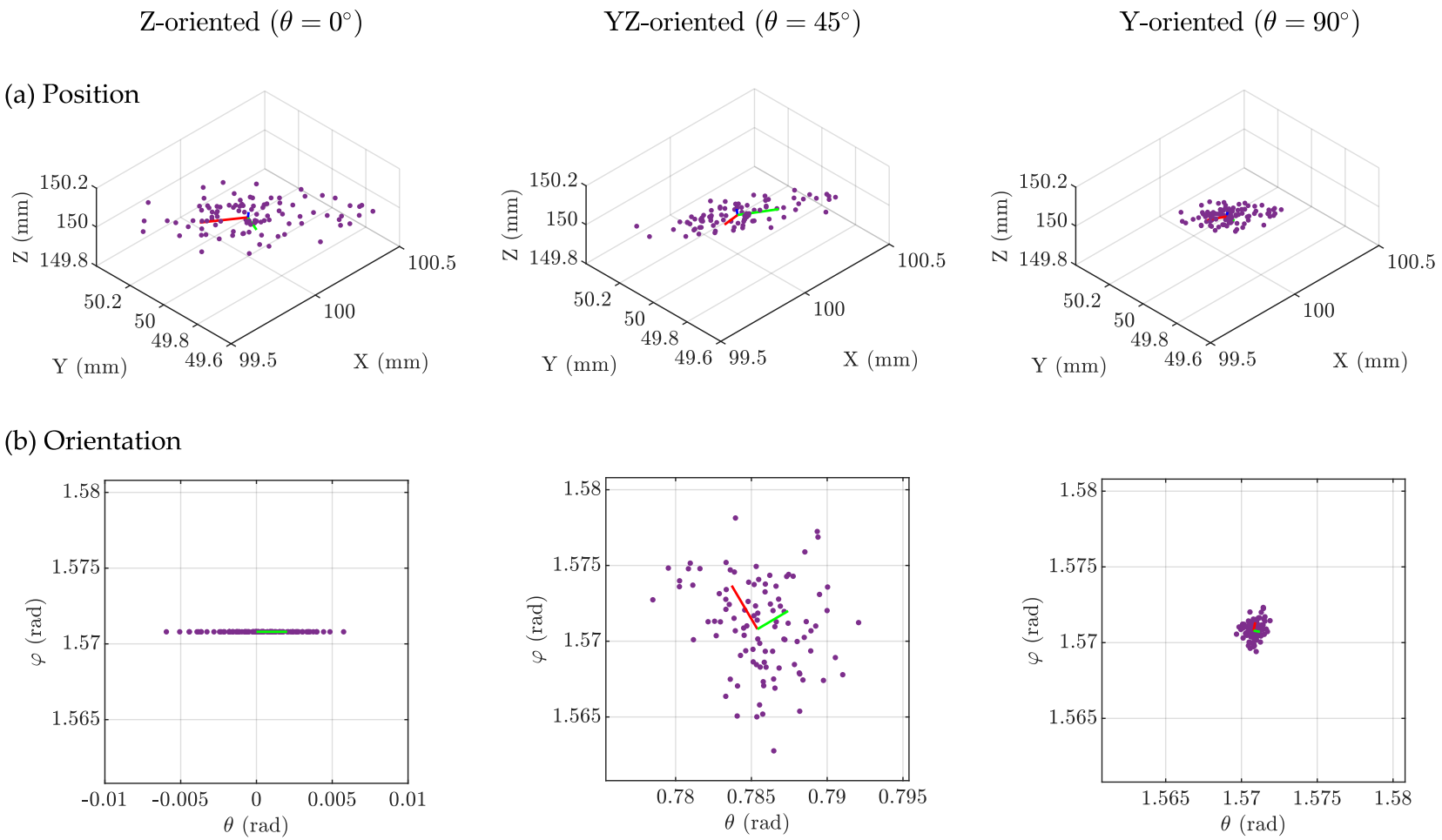


Figure 3.19: Sensor poses obtained from magnetic values measured with random white noise at -60 dB. The (a) position and (b) orientation errors follow a multivariate Gaussian distribution, where the equiprobability region has the shape of an ellipsoid. The ellipsoid semi-axes, indicating the main error directions, are identified in the figure in red, green, and blue. In ($\theta = 0°$, b), the solutions for φ are not visualised because the Z-orientation has no dependence on the yaw angle. The three cases are compared using the same scale to highlight how different orientations affect the jitter noise.

For the larger board, $40 \times 40 \times 40\,\text{cm}^3$ ROI starting at 10 cm was considered. The plane at $Z = 20\,\text{cm}$ was used, where the average field vector resulted in $687\,{}^{mA}/_{\text{m}}$.

Gaussian noise with standard deviation $\sigma = 1\,{}^{mA}/_{\text{m}}$ was considered for every emitter coil. This level corresponds to SNR values of -57.9 dB and -56.7 dB for the smaller and the larger boards, respectively, if the reference signal is calculated as the average signal between the eight emitter coils.

It must be noted that the average noise level observed in the typical configuration of the ANSER EMT system is -70 dB approximately. However, the selection of $1\,{}^{mA}/_{\text{m}}$ is justifiable as it leads to more easily interpretable results and because magnetic model errors are usually on the order of milliamperes per metre.

Because, in this experiment, the eight signal frequency components are assumed uncorrelated and the same standard deviation σ is utilised, it results that $\Sigma_{\mathbf{\Phi}} = \sigma^2 \mathbf{I_8}$, where $\mathbf{I_8}$ is the 8×8 identity matrix, and Equation 3.24 can be simplified to:

$$\Sigma_{\mathbf{p}} = \mathbf{J_p^\dagger} \cdot \sigma^2 \mathbf{I_8} \cdot \mathbf{J_p^\dagger}^T = \sigma^2 (\mathbf{J_p}^T \mathbf{J_p})^{-1} \tag{3.27}$$

The standard deviation (STD) of the position error was calculated as the largest eigenvalue of $\Sigma_{\mathbf{p}}$, which corresponds to the EMT position jitter along the direction with the largest variability.

The results are visualised in Figure 3.20 for three different sensor orientations, with pitch angles $\theta = 0°$, $\theta = 45°$, and $\theta = 90°$, indicating vertical, diagonal, and horizontal orientations, respectively.

It can be observed that points in the centre of the ROI demonstrate, in general, better position-tracking resolution. There are two reasons for this: in the central region, (1) the average magnetic field is stronger, thus ensuring a larger SNR, and (2) the spatial gradient of the magnetic field is higher. Both of these factors contribute to a greater magnitude of the Jacobian matrix $\mathbf{J_p}$, which has been demonstrated to play a crucial role in the propagation of errors.

This study shows that the volume range where accurate EMT can be maintained for any sensor orientation is theoretically limited to approx-

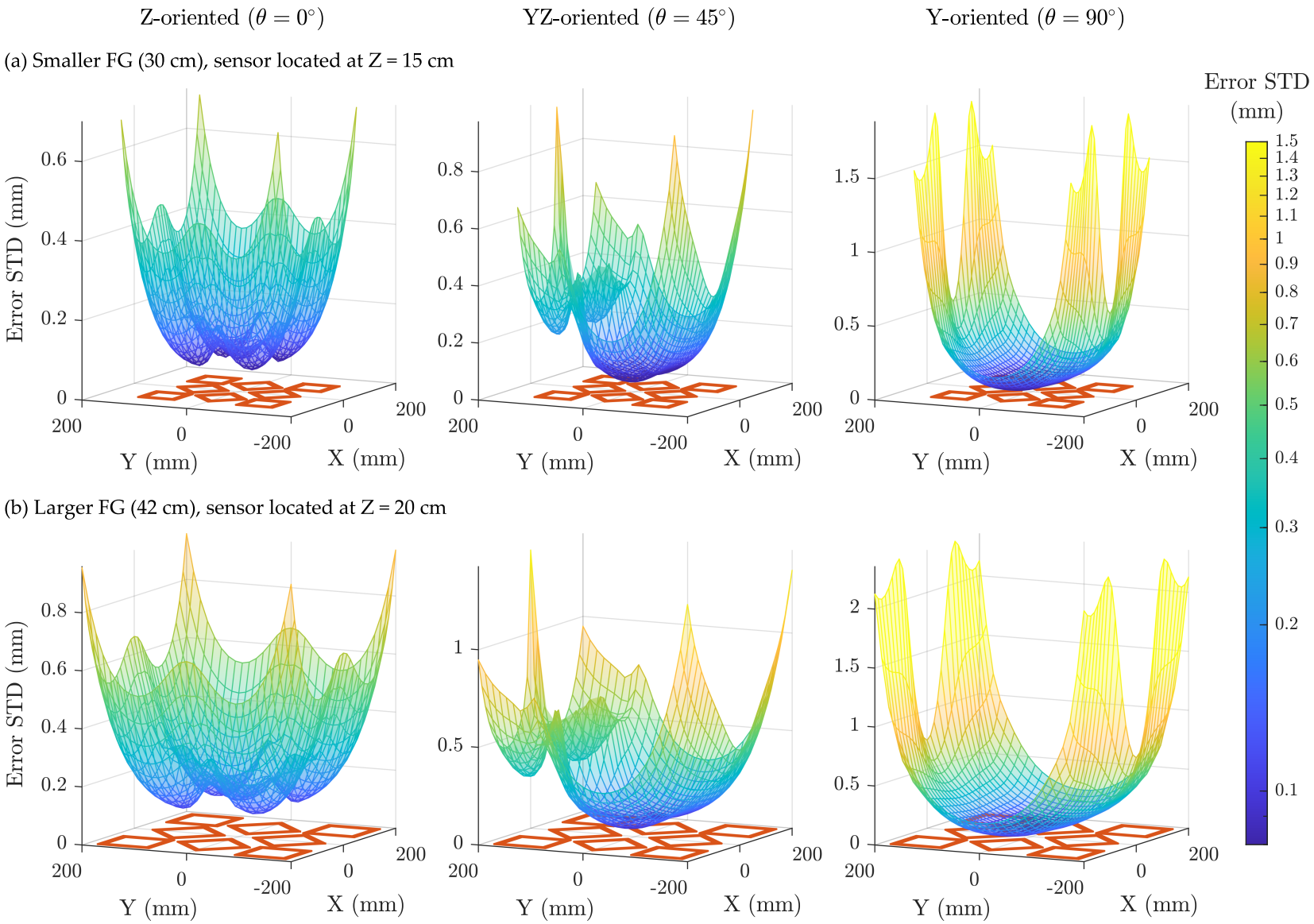


Figure 3.20: Position tracking resolution of the ANSER EMT system for three sensor orientations compared, using (a) the 30 cm and (b) the 42 cm field generator (FG) boards shown in Figure 3.2.

imately $30 \times 30 \times 30\,\text{cm}^3$ for the smaller field generator and $40 \times 40 \times 40\,\text{cm}^3$ for the larger board. Extending the tracking range in the horizontal plane can be attained by placing multiple field generators side by side, whereas increasing the distance range would require generating stronger fields. The second case is limited by the safety exposure levels imposed by the regulatory authority [22, 23]. However, foreseen clinical applications involve placing the planar board closely below the patient, so that the ROI is typically between 5 to 25 cm from the field generator.

Resolution analyses like the one described in this section may be conducted during the design phase when new EMT systems, topologies, or methods are being developed [90, 91].

3.6 Experimental performance

This section describes how the performance of the ANSER EMT system was measured under typical conditions. The three available software frameworks and solver implementations are compared.

Tool T introduced in Section 3.3 was placed at 81 different locations above the planar field generator in a 24×24 cm horizontal grid, and the magnetic measurements were recorded. The two sensors were aligned along axes Y and Z of the EMT reference, horizontally and vertically oriented relative to the field generator, respectively. The 2D linear actuator presented in Section 3.4 was used to move the sensors, using optical tracking for pose reference. The experiment was repeated for two heights, at $Z = 10$ cm and 20 cm, as shown in Figure 3.21.

The symmetry of the field generator allows for tracking a sensor oriented along the X-axis with the same accuracy as if the sensor were oriented along the Y-axis. Conversely, for sensors oriented along the Z-axis, EMT accuracy may differ. A sensor rotation by 90 degrees from the Y to Z orientation results in continuity variations in magnetic field measurements and tracking errors.

It should be noted that there is no guarantee that the error obtained with the YZ orientation falls within the range of errors obtained with sensors oriented along the Y and Z axes. However, it was observed

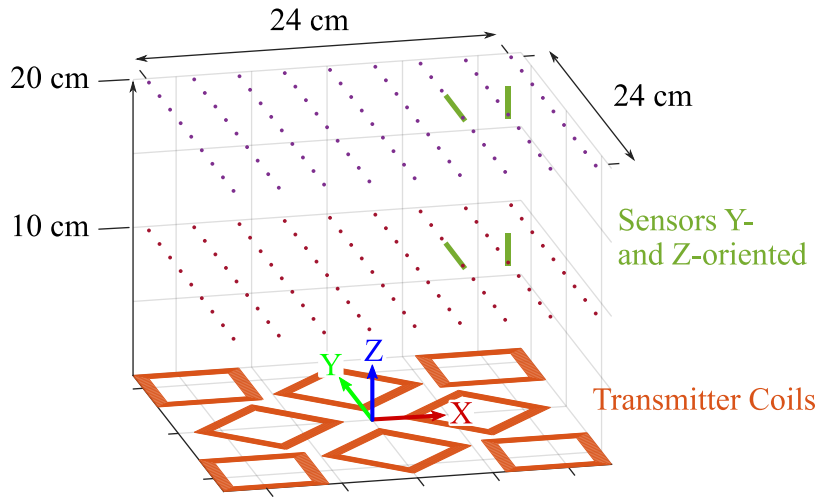


Figure 3.21: The magnetic field generated by the eight transmitter coils was measured at two grids of 81 points for two different sensor orientations, i.e. $\theta = 90°$ (Y-oriented) and $\theta = 0°$ (Z-oriented).

that this is generally the case and that, even when not true, the accuracy deviation is minimal. As a result, tracking tests using Y and Z-oriented sensors are sufficient to determine overall system accuracy. Furthermore, given the measured Y and Z magnetic field components, any other sensor orientation can be simulated by projecting the field vector onto the sensor axis.

The sampling and demodulation stages were implemented using MATLAB to isolate the performance comparison of the three solver implementations in MATLAB, Python, and C++ . For a given sampling frequency and acquisition time, there is no difference in the sampling stage for different languages since they all use the same background NI-DAQmx Windows driver, as presented in Section 3.2.1. The demodulation time, measured in Figure 3.8, is on the order of microseconds and has little or no impact on the overall speed and accuracy performance of the system as the majority of computation is made in the final solving stage.

3.6.1 Accuracy evaluation

The ISO 5725 standard [92] defines *trueness* as the degree of closeness between the arithmetic mean of multiple test results and the actual refer-

ence value, and *precision* as the degree of agreement among different test results. According to this definition, the *accuracy* refers to the combination of trueness and precision.

In order to assess the accuracy of collected data, multiple measurements must be considered to estimate trueness and precision separately. Averaging the measurements reduces random noise and enhances precision, thereby allowing for the determination of trueness in relation to a ground truth reference provided, for example, by the optical system. The precision can be evaluated by calculating the standard deviation.

At each test point, 50 field measurements were collected, and the tracking algorithm was used to estimate the reference sensor position and orientation, $\mathbf{p}$. The average solution was considered as the EMT pose, $\widetilde{\mathbf{p}}$.

By defining $\Delta\mathbf{p} = \widetilde{\mathbf{p}} - \mathbf{p}$, the first three elements of $\Delta\mathbf{p}$ correspond to the Cartesian position errors, Δx, Δy, and Δz, and the last two elements of $\Delta\mathbf{p}$ are the two spherical angle errors, $\Delta\theta$ and $\Delta\varphi$.

The position error was calculated as the Euclidean distance between the tracked and the reference sensor positions:

$$e = \sqrt{\Delta x^2 + \Delta y^2 + \Delta z^2} \quad [\text{mm}] \tag{3.28}$$

The angular error was obtained from $\Delta\theta$ and $\Delta\varphi$ as given by Equation 3.29 in the small angle error approximation:

$$e = \frac{180^\circ}{\pi}\sqrt{\Delta\theta^2 + \sin^2\left(\theta + \frac{\Delta\theta}{2}\right)\Delta\varphi^2} \tag{3.29}$$

Alternatively, the orientation unit vectors, $\widetilde{\mathbf{n}}$ and $\mathbf{n}$, can be calculated from Equation 3.13, and the exact angular error is given by:

$$e = \frac{180^\circ}{\pi}\left|\cos^{-1}\left(\widetilde{\mathbf{n}}^T \cdot \mathbf{n}\right)\right| \tag{3.30}$$

Considering P test points, the position error vector $\mathbf{e}$ is defined with entries e_i, which is the position error at the test point i, calculated as per Equation 3.28. The orientation error vector is defined similarly, where the entries are calculated as per Equation 3.29. Average position and

orientation errors were expressed as the root mean square error (RMSE) and the mean error (ME), calculated between the number of observations:

$$\mathrm{RMSE}(\mathbf{e}) = \sqrt{\frac{1}{P}\sum_{i=1}^{P} e_i^2}; \qquad \mathrm{ME}(\mathbf{e}) = \frac{1}{P}\sum_{i=1}^{P} e_i, \tag{3.31}$$

where $P = 81$ in the four experimental datasets presented in this section.

Another statistical measure of global trueness is the 95^{th} percentile (PRC95). With a total number of 81 test points, the PRC95 was determined by the first 77 test points, sorted by the minor Euclidean error. In other words, four test points resulted in positional errors larger than the PRC95 reported.

At each test point, the standard deviation of the 50 solutions was calculated for the three Cartesian coordinates separately, σ_x, σ_y, and σ_z. The local position precision, σ_i, was measured as the sum in quadrature of the standard deviations in the three directions. The root-mean-square was taken to determine a global value for the average precision between the 81 test points:

$$\overline{\sigma} = \sqrt{\frac{1}{P}\sum_{i=1}^{P} \sigma_i^2} = \sqrt{\frac{1}{P}\sum_{i=1}^{P} \sigma_{xi}^2 + \sigma_{yi}^2 + \sigma_{zi}^2} = \sqrt{\overline{\sigma}_x^2 + \overline{\sigma}_y^2 + \overline{\sigma}_z^2} \tag{3.32}$$

where $\overline{\sigma}_x^2$, $\overline{\sigma}_y^2$, and $\overline{\sigma}_z^2$ are the values of global precision calculated for the x, y, and z coordinates, separately.

3.6.2 Computation time and memory requirements

Solver time is a critical parameter for EMT systems because it directly reflects on the update rate and latency of the system, which are essential for smooth, real-time navigation. Timing values for each solver implementation were determined by looping the solving section of the code 50 times and recording the average time to solve a given grid of points. This gave a better estimate of mean solving times and update rates.

Memory usage was determined using the *memory* function in MATLAB, which returns the total amount of RAM used by MATLAB [93]. Unlike

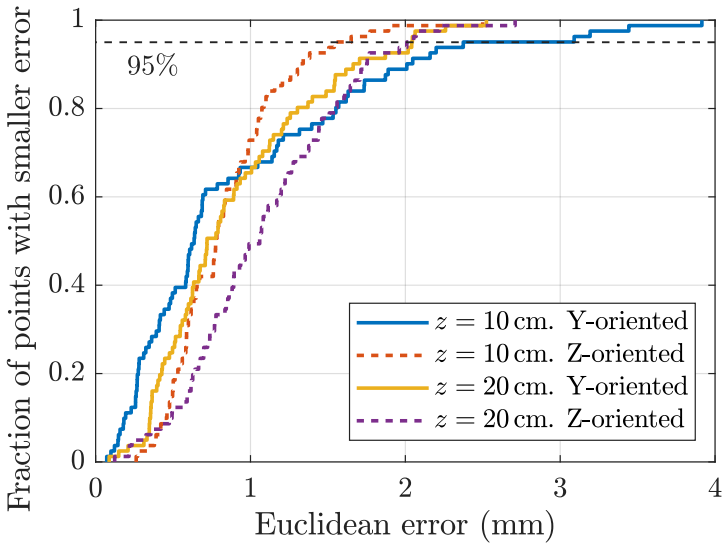


Figure 3.22: Cumulative distribution function of the Euclidean position error calculated at test points as per Equation 3.28.

Python and C++ , the whole instance of MATLAB is required for operation, so this is the minimum amount of memory necessary. The *psutil* library was imported when determining memory usage in Python [94]. This library can retrieve information on running processes and system utilisation. Visual Studio natively provides memory usage when a process is running.

The values were obtained for a laptop PC mounting an Intel i5-6200u CPU, 8 GB RAM, and Windows 10 OS, using MATLAB 2017b, Python 3 in VS Code, and the Visual C++ compiler in Visual Studio 2019.

3.6.3 Results

For the four static tracking experiments, the EMT position error results are plotted in Figures 3.22 and 3.23. Figure 3.22 shows the cumulative distribution function (CDF) of the Euclidean error at each test point, while Figure 3.23 displays how this error is correlated to the distance from the field generator centre. The global accuracy and precision calculated from Equations 3.31 and 3.32 are reported in Table 3.1, both for position and orientation errors.

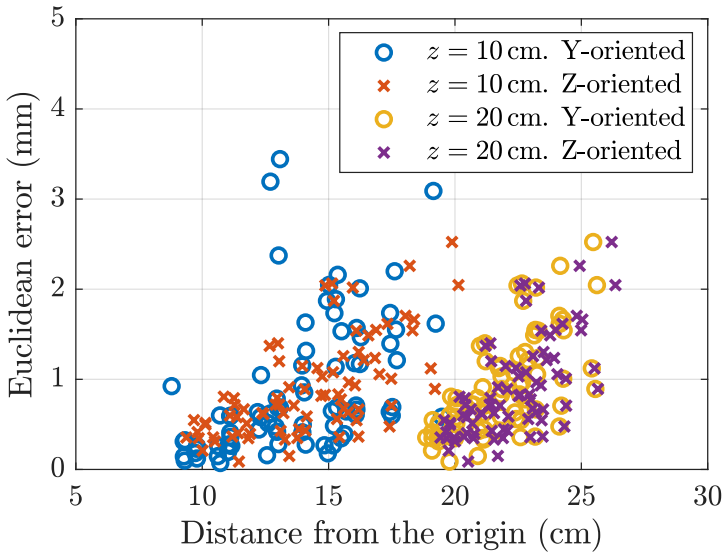


Figure 3.23: Scatter plot of the Euclidean position error as a function of the distance of the test point from the field generator centre.

Table 3.1: ANSER EMT accuracy and precision assessment, computed as per Equations 3.31 and 3.32.

	RMSE mm / deg	ME mm / deg	PRC95 mm / deg	$\overline{\sigma}$ mm
z=10 cm, horizontal	1.23 / 1.22	0.93 / 0.87	2.37 / 2.68	0.10
z=10 cm, vertical	0.93 / 0.75	0.84 / 0.64	1.54 / 1.24	0.07
z=20 cm, horizontal	1.05 / 0.54	0.90 / 0.42	2.04 / 1.22	0.17
z=20 cm, vertical	1.20 / 0.81	1.09 / 0.72	2.01 / 1.29	0.22
Aurora[1]	1.20 / 0.50	N/A	1.80 / 0.70	N/A
3D Guidance[2]	1.19 / 9.45	1.02 / 9.35	2.33 / 11.1	0.61

[1]with Tabletop field generator, as reported in the datasheet [95].
[2]with Flat field generator, calculated in [96, 97].

Table 3.2: Solver performance for each programming environment. The entire grid of points was solved 50 times, and the average result is shown.

	MATLAB	Python	C++	Aurora	3D G.
Solving time (ms)	25.9	32.75	18.4	N/A	N/A
Memory usage (MB)	1473	97	1.2	N/A	N/A
Update rate (Hz)	38	31	54	40	80

A thorough comparison of the main optical and magnetic tracking systems available on the market can be found in [98]. The NDI Aurora with Tabletop field generator and the Ascension (now NDI) 3D Guidance system (Ascension Technology Corp., Milton, VT, USA) with Flat field generator are the systems most similar to the ANSER EMT system studied in this work because they all operate with a planar magnetic field generator. For convenience, the position errors of NDI Aurora and Ascension 3D Guidance are reported in Table 3.1.

The speed of each solver and their corresponding memory requirements are summarised in Table 3.2, where the update rates of NDI Aurora and 3D Guidance are also included.

3.6.4 Discussion

The results of Table 3.1 demonstrate that the ANSER EMT system can achieve millimetre and degree accuracy with high repeatability in a tracking volume of $24 \times 24 \times 20$ cm. It has been observed that position and orientation errors expressed in millimetres and in degrees, respectively, are in the same range.

In general, Y-oriented (horizontal) and Z-oriented (vertical) sensor orientations show similar average accuracy, but in the first case, the PRC95 is larger. In agreement with this observation, Figure 3.22 shows different error distributions in the two cases. Such an outcome can be explained by the system resolution shown in Figure 3.20, where the sensor Y-orientation has lower tracking error at the centre of the region of interest (ROI), but the error diverges faster as the sensor is moved towards the boundaries.

As expected, points in the centre of the ROI can be solved with higher accuracy, as shown in Figure 3.23. On the other hand, the distance of 10 or 20 cm from the field generator does not have a significant impact on trueness and mainly affects the precision, as seen in Table 3.1. The reason for this is that reduced signal magnitude implies a lower signal-to-noise ratio (SNR) and, therefore, higher jitter noise.

Table 3.2 shows that the average solving time is almost 180% faster using C++ compared to the Python implementation. Comparison with the MATLAB solver is also included, although the significant memory overhead associated with this approach makes MATLAB impractical in many real-life applications. The expected efficiency in memory allocation from C++ versus Python is significant, with an approximate 81% decrease in memory requirements.

It should be noted that the solver speed depends on the options chosen for the iterative algorithm, such as the maximum number of iterations, the maximum number of function evaluations, the termination tolerance on the function value, and the termination tolerance on the step value. These values can be optimised as a trade-off between convergence speed and accuracy.

Moreover, the algorithm is typically faster during dynamic tracking because the initial point can be initialised from the previously solved pose. For this reason, the solving time can be reduced to as low as 5 ms per sensor in the MATLAB environment. Therefore, the system bottleneck is the signal acquisition time, which must be long enough to guarantee a minimum precision level, as seen in Section 3.2.2. The precision results shown in Table 3.1 were obtained with an acquisition time of 20 ms, which allows for a maximum update rate of $1/0.02 = 50$ Hz and minimum latency of $20/2 = 10$ ms.

With these considerations, if multiple sensors are tracked, every sensor adds approximately 5 to 10 ms in latency due to the tracking algorithm solving time in the MATLAB implementation. Therefore, the update rate is limited by the acquisition step when less than five sensors are used, and it becomes limited by the overall solving time after that.

The system performance in terms of accuracy and speed reported in Tables 3.1 and 3.2 meets the clinical requirements for a variety of surgical procedures, e.g. pedicle screw insertion, tumour therapy, needles placement for percutaneous interventions, and thoracic–abdominal procedures [97, 99].

The results demonstrate the significant speed and efficiency benefits of a low-level C++ implementation, compared to previously reported approaches, and the importance in the further development of open architectures for EMT, enabling low-level solver implementations in applications where high speed and precision are required, e.g. in the next generation of robotic surgery devices.

3.7 Conclusions

The chapter provided insights into the functioning of the ANSER EMT system, the methods employed, and the current limitations. This presentation establishes a foundation for the research and solutions explored in the following chapters.

In particular, some limitations of the current system are summarised as follows.

- The analytical magnetic model presented in Section 3.2.3 is based on theoretical considerations and leads to EMT errors up to more than 2 mm even under ideal conditions, as shown in Section 3.6. One solution will be proposed in Section 4.2, where a data-driven model is introduced to correct systematic errors.

- The model approximates the sensor as a single point, which may be inaccurate if the sensor is spatially extended. Chapters 6 and 7 will introduce alternative formulations for the theoretical magnetic model that are better suited to sensors with elongated or planar shapes, respectively.

- The system is sensitive to metallic distortion, and the EMT solution is provided without estimation of the tracking accuracy. In Section 4.3,

magnetic shielding solutions will be analysed and tested, while Section 4.4 will introduce techniques for real-time detection of accuracy reduction due to metallic distortion.

- The EMT algorithm described in Section 3.2.4 allows for concurrently tracking a limited number of sensors, as demonstrated in Table 3.2. A faster algorithm will be presented in Chapter 5, which includes Kalman filtering for increased update rate and reduced noise.

References

[1] M. Cavaliere, C. Walsh, H. A. Jaeger, K. O'Donoghue, and P. Cantillon-Murphy, "Magnetic tracking using a modular C++ environment for image-guided interventions," *Computer Methods in Biomechanics and Biomedical Engineering: Imaging & Visualization*, vol. 10, no. 4, pp. 383–389, 2021, ISSN: 2168-1163. DOI: 10.1080/21681163.2021.1998926.

[2] H. A. Jaeger *et al.*, "Anser EMT: The first open-source electromagnetic tracking platform for image-guided interventions," *International Journal of Computer Assisted Radiology and Surgery*, vol. 12, pp. 1059–1067, 2017. DOI: 10.1007/s11548-017-1568-7.

[3] "AnserEMT (git repository)," [Online]. Available: https://github.com/BioDesignUCC/AnserEMT.

[4] Open Science Framework, *Anser EMT*. [Online]. Available: https://osf.io/47q8q/ (visited on 07/16/2021).

[5] Biodesign UCC, *Anser EMT*. [Online]. Available: https://biodesignucc.ie/build/html/anseremt.html (visited on 12/22/2022).

[6] J. Tokuda *et al.*, "OpenIGTLink: An open network protocol for image-guided therapy environment," *International Journal of Medical Robotics and Computer Assisted Surgery*, vol. 5, no. 4, pp. 423–434, 2009, ISSN: 14785951. DOI: 10.1002/rcs.274.

[7] I. Wolf *et al.*, "The medical imaging interaction toolkit (MITK): A toolkit facilitating the creation of interactive software by extending VTK and ITK," in *Medical Imaging 2004: Visualization, Image-Guided Procedures, and Display*, vol. 5367, SPIE, 2004, pp. 16–27. DOI: 10.1117/12.535112.

[8] C. Askeland *et al.*, "CustusX: An open-source research platform for image-guided therapy," *International Journal of Computer Assisted Radiology and Surgery*, vol. 11, no. 4, pp. 505–519, 2016, ISSN: 1861-6429. DOI: 10.1007/s11548-015-1292-0.

[9] R. Kikinis, S. D. Pieper, and K. G. Vosburgh, "3D Slicer: A Platform for Subject-Specific Image Analysis, Visualization, and Clinical Support," in *Intraoperative Imaging and Image-Guided Therapy*, F. A. Jolesz, Ed., New York, NY: Springer, 2014, pp. 277–289, ISBN: 978-1-4614-7657-3. DOI: 10.1007/978-1-4614-7657-3_19.

[10] A. M. Franz, H. A. Jaeger, A. Seitel, P. Cantillon-Murphy, and L. Maier-Hein, "Open-Source Tracked Ultrasound with Anser Electromagnetic Tracking," in *Bildverarbeitung für die Medizin 2019*, H. Handels, T. M. Deserno, A. Maier, K. H. Maier-Hein, C. Palm, and T. Tolxdorff, Eds., ser. Informatik aktuell, Wiesbaden: Springer Fachmedien, 2019, pp. 232–237, ISBN: 978-3-658-25326-4. DOI: 10.1007/978-3-658-25326-4_52.

[11] M. Cavaliere, O. McVeigh, H. A. Jaeger, S. Hinds, K. O'Donoghue, and P. Cantillon-Murphy, "Inductive Sensor Design for Electromagnetic Tracking in Image Guided Interventions," *IEEE Sensors Journal*, vol. 20, no. 15, pp. 8623–8630, 2020, ISSN: 1558-1748. DOI: 10.1109/JSEN.2020.2984323.

[12] H. A. Jaeger and P. Cantillon-Murphy, "Electromagnetic Tracking Using Modular, Tiled Field Generators," *IEEE Transactions on Instrumentation and Measurement*, vol. 68, no. 12, pp. 4845–4852, 2019, ISSN: 1557-9662. DOI: 10.1109/TIM.2019.2900884.

[13] H. A. Jaeger and P. Cantillon-Murphy, "Distorter Characterisation Using Mutual Inductance in Electromagnetic Tracking," *Sensors*, vol. 18, no. 9, p. 3059, 2018. DOI: 10.3390/s18093059.

[14] M. Cavaliere, H. A. Jaeger, K. O'Donoghue, and P. Cantillon-Murphy, "Planar Body-Mounted Sensors for Electromagnetic Tracking," *Sensors*, vol. 21, no. 8, p. 2822, 2021. DOI: 10.3390/s21082822.

[15] P. Cantillon-Murphy and H. A. Jaeger, *Anser EMT, OSF repository*, 2016. DOI: 10.17605/OSF.IO/47Q8Q.

[16] O. Shafrir, E. Paperno, and A. Plotkin, *Magnetic Tracking with a Flat Transmitter*. LAP LAMBERT Academic Publishing, 2010, ISBN: 978-3-8383-4436-2. [Online]. Available: https://www.morebooks.shop/store/gb/book/magnetic-tracking-with-a-flat-transmitter/isbn/978-3-8383-4436-2 (visited on 02/10/2020).

[17] K. O'Donoghue, "Electromagnetic tracking and steering for catheter navigation," Ph.D. dissertation, University College Cork, Cork, Ireland, 2014. [Online]. Available: https://cora.ucc.ie/handle/10468/2025.

[18] M. Šmelko *et al.*, "Low Frequency Magnetic Fields and Safety," *Acta Physica Polonica A*, vol. 137, no. 5, pp. 693–696, 2020, ISSN: 1898-794X, 0587-4246. DOI: 10.12693/APhysPolA.137.693.

[19] W. Kaune, J. Guttman, and R. Kavet, "Comparison of coupling of humans to electric and magnetic fields with frequencies between 100 Hz and 100 kHz," *Bioelectromagnetics*, vol. 18, no. 1, pp. 67–76, 1997, ISSN: 1521-186X. DOI: 10.1002/(SICI)1521-186X(1997)18:1<67::AID-BEM10>3.0.CO;2-N.

[20] D. Formica and S. Silvestri, "Biological effects of exposure to magnetic resonance imaging: An overview," *Biomedical engineering online*, vol. 3, no. 1, pp. 1–12, 2004, ISSN: 1475-925X.

[21] A. Barbault *et al.*, "Amplitude-modulated electromagnetic fields for the treatment of cancer: Discovery of tumor-specific frequencies and assessment of a novel therapeutic approach," *Journal of Experimental & Clinical Cancer Research*, vol. 28, no. 1, pp. 1–10, 2009, ISSN: 1756-9966.

[22] ICNIRP, "Guidelines for limiting exposure to time-varying electric and magnetic fields (1 Hz to 100 kHz)," *Health Physics*, vol. 99, no. 6, pp. 818–836, 2010, ISSN: 0017-9078. DOI: 10.1097/HP.0b013e3181f06c86.

[23] IEEE, "IEEE Standard for Safety Levels with Respect to Human Exposure to Electric, Magnetic, and Electromagnetic Fields, 0 Hz to 300 GHz," *IEEE Std C95.1-2019 (Revision of IEEE Std C95.1-2005/ Incorporates IEEE Std C95.1-2019/Cor 1-2019)*, pp. 1–312, 2019. DOI: 10.1109/IEEESTD.2019.8859679.

[24] K. O'Donoghue, H. A. Jaeger, and P. Cantillon-Murphy, "A Radiolucent Electromagnetic Tracking System for Use with Intraoperative X-ray Imaging," *Sensors*, vol. 21, no. 10, p. 3357, 2021. DOI: 10.3390/s21103357.

[25] G. Dehmel, "Magnetic Field Sensors: Induction Coil (Search Coil) Sensors," in *Sensors*, R. Boll and K. J. Overshott, Eds., Weinheim, Germany: Wiley-VCH Verlag GmbH, 2008, pp. 205–253, ISBN: 978-3-527-62016-6 978-3-527-26771-2. DOI: 10.1002/9783527620166.ch6.

[26] Northern Digital Inc., *Aurora Sensors*. [Online]. Available: https://www.ndigital.com/electromagnetic-tracking-technology/aurora/aurora-sensors/ (visited on 09/13/2022).

[27] C. Coillot and P. Leroy, "Induction Magnetometers Principle, Modeling and Ways of Improvement," in *Magnetic Sensors - Principles and Applications*, K. Kuang, Ed., InTech, 2012, ISBN: 978-953-51-0232-8. DOI: 10.5772/1361.

[28] H. Jaeger, K. O'Donoghue, and P. Cantillon-Murphy, "Induction sensor characterisation for electromagnetic tracking systems," in *IEEE I2MTC 16-19 May 2022*, Ottawa, ON, Canada, 2022.

[29] "Induction Sensors," in *Magnetic Sensors and Magnetometers*, ser. Artech House Remote Sensing Library, P. Ripka, Ed., Boston: Artech House, 2001, ISBN: 978-1-58053-057-6.

[30] S. Tumanski, "Induction coil sensors - A review," *Measurement Science and Technology*, 2007, ISSN: 13616501. DOI: 10.1088/0957-0233/18/3/R01.

[31] R. M. Bozorth and D. M. Chapin, "Demagnetizing Factors of Rods," *Journal of Applied Physics*, vol. 13, no. 5, pp. 320–326, Apr. 16, 2004, ISSN: 0021-8979. DOI: 10.1063/1.1714873.

[32] B. Kaplan, "A new interpretation of the relationship existing between demagnetizing factor and inductance," *IEEE Transactions on Magnetics*, vol. 30, no. 5, pp. 2788–2794, Sep. 1994, ISSN: 1941-0069. DOI: 10.1109/20.312520.

[33] D. Tho and L. Beaulieu, "Technical Note: Identification of an optimal electromagnetic sensor for in vivo electromagnetic-tracked scintillation dosimeter for HDR brachytherapy," *Medical Physics*, vol. 46, no. 5, pp. 2031–2036, 2019, ISSN: 2473-4209. DOI: 10.1002/mp.13508.

[34] M. Denny. "6DOF Explained," NDI. (Jun. 17, 2020), [Online]. Available: https://www.ndigital.com/6dof-explained/ (visited on 05/11/2023).

[35] H. A. Jaeger, S. Hinds, and P. Cantillon-Murphy, "An Open Framework Enabling Electromagnetic Tracking in Image-Guided Interventions," in *Lecture Notes in Computer Science (Including Subseries Lecture Notes in Artificial Intelligence and Lecture Notes in Bioinformatics)*, vol. 11073 LNCS, Cham: Springer International Publishing, 2018, pp. 168–175, ISBN: 978-3-030-00936-6. DOI: 10.1007/978-3-030-00937-3_20.

[36] S. Hinds *et al.*, "An open electromagnetic tracking framework applied to targeted liver tumour ablation," *International Journal of Computer Assisted Radiology and Surgery*, vol. 14, no. 9, pp. 1475–1484, 2019, ISSN: 1861-6429. DOI: 10.1007/s11548-019-01983-5.

[37] T. Ungi, A. Lasso, and G. Fichtinger, "Open-source platforms for navigated image-guided interventions," *Medical Image Analysis*, 20th Anniversary of the Medical Image Analysis Journal (MedIA), vol. 33, pp. 181–186, 2016, ISSN: 1361-8415. DOI: 10.1016/j.media.2016.06.011.

[38] MathWorks, *Data Acquisition Toolbox*. [Online]. Available: https://uk.mathworks.com/products/data-acquisition.html (visited on 01/16/2023).

[39] National Instruments, *NI-DAQmx Python Documentation*. [Online]. Available: https://nidaqmx-python.readthedocs.io/en/latest/ (visited on 01/16/2023).

[40] Pierre Cladé, *PyDAQmx 1.0.0 documentation*. [Online]. Available: https://pythonhosted.org/PyDAQmx/ (visited on 01/16/2023).

[41] National Instruments, *Using NI-DAQmx in Text Based Programming Environments*. [Online]. Available: https://www.ni.com/en-ie/support/documentation/supplemental/21/using-ni-daqmx-in-text-based-programming-environments.html (visited on 01/18/2023).

[42] X. Wang, S. Song, and C. Hu, "The extraction technology of weak coupling AC signal in an electromagnetic localization system," in *2010 IEEE International Conference on Robotics and Biomimetics*, 2010, pp. 1170–1175. DOI: 10.1109/ROBIO.2010.5723494.

[43] G. Machel and M. von Ortenberg, "A digital lock-in-technique for pulsed magnetic field experiments," *Physica B: Condensed Matter*, Research in High Magnetic Fields, vol. 211, no. 1, pp. 355–359, 1995, ISSN: 0921-4526. DOI: 10.1016/0921-4526(94)01062-6.

[44] R. N. Bracewell, "Discrete Hartley transform," *JOSA*, vol. 73, no. 12, pp. 1832–1835, 1983. DOI: 10.1364/JOSA.73.001832.

[45] E. Jacobsen and R. Lyons, "The sliding DFT," *IEEE Signal Processing Magazine*, vol. 20, no. 2, pp. 74–80, 2003, ISSN: 1558-0792. DOI: 10.1109/MSP.2003.1184347.

[46] K. O'Donoghue and P. Cantillon-Murphy, "Low cost super-nyquist asynchronous demodulation for use in em tracking systems," *IEEE Transactions on Instrumentation and Measurement*, vol. 64, no. 2, pp. 458–466, 2015. DOI: 10.1109/TIM.2014.2343431.

[47] S. Haykin and B. Van Veen, *Signals and Systems*. John Wiley & Sons, 2007, ISBN: 81-265-1265-2.

[48] S. J. Orfanidis, *Optimum Signal Processing* (McGraw-Hill International Editions. Electrical Engineering Series). New York: McGraw-Hill, copyr. 1990, vol. 2. ed, ISBN: 0-07-100834-9.

[49] J. Begin, *FFT Spectrum and Spectral Densities – Same Data, Different Scaling*, 2019. [Online]. Available: https://www.ap.com/blog/fft-spectrum-and-spectral-densities-same-data-different-scaling/ (visited on 12/13/2022).

[50] Renesas, *Tutorial in Coherent and Windowed Sampling with A/D Converters*, 1997. [Online]. Available: https://www.renesas.com/eu/en/document/apn/an9675-tutorial-coherent-and-windowed-sampling-ad-converters (visited on 11/21/2022).

[51] M. Cerna and A. F. Harvey, "The Fundamentals of FFT-Based Signal Analysis and Measurement," *National Instruments*, vol. Application Note 041, p. 20, 2000.

[52] F. Harris, "On the use of windows for harmonic analysis with the discrete Fourier transform," *Proceedings of the IEEE*, vol. 66, no. 1, pp. 51–83, 1978, ISSN: 0018-9219, 1558-2256. DOI: 10.1109/PROC.1978.10837.

[53] G. Heinzel, A. Rüdiger, and R. Schilling, "Spectrum and spectral density estimation by the Discrete Fourier transform (DFT), including a comprehensive list of window functions and some new at-top windows," 2002. [Online]. Available: https://pure.mpg.de/pubman/faces/ViewItemOverviewPage.jsp?itemId=item_152164 (visited on 11/18/2019).

[54] K. R. Rao and P. C. Yip, Eds., *The Transform and Data Compression Handbook* (The Electrical Engineering and Signal Processing Series). Boca Raton, Fla: CRC Press, 2001, ISBN: 978-0-8493-3692-8.

[55] M. Frigo and S. Johnson, *FFTW*. [Online]. Available: http://fftw.org/ (visited on 11/17/2022).

[56] M. Frigo and S. Johnson, "FFTW: An adaptive software architecture for the FFT," in *Proceedings of the 1998 IEEE International Conference on Acoustics, Speech and Signal Processing, ICASSP '98 (Cat. No.98CH36181)*, vol. 3, 1998, 1381–1384 vol.3. DOI: 10.1109/ICASSP.1998.681704.

[57] MathWorks, *Fast Fourier transform*. [Online]. Available: https://uk.mathworks.com/help/matlab/ref/fft.html (visited on 11/17/2022).

[58] SciPy v1.9.3 Manual, *Discrete Fourier transforms (scipy.fft)*. [Online]. Available: https://docs.scipy.org/doc/scipy/reference/fft.html#module-scipy.fft (visited on 11/17/2022).

[59] PyFFTW, *A pythonic python wrapper around FFTW*. [Online]. Available: https://pyfftw.readthedocs.io/en/latest/ (visited on 11/17/2022).

[60] S. Johnson and M. Frigo, "Implementing FFTs in Practice," in *Fast Fourier Transforms*, OpenStax CNX, 2012. [Online]. Available: https://cnx.org/contents/ba55ed41-b37b-45bd-89c9-e6b67725401e@15/Implementing-FFTs-in-Practice (visited on 11/17/2022).

[61] D. L. Jones and I. Selesnick, "Goertzel's Algorithm," in *The DFT, FFT, and Practical Spectral Analysis - OpenStax CNX*, Rice University, Houston, Texas: Connexions, 2007. [Online]. Available: https://cnx.org/contents/0sbTkzWQ@2.2:kw4ccwOo/Goertzel-s-Algorithm (visited on 12/14/2022).

[62] H. Hassanieh, P. Indyk, D. Katabi, and E. Price, "Simple and Practical Algorithm for Sparse Fourier Transform," in *Proceedings of the Twenty-Third Annual ACM-SIAM Symposium on Discrete Algorithms*, Society for Industrial and Applied Mathematics, 2012, pp. 1183–1194, ISBN: 978-1-61197-210-8 978-1-61197-309-9. DOI: 10.1137/1.9781611973099.93.

[63] F. Harris, *Multirate Signal Processing for Communication Systems*. Upper Saddle River, N.J: Prentice Hall PTR, 2004, ISBN: 978-0-13-146511-4.

[64] H. A. Haus and J. R. Melcher, *Electromagnetic Fields and Energy*. Prentice Hall Englewood Cliffs, NJ, 1989, vol. 107.

[65] C. L. W. Sonntag, M. Sprée, E. A. Lomonova, J. L. Duarte, and A. J. A. Vandenput, "Accurate Magnetic Field Intensity Calculations for Contactless Energy Transfer Coils," in *Proceedings of the 16th International Conference on the Computation of Electromagnetic Fields, Achen, Germany*, 2007, pp. 1–4.

[66] P. K. Sharma and S. K. Guha, "Transmission of time varying magnetic field through body tissue," *Journal of Biological Physics*, vol. 3, no. 2, pp. 95–102, 1975, ISSN: 1573-0689. DOI: 10.1007/BF02309611.

[67] K. O'Donoghue *et al.*, "Catheter Position Tracking System Using Planar Magnetics and Closed Loop Current Control," *IEEE Transactions on Magnetics*, vol. 50, no. 7, pp. 1–9, 2014, ISSN: 0018-9464. DOI: 10.1109/tmag.2014.2304271.

[68] M. Rustom and C. Sideris, "Wireless Frequency-Division Multiplexed 3D Magnetic Localization for Low Power Sub-mm Precision Capsule Endoscopy," in *2022 IEEE Custom Integrated Circuits Conference (CICC)*, 2022, pp. 01–02. DOI: 10.1109/CICC53496.2022.9772802.

[69] MathWorks, *Symbolic Math Toolbox*. [Online]. Available: https://uk.mathworks.com/products/symbolic.html (visited on 11/11/2022).

[70] A. Plotkin, V. Kucher, Y. Horen, and E. Paperno, "A New Calibration Procedure for Magnetic Tracking Systems," *IEEE Transactions on Magnetics*, vol. 44, no. 11, pp. 4525–4528, 2008, ISSN: 1941-0069. DOI: 10.1109/TMAG.2008.2003056.

[71] A. J. Chung, P. J. Edwards, F. Deligianni, and G.-Z. Yang, "Freehand Cocalibration of Optical and Electromagnetic Trackers for Navigated Bronchoscopy," in 2004, pp. 320–328. DOI: 10.1007/978-3-540-28626-4_39.

[72] H. A. Jaeger, "Creating an open source electromagnetic tracking platform," Ph.D. dissertation, University College Cork, 2018.

[73] D. D. Frantz, A. D. Wiles, S. E. Leis, and S. R. Kirsch, "Accuracy assessment protocols for electromagnetic tracking systems," *Physics in Medicine and Biology*, vol. 48, no. 14, pp. 2241–2251, 2003, ISSN: 0031-9155, 1361-6560. DOI: 10.1088/0031-9155/48/14/314.

[74] J. E. Dennis and R. B. Schnabel, *Numerical Methods for Unconstrained Optimization and Nonlinear Equations* (Classics in Applied Mathematics 16). Philadelphia: Society for Industrial and Applied Mathematics, 1996, ISBN: 978-0-89871-364-0.

[75] F. Vanden Berghen, "Constrained, non-linear, derivative-free parallel optimization of continuous, high computing load, noisy objective functions.," Ph.D. dissertation, Université Libre de Bruxelles, Faculté des Sciences, Bruxelles, 2004.

[76] MathWorks, *Solve nonlinear least-squares (nonlinear data-fitting) problems*. [Online]. Available: https://uk.mathworks.com/help/optim/ug/lsqnonlin.html (visited on 01/18/2023).

[77] C. R. Harris *et al.*, "Array programming with NumPy," *Nature*, vol. 585, no. 7825, pp. 357–362, 2020. DOI: 10.1038/s41586-020-2649-2.

[78] P. Virtanen *et al.*, "SciPy 1.0: Fundamental algorithms for scientific computing in python," *Nature Methods*, vol. 17, pp. 261–272, 2020. DOI: 10.1038/s41592-019-0686-2.

[79] G. Guennebaud, B. Jacob, *et al.*, *Eigen v3*, 2010. [Online]. Available: http://eigen.tuxfamily.org (visited on 01/18/2023).

[80] Grupo Premo, *VR Sensors - Rx EM Motion Tracking*. [Online]. Available: https://www.grupopremo.com/en/613-vr-sensors-rx-em-motion-tracking- (visited on 01/23/2023).

[81] A. Brown, A. Uneri, T. D. Silva, A. Manbachi, and J. H. Siewerdsen, "Design and validation of an open-source library of dynamic reference frames for research and education in optical tracking," *Journal of Medical Imaging*, vol. 5, no. 2, 2018, ISSN: 2329-4302. DOI: 10.1117/1.JMI.5.2.021215.

[82] *Polaris Vega - NDI*. [Online]. Available: https://www.ndigital.com/products/polaris-vega/ (visited on 03/30/2022).

[83] A. Lasso, T. Heffter, A. Rankin, C. Pinter, T. Ungi, and G. Fichtinger, "PLUS: Open-Source Toolkit for Ultrasound-Guided Intervention Systems," *IEEE Transactions on Biomedical Engineering*, vol. 61, no. 10, pp. 2527–2537, 2014, ISSN: 1558-2531. DOI: 10.1109/TBME.2014.2322864.

[84] A. Tabb and K. M. A. Yousef, "Solving the Robot-World Hand-Eye(s) Calibration Problem with Iterative Methods," *Machine Vision and Applications*, vol. 28, no. 5-6, pp. 569–590, 2017, ISSN: 0932-8092, 1432-1769. DOI: 10.1007/s00138-017-0841-7. arXiv: 1907.12425 [cs].

[85] MathWorks, *Solve systems of linear equations xA = B*. [Online]. Available: https://uk.mathworks.com/help/matlab/ref/mrdivide.html (visited on 09/14/2022).

[86] O. Sorkine-Hornung and M. Rabinovich, "Least-Squares Rigid Motion Using SVD," p. 5, 2017.

[87] Makeblock, *XY Plotter Robot Kit*. [Online]. Available: https://web.archive.org/web/20200921140306/https://www.makeblock.com/project/xy-plotter-robot-kit (visited on 01/24/2023).

[88] TRINAMIC Motion Control, *TMC2208*, 2019. [Online]. Available: https://www.trinamic.com/fileadmin/assets/Products/ICs_Documents/TMC220x_TMC2224_datasheet_Rev1.09.pdf (visited on 01/24/2023).

[89] Arduino Reference, *AccelStepper*. [Online]. Available: https://www.arduino.cc/reference/en/libraries/accelstepper/ (visited on 01/24/2023).

[90] S. Su *et al.*, "Investigation of the Relationship Between Tracking Accuracy and Tracking Distance of a Novel Magnetic Tracking System," *IEEE Sensors Journal*, vol. 17, no. 15, pp. 4928–4937, 2017, ISSN: 2379-9153. DOI: 10.1109/JSEN.2017.2713886.

[91] M. A. Ragolia, F. Attivissimo, A. D. Nisio, and A. Maria Lucia Lanzolla, "Evaluation of Position RMS Error from Magnetic Field Gradient for Surgical EM Tracking Systems," in *2020 IEEE International Instrumentation and Measurement Technology Conference (I2MTC)*, 2020, pp. 1–6. DOI: 10.1109/I2MTC43012.2020.9128837.

[92] International Organization for Standardization, *ISO 5725-1:1994(en), Accuracy (trueness and precision) of measurement methods and results — Part 1: General principles and definitions*. [Online]. Available: https://www.iso.org/obp/ui/#iso:std:iso:5725:-1:ed-1:v1:en (visited on 01/25/2023).

[93] MathWorks, *Memory information - MATLAB memory*. [Online]. Available: https://uk.mathworks.com/help/matlab/ref/memory.html (visited on 01/23/2023).

[94] G. Rodola, *Psutil: Cross-platform lib for process and system monitoring in Python.* [Online]. Available: https://github.com/giampaolo/psutil (visited on 01/23/2023).

[95] NDI, *Aurora - NDI's premier electromagnetic tracking solution.* [Online]. Available: https://www.ndigital.com/electromagnetic-tracking-technology/aurora/ (visited on 10/07/2022).

[96] E. Wilson, Z. Yaniv, D. Lindisch, and K. Cleary, "A buyer's guide to electromagnetic tracking systems for clinical applications," in *Medical Imaging 2008: Visualization, Image-Guided Procedures, and Modeling*, vol. 6918, SPIE, 2008, pp. 777–788. DOI: 10.1117/12.770509.

[97] Z. Yaniv, E. Wilson, D. Lindisch, and K. Cleary, "Electromagnetic tracking in the clinical environment," *Medical Physics*, vol. 36, no. 3, pp. 876–892, 2009, ISSN: 00942405. DOI: 10.1118/1.3075829.

[98] A. Sorriento *et al.*, "Optical and Electromagnetic Tracking Systems for Biomedical Applications: A Critical Review on Potentialities and Limitations," *IEEE Reviews in Biomedical Engineering*, vol. 13, pp. 212–232, 2020, ISSN: 1941-1189. DOI: 10.1109/RBME.2019.2939091.

[99] E. Lugez, H. Sadjadi, D. R. Pichora, R. E. Ellis, S. G. Akl, and G. Fichtinger, "Electromagnetic tracking in surgical and interventional environments: Usability study," *International Journal of Computer Assisted Radiology and Surgery*, vol. 10, no. 3, pp. 253–262, 2015, ISSN: 1861-6410. DOI: 10.1007/s11548-014-1110-0.

Chapter 4

Magnetic distortion detection and compensation techniques

This chapter explores the limitations of conventional methods for characterising magnetic fields in EMT and presents a novel field modelling approach based on a virtual distribution of magnetic dipole sources. The technique enables the correction of systematic errors and real-time distortion compensation. Furthermore, novel EMT distortion detection methods are proposed.

The modelling technique is introduced in Section 4.1 and its effectiveness in correcting systematic errors in the ANSER EMT field model under standard conditions is demonstrated in Section 4.2. Magnetic shielding is analysed in Section 4.3 for the reduction of magnetic distortions passively. The new technique is employed to model the shielded field generator, and distortion reduction in a clinical environment using shielding is obtained. Systematic error correction and passive shielding are *offline* solutions, which need implementation before the operation of the system.

Parts of this chapter are based on M. Cavaliere and P. Cantillon-Murphy, "Intraoperative compensation of magnetic field distortions for fluoroscopic and electromagnetic hybrid navigation," *International Journal of Computer Assisted Radiology and Surgery*, vol. 17, pp. 1717–1721, 2022 [1], M. Cavaliere *et al.*, "Magnetic Model Calibration and Distortion Compensation for Electromagnetic Tracking in a Clinical Environment," *IEEE Transactions on Magnetics*, vol. 59, no. 7, pp. 1–12, 2023 [2], and M. Cavaliere and P. Cantillon-Murphy, "Enhancing electromagnetic tracking accuracy in medical applications using pre-trained witness sensor distortion models," *International Journal of Computer Assisted Radiology and Surgery*, 2023 [3].

However, for dynamic distortions, passive methods are not effective. To address this problem, Section 4.4 proposes novel distortion detection techniques to quantify metallic distortion in real time. Therefore, a *semi-online* approach is enabled where the user can manually intervene if the tracking is detected to be inaccurate. The detection techniques are tested by evaluating the distortion caused by a CT scanner machine.

Finally, in Section 4.5, two *online* methods are presented to compensate for the distortion introduced by a fluoroscopy imaging system in a clinical environment. In the first case, an array of triaxial sensors is used to measure the magnetic field at known positions, and a magnetic model is created in real time using the technique proposed at the beginning of the chapter. The second approach involves characterising the distortion variation at a witness point for different positions of a distorter. In this way, the distortion is used to estimate the distorter's position in real time, and an updated magnetic model is interpolated from previously characterised field maps.

4.1 Model based on virtual dipole sources

As will be seen in Section 4.4.4, the presence of conductive or ferromagnetic materials modifies the magnetic field shape causing deviation from the ideal model. Moreover, even under standard conditions, systematic tracking errors can be due to the inability of theoretical models to describe the real magnetic field, as demonstrated in Section 3.6. Either case can be considered a magnetic distortion in the sense that the magnetic model used for tracking is different from the actual field measured by the sensor.

As discussed in Section 2.4.2, volume characterisation can effectively be used to reduce static distortion and systematic errors. However, this task is time-consuming, unsuitable in dynamic distortion scenarios, and challenging to integrate into the clinical workflow. Furthermore, characterisation is impossible during a procedure because the region of interest (ROI) is often located inside the patient's body, making access to it impossible.

A magnetic field model consistent with physical principles may be used to overcome some of the limitations of characterisation. Physical constraints reduce the number of degrees of freedom and the amount of data required to build the model. For example, in a system where magnetic dipoles represent the emitter coils, the free calibration parameters might be the position, orientation, and magnetic moment of the dipoles, like in a reverse tracking problem [4, 5]. However, this approach cannot always capture local variations of the tracking error due to the limits of the simplified model, especially in the proximity to the field generator, or due to the presence of static distorters.

In this section, a novel technique is proposed to create a general magnetic model that can adapt to different distortion scenarios. The model is based on the field generated by a virtual distribution of magnetic dipoles. In this way, it is not required for the characterisation data points to lie on precise grids, homogeneously distributed within the ROI or to use orthogonal three-axis sensors because the model calibration is achieved by using the real field measurements to fit the free parameters of the structured magnetic model. Moreover, the limited number of fitting parameters can help reduce random measurement errors.

The quasi-static magnetic field in a region free of current sources can be expressed as a gradient of a harmonic scalar potential [6, 7]. The potential within the volume is uniquely defined by the boundary conditions on the surface enclosing the domain. These conditions could also be represented by a magnetic dipole density on the same surface [8–10].

The dipole density is equivalent to a distribution of surface currents [11, 12]. However, when a finite number of field measurements are sampled from the magnetic field in the volume of interest, it is impossible to find a continuous dipole density. The surface must be discretised in a finite number of magnetic dipoles.

If the position of the sources of the magnetic field and the distorters is known, it is convenient to place the magnetic dipoles at these locations. In this way, the electric current distribution that generates the target magnetic flux density can be modelled more accurately. The approximation works better if the currents are far from the ROI.

Using this approach, the magnetic field can be expressed as the sum of the fields generated by a set of magnetic dipoles. The approximation can be seen as a series expansion, where the field of the dipoles constitutes basis functions that are linearly summed to fit the field samples.

The magnetic flux density, $\mathbf{B}$ [T], generated by a magnetic dipole is expressed as follows:

$$\mathbf{B}(\mathbf{r}) = \frac{\mu_0}{4\pi}\left[\frac{3\left(\mathbf{m}\cdot\mathbf{u_r}\right)\mathbf{u_r}-\mathbf{m}}{R^3}\right] \tag{4.1}$$

where $\mathbf{m} = X\cdot\mathbf{u_m}\,[\mathrm{A}\cdot\mathrm{m}^2]$ is the magnetic moment, and $\mathbf{u_m}$ and $\mathbf{u_r}$ are unit vectors. The position vector $\mathbf{r} = R\cdot\mathbf{u_r}\,[\mathrm{m}]$ identifies the evaluation point relative to the dipole position. Magnitudes $X\,[\mathrm{A}\cdot\mathrm{m}^2]$ and $R\,[\mathrm{m}]$ are scalars.

If the dipole magnitude X is isolated, Equation 4.1 can be rewritten as follows:

$$\mathbf{B}(\mathbf{r}) = \frac{\mu_0}{4\pi}\left[\frac{3\left(\mathbf{u_m}\cdot\mathbf{u_r}\right)\mathbf{u_r}-\mathbf{u_m}}{R^3}\right]X = f(\mathbf{r})\,X \tag{4.2}$$

Considering the magnetic sensor as a uniaxial inductive coil oriented along the unit vector $\mathbf{n}$, the measured field component is parallel to the sensor direction:

$$V_s(\mathbf{r},\mathbf{n}) = C_s\,\mathbf{n}^T\cdot\mathbf{B}(\mathbf{r}) \tag{4.3}$$

where C_s includes all the physical constants associated with the sensor gain, the magnetic field frequency, and the signal acquisition channel, as explained in Section 3.2.3.2.

Model training involves the collection of P sensor measurements at different locations, $\mathbf{r}^i$, and with different sensor orientations, $\mathbf{n}^i$. The proposed method approximates the unknown magnetic field in the ROI as the field due to a set of N virtual magnetic dipoles placed at positions $\mathbf{r}^j$. According to this model, the i^{th} sensor measurement is approximated as a sum of N contributions each calculated as per equations Equations 4.2

and 4.3:

$$\begin{aligned} V_s^i\left(\mathbf{r}^i, \mathbf{n}^i\right) &= \mathbf{n}^{i\,T} \cdot \sum_{j=1}^{N} f\left(\mathbf{r}^i - \mathbf{r}^j\right) X^j \\ &= \sum_{j=1}^{N} f\left(\mathbf{n}^i, \mathbf{r}^{ij}\right) X^j \end{aligned} \tag{4.4}$$

where $\mathbf{r}^{ij} = \mathbf{r}^i - \mathbf{r}^j$ is the relative position.

Equation 4.4 can be rewritten in matrix form by defining $\mathbf{M}$ as the P by N coupling matrix, whose entries M_{ij} are given by $f\left(\mathbf{n}^i, \mathbf{r}^{ij}\right)$; $\mathbf{X} = [\cdots X^j \cdots]^T$, with $1 \leq j \leq N$, as the vector including the magnitudes of the dipoles; and $\mathbf{V_s} = [\cdots V_s^i \cdots]^T$, with $1 \leq i \leq P$, as the vector of field measurements. In this way, Equation 4.4 becomes:

$$\mathbf{V_s} = \mathbf{M} \cdot \mathbf{X} \tag{4.5}$$

which is solved for the dipole magnitudes that best fit the field measurements in a least-squares sense. When $P > N$, Equation 4.5 is an overdetermined linear system, which can be solved using typical methods for linear least-squares problems.

If there is no assumption on the orientations of the dipoles, the method can be extended by considering the three dipole components as independent dipoles. If the dipoles' positions are not fixed, they become part of the optimisation process as independent variables in matrix $\mathbf{M}$. In this case, the problem is non-linear and can be solved using iterative methods. It is worth mentioning that the global problem where the magnetic flux density is calibrated in the ROI can be decomposed into smaller local problems where $\mathbf{X}$ is optimised for different sub-regions.

In this work, the position and orientation of the virtual dipole sources were defined in advance, and Equation 4.5 was solved using the *backslash* operator in MATLAB, \, or *mldivide* function [13]:

$$\mathbf{X} = \mathbf{M} \backslash \mathbf{V_s} \tag{4.6}$$

which returns the individual magnitudes of the virtual dipole sources.

4.2 Compensated model for ANSER EMT

The method presented in Section 4.1 was tested in a laboratory setting to demonstrate its capability to fit real field measurements and to predict new values. In this experiment, a new analytical model was created for each emitter coil of the ANSER EMT $30 \times 30\,\text{cm}^2$ field generator. The model is based on a virtual distribution of magnetic dipoles whose magnitude was trained on real field measurements.

4.2.1 Methods

Tools *C* and *T* of Figure 4.1a were used for characterisation and tracking, respectively, to demonstrate that the magnetic model is generally independent of the sensor used as a tracking marker in the final application.

The magnetic sensors were moved in two directions by the robotic actuator presented in Section 3.4, as shown in Figure 4.1b. Tolerances of the motorised system did not add to the measurement uncertainty because the Polaris Vega optical system (Northern Digital Inc., Waterloo, Canada) introduced in Section 3.3 was used for pose reference.

The optical accuracy is rated as 0.15 mm RMS [14], which is sufficiently smaller than the EMT errors in the order of millimetres demonstrated in Section 7.4.3. In any case, as the same setup is used in this experiment for the EMT training and testing phases, any possible systematic or registration errors of the optical system are automatically incorporated and compensated by the data-driven magnetic model.

Tool *C* was utilised to collect triaxial measurements on a $31 \times 31 \times 3$ grid of points in a volume of $30 \times 30 \times 6\,\text{cm}^3$ located approximately 15 cm above the planar field generator, leading to a total of $P = 3 \times 31 \times 31 \times 3 = 8649$ measurements used for model training. The position of the virtual dipole sources was initialised in proximity to the actual position of the field generator, and the same virtual dipole distribution was used for all emitter coils.

The optimal number of dipoles must be large enough to adequately model the real magnetic field but sufficiently small to avoid over-fitting and allow accurate interpolation and extrapolation at different positions.

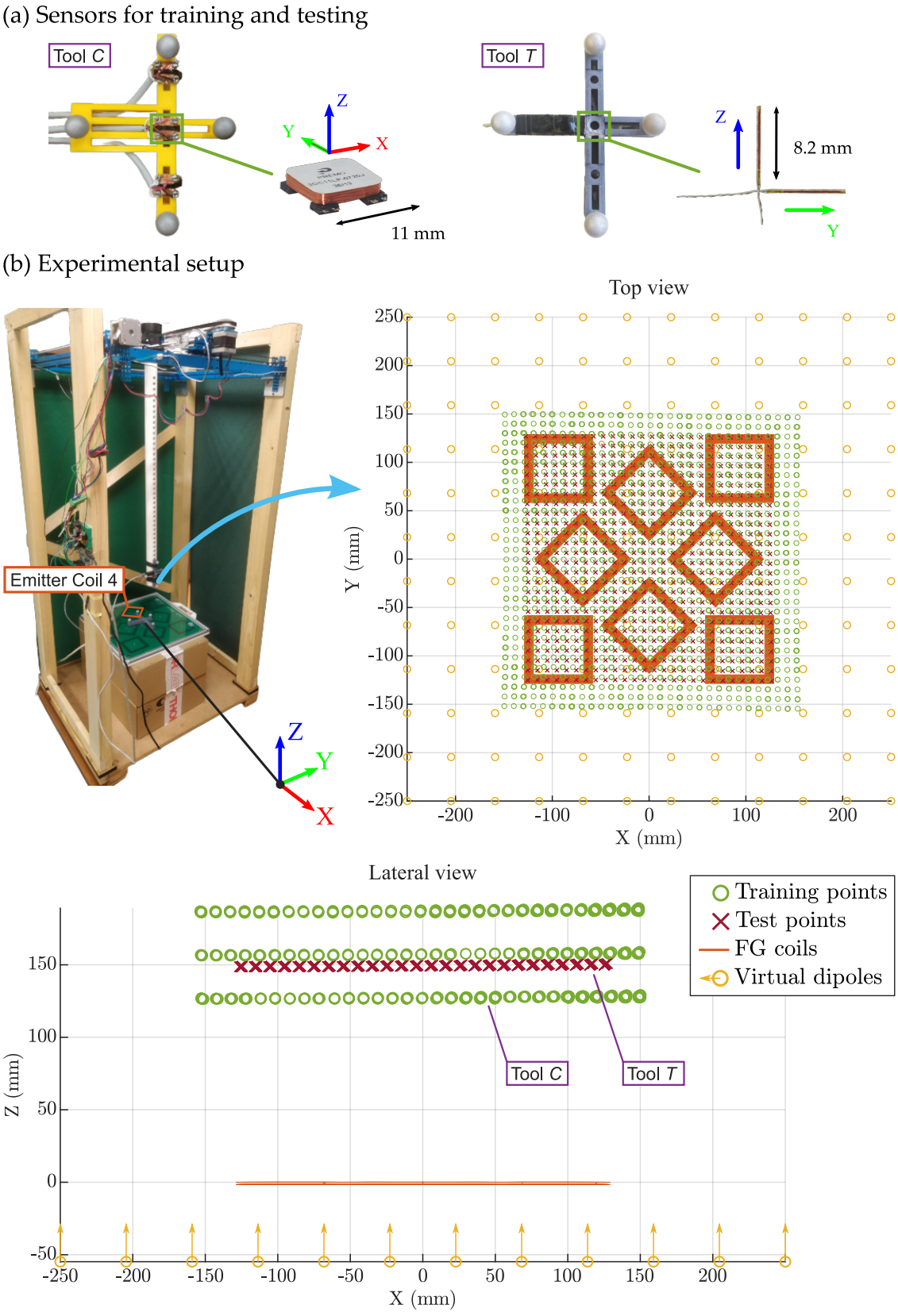


Figure 4.1: (a) Sensors used for characterisation (tool C) and tracking (tool T). (b) Experimental setup to characterise a volume within the ROI.

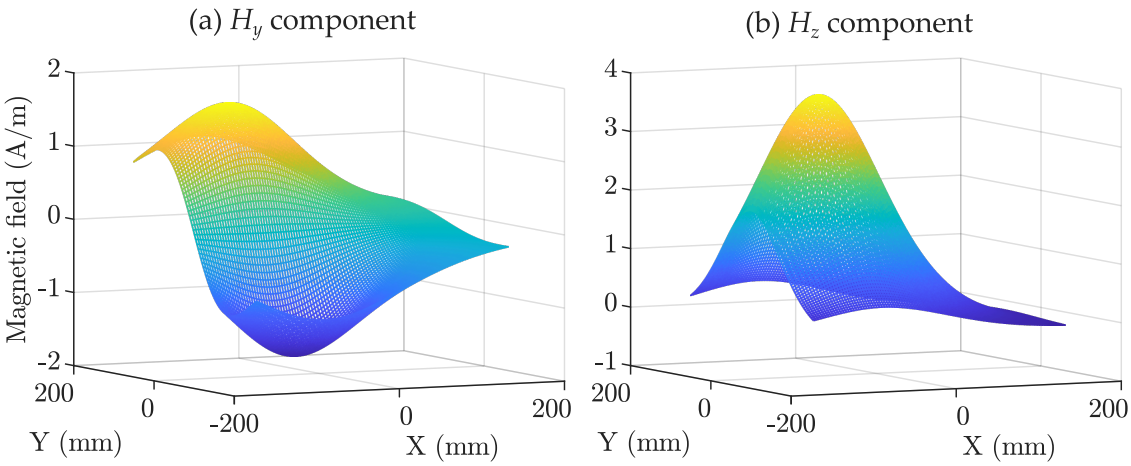


Figure 4.2: Data-driven magnetic field model, fit results. (a) Y component and (b) Z component of the magnetic field modelled for emitter coil 4, which is defined in Figure 4.1. The values are captured on a horizontal plane located 150 mm above the field generator.

In theory, each emitter coil could be modelled by a different dipole distribution, with higher density in the proximity to the coil position. However, using the same array of virtual dipoles for the eight coils of the field generator allows solving Equation 4.6 in a single step. In this case, V results as an $N \times 8$ matrix where every column is the vector of the dipole moments that optimally model the correspondent emitter coil.

The number of dipoles was determined by optimising the fitting performance at a selection of validation points randomly selected from the training set and not used for training. Visual inspection of the magnetic model obtained, such as the plot shown in Figure 4.2, was also used to determine if the real magnetic field could be adequately modelled while avoiding over-fitting. After determining the optimal number of $N = 12 \times 12 = 144$ dipoles, the fit was calculated as per Equation 4.6.

To visually demonstrate the magnetic model generated using the proposed technique, Figure 4.2 shows the Y and Z components of the magnetic field from emitter coil 4, defined in Figure 4.1. The values are taken from the horizontal plane at 150 mm above the field generator.

The EMT trueness of the new data-driven model was evaluated on a plane approximately at the centre of the training grid used to build the model, as shown in Figure 4.1. A 2D grid of 26×26 points was collected

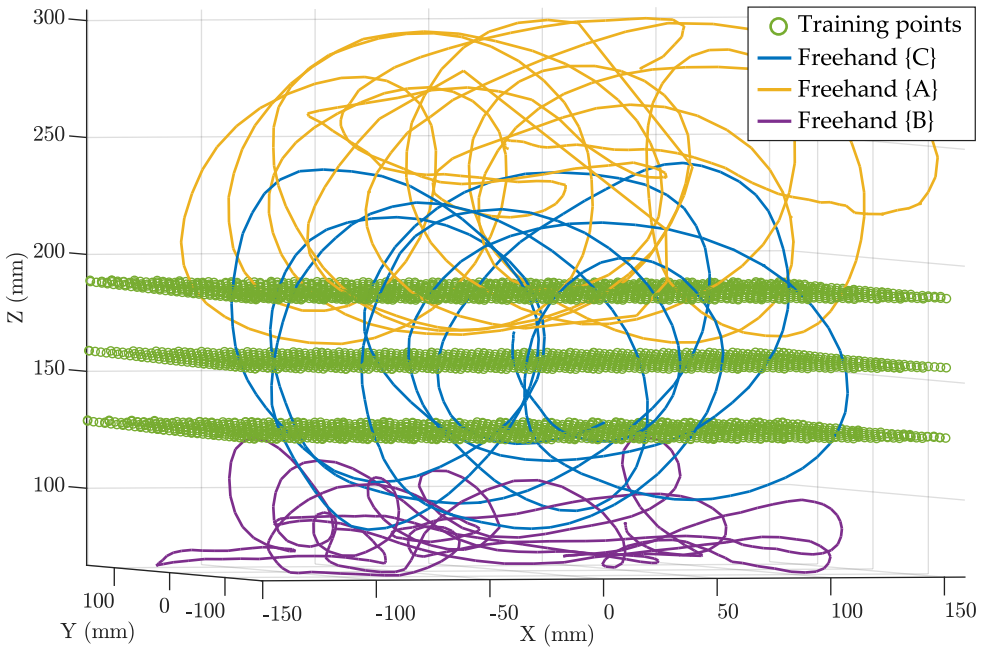


Figure 4.3: Trajectories of the three freehand tests performed in the central region, {C}, above {A}, and below {B} the training points used to build the data-driven magnetic model.

on a plane of $25 \times 25\,\text{cm}^2$, using tool T with the two clinical-size sensors horizontally and vertically oriented relative to the field generator along the Y and Z axes defined in Figure 4.1, respectively.

Three dynamic EMT tests were performed by freely moving one sensor within the region of interest (ROI). One test was centred around the volume characterised, region {C}. The two other tests were localised in the regions above, {A}, and below, {B}, respectively, relative to the grid of training points. The three random trajectories are shown in Figure 4.3.

4.2.2 Static tracking results

The results obtained with the new compensated model were compared to those obtained using the theoretical model based on approximating the emitter coils as sets of straight filaments and using the Biot-Savart solution, introduced in Section 3.2.3.

The static tracking test showed an accuracy improvement using the new data-driven model based on virtual dipole sources with respect to the

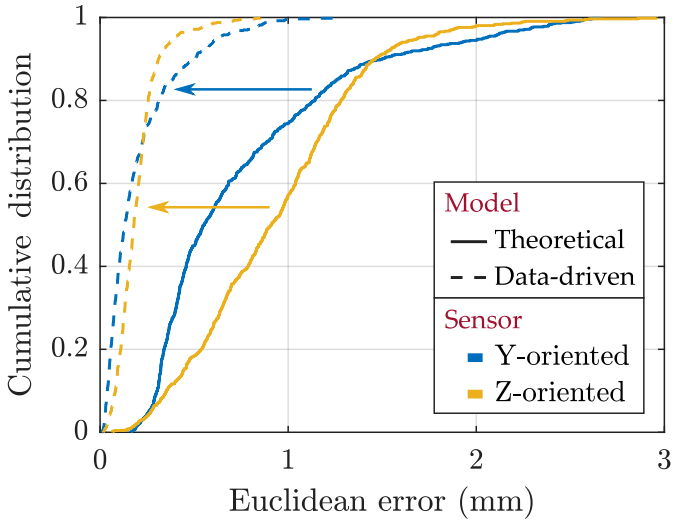


Figure 4.4: Cumulative distribution of EMT position errors obtained in a distortion-free environment with the existing theoretical model and the new data-driven model for the static tracking measurements indicated in Figure 4.1. Two commercial miniature sensors, Y and Z-oriented (horizontal and vertical), were placed on a $25 \times 25\,\text{cm}^2$ grid approximately 15 cm above the field generator.

previous analytical model. Position and orientation tracking errors were calculated relative to the optical reference using the Euclidean distance and the absolute angular difference, as discussed in Section 3.6.1.

Figure 4.4 shows the empirical cumulative distribution function (CDF) of the position error at the static test points of Figure 4.1 for the two models under test and the two sensors horizontally and vertically oriented, along Y and Z axes, respectively.

Statistical error metrics are summarised in Table 4.1, where the root-mean-square error (RMSE), mean error (ME), the median or 50 percentile (PRC50), and the 95 percentile (PRC95) are reported.

It can be observed that the orientation error is highly correlated to the position error. This result can be explained by the nature of the tracking algorithm presented in Section 3.2.4, where a cost function is minimised to simultaneously find the five degrees of freedom of the uniaxial sensor.

Using the novel magnetic field model, the position RMSE decreased from 0.93 mm to 0.28 mm (−69%) for the Y-oriented sensor and from

Table 4.1: Tracking test results using the new analytical data-driven model, compared to the current ANSER EMT model based on Biot-Savart's law. The position error of this test is also visualised in Figure 4.4.

Model	Biot-Savart		Data-driven	
Error	Horizontal mm / deg	Vertical mm / deg	Horizontal mm / deg	Vertical mm / deg
RMSE	0.93 / 0.61	1.03 / 0.80	0.28 / 0.23	0.23 / 0.21
ME	0.76 / 0.45	0.93 / 0.71	0.20 / 0.20	0.20 / 0.17
PRC50	0.55 / 0.31	0.91 / 0.67	0.13 / 0.17	0.18 / 0.15
PRC95	2.04 / 1.43	1.69 / 1.32	0.62 / 0.45	0.39 / 0.42

1.03 mm to 0.23 mm (-78%) for the Z-oriented sensor. The orientation RMSE decreased by -62% and -73% in the two cases, respectively.

4.2.3 Freehand trajectory results

Figure 4.5 shows the position error CDF obtained using the two models during the three freehand tests represented by Figure 4.3. As expected, the novel data-driven model outperformed the theoretical model when the sensor was moved in the volume centred around the characterisation grid, region {C}.

Above the training grid, region {A}, the data-driven model gave smaller errors for some points and larger for others, compared to the theoretical model. This outcome can be explained by the trajectory path followed by the sensor during this test, which sometimes entered the characterised region, as shown in Figure 4.3.

In the freehand test below the training grid, region {B}, the theoretical model demonstrated a higher accuracy. In this case, the data-driven model caused EMT errors as large as 8 mm, while the maximum error obtained with the theoretical model was below 3.5 mm.

4.2.4 Discussion

The new data-driven model for ANSER EMT field generator demonstrated a higher tracking accuracy within the region characterised. In regions

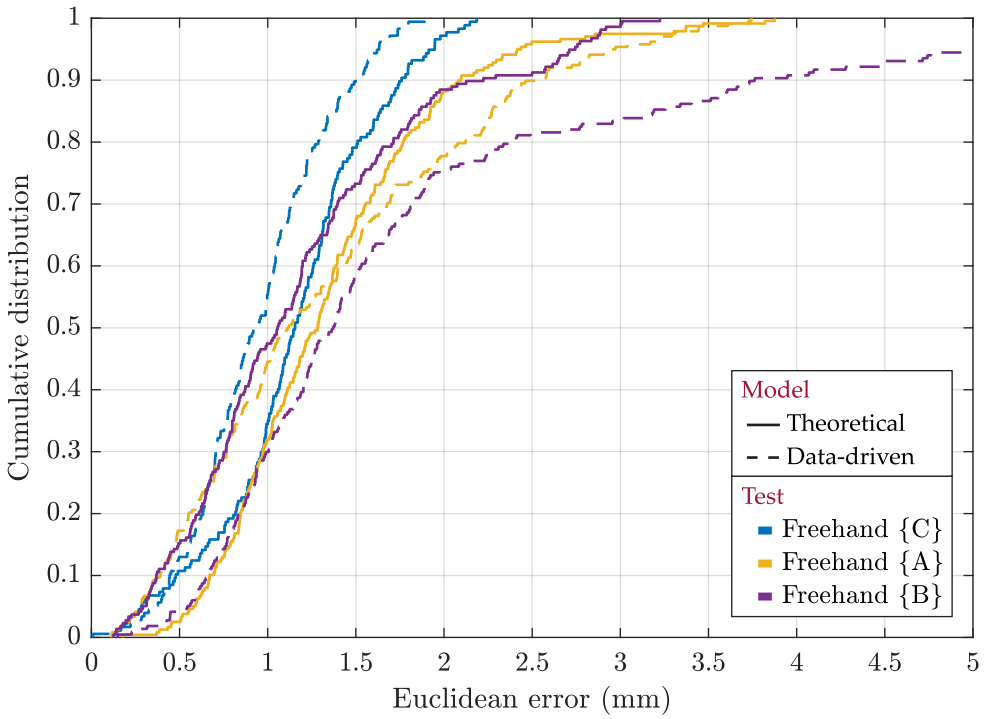


Figure 4.5: Cumulative distribution of EMT position errors obtained in a distortion-free environment with the theoretical model and the compensated data-driven model for freehand trajectory tracking as represented in Figure 4.3. One sensor was moved freehand within three regions, respectively centred {C}, above {A}, and below {B} the training grid.

outside the compensated volume, tracking was still possible using the new model but with lower accuracy. Therefore, before updating the existing ANSER EMT model, the calibrated model must be expanded to cover a larger volume. Nevertheless, this result is a significant improvement compared to traditional characterisation methods, which require tracking within the region where the calibration data was collected [15].

The method presented in this section can be easily extended to larger volumes and different field generators. The requirements are sampling enough training points and optimising the virtual dipole distribution that best fits the real data. Suppose a single dipole distribution is not effective in accurately modelling the real magnetic field. In this case, different distributions might be used which are specific to each emitter coil, or the region of interest (ROI) might be decomposed into sub-regions.

This section demonstrated the effectiveness of the proposed modelling method within a portion of the ROI. The complete ROI characterisation is time-consuming and specific to the field generator, the surrounding environment, and the field frequencies. Therefore, it should be performed once the system is configured and installed in the final application environment.

4.3 Magnetic shielding

Planar magnetic shielding can typically be used to reduce the effect of metallic objects under the field generator [16–18]. As demonstrated in Figure 4.6, low-frequency AC magnetic fields, such as those used in the ANSER EMT system, can be shielded by conductive or high-permeability materials or a combination of both.

In the first case, the magnetic flux crossing the conductive shield induces eddy currents that oppose the flux variation, effectively nullifying the magnetic field component entering the shield. In the second case, the material with high permeability provides a low-reluctance path, redirecting the magnetic field lines within the shield and preventing them from crossing through it.

The magnetic flux density visualised in Figure 4.6 was simulated using the open-source software Finite Element Method Magnetics (FEMM) [19]. A 3D axisymmetric finite element analysis (FEA) was chosen to address the problem. The planar transmitter coil was modelled comprising 25 turns of 10 AWG Copper wire, with an inner diameter of 5 cm, an outer diameter of 7 cm, and 2 mm in thickness. Such geometry resembles the coils of the ANSER EMT field generator, apart from the square footprint, which cannot be represented in the axisymmetric domain. The AC electric current was set to 1 A in amplitude and 25 kHz in frequency.

The unshielded case (a) is compared with different shielding materials placed under the emitter coil. In particular, plates of 5 mm in thickness were considered made of: (b) pure aluminium, conductive and not magnetic; (c) pure iron, conductive and ferromagnetic; (d) mu-metal, not conductive and ferromagnetic; (e) mu-metal for the upper layer and

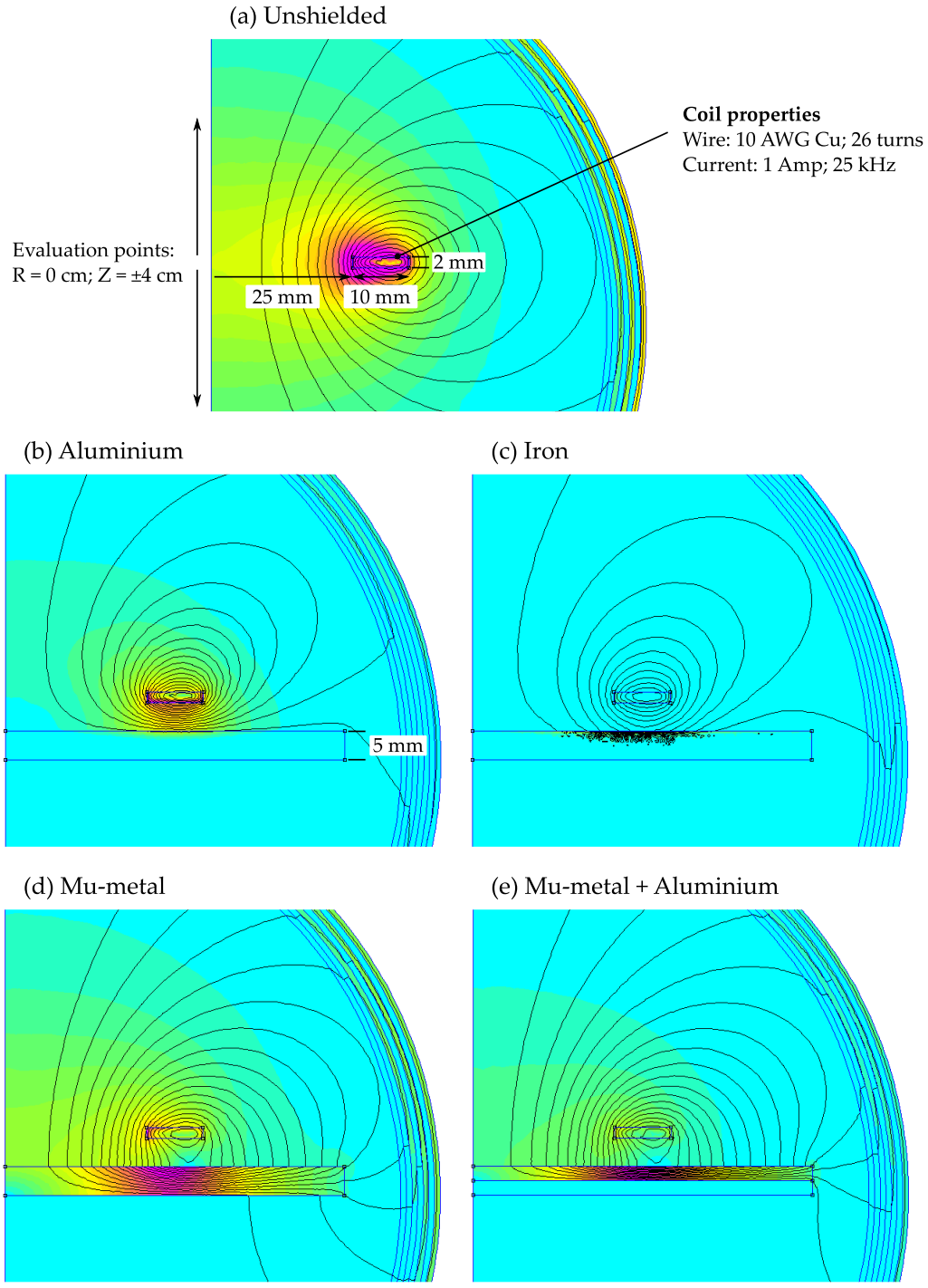


Figure 4.6: FEA simulation results showing the magnetic flux magnitude for different shielding materials placed under an emitter coil. Shielding effectiveness is reported in Table 4.2.

Table 4.2: Effectiveness of the shielding solutions shown in Figure 4.6. The magnetic flux density magnitude is reported, calculated 4 cm above and below the coil plane. The ratio between the two values is also expressed in decibels.

	B (μT) [above]	**B** (μT) [below]	Attenuation (dB)
Unshielded	123.983	123.983	0
Aluminium	55.131	0.6835	-38
Iron	80.132	2.1036	-32
Mu-metal	176.27	21.17	-18
Mu-metal + Al.	171.9	5.048	-31

aluminium for the lower layer, where each layer measured 2.5 mm in thickness.

The shielding effectiveness was evaluated by comparing the magnetic flux density magnitude at two points on the coil axis, placed 4 cm above and below the coil plane, respectively. The values are reported in Table 4.2 for the different shielding configurations simulated, where the ratio between the values above and below is expressed in decibels.

Table 4.2 shows that the best shielding results are obtained utilising the aluminium shield, with an attenuation of -38 dB. However, this comes at the cost of a lower magnetic signal above the transmitter coil, which decreases from 124 μT to 55 μT, leading to increased power consumption and ohmic heating if the same signal magnitude is maintained relative to the unshielded case. Similar considerations are valid for the conductive iron plate, where eddy currents that oppose the magnetic field variation are generated in the shield.

This problem is solved by the mu-metal material, which is not conductive. In this case, the ferromagnetic behaviour increases the magnetic flux density to 176 μT in the region of interest. Nevertheless, the shielding capacity is less effective, resulting in -18 dB attenuation.

The best results are obtained with a compromise between signal damping and shielding effectiveness, using the combination of two materials. The first layer of high-permeability material helps to increase the field magnitude above the emitter coil and partially attenuates the field be-

Table 4.3: Parameters of the two square shielding plates used in the experiment of Section 4.3.1.

Material	Conductivity (MS/m)	Relative permeability	Edge (mm)	Thickness (mm)
Aluminium	35	1	250	1
Mu-metal	1.8	$> 100k$	250	1

low it. The lower conductive layer further reduces any remaining field components to improve the shielding performance.

4.3.1 Shielded magnetic field generator model

The presence of a magnetic shield produces a distortion of the magnetic field, which must be accurately modelled prior to sensor tracking. In this experiment, the effects of aluminium and mu-metal planar shields placed 5 mm below the field generator are studied. The parameters of the two shielding plates are detailed in Table 4.3. Furthermore, the fitting and interpolation performance of the modelling method proposed in Section 4.1 is evaluated considering the distortion caused by the metallic shielding materials.

As will be seen in this section, the eddy currents appearing in the shields introduce a quadrature component to the AC magnetic field. The sum of out-of-phase vectors results in magnetic fields that rotate in ellipses at every point within the ROI. The three-axis coils of tool *C* showed non-linear behaviour in this case, which has to be ascribed to the effect of the rotating field vectors in the larger ferromagnetic cores, causing cross-talk between the orthogonal coils. For this reason, tool *T* was used in this experiment, and the two uniaxial sensors in orthogonal directions provided the information to model the 3D magnetic field vector.

A grid of points was sampled at the approximate height of 15 cm above the field generator, as shown in Figure 4.7. The measured data was split into a set of training points used to calculate the virtual dipole sources distribution as described in Section 4.1 and a set of test points for independent evaluation. The distribution of the virtual dipole sources

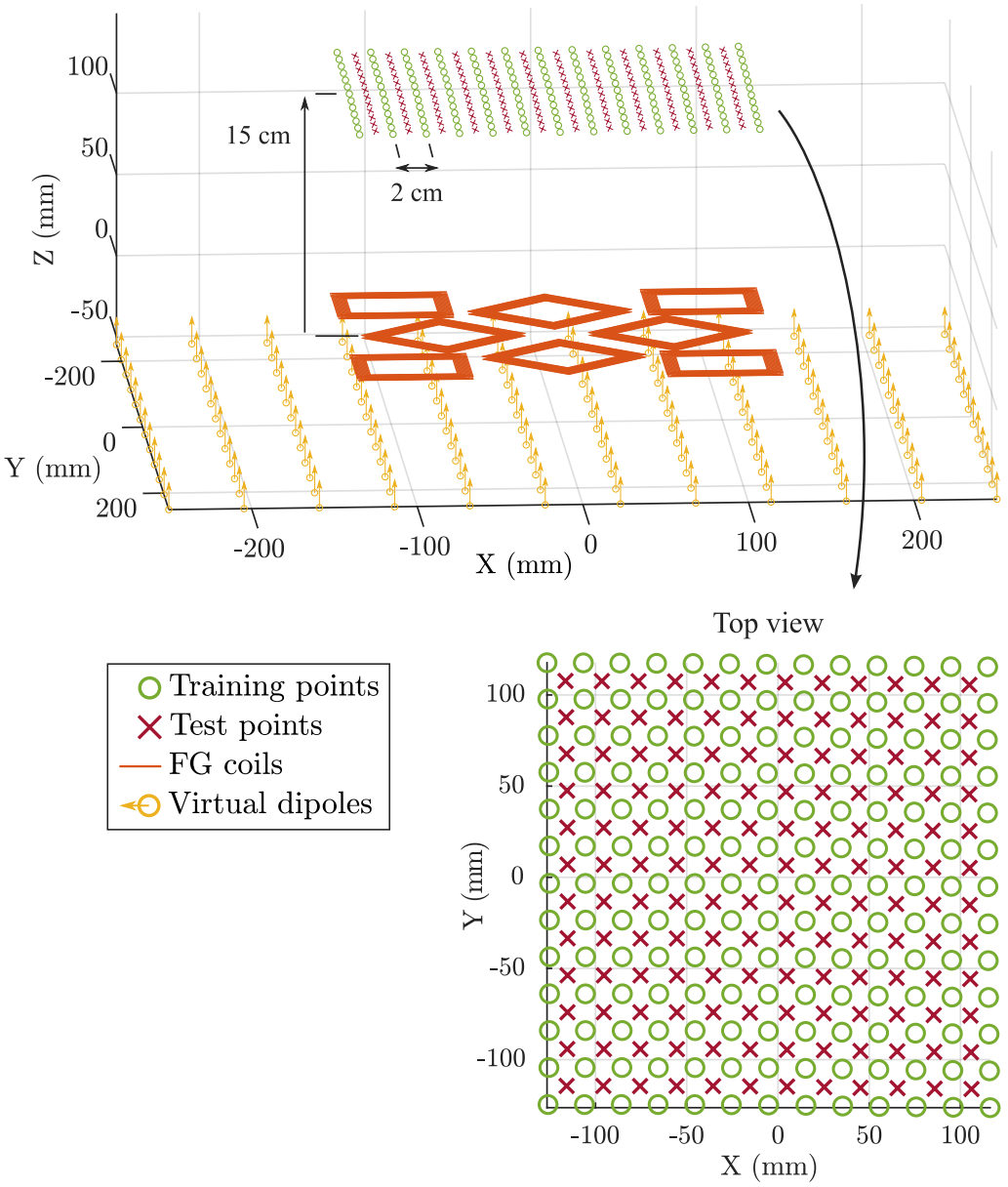


Figure 4.7: Modelling of the highly distorted magnetic field in the presence of metallic shields under the field generator. The model was represented by an array of 12×12 virtual magnetic dipole sources, the magnitude of which was optimised to match the training points magnetic measurements. Interpolation results were evaluated on the test points.

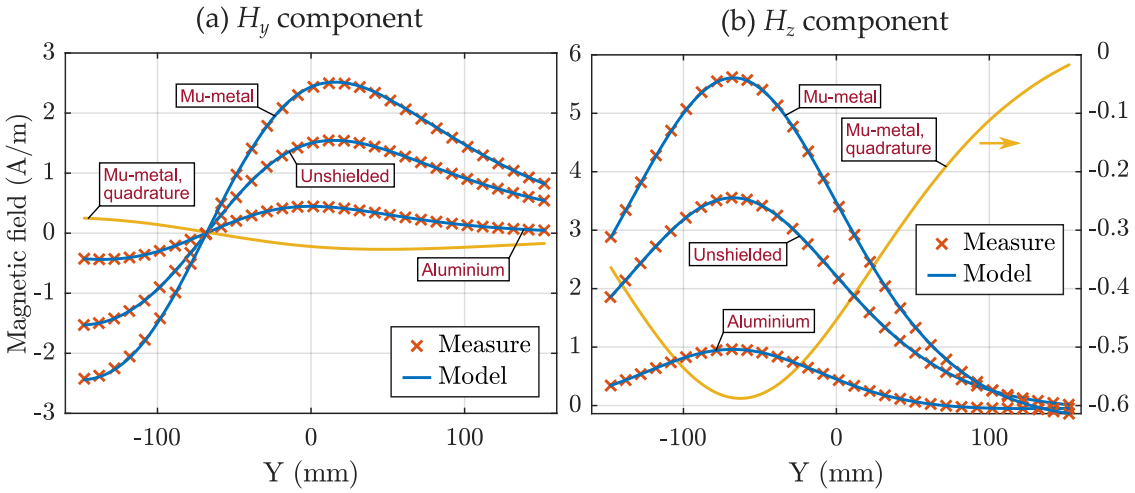


Figure 4.8: Effect of shielding on the magnetic field of the emitter coil number 4, which is defined in Figure 3.2, at $X = 0\,\text{mm}$ and $Z = 150\,\text{mm}$. (a) Y component and (b) Z component of the field. The quadrature field component, which appeared in the presence of the mu-metal shield, is plotted in yellow.

was placed at the approximate shield location to model the eddy currents and magnetisation effects within the shielding material. The experimental points and dipole sources are shown in Figure 4.7 relative to the emitter coils.

Figure 4.8 shows the magnetic field of emitter coil number 4 of the field generator, defined in Figure 4.1, in the three cases of no shielding, aluminium, and mu-metal shielding plates. The Y and Z components are plotted for a set of points located at Y from $-15\,\text{cm}$ to $+15\,\text{cm}$, $X = 0\,\text{cm}$, and $Z = 15\,\text{cm}$. The analytical model presented in Section 4.1 was used to fit the data points by training the virtual dipole distribution on the measured values, resulting in an accurate and smooth fit.

The effect of the aluminium and mu-metal shields is apparent in decreasing and increasing the field magnitude, respectively. The eddy currents induced in the shields generated a quadrature AC field component, around one-tenth the magnitude of the main in-phase component. Figure 4.8 shows the quadrature component for the mu-metal shield case only because it is large enough to be appreciated. The quadrature component must be taken into consideration to avoid tracking errors. One solution

is to synchronise to a specific signal phase, which must be consistent but does not necessarily have to be in phase.

The following metrics were used to evaluate the fitting performance on the training points and the interpolation effectiveness on the test points for the magnetic fields modelled. Considering a total of P observations from the two sensors and eight emitter coils, the field error at each observation point is the difference between the vector of eight measured magnetic flux values, $\widetilde{\mathbf{\Phi}}$, and the model prediction, $\mathbf{\Phi}$.

The mean absolute error (MAE) and the root-mean-square error (RMSE) were calculated by aggregating all eight times P error values. The normalised MAE (NMAE) and the normalised RMSE (NRMSE) were obtained by normalising for the difference between the maximum and the minimum field values measured, as given by Equation 4.7:

$$\text{NMAE} = \frac{1}{8P}\sum_{i=1}^{8P}\left|\widetilde{\Phi}_i - \Phi_i\right| \Big/ \left(\max_i \widetilde{\mathbf{\Phi}} - \min_i \widetilde{\mathbf{\Phi}}\right) \tag{4.7}$$

$$\text{NRMSE} = \sqrt{\frac{1}{8P}\sum_{i=1}^{8P}\left(\widetilde{\Phi}_i - \Phi_i\right)^2} \Big/ \left(\max_i \widetilde{\mathbf{\Phi}} - \min_i \widetilde{\mathbf{\Phi}}\right) \tag{4.8}$$

Table 4.4 reports the fitting results of the training and test sets for the two materials. The field error on the test points is also expressed in terms of positional and angular accuracy separately for the Y and Z sensor orientations, following the procedure described in Section 3.5.2. The EMT position error metrics introduced in Section 4.2.2 are reported in Table 4.4.

The model proves effective in accurately modelling the highly distorted magnetic field in the presence of large metallic shielding materials placed 5 mm under the field generator. The EMT position trueness at the test points is demonstrated to be less than 0.2 mm RMS both for horizontal and vertical sensor orientations, as seen in Table 4.4.

4.3.2 Shielding performance in a clinical environment

The effectiveness of the aluminium and mu-metal plates in shielding the region of interest (ROI) was tested in a clinical environment. In this

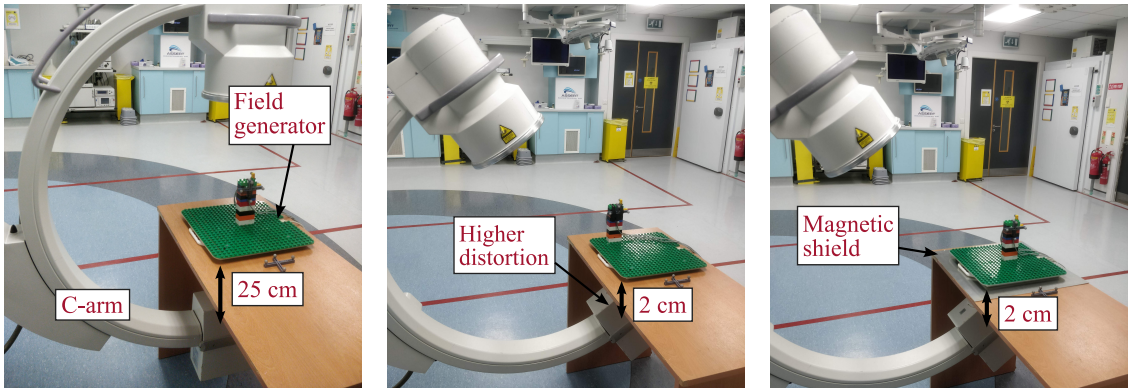
Table 4.4: Fitting results of the training data and interpolation performance at the test points, as defined in Figure 4.7. For the test set, the magnetic field error is also translated to the correspondent tracking position error.

Field error	Training	Test	EMT error (Test)	Horiz.	Vert.
Aluminium					
MAE (mA/m)	0.1377	0.2082	RMSE (mm)	0.16	0.13
NMAE (%)	0.0085	0.0131	ME (mm)	0.11	0.11
RMSE (mA/m)	0.1885	0.2854	PRC50 (mm)	0.07	0.09
NRMSE (%)	0.0116	0.0179	PRC95 (mm)	0.32	0.27
Mu-metal					
MAE (mA/m)	0.7827	1.4106	RMSE (mm)	0.17	0.16
NMAE (%)	0.0088	0.0160	ME (mm)	0.12	0.14
RMSE (mA/m)	1.0817	1.8508	PRC50 (mm)	0.09	0.12
NRMSE (%)	0.0122	0.0210	PRC95 (mm)	0.36	0.29

experiment, using the robotic actuator was not feasible, so tools *C* and *T* presented in Figures 3.11 and 4.1a were mounted on Duplo blocks (The Lego Company, Billund, Denmark) and moved on a planar Duplo plate placed on the field generator. The blocks served to keep the sensors stable at test points while collecting the magnetic measurements and for moving the tools repeatedly and consistently. Even if positions on the Duplo grid have a defined spacing, the Polaris Vega optical system was used for ground-truth pose reference because it provided higher accuracy.

A mobile X-ray machine (OEC Fluorostar 7900, General Electric Company, Boston, MA, USA), also called *C-arm* in this section, was used to demonstrate the distortion effect on the unshielded ANSER EMT system. The C-arm is composed of metallic materials, both conductive and ferromagnetic, and can cause EMT errors that depend on the position of the machine.

The X-ray collimator of the C-arm was placed below the field generator and moved at different distances from it, as shown in Figure 4.9. For every distortion configuration, EMT tests were performed on a planar grid of 64 test points approximately 15 cm above the field generator. Tool *T* was used for the tracking test. The two NDI miniature sensors were aligned along the Y and Z axes of the field generator, horizontally and vertically,



(a) (b) (c)

Figure 4.9: The C-arm effect was evaluated at different distances from the field generator, (a) from 25 cm, which caused the smallest distortion, (b) to the minimum distance of 2 cm, which caused the largest distortion. (c) Aluminium and mu-metal magnetic shields placed below the field generator were tested as a possible solution against static and dynamic distorters below the field generator.

respectively. A test was also included when the C-arm was removed for comparison to the undistorted scenario.

The uncompensated theoretical field model presented in Section 3.2.3 was used to find the EMT sensor pose from the magnetic measurements. Initially, no shielding or compensation technique was applied. Then, the same experiment was repeated with the addition of a shielding plate below the field generator.

For each shielding material, a data-driven model was trained using the technique proposed in Section 4.3.1, while the C-arm was removed and did not introduce magnetic distortion. The tracking test was carried out using the new magnetic field model, with the X-ray collimator placed at the minimum distance from the ROI, 2 cm below the field generator, as shown in Figure 4.9c. This C-arm position configuration caused the most significant EMT error in the experiment without shielding.

The results of all the tracking tests with the C-arm at different distances are reported in Figure 4.10, which shows the empirical cumulative distribution function (CDF) of the position error for the Y and Z sensor orientations. As expected, the distorter effect increases when the C-arm is placed closer to the field generator.

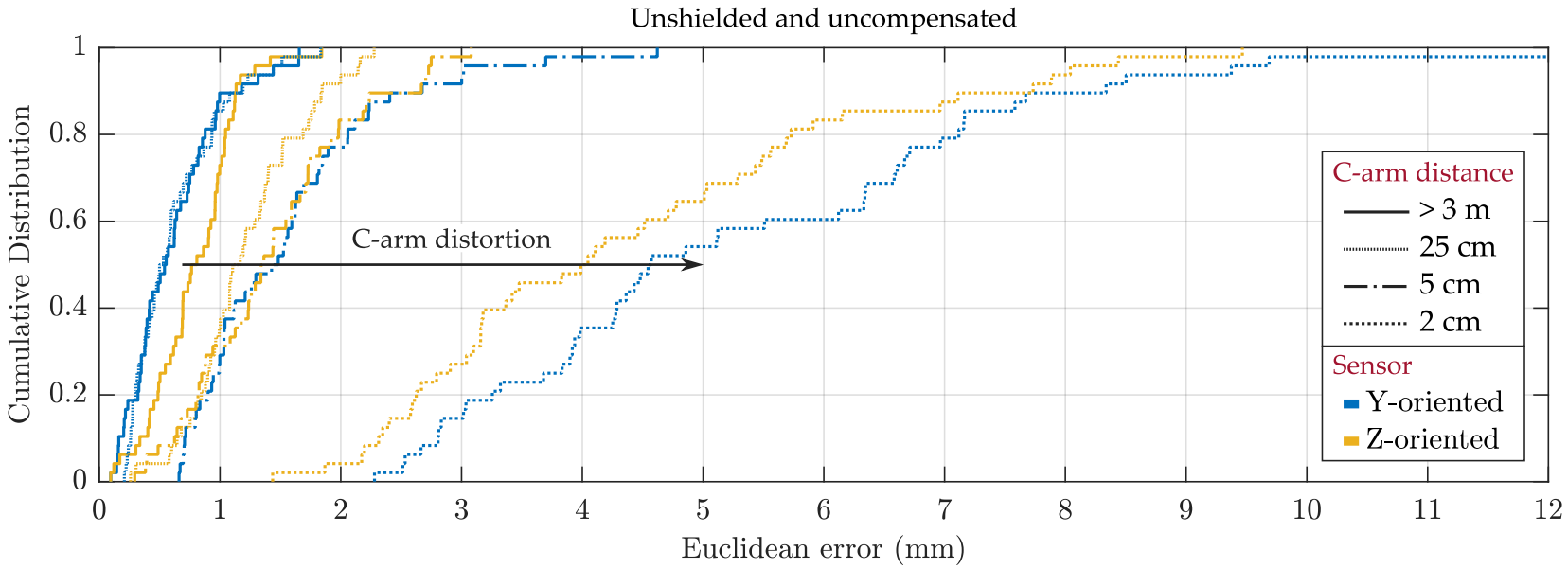


Figure 4.10: Unshielded and uncompensated EMT errors for varying distance between the C-arm and the field generator, from a far position where it did not cause magnetic distortion to 2 cm (maximum distortion). The error distribution in the last case, when the fluoroscopy C-arm was placed at 2 cm, is visualised in Figure 4.11 using meshes of the tracked and reference position. It must be compared to the error distribution obtained with magnetic shielding, shown in Figure 4.12. The corresponding error metrics are reported in Table 4.5.

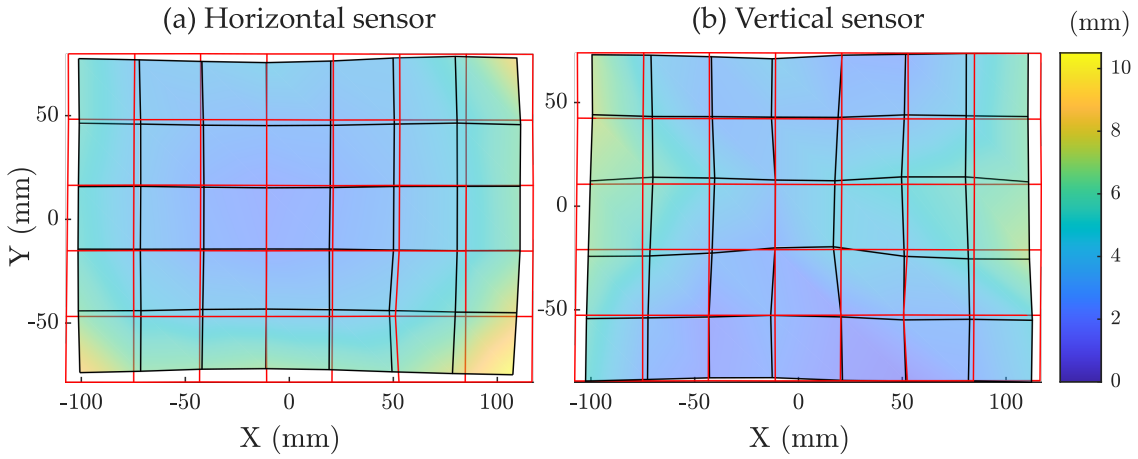


Figure 4.11: Effect of the C-arm on the position tracking error when it was placed directly below (2 cm) the planar field generator, without magnetic shielding or distortion compensation, when the magnetic sensor was (a) Y oriented (horizontal) or (b) Z-oriented (vertical). The red grid is formed by joining the test points, and the black grid represents the EMT sensor position. The colour map, in mm, also accounts for the error in the Z direction, which is not appreciable from the 2D grids.

Distortion visualisation was obtained using lattices of the tracked position [20, 21]. Figure 4.11 shows the error map for the distortion introduced by the fluoroscopy C-arm placed 2 cm below the field generator. The ground truth and the tracked position of the test points are combined to form two meshes representing the undistorted (red) and distorted (black) volumes, respectively. The grids show the error evident in the X and Y directions. The colour map is based on the total position error, including the Z coordinate, calculated as the Euclidean distance.

Figure 4.12 shows the empirical CDF of the position error when the magnetic shields were used to block the C-arm distortion. The error metrics are reported in Table 4.5, together with the tracking error obtained in the correspondent unshielded case.

Both shielding materials demonstrated effectiveness. Positional RMSE of 0.31 / 0.23 mm (aluminium / mu-metal) was obtained for the Y-oriented sensor, and positional RMSE of 0.46 / 0.51 mm (aluminium / mu-metal) for the Z-oriented sensor. These values must be compared with the RMSE

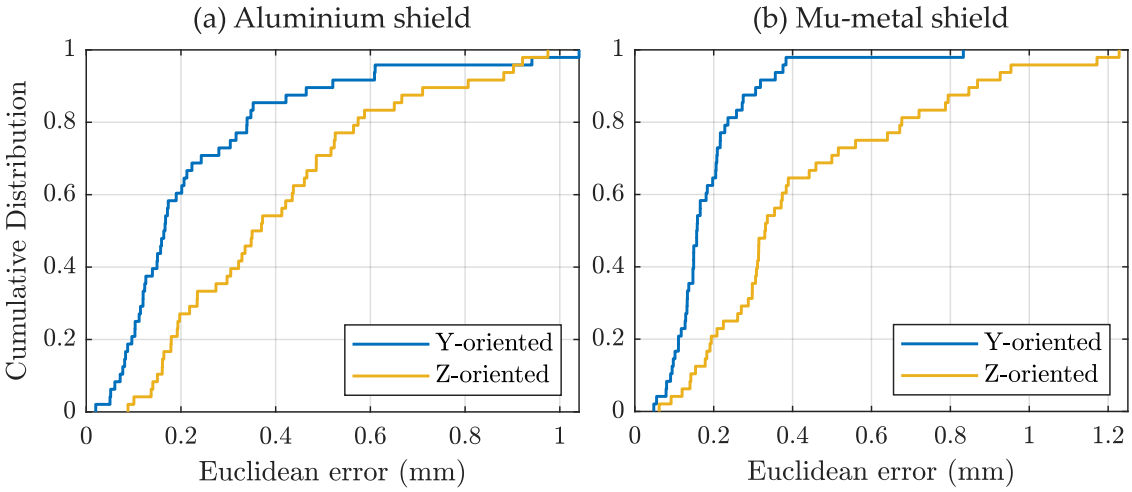


Figure 4.12: Tracking errors when the fluoroscopy system was at minimum distance, 2 cm below the field generator, using (a) an aluminium plate and (b) a mu-metal plate to shield the distortion. The field model used to find the sensor position was trained on data collected in an undistorted environment where the fluoroscopy C-arm was removed.

Table 4.5: Tracking test results with the C-arm at 2 cm to show the effect of the shields. The cumulative distribution of the error can be found in Figure 4.10 (at 2 cm) for the unshielded case and in Figure 4.12 with shielding. The position error of the unshielded case is visualised in Figure 4.11.

Shield	Unshielded		Aluminium		Mu-metal	
	Y	Z	Y	Z	Y	Z
RMSE (mm)	5.72	4.74	0.31	0.46	0.23	0.51
ME (mm)	5.28	4.37	0.23	0.40	0.19	0.43
PRC50 (mm)	4.56	4.02	0.16	0.36	0.16	0.33
PRC95 (mm)	9.39	7.82	0.63	0.89	0.38	0.97

of 5.72 mm and 4.74 mm obtained with Y and Z-oriented sensors in the unshielded case.

4.3.3 Discussion

Both shielding materials under test demonstrated effectiveness against large field distorters placed under the shielded field generator. As expected, the magnetic field in the region above the field generator was increased when using the mu-metal shield and reduced with the aluminium shield.

This effect is due to different shielding working principles. Mu-metal provides a path for magnetic field lines rather than blocking them. The material becomes magnetised along the field direction, adding to the effect of the field generator. Aluminium provides a conductive path for eddy currents induced by AC-varying magnetic fields. These currents generate fields that oppose the original field, effectively reducing the overall magnetic field strength.

The field magnitude is typically regulated to match the safety levels allowed for human exposure to electromagnetic fields [22]. In that case, the mu-metal could be preferred to decrease the system power consumption.

However, other factors must be considered when choosing the optimal shielding material, depending on the final application. For example, the mu-metal relative permeability is sensitive to temperature and mechanical stress and can be affected by magnetic saturation or demagnetisation, causing a change in the field shape that must be recalibrated. This concern may not be relevant in applications where the system is calibrated often or if real-time compensation techniques, such as those proposed in Section 4.5, are applied. Aluminium has the advantages of being lightweight, electrically and mechanically more stable over time, cost-effective, and more translucent to X-rays [23].

In addition to the aluminium and mu-metal shields, other shielding solutions are available, including non-conductive high-permeability materials, the combination of materials on multiple layers, and different configurations for the dimensions of the shielding plate and its distance

from the field generator. However, the simple single-layer plates analysed in this study already showed efficacy for the intended environment.

It should be noticed that if the shield is moved relative to the field generator or if the material is changed, the characterisation of the ROI must be repeated to create the correct magnetic model. Therefore, similarly to what was observed in Section 4.2.4, characterisation of larger volumes should only be carried out once the shielding solution has been defined.

4.4 Distortion detection techniques

The previous sections introduced methods for *offline* distortion compensation by calibrating for systematic errors or mitigating the effects of magnetic distortion through shielding. However, EMT errors can still occur when metal objects are moved near the region of interest.

This section proposes methods for real-time detection of EMT distortion in ANSER EMT, which is an essential first step in implementing *semi-online* solutions. By raising a warning when the distortion level exceeds a pre-set threshold, users can manually take action to remove the source of distortion until accurate tracking is restored.

Three techniques are presented based on the mechanical constraints between multiple sensors rigidly connected, the residual value obtained after convergence of the tracking algorithm, and the phase shift measured in the received magnetic flux. Finally, the methods are tested in a clinical environment.

4.4.1 Multiple sensors rigidly connected

When multiple sensors are in a fixed position relative to each other, the known distance and orientation between the sensors can be compared with the measured pose, and the deviation is an indicator of the EMT distortion level [24, 25]. For example, reference sensors may be installed at known static positions, or a customised tool containing an array of sensors may be moved in the region of interest to detect distortions.

In the case of tool C, the pose of the tool can be estimated by finding the best fit, in a least-squares sense, to the set of nine coils independently tracked, similar to the procedure outlined in Section 3.3.3. Alternatively, if optical tracking is available, the pose of the sensor array might be determined by optical methods.

The poses of the nine coils are derived according to the estimated pose of the dynamic reference frame, and a distortion score is calculated based on the error between the original EMT pose and the estimated pose that is subject to mechanical constraints, as was shown in Equation 3.21. In addition, the error affecting the nine coils can be kept distinct to provide insight into which positions and orientations are most influenced by distortion.

4.4.2 Residual of the tracking algorithm

The EMT algorithm presented in Section 3.2.4 estimates the sensor pose, $\widetilde{\mathbf{p}} \in \mathbb{R}^{5\times 1}$, by minimising the difference between the vector of magnetic flux measurements, $\widetilde{\mathbf{\Phi}} \in \mathbb{R}^{8\times 1}$, and the values modelled at $\widetilde{\mathbf{p}}$, $\mathbf{\Phi} = f(\widetilde{\mathbf{p}})$.

A unique vector of eight flux values can be determined for each position and orientation. However, the opposite is not true, as a general set of eight flux values cannot be linked to a specific sensor position and orientation.

The proximity of conductive or ferromagnetic materials causes the eight values of $\widetilde{\mathbf{\Phi}}$ to deviate from the expected values, leading to a mismatch between $\mathbf{\Phi}(\widetilde{\mathbf{p}})$ and $\widetilde{\mathbf{\Phi}}$. The result is an increase in the residual of the cost function, as given by Equation 4.10:

$$\sqrt{\sum_{ec=1}^{8}\left(\widetilde{\Phi}_{ec} - \Phi_{ec}(\widetilde{\mathbf{p}})^2\right)} \quad \left[\frac{\mathrm{A}}{\mathrm{m}}\right] \tag{4.9}$$

which can be monitored to recognise inaccurate tracking.

4.4.3 Signal phase shift

As seen in Section 2.4.1, conductive materials cause a magnetic distortion that introduces a shift in the phase of the measured signal. This effect was also observed in Section 4.3.1 when using magnetic shielding.

The signal phase should ideally be shifted by $\pi/2$ with respect to the phase of the magnetic field. However, in practice, a constant phase offset arises from the signal acquisition process, as explained in Section 3.2.2.4. After calibration of the offset, the phase difference is expected to remain consistently at $\pi/2$. Any deviation from this can indicate the presence of out-of-phase currents that generate secondary magnetic fields, causing distortion.

The conductive distortion factor was calculated as the phase deviation from $\pi/2$ averaged between the eight signal frequencies, as given by Equation 4.10:

$$\frac{\sum_{ec=1}^{8} |\widetilde{\Phi}_{ec}| \cdot (|\alpha_{ec}| - \pi/2)}{\sum_{ec=1}^{8} |\widetilde{\Phi}_{ec}|} \quad [\text{rad}] \tag{4.10}$$

where α_{ec} is the measured phase of the magnetic flux due to the emitter coil number ec.

The magnitude of the measured flux was used as a weighting factor in Equation 4.10 to reduce the impact of large phase errors that occur with low signals, for example, when the sensor orientation is perpendicular to one of the field vectors. In this case, the signal-to-noise ratio (SNR) is low and substantial errors might be present in the phase measurement even without any distortions.

4.4.4 Distortion detection in a clinical environment

Typical medical environments contain sources of metallic distortion such as surgical instruments, C-arms, and the operating table [26]. In this section, the distortion detection techniques presented above are tested in a computed tomography (CT) room. In particular, the operation of the ANSER EMT system was simulated in conjunction with a CT scanner machine (SOMATOM Force, Siemens Healthineers, Erlangen, Germany), and the effect of the bed and the main CT gantry was tested.

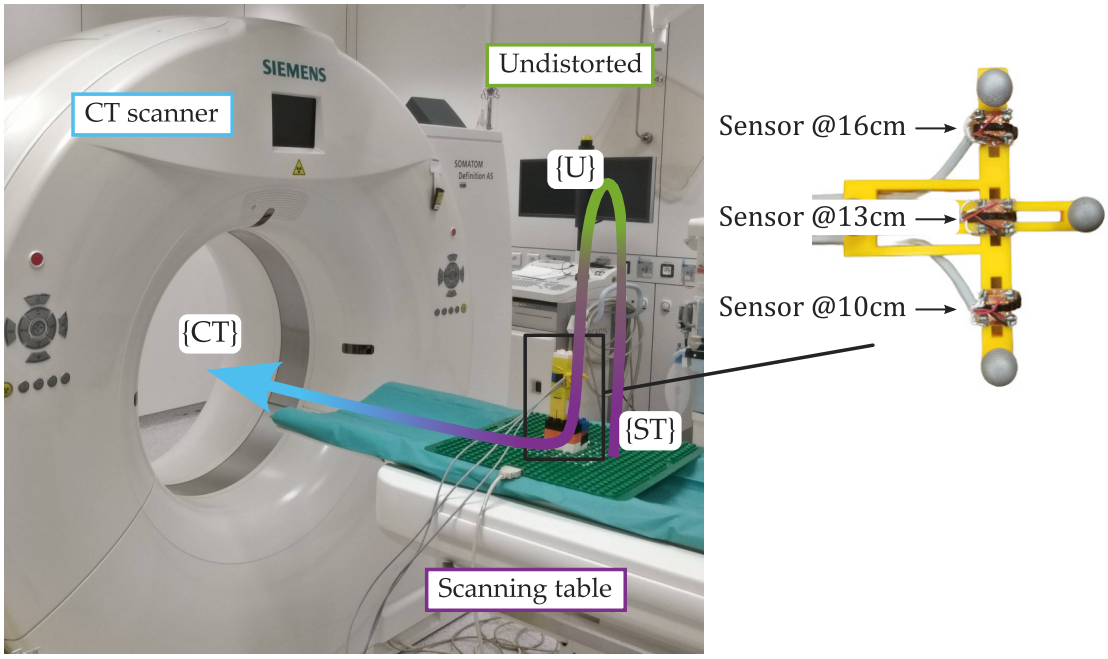


Figure 4.13: Tool *C* was mounted on Duplo blocks at a fixed position on the field generator, which was positioned on the scanner table, position {ST}. The assembly was then lifted to obtain undistorted measurements, position {U}. Finally, the field generator was placed back on the bed and slid into the CT scanner, position {CT}. Throughout the entire process, the EMT algorithm and distortion detection techniques were continuously in operation.

Tool *C* was mounted on Duplo blocks at a fixed position on the field generator, as shown in Figure 4.13. The field generator was first positioned on the scanner table, position {ST}, then lifted by hand to remove the distortion introduced by the table and obtain undistorted measurements, position {U}, before being placed back on the bed, which was finally slid into the "doughnut hole" of the CT scanner, position {CT}. Throughout the entire process, the EMT algorithm and distortion detection techniques were continuously in operation.

Figure 4.14 shows the EMT poses obtained for the nine sensor coils in tool *C* in the three different distortion scenarios. Ideally, the three coils in each triaxial sensor should be coincident and perpendicular, as demonstrated in Figure 4.14a. Significant distortion is visible in Figure 4.14b,

mainly impacting the coils with vertical axis, while a smaller degree of distortion is apparent in Figure 4.14c.

For every sampled point, the EMT position and orientation errors were calculated relative to the EMT pose obtained without distortion. Figure 4.15 presents the results obtained for the three triaxial sensors of tool *C*, which were placed at heights of 10, 13, and 16 cm above the field generator, respectively. Each plot shows the three coils contained in the triaxial sensors, with orientations along the X, Y, and Z axes of the field generator.

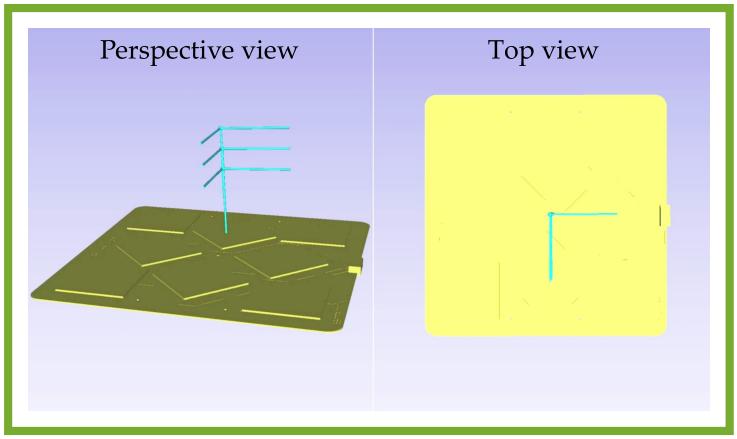
It can be observed from Figure 4.15 that the Z-oriented coil is affected the most by the source of distortion placed below the field generator, whereas the X and Y-axis coils reach a maximum error of 5 mm and always remain below an orientation error of 1°. In general, the variation in distortion scores is correlated with the variation in EMT errors. Therefore, the proposed techniques can detect when the tracking accuracy might be low due to distortion.

The residual value that indicates distortion is not absolute, as shown in Figure 4.15a. For instance, the residual obtained for the non-distorted Z-oriented coil is higher than that for the X-axis when distorted. The reasons for this are attributed to the different magnitudes of the vertical and horizontal components of the magnetic field, as well as the potential inaccuracies in the field model, which might be more pronounced for specific sensor poses.

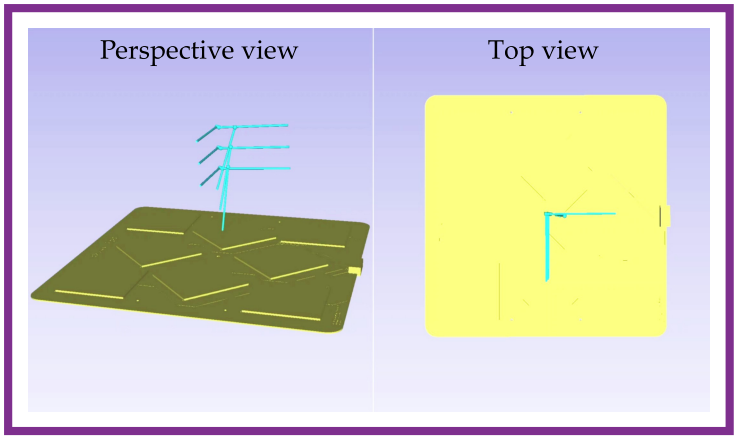
One solution is to characterise in advance the residual value without distortions within the region of interest (ROI). Another possibility is calculating the distortion score based on the residual variation or normalising it by the average field magnitude.

Conversely, the phase shift appears to be more closely associated with the EMT error, as shown in Figure 4.15b. However, the phase only indicates distortion resulting from conductive materials and is not sensitive to ferromagnetic distortions. Therefore, a global distortion score or quality factor may be calculated as a combination of the residual value and the phase shift.

(a) No distortion {U}



(b) Scanner table distortion {ST}



(c) CT scanner distortion {CT}

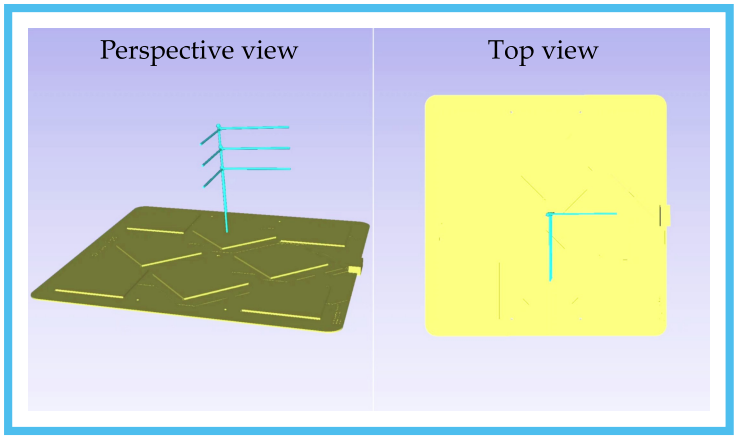


Figure 4.14: Snapshots of the EMT poses at three stages of the experiment: (a) when the field generator was lifted to obtain undistorted measurements, position {U}; (b) with the field generator sitting on the scanning table, position {ST}; and (c) at the centre of the CT scanner gantry, position {CT}.

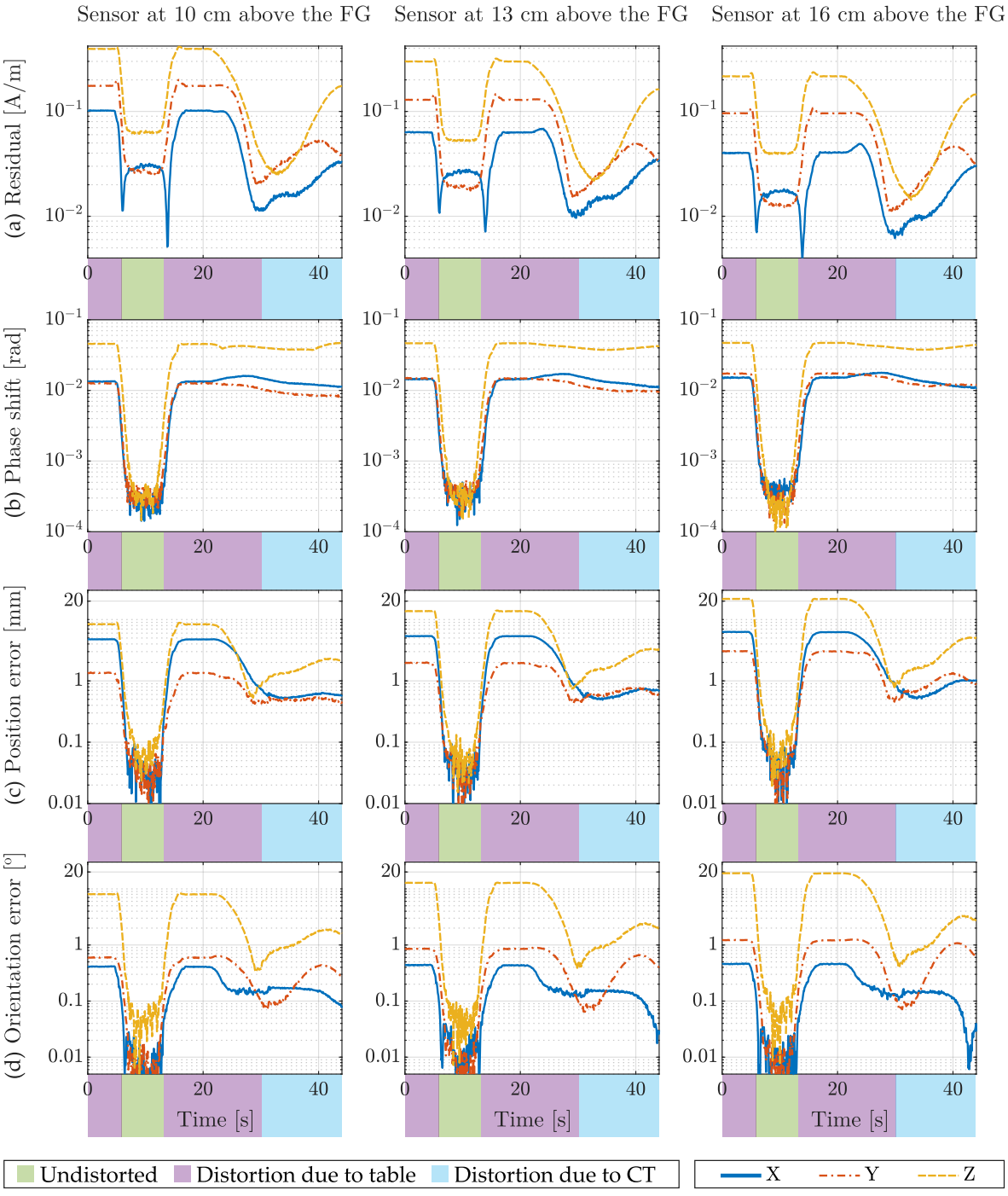


Figure 4.15: Distortion detection compared to the corresponding EMT errors, for three triaxial sensors, at 10, 13, and 16 cm from the field generator (FG), with axes oriented along X, Y, and Z. (a) EMT algorithm residual, as given by Equation 4.9. (b) Signal phase shift, calculated according to Equation 4.10. (c) Position error in millimetres, relative to the position measured without distortion {U}. (d) Orientation error in degrees, in relation to the same EMT point used for the position error.

The primary source of distortion appears to be from the bed structure beneath the table rather than the sliding table. The bed structure, which is the white metallic object located at the bottom right of Figure 4.13, is mainly made of aluminium and steel. On the other hand, the sliding bar made of carbon fibre did not seem to cause any significant distortion, despite being in direct contact with the field generator.

This is visible in Figures 4.15c and 4.15d, where the EMT position and orientation errors for all sensors fall below 1 mm and 1°, respectively, between {ST} and {CT}. This stage is during the sliding of the bed into the CT gantry, when the field generator was approximately 50 cm away from both the bed structure and the CT gantry.

These observations indicate that the ANSER EMT system, even without shielding, is compatible with carbon fibre, which is typically non-conductive and weakly magnetic.

4.5 Real-time distortion compensation

Real-time compensation techniques for dynamic distortions have been proposed in the literature, which make use of sensor arrays [27–29], simultaneous localisation and tracking [30], artificial neural networks [31, 32], and fusion of inertial and magnetic sensors [33–35]. However, these methods typically require a large amount of training data, involve sensor assemblies that are difficult to miniaturise, or have limited extrapolation capabilities.

In contrast, the physical interpretation of the calibration model reduces the number of reference sensors required and enhances the extrapolation capabilities, both of which are essential factors for a real-time compensation technique where the real field inside the region of interest (ROI) is derived from field measurements collected at known positions around it.

Clinical applications that would particularly benefit from online distortion compensation are those procedures where intraoperative fluoroscopy is utilised. Fluoroscopic X-ray imaging is considered the gold standard to localise the tool position in cardiology, radiology, and minimally invasive surgery, due to its high accuracy and reliability [36]. However, the tech-

nology involves radiation exposure to the patient and the surgical team [37, 38].

EMT can be combined with X-ray interventional imaging to reduce the radiation dose if a hybrid navigation framework is considered, where EMT is used for continuous navigation and X-ray is delegated to on-demand use during delicate manoeuvres or for confirmation [39].

Unfortunately, the X-ray machine, typically in the shape of a *C-arm*, is a source of metallic distortion for the EMT system, the nature of which depends on the C-arm position and cannot be predetermined. The C-arm can introduce large distortions to the magnetic field used for tracking if not moved back after use, adding complexity to the procedure.

This work presents two novel techniques for intraoperative calibration and real-time compensation of dynamic field distortions. The workflows are summarised in Table 4.6. The methods were tested by simulating realistic distortion scenarios in the presence of commercially available fluoroscopy systems.

4.5.1 Intraoperative magnetic modelling

The modelling method presented in Section 4.1 was employed for the proof-of-concept of an *online* distortion compensation technique, i.e. during a procedure where EMT is used. The reduced number of calibration parameters and reference sensors enables the potential for real-time magnetic modelling based on redundant measurements of external arrays of sensors.

The updated field model takes into consideration the presence of magnetic distortion and can be used to increase EMT accuracy. Similar ideas have been expressed in previous publications [40–42], but a practical working solution for field modelling has never been demonstrated.

A hybrid navigation scenario was investigated by combining the ANSER EMT system and a fluoroscopy imaging system (OEC Fluorostar 7900, General Electric Company, Boston, MA, USA). The field generator was placed directly above the X-ray collimator of the C-arm, as shown in Figure 4.16a. Although not a realistic arrangement, this configuration

(a) Use an array of redundant sensors to generate an updated magnetic model in real time (Section 4.5.1)

Version A. Automatic compensation

1. Apply the array of redundant sensors on the patient in proximity to the ROI
2. Start the procedure using classical EMT methods
3. The redundant sensors are localised by the system using intraoperative fluoroscopy or optical tracking
4. A compensated magnetic model is generated in real time and used for accurate EMT

Version B. Manual compensation

1. Start the procedure using classical EMT methods
2. When distortion is detected or if a critical position is reached, hand-wave the array of redundant sensors around the ROI
3. The redundant sensors are dynamically localised by the system using optical tracking
4. New compensated magnetic models are generated until a low distortion is detected

(b) Locate the distorter and interpolate between pre-characterised magnetic model maps (Section 4.5.2)

Before the procedure

1. Fix the field generator and the witness sensor(s) and do not change their position
2. Move the external distorter, e.g. C-arm, to typical positions and orientations
3. For every distortion scenario, record the witness sensor measurement and collect a static distortion magnetic field map
4. Interpolate between the measurements to extend to distortion scenarios that were not recorded

During the procedure

1. Start the procedure using classical EMT methods
2. The witness sensor(s) are used to estimate the distorter position and orientation
3. The magnetic model map that corresponds to the current distortion scenario is used for EMT

Table 4.6: Schematic workflows of the two real-time distortion compensation techniques proposed in Section 4.5.

was chosen because it introduced the maximum field distortion and EMT error, allowing for testing the proposed method in a challenging distortion environment.

Tool *C* was used to sample an 8×8 grid of triaxial magnetic measurements at $Z = 18$ cm above the field generator. This plane represented an array of reference sensors and was used to create an updated field model of the magnetic distortion using the procedure described in Section 4.1. The EMT accuracy was tested on two lower planes of 6×6 points at 3 cm and 6 cm from the top plane, as shown in Figure 4.16b. Duplo blocks were used to hold the sensors steadily during acquisition, and optical tracking provided position and orientation reference.

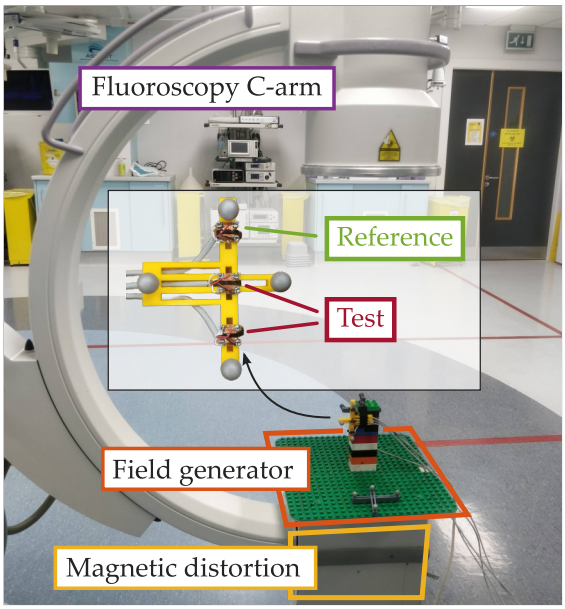
The effect of the C-arm distortion is visible in Figure 4.17 for the test points at $Z = 12$ cm above the field generator or equivalently at 6 cm from the plane of reference sensors. The black grids represent the positions obtained from the EMT system, and the red grids are the same points obtained with optical methods. Figure 4.17 also shows the EMT solution when the proposed distortion compensation technique was applied.

EMT accuracy results are reported for Y and Z-oriented sensor coils, which are parallel and perpendicular to the field generator, respectively. Errors were calculated between the EMT and the optical poses, using the Euclidean distance in millimetres for the position and the angular displacement in degrees for the orientation.

Figure 4.18 shows the cumulative distribution of the tracking errors obtained for the uncompensated case and after applying the distortion compensation technique described in this section. The plots show the results for both evaluation planes at 3 cm and 6 cm from the top plane, as shown in Figure 4.16. Position and orientation error metrics are reported in Table 4.7.

For the test points at a closer distance from the reference sensors, the RMS error decreased from 12.0 mm to 0.53 mm for the horizontal sensor, and from 25.7 mm to 0.87 mm for the vertical sensor. For the evaluation plane at 6 cm from the reference sensors, the RMS error decreased from 9.84 mm to 0.90 mm for the horizontally-oriented sensor, and from 16.9 mm to 1.66 mm for the sensor aligned along the vertical axis.

(a) Experimental setup



(b) Magnetic field measurements

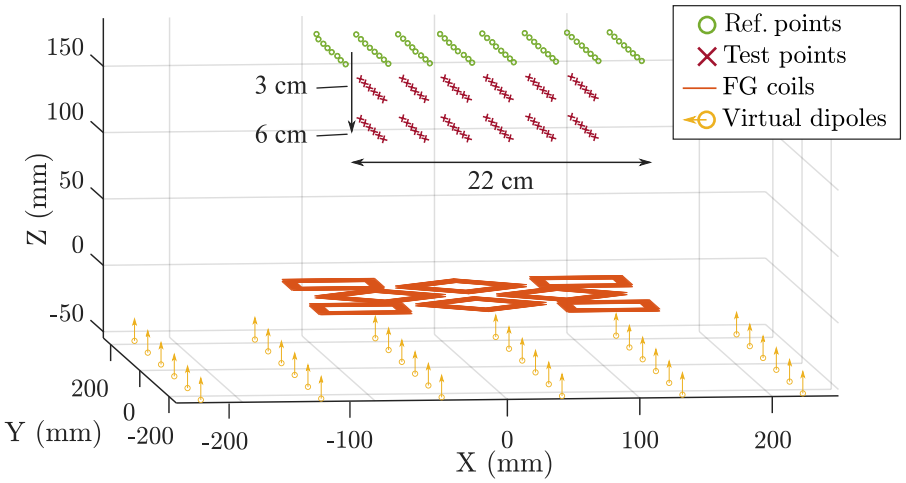


Figure 4.16: Online distortion compensation technique. (a) The field generator was placed on top of the X-ray collimator, which introduced large metallic distortion. (b) Magnetic field measurements were collected on a plane that represented an array of reference sensors. This data was used to generate an updated field model, allowing for distortion compensation. EMT accuracy was evaluated on two lower planes, at 3 cm and 6 cm from the top plane, respectively.

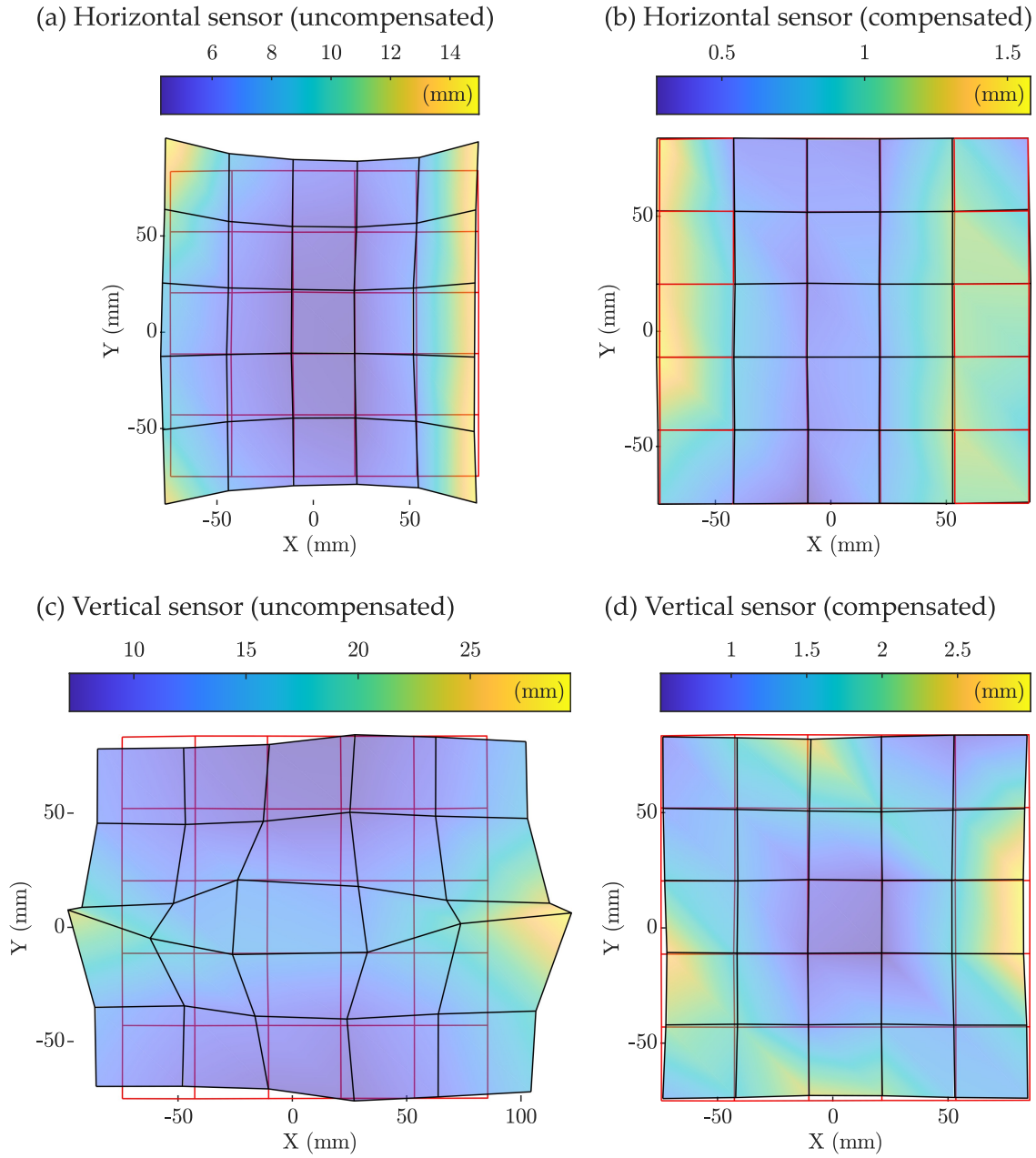


Figure 4.17: EMT accuracy with the field generator placed on top of the fluoroscopy system, evaluated on the plane at 6 cm from the reference plane shown in Figure 4.16. The results are shown for (a,b) horizontally and (c,d) vertically oriented sensors, (a,c) before and (b,d) after applying the compensation technique proposed in this section. The red grids are formed by joining the undistorted optical positions, while the black grids represent the EMT points. The colour maps show the error in millimetres. The distortion in the Z-direction is not appreciable from these 2D plots.

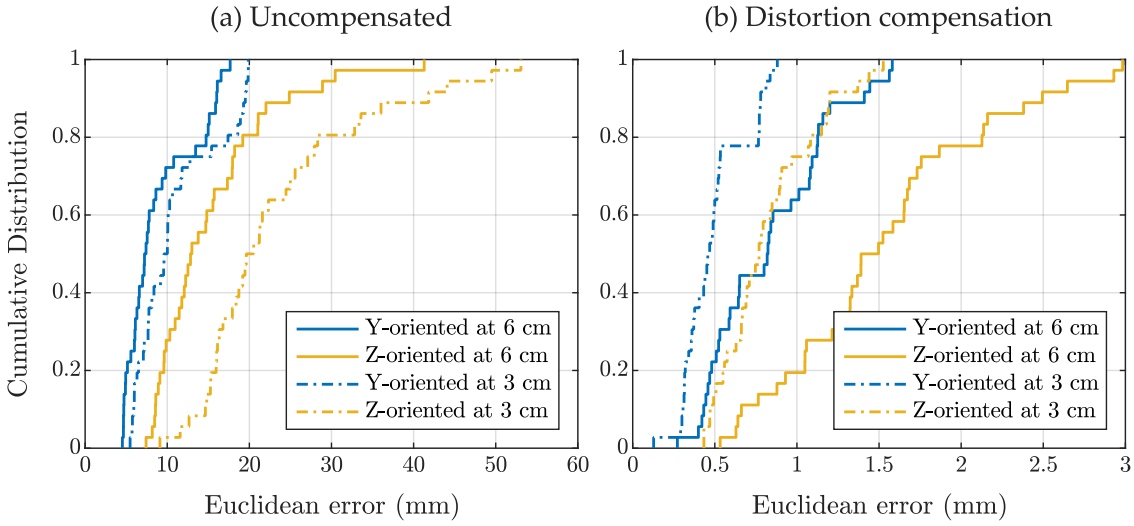


Figure 4.18: EMT errors with the field generator placed on top of the X-ray collimator. (a) Errors caused by metallic distortion before compensation. (b) Errors obtained using the calibrated magnetic field model. The results are reported for the two evaluation planes shown in Figure 4.16.

Table 4.7: Tracking test results with the field generator placed on top of the X-ray collimator before and after applying distortion compensation. For the four cases, the error distributions are visualised in Figure 4.18.

	With distortion	Distortion compensation	With distortion	Distortion compensation
	Sensor plane at 3 cm		Sensor plane at 6 cm	
Horizontal sensor (Y-oriented)				
Error	mm / deg	mm / deg	mm / deg	mm / deg
RMSE	12.0 / 2.69	0.53 / 0.26	9.84 / 2.35	0.90 / 0.48
PRC50	9.81 / 1.04	0.46 / 0.24	7.32 / 1.34	0.82 / 0.40
MAXE	19.9 / 6.61	0.88 / 0.39	17.7 / 5.41	1.58 / 1.09
Vertical sensor (Z-oriented)				
Error	mm / deg	mm / deg	mm / deg	mm / deg
RMSE	25.7 / 16.6	0.87 / 0.74	16.9 / 11.2	1.66 / 1.42
PRC50	20.1 / 12.7	0.77 / 0.70	12.9 / 9.01	1.44 / 1.36
MAXE	53.1 / 39.2	1.53 / 1.17	41.3 / 26.1	2.98 / 2.34

These experimental results demonstrate that the magnetic modelling technique proposed in Section 4.1 is effective in extrapolating data beyond reference measurements. Traditional characterisation techniques require data to be collected on closely-spaced grid points, as close as 2.5 mm, and interpolate for points in between [43]. In the experiment presented in this section, reference sensors were spaced 24 mm apart and placed outside the region of interest (ROI). Despite this, it was possible to correct a significant portion of the error, even at a distance of 6 cm between the reference sensor plane and the test points subject to distortion.

The calibration algorithm took an average of 20 ms to calculate the mutual inductance matrix between every virtual dipole and every reference measurement on a laptop with i5-11th Gen. Intel Core Processor. In contrast, finding the optimal dipole magnitudes took an average of 1.5 ms. These values are compatible with real-time calibration because the data-driven magnetic field model is valid until the sources of field distortion are moved. Moreover, the matrix can be calculated in advance if the positions of the reference sensors do not change.

The envisioned application involves placing redundant sensors at fixed positions in proximity to the ROI. Such sensors can be localised using an undistorted tracking system, such as an optical camera. Alternatively, intraoperative recalibration of their position can also be obtained from X-ray snapshots. The reference measurements may be used to calculate the magnetic model in real time, compensating for the dynamic field distortion that affects the tracking accuracy of target sensors.

The proposed method requires a high number of redundant sensors, with possible occlusion of the operative space. Solutions might come from an application-specific optimisation of their positions, as well as miniaturisation and wireless sensing. Chapter 7 will investigate the use of planar sensor coils that can be printed on flexible PCB and potentially integrated into external body-mounted patches for future clinical applications.

4.5.2 Interpolation between pre-trained models

While magnetic distortion is a limitation for EMT, it can also be considered as an effect to leverage. By pre-training a model on different distortion configurations, the aim is to predict the position and orientation of the instrument causing distortion.

In this section, the method is demonstrated for one degree of freedom (1 DOF) applications where a static sensor is used to *witness* the deviation of the magnetic field due to distortion introduced by medical equipment.

Distortion detection by monitoring the field variation at known positions has been proposed in the literature [41, 44]. However, using that information to localise the instrument has never been investigated with experimental methods.

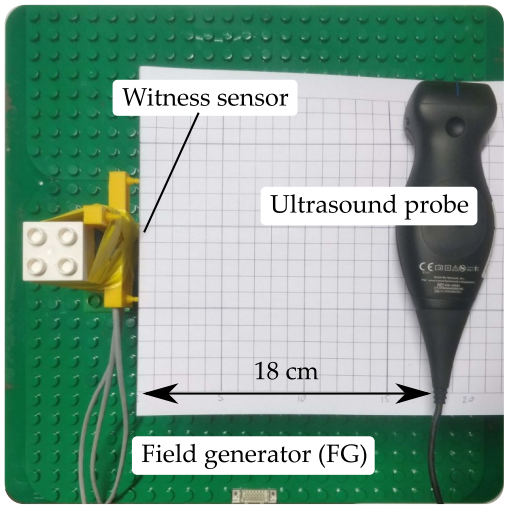
As said, offline volume characterisation is a solution for static distortion scenarios [15]. In dynamic environments, however, it is not feasible to pre-characterise all possible distortion configurations. The proposed solution is to collect a finite number of static compensation maps and interpolate between them in real time.

An external optical tracking system might typically identify the position of the distorting object to determine the correct interpolation plane [45]. In contrast, in this work, the effect of distortion on a static witness sensor was used to estimate the appropriate compensation map without the need for additional tracking systems.

Two experiments were performed to demonstrate possible applications of the proposed technique. In the first case, the distortion introduced by a commercially available (US) probe (Butterfly iQ+, Butterfly Network, Burlington, MA, US) was characterised and subsequently used to track the probe position on a line. In the second application, the measurement was used to estimate the distance of a cone beam computed tomography (CBCT) scanner (Artis zeego, Siemens Healthineers, Erlangen, Germany) and apply the correct compensation model.

In the first experiment, tool *C* was placed at approximately 15 cm above the planar field generator, and the US probe was moved on a line in steps of 1 cm, as shown in Figure 4.19a, where it is noted that there is no sensor connected to the probe itself. One of the sensor coils in

(a) Experimental setup



(b) Distortion effect

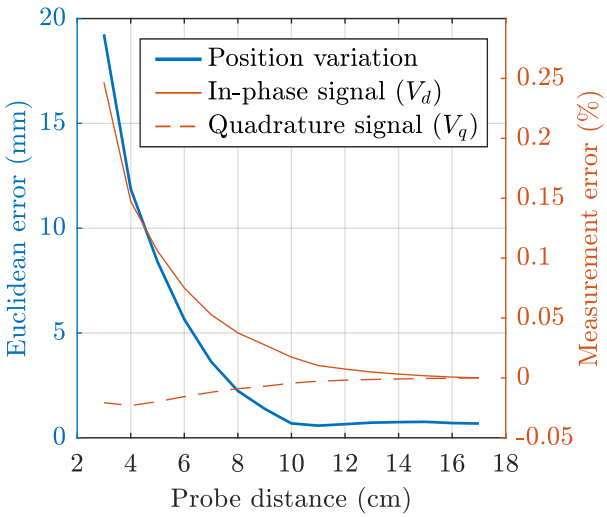


Figure 4.19: (a) The US probe was moved on a line approximately 15 cm above the field generator, and a witness sensor at a fixed position recorded the magnetic field variation. (b) The magnetic distortion affects the EMT position error and the direct and quadrature components of the field measurement.

tool C was used to record the distortion effect on its EMT position and the associated magnetic measurements. The distortion variation is visualised in Figure 4.19b.

The AC magnetic field was configured at a frequency between 2 kHz and 3 kHz for this experiment. Therefore, the distortion was mainly caused by eddy currents induced in the conductive distorter [46], as demonstrated by the appearance of an out-of-phase quadrature component, V_q, in the received signal, which is evident in Figure 4.19b.

A polynomial function was found to accurately model the 1D relation between the distorted signal and the probe distance:

$$V_d = p_{00} + p_{01}V_q + p_{02}V_q^2 + p_{10}D + p_{11}V_qD \tag{4.11}$$

where V_d is the in-phase direct component of the signal, and D is the distance from the US probe. The proposed technique involves extracting the signal components V_d and V_q from a new field measurement, then

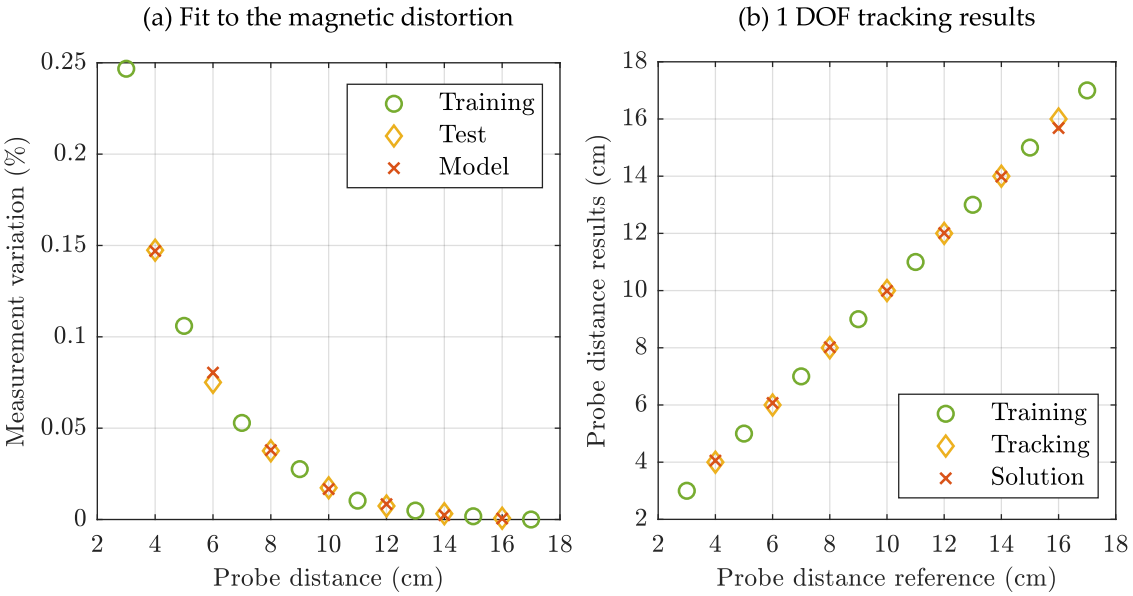


Figure 4.20: (a) Fitting effectiveness of the distortion model outlined in Equation 4.11. (b) Distortion-based tracking with one degree of freedom.

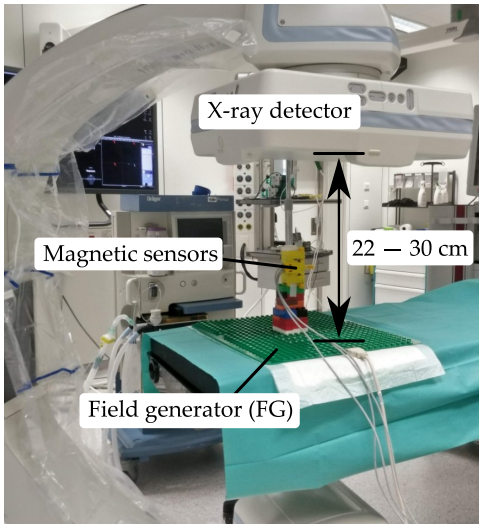
using Equation 4.11 to determine D and, in this way, track the probe on the line without a sensor connected to it.

The effectiveness of the distortion model outlined in Equation 4.11 is demonstrated in Figure 4.20. To prevent overfitting, the polynomial coefficients of Equation 4.11 were fitted using every second point with a spacing of 2 cm, whereas the test and tracking were carried out on the points in between, as seen in Figure 4.20a. The results of the 1 DOF tracking of the US probe are presented in Figure 4.20b.

The root-mean-square error (RMSE) calculated over the seven test points is 1.25 mm. The maximum error (MAXE) of 3.16 mm was obtained with the instrument placed at the highest distance of 16 cm when the distortion effect and, consequently, the information captured by the witness sensor were at a minimum.

In the second experiment, the CBCT scanner was used in combination with the ANSER EMT system to simulate a hybrid EMT and X-ray navigation framework [32]. The proximity of the interventional C-arm caused significant metallic distortion that led to the degradation of the EMT accuracy.

(a) Experimental setup



(b) Measurement grids

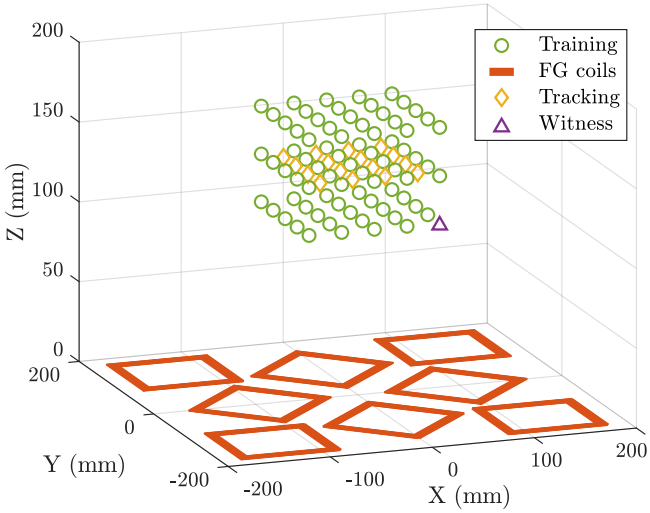


Figure 4.21: (a) The X-ray detector was moved to different vertical distances from the field generator ($Z = 22$, 24, 26, and 30 cm), and the magnetic field vector was captured on the training grid. Then, the X-ray detector was placed at $Z = 28$ cm, and the distance was estimated from the witness sensor measurement. A new calibrated field model was calculated based on the values pre-characterised and used to evaluate the EMT error on the tracking grid. (b) Position of the training grid, the tracking grid, and the witness sensor relative to the field generator coils.

The distorted magnetic field was pre-characterised within the tracking volume by moving magnetic sensors on a grid of $5 \times 5 \times 3$ training points, where the magnetic field vector was captured. The characterisation procedure was repeated for different distances of the X-ray detector above the field generator at $Z = 22$, 24, 26, and 30 cm. Duplo blocks were used to provide accurate and consistent support, and the defined grid spacing was used for sensor position and orientation reference. The experimental setup is shown in Figure 4.21.

The X-ray detector was then moved to a height of $Z = 28$ cm, generating a new distortion scenario not previously characterised. The technique presented in this work was used to estimate the unseen distorter's position from the witness sensor measurement. A compensated magnetic field model was obtained using a second-degree polynomial fit of the tabulated

characterisation maps, with cubic spline interpolation between the grid points.

Based on the witness sensor measurement, the distance of the X-ray detector was predicted as 28.1 cm using Equation 4.11. Considering that the reference distance of 28 cm was known within 0.5 cm tolerance, this likely accounts for the 1 mm error.

The EMT accuracy of the system was evaluated on a grid of 4×4 test points, comparing both the distorted and the compensated magnetic models to solve for the sensor pose. It should be noted that, in this case, the sensors were tracked using traditional EMT methods. In contrast, the witness sensor was used to estimate the X-ray detector location and enable real-time distortion compensation.

The static tracking test was carried out in the presence of the distorter at 28 cm, both before and after applying the distortion compensation method described above. The accuracy is evaluated for horizontal and vertical orientations of the magnetic marker along the Y-axis and the Z-axis, respectively. The results obtained in a distortion-clean environment were also included for comparison.

Position errors were calculated as the Euclidean distance between the EMT solution and the reference defined by the Duplo grid. The orientation errors were calculated as the absolute angular difference. Position and orientation error statistics are summarised in Table 4.8, and the cumulative position EMT error is visualised in Figure 4.22.

It is observed that the X-ray detector above the tracking volume introduced significant EMT errors, mainly affecting the sensor aligned vertically along the Z-axis of the planar field generator. In this case, the distortion caused an RMSE increment from 2.9 mm to 11.5 mm, which was reduced to 1.7 mm after compensation. The orientation error followed a similar pattern, increasing from 1.5° to 9.5° and reduced below 1° after correction.

The current study is limited to one witness sensor and 1 DOF tracking, but the method might be extended to multiple dimensions if additional witness sensors are included. Even so, the technique requires specific

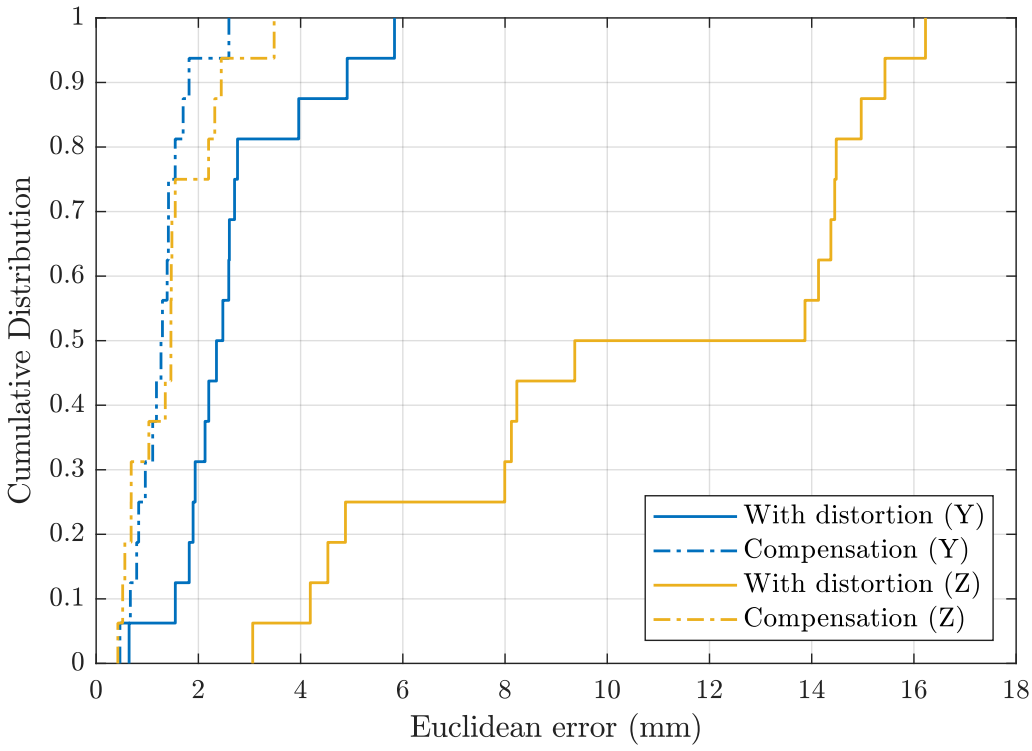


Figure 4.22: Position error with the X-ray detector placed $Z = 28$ cm above the field generator, for Y and Z-orientations. Errors are shown before and after applying the compensated magnetic field model to track the sensor.

pre-characterisation and training for every instrument to be tracked, and simultaneous tracking of multiple targets might not be feasible.

4.6 Conclusions

This chapter presented techniques for correcting systematic errors and static distortion, reducing metallic distortion by magnetic shielding, real-time detection of EMT accuracy impairment, and online compensation of dynamic distortion.

Traditional methods for field volume characterisation rely on arranging a large number of data points on regular grids and collecting triaxial field measurements, which can be time-consuming and impractical in most applications. These challenges were addressed by introducing a characterisation technique based on an underlying analytical magnetic

Table 4.8: Tracking test results in a distortion-free environment, with the distortion caused by the X-ray detector, before and after distortion compensation. For the last two columns, the error distributions are visualised in Figure 4.22.

	Without distortion	With distortion	Distortion compensation
Horizontal sensor (Y-oriented)			
Error	mm / deg	mm / deg	mm / deg
RMSE	2.15 / 0.94	2.93 / 1.38	1.36 / 0.48
PRC50	1.78 / 0.87	2.42 / 1.24	1.27 / 0.35
MAXE	3.80 / 1.42	5.84 / 2.28	2.58 / 1.04
Vertical sensor (Z-oriented)			
Error	mm / deg	mm / deg	mm / deg
RMSE	2.89 / 1.48	11.5 / 9.35	1.66 / 0.92
PRC50	2.60 / 1.22	11.6 / 10.2	1.38 / 0.78
MAXE	5.46 / 2.96	16.2 / 12.5	3.54 / 1.88

model. The new approach allows the training data to be arranged in scattered clouds and to use uniaxial measurements.

The modelling technique was employed for different use cases. A new magnetic model was created for the ANSER EMT field generator and was compared to the existing model by showing the tracking accuracy obtained in the two cases. The technique demonstrated effectiveness in modelling the highly distorted fields of the field generator with magnetic shielding.

The distortion introduced by a fluoroscopy system was analysed for different distances to the field generator in a clinical environment. It was proven that aluminium and mu-metal plates could effectively shield the ROI in the presence of external distorters. It was also shown that the field model inside the ROI could be corrected using data collected outside the ROI, presenting the intriguing potential for a real-time distortion compensation technique based on redundant measurements of external arrays of sensors.

EMT errors below 1 mm and 1° were demonstrated after compensation in all the experiments. Although the accuracy requirements vary depending on the specific procedure, tracking errors at millimetre and

degree levels are sufficient for most endoscopic and surgical navigation tasks [47–49].

References

[1] M. Cavaliere and P. Cantillon-Murphy, "Intraoperative compensation of magnetic field distortions for fluoroscopic and electromagnetic hybrid navigation," *International Journal of Computer Assisted Radiology and Surgery*, vol. 17, pp. 1717–1721, 2022, ISSN: 1861-6429. DOI: 10.1007/s11548-022-02663-7.

[2] M. Cavaliere, D. Crowley, H. A. Jaeger, K. O'Donoghue, and P. Cantillon-Murphy, "Magnetic Model Calibration and Distortion Compensation for Electromagnetic Tracking in a Clinical Environment," *IEEE Transactions on Magnetics*, vol. 59, no. 7, pp. 1–12, 2023, ISSN: 1941-0069. DOI: 10.1109/TMAG.2023.3275297.

[3] M. Cavaliere and P. Cantillon-Murphy, "Enhancing electromagnetic tracking accuracy in medical applications using pre-trained witness sensor distortion models," *International Journal of Computer Assisted Radiology and Surgery*, 2023, ISSN: 1861-6429. DOI: 10.1007/s11548-023-02994-z.

[4] A. Plotkin, V. Kucher, Y. Horen, and E. Paperno, "A New Calibration Procedure for Magnetic Tracking Systems," *IEEE Transactions on Magnetics*, vol. 44, no. 11, pp. 4525–4528, 2008, ISSN: 1941-0069. DOI: 10.1109/TMAG.2008.2003056.

[5] T. Bien and G. Rose, "Algorithm for calibration of the electromagnetic tracking system," in *Proceedings of 2012 IEEE-EMBS International Conference on Biomedical and Health Informatics*, 2012, pp. 85–88. DOI: 10.1109/BHI.2012.6211512.

[6] J. D. Jackson, *Classical Electrodynamics*, 3rd ed. New York: Wiley, 1999, pp. 174–236, ISBN: 978-0-471-30932-1.

[7] J. Vanderlinde, *Classical Electromagnetic Theory* (Fundamental Theories of Physics v. 145), 2nd ed. Dordrecht Boston: Kluwer Academic Publishers, 2004, pp. 26–28, ISBN: 978-1-4020-2700-0.

[8] J.-C. Nedelec, *Acoustic and Electromagnetic Equations: Integral Representations for Harmonic Problems*. New York; London: Springer, 2011, pp. 110–149, ISBN: 978-1-4419-2889-4.

[9] W. Hackbusch, *Integral Equations: Theory and Numerical Treatment* (International Series of Numerical Mathematics 120), 1. softcover ed.]; [Reprint of the orig. 1st ed. 1995. Basel: Birkhäuser, 2012, pp. 253–265, ISBN: 978-3-0348-9947-5.

[10] Encyclopedia of Mathematics, *Double-layer potential*. [Online]. Available: https://encyclopediaofmath.org/index.php?title=Double-layer_potential (visited on 12/10/2021).

[11] A. J. Mäkinen, R. Zetter, J. Iivanainen, K. C. J. Zevenhoven, L. Parkkonen, and R. J. Ilmoniemi, "Magnetic-field modeling with surface currents. Part I. Physical and computational principles of bfieldtools," *Journal of Applied Physics*, vol. 128, no. 6, p. 063 906, 2020, ISSN: 0021-8979. DOI: 10.1063/5.0016090.

[12] R. Zetter, A. J. Mäkinen, J. Iivanainen, K. C. J. Zevenhoven, R. J. Ilmoniemi, and L. Parkkonen, "Magnetic field modeling with surface currents. Part II. Implementation and usage of bfieldtools," *Journal of Applied Physics*, vol. 128, no. 6, p. 063 905, 2020, ISSN: 0021-8979. DOI: 10.1063/5.0016087.

[13] MathWorks, *Solve systems of linear equations $Ax = B$*. [Online]. Available: https://uk.mathworks.com/help/matlab/ref/mrdivide.html (visited on 09/14/2022).

[14] *Polaris Vega - NDI*. [Online]. Available: https://www.ndigital.com/products/polaris-vega/ (visited on 03/30/2022).

[15] V. V. Kindratenko, "A survey of electromagnetic position tracker calibration techniques," *Virtual Reality*, vol. 5, no. 3, pp. 169–182, 2000, ISSN: 1434-9957. DOI: 10.1007/BF01409422.

[16] K. O'Donoghue and P. Cantillon-Murphy, "Planar Magnetic Shielding for Use With Electromagnetic Tracking Systems," *IEEE Transactions on Magnetics*, vol. 51, no. 2, pp. 1–12, 2015, ISSN: 1941-0069. DOI: 10.1109/TMAG.2014.2352344.

[17] W. Ashe, "Magnetic position measurement system with field containment means," US6528991B2, 2003. [Online]. Available: https://patents.google.com/patent/US6528991B2/en (visited on 03/31/2021).

[18] W. Ashe, "Magnetic position and orientation measurement system with magnetic field permeable attenuator," US6784660B2, 2004. [Online]. Available: https://patents.google.com/patent/US6784660B2/en (visited on 03/31/2021).

[19] D. Meeker, *Finite Element Method Magnetics*. [Online]. Available: https://www.femm.info (visited on 02/15/2023).

[20] G. Zachmann, "Distortion Correction of Magnetic Fields for Position Tracking," in *Proc. Computer Graphics International*, Society Press, 1997, pp. 213–220.

[21] V. Harish, T. Ungi, A. Lasso, A. MacDonald, S. Nanji, and G. Fichtinger, "Intraoperative visualization and assessment of electromagnetic tracking error," in *Medical Imaging 2015: Image-Guided Procedures, Robotic Interventions, and Modeling*, vol. 9415, International Society for Optics and Photonics, 2015, 94152H. DOI: 10.1117/12.2082330.

[22] IEEE, "IEEE Standard for Safety Levels with Respect to Human Exposure to Electric, Magnetic, and Electromagnetic Fields, 0 Hz to 300 GHz," *IEEE Std C95.1-2019 (Revision of IEEE Std C95.1-2005/ Incorporates IEEE Std C95.1-2019/Cor 1-2019)*, pp. 1–312, 2019. DOI: 10.1109/IEEESTD.2019.8859679.

[23] K. O'Donoghue, H. A. Jaeger, and P. Cantillon-Murphy, "A Radiolucent Electromagnetic Tracking System for Use with Intraoperative X-ray Imaging," *Sensors*, vol. 21, no. 10, p. 3357, 2021. DOI: 10.3390/s21103357.

[24] W. Birkfellner, F. Watzinger, F. Wanschitz, R. Ewers, and H. Bergmann, "Calibration of tracking systems in a surgical environment," *IEEE Transactions on Medical Imaging*, vol. 17, no. 5, pp. 737–742, 1998, ISSN: 1558-254X. DOI: 10.1109/42.736028.

[25] T. Bien, M. Li, Z. Salah, and G. Rose, "Electromagnetic tracking system with reduced distortion using quadratic excitation," *International Journal of Computer Assisted Radiology and Surgery*, vol. 9, no. 2, pp. 323–332, 2014, ISSN: 1861-6429. DOI: 10.1007/s11548-013-0925-4.

[26] C. Nafis, V. Jensen, and R. v. J. M.d, "Method for evaluating compatibility of commercial electromagnetic (EM) microsensor tracking systems with surgical and imaging tables," in *Medical Imaging 2008: Visualization, Image-Guided Procedures, and Modeling*, vol. 6918, International Society for Optics and Photonics, 2008, p. 691 820. DOI: 10.1117/12.769513.

[27] G. Shechter, "Electromagnetic tracking method and apparatus for compensation of metal artifacts using modular arrays of reference sensors," US7902816B2, 2011. [Online]. Available: https://patents.google.com/patent/US7902816B2/en (visited on 09/20/2021).

[28] E. Shen, "System and method for dynamic metal distortion compensation for electromagnetic tracking systems," US20110270083A1, 2011. [Online]. Available: https://patents.google.com/patent/US20110270083A1/en (visited on 09/20/2021).

[29] E. Shen and J. Kruecker, "System for local error compensation in electromagnetic tracking systems," EP2005208B1, 2017. [Online]. Available: https://patents.google.com/patent/EP2005208B1/en (visited on 09/20/2021).

[30] H. Sadjadi, K. Hashtrudi-Zaad, and G. Fichtinger, "Simultaneous localization and calibration for electromagnetic tracking systems," *The International Journal of Medical Robotics and Computer Assisted Surgery*, vol. 12, no. 2, pp. 189–198, 2016, ISSN: 1478-596X. DOI: 10.1002/rcs.1670.

[31] H. Krumb *et al.*, "Leveraging spatial uncertainty for online error compensation in EMT," *International Journal of Computer Assisted Radiology and Surgery*, vol. 15, no. 6, pp. 1043–1051, 2020, ISSN: 1861-6410, 1861-6429. DOI: 10.1007/s11548-020-02189-w.

[32] H. Krumb, D. Das, R. Chadda, and A. Mukhopadhyay, "CycleGAN for interpretable online EMT compensation," *International Journal of Computer Assisted Radiology and Surgery*, vol. 16, no. 5, pp. 757–765, 2021, ISSN: 1861-6410, 1861-6429. DOI: 10.1007/s11548-021-02324-1.

[33] H. Ren, D. Rank, M. Merdes, J. Stallkamp, and P. Kazanzides, "Multisensor Data Fusion in an Integrated Tracking System for Endoscopic Surgery," *IEEE Transactions on Information Technology in Biomedicine*, vol. 16, no. 1, pp. 106–111, 2012, ISSN: 1089-7771, 1558-0032. DOI: 10.1109/TITB.2011.2164088.

[34] Y. Zhang, K. Wang, J. Jiang, and Q. Tan, "Research on Intraoperative Organ Motion Tracking Method Based on Fusion of Inertial and Electromagnetic Navigation," *IEEE Access*, vol. 9, pp. 49 069–49 081, 2021, ISSN: 2169-3536. DOI: 10.1109/ACCESS.2021.3068741.

[35] D. K. O'Donoghue, D. H. A. Jaeger, and D. P. C. Murphy, "Sensor fusion hardware platform for robust electromagnetic navigation," in *IEEE I2MTC 2022*, Ottawa, Canada, 2022.

[36] O. V. Ivashchenko *et al.*, "CBCT-based navigation system for open liver surgery: Accurate guidance toward mobile and deformable targets with a semi-rigid organ approximation and electromagnetic tracking of the liver," *Medical Physics*, vol. 48, no. 5, pp. 2145–2159, 2021, ISSN: 2473-4209. DOI: 10.1002/mp.14825.

[37] K. Lee, K. M. Lee, M. S. Park, B. Lee, D. G. Kwon, and C. Y. Chung, "Measurements of Surgeons' Exposure to Ionizing Radiation Dose During Intraoperative Use of C-Arm Fluoroscopy," *Spine*, vol. 37, no. 14, pp. 1240–1244, 2012, ISSN: 0362-2436. DOI: 10.1097/BRS.0b013e31824589d5.

[38] US-EPA, *Radiation Health Effects*, Overviews and Factsheets, 2014. [Online]. Available: https://www.epa.gov/radiation/radiation-health-effects (visited on 03/01/2023).

[39] B. J. Wood *et al.*, "Navigation with Electromagnetic Tracking for Interventional Radiology Procedures: A Feasibility Study," *Journal of Vascular and Interventional Radiology*, vol. 16, no. 4, pp. 493–505, 2005, ISSN: 1051-0443. DOI: 10.1097/01.RVI.0000148827.62296.B4.

[40] Z. Xiong, J. E. McGary, and J. Chen, "Self-Correcting Magnetic Tracking in Dynamic Medical Environments," *IEEE Transactions on Magnetics*, vol. 51, no. 2, pp. 1–9, 2015, ISSN: 1941-0069. DOI: 10.1109/TMAG.2014.2345333.

[41] B. Ramachandran and A. K. Jain, "Distortion fingerprinting for EM tracking compensation, detection and error correction," US9522045B2, 2016. [Online]. Available: https://patents.google.com/patent/US9522045B2/en.

[42] M. R. Schneider and K. Fujioka, "Compensating for Distortion in an Electromagnetic Tracking System," US20190242952A1, 2019. [Online]. Available: https://patents.google.com/patent/US20190242952A1/en (visited on 05/12/2020).

[43] S. Sharma *et al.*, "Wireless 3D Surgical Navigation and Tracking System with 100μm Accuracy Using Magnetic-Field Gradient-Based Localization," *IEEE Transactions on Medical Imaging*, pp. 2066–2079, 2021, ISSN: 0278-0062, 1558-254X. DOI: 10.1109/TMI.2021.3071120.

[44] P. L. Bono, J. D. Lark, and J. S. Scales, "System and method for reducing interference in positional sensors for robotic surgery," US20200337783A1, 2020. [Online]. Available: https://patents.google.com/patent/US20200337783A1/en.

[45] M. Feuerstein, T. Reichl, J. Vogel, J. Traub, and N. Navab, "Magneto-Optical Tracking of Flexible Laparoscopic Ultrasound: Model-Based Online Detection and Correction of Magnetic Tracking Errors," *IEEE Transactions on Medical Imaging*, vol. 28, no. 6, pp. 951–967, 2009, ISSN: 1558-254X. DOI: 10.1109/TMI.2008.2008954.

[46] M. A. Nixon, B. C. McCallum, W. R. Fright, and N. B. Price, "The Effects of Metals and Interfering Fields on Electromagnetic Trackers," *Presence: Teleoperators and Virtual Environments*, vol. 7, no. 2, pp. 204–218, 1998, ISSN: 1054-7460, 1531-3263. DOI: 10.1162/105474698565587.

[47] Z. Yaniv, E. Wilson, D. Lindisch, and K. Cleary, "Electromagnetic tracking in the clinical environment," *Medical Physics*, vol. 36, no. 3, pp. 876–892, 2009, ISSN: 00942405. DOI: 10.1118/1.3075829.

[48] G. Ahmad *et al.*, "Impact of Fluoroscopy Unit on the Accuracy of a Magnet-Based Electroanatomic Mapping and Navigation System: An In Vitro and In Vivo Validation Study," *Pacing and Clinical Electrophysiology*, vol. 37, no. 2, pp. 157–163, 2014, ISSN: 1540-8159. DOI: 10.1111/pace.12231.

[49] A. Ramadani, M. Bui, T. Wendler, H. Schunkert, P. Ewert, and N. Navab, "A survey of catheter tracking concepts and methodologies," *Medical Image Analysis*, vol. 82, 2022, ISSN: 1361-8415. DOI: 10.1016/j.media.2022.102584.

Chapter 5

Tracking algorithm with increased update rate

In this chapter, a novel tracking algorithm for ANSER EMT is proposed, and the implementation is tested in MATLAB.

The method enables multiple sensor tracking at update rates above 100 Hz. Such high rates limit the time available for signal acquisition and cause increased jitter noise in the measurements if not properly filtered.

Low-pass filtering techniques, such as a sliding window DFT and a simple or exponential moving average, are presented in Section 5.2. The drawback is the latency added to the system. For this reason, Sections 5.2.3 and 5.3 introduce more advanced filters with the estimation of the linear motion to predict the object trajectory and reduce the latency.

In Section 5.4, the novel algorithms are analysed through a dynamic tracking test. The Kalman filter resulted as the preferred choice because it demonstrated optimal smoothing effect and reduced delay, with low calculation requirements and high speed.

5.1 Improvements to the algorithm and to the magnetic model

In this section, we propose a novel accelerated algorithm to update the pose estimate of a sensor from a previously known pose and recommendations for increasing the speed of the magnetic model.

5.1.1 Algorithm for a faster pose update

The target objects to be tracked are mostly instruments used in endoscopic operations, and their movements are relatively slow. Therefore, a reasonable assumption is to consider the target speed not larger than 50 mm per second. Considering a typical update rate of 25 Hz, as seen in Section 3.2, the maximum displacement of the sensor between subsequent acquisitions is around $^{50}/_{25} = 2$ mm. Similar considerations apply to the change in orientation. Moreover, thanks to the methods described in this section, higher update rates are possible, and the difference between consecutive poses can be further reduced.

The method is based on a local linearisation of the flux model, which allows transformation of the non-linear least-squares problem presented in Section 3.2.4 into a linear algorithm, which requires less time and calculation power.

As seen in Section 3.2.3, the signal component induced by each of the eight ANSER EMT emitter coils is a function of the sensor pose, $\mathbf{p}$. A change in the pose from $\mathbf{p^k}$ to $\mathbf{p^{k+1}}$ causes a change in the flux model that can be approximated by a Taylor expansion:

$$\Phi_{ec}(\mathbf{p^{k+1}}) \approx \Phi_{ec}(\mathbf{p^k}) + \mathbf{J^k_{ec}} \cdot \left(\mathbf{p^{k+1}} - \mathbf{p^k}\right) \tag{5.1}$$

where $1 \leq ec \leq 8$ identifies the emitter coil and the row vector $\mathbf{J^k_{ec}}$ comprises the partial derivatives with respect to the variables in $\mathbf{p}$, as given by Equation 5.2:

$$\mathbf{J^k_{ec}} = \left[\frac{\partial\Phi(\mathbf{p^k})}{\partial x}\ \frac{\partial\Phi(\mathbf{p^k})}{\partial y}\ \frac{\partial\Phi(\mathbf{p^k})}{\partial z}\ \frac{\partial\Phi(\mathbf{p^k})}{\partial \theta}\ \frac{\partial\Phi(\mathbf{p^k})}{\partial \varphi}\right]_{ec} \tag{5.2}$$

Equation 5.1 can be expressed for every *ec* in a compact equation by defining $\mathbf{\Phi^k} = [\cdots \Phi_{ec}(\mathbf{p^k}) \cdots]^T$ as the vector of eight flux models and by introducing the 8×5 Jacobian matrix, $\mathbf{J}$, which includes eight rows in the form of Equation 5.2:

$$\mathbf{\Phi^{k+1}} \approx \mathbf{\Phi^k} + \mathbf{J} \cdot \left(\mathbf{p^{k+1}} - \mathbf{p^k}\right) \tag{5.3}$$

Even if the superscript k is neglected, matrix $\mathbf{J}$ is evaluated in $\mathbf{p^k}$.

By defining $\widetilde{\mathbf{\Phi}}^{\mathbf{k+1}}$ as the column vector comprising the eight demodulated signal values at time $k+1$, the tracking algorithm aims to find $\mathbf{\Phi^{k+1}}$ that minimises the two-norm $\|\widetilde{\mathbf{\Phi}}^{\mathbf{k+1}} - \mathbf{\Phi^{k+1}}\|_2$.

An idea is to substitute $\mathbf{\Phi^{k+1}}$ with $\widetilde{\mathbf{\Phi}}^{\mathbf{k+1}}$ in Equation 5.3 and to resolve for $\mathbf{p^{k+1}}$:

$$\mathbf{p^{k+1}} = \mathbf{p^k} + \mathbf{J^\dagger} \cdot \left(\widetilde{\mathbf{\Phi}}^{\mathbf{k+1}} - \mathbf{\Phi^k}\right) \tag{5.4}$$

where $\mathbf{J^\dagger} = \left(\mathbf{J^T J}\right)^{-1} \mathbf{J^T}$ is the Moore–Penrose inverse of the matrix $\mathbf{J}$, which is not calculated explicitly because the least-squares solution for $\mathbf{p^{k+1}}$ can be obtained from optimised algorithms used in the *backslash* operator of MATLAB [1].

In fact, it can be demonstrated that Equation 5.4 corresponds to one step of the Gauss-Newton algorithm [2]. Vector $\widetilde{\mathbf{p}}$ is the set of parameters that minimises the sum of squares:

$$\begin{aligned} \widetilde{\mathbf{p}} &= \arg\min_{\mathbf{p}} \sum_{ec=1}^{8} \left[\widetilde{\Phi}_{ec}^{k+1} - \Phi_{ec}^{k+1}\right]^2 \\ &= \arg\min_{\mathbf{p}} \sum_{ec=1}^{8} \left[\widetilde{\Phi}_{ec}^{k+1} - \Phi_{ec}^{k} - \mathbf{J_{ec}^k} \cdot \Delta\mathbf{p})\right]^2 \end{aligned} \tag{5.5}$$

where the linearisation step of Equation 5.1 was used in the second part of Equation 5.5, with $\Delta\mathbf{p} = \mathbf{p^{k+1}} - \mathbf{p^k}$.

The minimum is obtained when the gradient is null. Taking the derivative with respect to the unknown increments $\Delta\mathbf{p}$, and setting the derivative equal to 0 to minimise the difference between the actual pose and the esti-

mator, gives:

$$\begin{aligned}
&\frac{\partial}{\partial \Delta \mathbf{p}} \sum_{ec=1}^{8} \left[\widetilde{\Phi}_{ec}^{k+1} - \Phi_{ec}^{k} - \mathbf{J_{ec}^{k}} \cdot \Delta \mathbf{p}) \right]^2 = \\
&= \begin{pmatrix} \sum_{ec=1}^{8} 2 \left[\widetilde{\Phi}_{ec}^{k+1} - \Phi_{ec}^{k} - \mathbf{J_{ec}^{k}} \cdot \Delta \mathbf{p} \right] \frac{\partial \Phi_{ec}^{k}}{\partial x} \\ \vdots \\ \sum_{ec=1}^{8} 2 \left[\widetilde{\Phi}_{ec}^{k+1} - \Phi_{ec}^{k} - \mathbf{J_{ec}^{k}} \cdot \Delta \mathbf{p} \right] \frac{\partial \Phi_{ec}^{k}}{\partial \varphi} \end{pmatrix} \\
&= 2 \left[\left(\mathbf{J_1}^T \right) \cdots \left(\mathbf{J_8}^T \right) \right] \cdot \left(\widetilde{\mathbf{\Phi}}^{\mathbf{k+1}} - \mathbf{\Phi^{k}} - \mathbf{J} \cdot \Delta \mathbf{p} \right) \\
&= 2 \mathbf{J^{T}} \left(\widetilde{\mathbf{\Phi}}^{\mathbf{k+1}} - \mathbf{\Phi^{k}} - \mathbf{J} \Delta \mathbf{p} \right) = 0
\end{aligned} \tag{5.6}$$

From Equation 5.6, the solution for $\Delta \mathbf{p}$ results:

$$\Delta \mathbf{p} = \left(\mathbf{J^{T}J} \right)^{-1} \mathbf{J^{T}} \left(\widetilde{\mathbf{\Phi}}^{\mathbf{k+1}} - \mathbf{\Phi^{k}} \right) \tag{5.7}$$

which is equivalent to Equation 5.4, with $\Delta \mathbf{p} = \mathbf{p^{k+1}} - \mathbf{p^{k}}$ and $\mathbf{J^{\dagger}} = \left(\mathbf{J^{T}J} \right)^{-1} \mathbf{J^{T}}$.

The novel algorithm presented in this section requires the current pose to be known. Therefore, if a new sensor is added to the system or if a sensor moves out of range, the global search algorithm described in Section 3.2.4 must be used for pose initialisation.

Moreover, for the proposed method to converge to the correct solution, it is important that the sensor pose does not change significantly between subsequent magnetic measurements.

Particular care should be taken for the sensor orientation because even when the spatial variation of the three magnetic field components is linear, the orientation unit vector has a trigonometric dependence on the spherical angles. In the limit of orthogonal angles, uncorrelated magnetic flux components are picked up by the coil.

It was observed that the algorithm typically converges when the difference between consecutive is below 2 cm and $\pi/4$ rad, for positions at more than 15 cm from the field generator.

A robust implementation of the algorithm was obtained by monitoring the residual $\|\widetilde{\mathbf{\Phi}} - \mathbf{\Phi}\|_2$. If the residual does not fall under a threshold value in 5 iterations, the initial pose guess is re-initialised, and the complete Trust-region algorithm presented in Section 3.2.4 is employed.

5.1.2 Increased-speed magnetic model

The analytical magnetic model presented in Section 3.2.3 requires approximately 40 µs to calculate the eight signal values on a Windows 10 laptop with i5-11th Gen. Intel Core Processor.

The speed can be approximately doubled if the model is pre-evaluated at grid points within the region of interest (ROI) and interpolated using, for example, the *griddedInterpolant* command [3]. Analysis of the grid density requirements and interpolation error will be presented in Section 6.4.2.

It should be noticed that, when using an *Interpolant* object in MATLAB, most of the computation time is spent loading the look-up table (LUT) into memory. For example, a table of $30 \times 30 \times 30$ points required around 50 ms to evaluate one position on the first call, and the evaluation time dropped to 20 µs for subsequent calls. Therefore, it is essential to use the interpolating function at least once when the system is initialised.

The *lsqnonlin* EMT algorithm introduced in Section 3.2.4 was evaluated on 1000 random positions and orientations, using the analytical and the tabulated models. Although a small improvement was demonstrated using the faster model, a convergence time of approximately 5 ms was obtained in either case, showing that the evaluation time of the objective function is not the only factor affecting the speed of the optimisation algorithm.

The interpolating function can be evaluated at multiple query points at the same time. In this way, the calculation of the eight magnetic fluxes at 1000 random poses was reduced from 20 to 1 µs per pose.

This solution is useful when multiple locations must be evaluated at the same time, for example for faster simulations and system optimisation studies, for the calibration of multiple-sensors tools, such as the method seen in Section 3.2.3.2, as well as for a more efficient way to numerically

estimate the Jacobian matrix, which requires ten model evaluations to calculate five finite differences, as seen in Section 3.2.3.1.

Another useful application was found when multiple sensors are tracked in real time, using the linearised algorithm introduced in Section 5.1.1, where Equation 5.4 can be solved with the *MultiSolver* function [4]. Using this approach, the average solution time per sensor resulted in 0.4 ms for one sensor, 0.18 ms per sensor for ten sensors, and 0.17 ms per sensor for one hundred sensors tracked simultaneously.

5.2 Random noise reduction

As seen in Section 3.2.4, the system update rate is typically limited by the speed of the solver block, which employs Trust-region or Levenberg-Marquart algorithms to ensure robustness and global convergence at the cost of more iterations and function evaluations.

When using faster methods, such as those presented in Section 5.1.1, it is possible to increase the update rate, and the limiting factor becomes the signal window acquisition time. However, as explained in Section 3.2.2, the random noise distributes equally among the frequency bins. Therefore, if the window period T_w is halved, the noise power is doubled for every frequency component, including for the eight frequencies of interest. This results in a noise amplitude $\sqrt{2}$ times larger, or equivalently a signal-to-noise ratio (SNR) reduced by 3 dB.

In this section, some basic noise-filtering techniques are introduced, and in the next Section 5.3, the more advanced Kalman filter algorithm is presented.

5.2.1 Sliding window DFT

In Section 3.2.2, it was shown how the signal is extracted from the raw acquired data, using the discrete Fourier transform (DTF) calculated on subsequent windows.

Using a sliding window approach, consecutive windows of length N_s are used that overlap on a number of samples $N_s - N_w$, as shown in

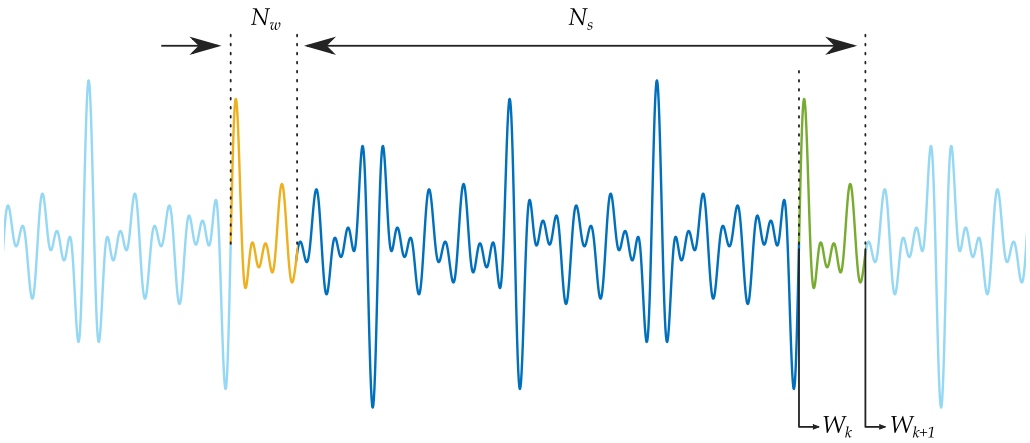


Figure 5.1: A sliding window of size N_s is updated every N_w samples, for an increased update-rate. The latency does not change, as the average delay remains of $N_s/2$ samples.

Figure 5.1. In this way, the demodulated signal can be updated at a rate of F_s/N_w, where F_s is the sampling frequency, without the necessity to increase the base bin frequency $F_b = F_s/N_s$, which is proportional to the bin noise power.

The signal at time $k+1$ can be calculated from the signal at time k as:

$$\begin{aligned}\overline{\Phi_{ec}}^{(k+1)} &= \frac{1}{N_s}\sum_{n=N_w}^{N_s-1+N_w} s[n]\cdot e^{-i\frac{2\pi n}{N_s}m_{ec}} \\ &= \overline{\Phi_{ec}}^{(k)} - \frac{1}{N_s}\sum_{n=0}^{N_w-1} s[n]\cdot e^{-i\frac{2\pi n}{N_s}m_{ec}} + \frac{1}{N_s}\sum_{n=N_s}^{N_s-1+N_w} s[n]\cdot e^{-i\frac{2\pi n}{N_s}m_{ec}}\end{aligned} \tag{5.8}$$

where $i = \sqrt{-1}$ is the imaginary unit, and $m_{ec} = F_{ec}/F_b$ is the frequency index, as explained in Section 3.2.2.

In Equation 5.8, the oldest sub-window of data is removed, and the newest N_w samples are added to the sum. This provides a fast way to compute the DFT recursively at the cost of memory because a number of N_s/N_w sub-windows must be stored. In the limit of the difference between

two consecutive DFTs being of one sample, $N_w = 1$, Equation 5.8 becomes:

$$\overline{\Phi_{ec}}^{(k+1)} = \overline{\Phi_{ec}}^{(k)} - \frac{1}{N_s} s[0] + \frac{1}{N_s} s[N_s] \tag{5.9}$$

given that $e^{-i\frac{2\pi 0}{N_s} m_{ec}} = e^{-i\frac{2\pi N_s}{N_s} j m_{ec}} = 1$.

If an integer number of periods of the AC signals of interest is contained in the time N_w/F_s, then the new N_w samples are also a valid size for a DFT, and Equation 5.8 becomes equivalent to a moving average over the last $N_{av} = N_s/N_w$ sub-windows of size N_w.

For example, $N_{av} = 2$ is the case of consecutive windows overlapping for half of the size of the previous window. The demodulated signal is:

$$\begin{aligned}\overline{\Phi_{ec}} &= \frac{1}{N_s}\left(\sum_{n=0}^{N_w-1} s[n]\cdot e^{-i\frac{2\pi n}{N_s} m_{ec}} + \sum_{n=N_w}^{N_s-1} s[n]\cdot e^{-i\frac{2\pi n}{N_s} m_{ec}}\right) \\ &= \frac{1}{2}\left(\frac{1}{N_w}\sum_{n=0}^{N_w-1} s[n]\cdot e^{-i\frac{2\pi n}{N_w}\frac{m_{ec}}{2}} + \frac{1}{N_w}\sum_{n=0}^{N_w-1} s[n+N_w]\cdot e^{-i\frac{2\pi n}{N_w}\frac{m_{ec}}{2}}\right)\end{aligned} \tag{5.10}$$

which is the mean of two DFTs of size N_w.

With the moving-average interpretation of the sliding window method, it can be noticed that it is not, in fact, required for subsequent windows to be consecutive. A gap between windows is allowed as long as there is a common phase reference for every window, such as the phase of the electric current in the coils, as explained in Section 3.2.2.

Averaging the N_{av} signals and then running the search algorithm once is equivalent to running the algorithm N_{av} times and calculating the average of the resulting poses if the displacement between subsequent poses is such that the magnetic model can be considered to vary approximately linearly. The first solution is preferred because it allows for running the optimisation algorithm on a cleaner signal and therefore getting faster convergence. Note that in either case, the algorithm is called the same number of times, once every N_w/F_s seconds.

The moving average has a low-pass filtering effect; the random noise is reduced, but the latency of the system is increased because older data

is used in the mean. The trade-off is between the SNR and the latency, whereas the upper limit for the update rate is given by the communication link from the device to the laptop and by the EMT algorithm speed.

5.2.2 Exponential moving average

The exponential moving average (EMA), or exponentially weighted moving average (EWMA), is an alternative way to low-pass filter the signal, using weighting factors which decrease exponentially [5].

If $\widetilde{\mathbf{\Phi}}^{\mathbf{k+1}}$ is the vector of measured magnetic values at time $k+1$, the filtered output, $\mathbf{S}^{\mathbf{k+1}}$, is given by the recursive formula in Equation 5.11.

$$\mathbf{S}^{\mathbf{k+1}} = (1-\lambda)\mathbf{S}^{\mathbf{k}} + \lambda\widetilde{\mathbf{\Phi}}^{\mathbf{k+1}} \tag{5.11}$$

where $0 \leq \lambda \leq 1$ is the smoothing parameter.

It can be observed that the weights decrease exponentially like $\lambda(1-\lambda)^t$ for observations that are t steps in the past:

$$\begin{aligned} \mathbf{S}^{\mathbf{k+1}} &= (1-\lambda)\mathbf{S}^{\mathbf{k-1}} + \lambda(1-\lambda)\widetilde{\mathbf{\Phi}}^{\mathbf{k}} + \lambda\widetilde{\mathbf{\Phi}}^{\mathbf{k+1}} \\ &= \sum_{t=0}^{k} \lambda(1-\lambda)^t \widetilde{\mathbf{\Phi}}^{\mathbf{k+1-t}} \end{aligned} \tag{5.12}$$

assuming that the algorithm is initialised with $\mathbf{S}^{\mathbf{0}} = \mathbf{0}$.

The average latency introduced by the EMA filter can be calculated from the response to a unit step function:

$$\mathbf{S}^{\mathbf{k}} = \lambda \sum_{t=0}^{k} (1-\lambda)^t = \lambda \frac{1-(1-\lambda)^k}{1-(1-\lambda)} = 1-(1-\lambda)^k \tag{5.13}$$

whose time constant, τ, is the value of k when the exponential law of Equation 5.13 reaches $1 - 1/e \approx 63.2\%$ of the original signal:

$$1-(1-\lambda)^{\tau} = 1-\frac{1}{e} \rightarrow \tau = -\frac{1}{\log(1-\lambda)} \tag{5.14}$$

For example, a lag of five steps, corresponding to the latency obtained from the moving average of ten subsequent windows, is obtained with $\lambda = 1 - e^{-1/5} \approx 0.18$. As a rule of thumb, we allow $\tau \approx 1/\lambda$.

5.2.3 EMA with speed estimation

Compensation for the latency can be obtained by estimating the time variation of the signal. This solution also applies to any other low-pass filtering technique, including the moving average approach introduced in Section 5.2.1. When the filter is applied to the EMT pose, the signal time variation corresponds to the positional and angular velocity of the sensor.

The speed, $\mathbf{V^{k+1}}$, was estimated as the finite difference between consecutive steps, $\widetilde{\mathbf{\Phi}}^{\mathbf{k+1}} - \widetilde{\mathbf{\Phi}}^{\mathbf{k}}$, where an exponential moving average was used to reduce the noise:

$$\mathbf{V^{k+1}} = (1-\lambda)\mathbf{V^{k}} + \lambda(\widetilde{\mathbf{\Phi}}^{\mathbf{k+1}} - \widetilde{\mathbf{\Phi}}^{\mathbf{k}}) \tag{5.15}$$

A prediction for the next signal was obtained with the following:

$$\mathbf{S^{k+1|k}} = \mathbf{S^{k}} + \mathbf{V^{k+1}} \tag{5.16}$$

which was subsequently averaged with the real signal:

$$\begin{aligned} \mathbf{S^{k+1}} &= (1-\lambda)\mathbf{S^{k+1|k}} + \lambda\widetilde{\mathbf{\Phi}}^{\mathbf{k+1}} \\ &= (1-\lambda)\mathbf{S^{k}} + \lambda\widetilde{\mathbf{\Phi}}^{\mathbf{k+1}} + (1-\lambda)\mathbf{V^{k+1}} \end{aligned} \tag{5.17}$$

Comparison with Equation 5.11 shows that the only difference is the addition of the term $(1-\lambda)\mathbf{V^{k+1}}$, accounting for the signal variation.

The two Equations 5.15 and 5.17 can be regarded as a method of double, or second-order, exponential smoothing, where the slope component $\mathbf{V^{k+1}}$ is introduced to take into account the linear trend in the data.

The main advantage of the EMA approach is the small number of calculations required, thanks to the recursive formulation, and the fact that only two arrays need to be kept in memory, the smoothed sum $\mathbf{S^{k}}$ and the velocity estimate $\mathbf{V^{k}}$.

5.3 Kalman Filtering

The Kalman filter (KF) is an algorithm commonly used in object tracking because of its high performance and low computational requirements [6].

The algorithm was first introduced in 1960 [7] and allows finding the best estimate for the state of a stochastic process in a recursive way [8]. The only assumptions are that the state vector follows a multi-variate Gaussian distribution and that both the system dynamics and observation equations are linear. More advanced filters, such as the extended Kalman filter (EKF) and the unscented Kalman filter (UKF), can be used for non-linear estimation [9–11].

In general, when a stochastic variable undergoes a linear transformation, the resulting probability distribution is still Gaussian, and the maximum likelihood estimate for the variable is the one that minimises the mean-squares error.

Kalman filtering is typically applied in the area of autonomous or assisted navigation to perform sensor fusion between an inertial measurement unit (IMU) and a global positioning system (GPS) [12]. The IMU estimates the object pose by integrating the linear and angular accelerations measured. This method provides high dynamics and low noise, but it is subject to drift due to the integration operation. The GPS offers a reference value that does not drift but is less precise. With a KF, the state vector estimate given by the IMU can be corrected using the GPS information to remove the drift.

Regarding biomedical applications, the UKF was applied for robust optical and magnetic fusion in surgical navigation [13], and EKF sensor fusion was used to correct errors due to magnetic distortion using inertial measurements [14], for endoscopic surgery [15] and for intraoperative tracking of target organs motion [16].

The KF also finds application in cases where EMT is the only source of information for position tracking, using underlying models to increase the tracking confidence. For example, in prostate brachytherapy, needle shape estimation can be improved by using two sensors, one larger and more accurate mounted at the base and a second miniaturised lower-sensitivity

sensor on the tip, combined together by an EKF using a tip deflection model [17, 18].

Kinematic models can be employed to estimate the object trajectory and suppress measurement noise by using Bayesian statistics. In this setting, KFs are typically used in EMT systems to guarantee smoother motion tracking [19–21]. Non-linear KFs can also be used as part of the search algorithm for tracking magnetic field sources [22], such as a vessel containing ferromagnetic material modelled at a distance as an equivalent magnetic dipole moment [23], or a portable magnetic position and orientation tracker containing three-axial sources and sensors [24].

A motion law is described in the next Section 5.3.1 to estimate and predict the sensor pose. The model prediction is used together with the raw EMT solution to obtain smoother, real-time tracking. The KF provides significant noise reduction with minimal latency.

5.3.1 Kalman filter

The sensor state was defined as the sensor pose and its linear and angular velocity:

$$\mathbf{s} = \begin{bmatrix} x\, y\, z\, \theta\, \varphi\, v_x\, v_y\, v_z\, \omega_\theta\, \omega_\varphi \end{bmatrix}^T \tag{5.18}$$

Given the sensor velocity and acceleration at a particular instant in time, k, we can predict where the sensor will move after a time step, T_s. For example, the law of motion in the x direction is:

$$\begin{aligned} x^{k+1} &= x^k + v_x^k T_s + \frac{1}{2} a_x^k T_s^2 \\ v_x^{k+1} &= v_x^k + a_x^k T_s \end{aligned} \tag{5.19}$$

Therefore, the dynamics of the motion is encoded in matrices $\mathbf{D}$ and $\mathbf{G}$:

$$\mathbf{D} = \begin{bmatrix} \mathbf{I_5} & \mathbf{I_5} Ts \\ \mathbf{0_5} & \mathbf{I_5} \end{bmatrix}; \quad \mathbf{G} = \begin{bmatrix} \mathbf{I_5} \frac{Ts^2}{2} \\ \mathbf{I_5} Ts \end{bmatrix} \tag{5.20}$$

where $\mathbf{I_5}$ and $\mathbf{0_5}$ are the 5×5 identity and empty matrices, respectively. The law of motion is expressed in matrix form for all the elements of the

state vector as:

$$\mathbf{s^{k+1}} = \mathbf{D} \cdot \mathbf{s^k} + \mathbf{G} \cdot \mathbf{a^k} \tag{5.21}$$

where $\mathbf{a} = \begin{bmatrix} a_x \, a_y \, a_z \, a_\theta \, a_\varphi \end{bmatrix}^T$ is the acceleration vector for the five degrees of freedom.

Because information on the linear and angular acceleration is not available, we consider $\mathbf{a}$ to be a random variable normally distributed with mean 0 and standard deviation σ_a. By setting higher values for σ_a, the estimated velocity is allowed to change faster, and therefore the inertia of the tracked position and the low-pass filtering effect is decreased. When an IMU is available, it could provide the mean and standard deviation of the acceleration vector.

The state vector is known up to a level of confidence described by the 10×10 covariance matrix $\mathbf{P}$, which comprises the variance of state variables on the diagonal, and their correlation on the out-of-diagonal entries.

The first step of the Kalman filter algorithm is the *prediction* of the next state vector based on the current state. The best estimate is given by:

$$\mathbf{s^{k+1|k}} = \mathbf{D} \cdot \mathbf{s^{k|k}} \tag{5.22}$$

where the acceleration term is not present because, having zero mean, the best estimate for it is null. The notation $\mathbf{k+1|k}$ indicates the *a priori* state estimate at time $k+1$, given the information available at time k.

The covariance matrix propagates through a linear transformation as per Equation 3.24, and therefore the covariance matrix of the state prediction vector is:

$$\mathbf{P^{k+1|k}} = \mathbf{D} \cdot \mathbf{P^{k|k}} \cdot \mathbf{D^T} + \mathbf{Q} \tag{5.23}$$

where matrix $\mathbf{Q} = \mathbf{G}\mathbf{G}^T\sigma_a^2$ accounts for the uncertainty associated with the acceleration of the sensor.

When a new pose solution, $\mathbf{p}$, is available from the EMT algorithm, the state prediction has to be updated with the new information.

The *update* step is given by:

$$\mathbf{s}^{\mathbf{k+1|k+1}} = \mathbf{s}^{\mathbf{k+1|k}} + \mathbf{K} \cdot \left(\mathbf{p} - \mathbf{L} \cdot \mathbf{s}^{\mathbf{k+1|k}}\right) \tag{5.24}$$

$$\mathbf{P}^{\mathbf{k+1|k+1}} = \mathbf{P}^{\mathbf{k+1|k}} - \mathbf{K} \cdot \mathbf{L} \cdot \mathbf{P}^{\mathbf{k+1|k}} \tag{5.25}$$

where $\mathbf{s}^{\mathbf{k+1|k+1}}$ is the *a posteriori* estimate for the state vector $\mathbf{s}$, given the new information available at time point $k+1$, and $\mathbf{P}^{\mathbf{k+1|k+1}}$ is the associated covariance matrix. Matrices $\mathbf{L}$ and $\mathbf{K}$ are defined as follows.

Matrix $\mathbf{L}$ is the linear transformation from the vector space of $\mathbf{s}$ to the vector space of $\mathbf{p}$. In this case, only the first five elements of $\mathbf{s}$ are retained, leading to:

$$\mathbf{L} = \begin{bmatrix} \mathbf{I_5} & \mathbf{0_5} \end{bmatrix} \tag{5.26}$$

The Kalman gain, $\mathbf{K}$, is calculated as per Equation 5.27:

$$\mathbf{K} = \mathbf{P}^{\mathbf{k+1|k}} \cdot \mathbf{L}^{\mathbf{T}} \left(\mathbf{L} \cdot \mathbf{P}^{\mathbf{k+1|k}} \cdot \mathbf{L}^{\mathbf{T}} + \mathbf{\Sigma_p}\right)^{-1} \tag{5.27}$$

where $\mathbf{\Sigma_p}$ is the 5×5 covariance matrix associated with the new solution's uncertainty.

Matrix $\mathbf{\Sigma_p}$ is, in general, a full matrix because the degrees of freedom are correlated in a way that depends on the position and orientation of the sensor, and it can be derived from the uncertainty of the field measurements, $\mathbf{\Sigma_\Phi}$, as shown in Section 3.5.2. The measurement uncertainty can be considered to be constant, pre-characterised within the region of interest, or estimated in real time from the signal noise level as described in Section 3.2.2.

For a lighter version of the algorithm, it is possible to consider the degrees of freedom as uncorrelated and initialise $\mathbf{\Sigma_p}$ as the diagonal matrix of the variance of the typical random error or, more rigorously, the jitter error can be pre-characterised for different positions and orientations in the tracking volume.

Equation 5.27 shows that the only function of matrix $\mathbf{L}$ is to select entries in $\mathbf{P}$. In practice, when implementing Equation 5.27, $\mathbf{L}$ is omitted, and matrix indexing is used to address the correct entries. Moreover, as the calculation of inverse matrices is very inefficient, it may be replaced by

the slash operator, /, in MATLAB or the function *numpy.linalg.solve* from Numpy library in Python [25, 26], as shown on line 29 of Listing 5.1 for a MATLAB implementation.

To understand how the Kalman filter can reduce the jitter error by blending the motion law to the raw noisy solutions, assume that $\|\mathbf{\Sigma_p}\| \gg \|\mathbf{P}\|$. In other words, this is the assumption that the new position from the EMT algorithm comes with large uncertainty and cannot be trusted, whereas we can be confident about the motion model.

In this limit, the Kalman gain of Equation 5.27 approaches zero and the second term in the sum of Equation 5.24 is negligible, giving $\mathbf{s^{k+1|k+1}} = \mathbf{s^{k+1|k}}$. Therefore, the update step is an identity, and the new best estimate is based solely on the prediction step.

On the other hand, we can analyse the case when the measurements are exact, $\mathbf{\Sigma_p} = \mathbf{0_5}$. For simplicity, we just focus on variable x, governed by Equation 5.19. At the time point k, we know the system state exactly from the new measurements: $x^{k|k} = p_x$, with $\mathbf{P^k} = \mathbf{0_2}$.

After the prediction step, we obtain:

$$\begin{bmatrix} x^{k+1|k} \\ v_x^{k+1|k} \end{bmatrix} = \begin{bmatrix} p_x^k + v_x^{k|k} T_s \\ v_x^{k|k} \end{bmatrix} \tag{5.28}$$

$$\mathbf{P^{k+1|k}} = \mathbf{D} \cdot \mathbf{0_2} \cdot \mathbf{D^T} + \mathbf{Q} = \mathbf{Q} = \begin{bmatrix} \frac{T_s^4}{4} & \frac{T_s^3}{2} \\ \frac{T_s^3}{2} & T_s^2 \end{bmatrix} \sigma_a^2 \tag{5.29}$$

$$\mathbf{K} = \begin{bmatrix} \frac{T_s^4}{4} \\ \frac{T_s^3}{2} \end{bmatrix} \sigma_a^2 \cdot \left(\frac{T_s^4}{4} \sigma_a^2 + \mathbf{0_1} \right)^{-1} = \begin{bmatrix} 1 \\ \frac{2}{T_s} \end{bmatrix} \tag{5.30}$$

and the update step becomes:

$$x^{k+1|k+1} = x^{k+1|k} + \left(p_x^{k+1} - x^{k+1|k} \right) = p_x^{k+1} \tag{5.31}$$

$$v_x^{k+1|k+1} = v_x^{k+1|k} + \frac{2}{T_s} \left(p_x^{k+1} - x^{k+1|k} \right) = 2 \frac{p_x^{k+1} - p_x^k}{T_s} - v_x^{k|k} \tag{5.32}$$

where Equation 5.28 was used in the second equivalence of Equation 5.32.

Listing 5.1: Kalman filtering algorithm to make motion tracking smoother and reduce the jitter error.

```
% Linear motion model
Ts = 0.01;
D = [eye(5) Ts*eye(5); zeros(5) eye(5)];
P = zeros(10);
% Motion standard deviation, or random acceleration
sigma_a = 100; % x, y, and z (accelerometer)
sigma_w = 100; % theta, and phi (gyroscope)
G = [diag([repelem(.5*Ts^2,3)*sigma_a,...
    repelem(.5*Ts^2,2)*sigma_w]);
    diag([repelem(Ts,3)*sigma_a,...
    repelem(Ts,2)*sigma_w])];
Q = G*G';
% Measurement standard deviation
sigma_meas = 0.01;
Sigma_Phi = sigma_meas^2*eye(5);
% The state vector is available from previous steps
...
while tracking
    % Prediction step
    prediction = D*state_vector;
    P = D*P*D' + Q;
    % Pose vector from the new field measurements
    pose = ...
    % Calculate the Jacobian, J
    J = ...
    % Propagate the uncertainty from fluxes to pose
    Sigma_p = Sigma_Phi/(J'*J);
    % Calculate the Kalman gain
    K = P(:,1:5)/(P(1:5,1:5)+Sigma_p);
    % Update step
    error = pose-prediction(1:5);
    error(4:5) = wrapToPi(error(4:5));
    state_vector = prediction+K*error;
    P = P-K*P(1:5,:);
    % Output the filtered 5DoF
    pose = state_vector(1:5);
end
```

By replacing $\mathbf{P}^{\mathbf{k+1|k}}$ and $\mathbf{K}$ in Equation 5.25, as given by Equations 5.29 and 5.30, respectively, we obtain $\mathbf{P}^{\mathbf{k+1}} = \mathbf{0_2}$, meaning that the new state is estimated without uncertainty, solely based on the measurements.

As shown in Equation 5.32, thanks to the Kalman filter algorithm proposed in this work, it is possible to estimate the sensor velocity and therefore compensate for the latency introduced by the low-pass filters presented in Section 5.2.

Finally, it is worth mentioning that *prediction* and *update* steps of the Kalman filter do not necessarily need to run together. Given an estimate for the current pose and velocity, it is possible to estimate the next poses at a rate higher than the rate at which the new measurements are taken. For example, if a longer acquisition time is used to reduce the jitter noise and new measured values are available at a rate of 10 Hz, Equation 5.23 can be used ten times to send the estimated pose at a rate of 100 Hz to the user interface. When updated EMT values are ready, Equation 5.25 is used to correct the prediction.

5.3.2 Extended Kalman filter

The extended Kalman filter (EKF) generalises the Kalman filter algorithm to the cases where the transformation from the state vector to the measurements is not linear [27, 28]. For the EMT application, the EKF can be employed to update the best estimate for the sensor pose directly from the field measurements, bypassing the use of the non-linear least-squares solver Section 3.2.4.

As seen in Section 3.2.3, the magnetic flux vector is a function of the sensor pose: $\mathbf{\Phi} = f(\mathbf{p})$. The EKF steps are the same as presented for the Kalman filter, where the linear transformation matrix $\mathbf{L}$ is replaced by the Jacobian matrix of f, calculated in $\mathbf{p}$ as shown in Section 3.2.3.1.

In particular, the Kalman gain and the update step are given by:

$$\mathbf{K} = \mathbf{P}^{\mathbf{k+1|k}} \cdot \mathbf{J}^{\mathbf{T}} \left(\mathbf{J} \cdot \mathbf{P}^{\mathbf{k+1|k}} \cdot \mathbf{J}^{\mathbf{T}} + \mathbf{\Sigma_p} \right)^{-1} \tag{5.33}$$

$$\mathbf{s}^{\mathbf{k+1|k+1}} = \mathbf{s}^{\mathbf{k+1|k}} + \mathbf{K} \cdot \left(\widetilde{\mathbf{\Phi}}^{\mathbf{k+1}} - f(\mathbf{p}^{\mathbf{k+1|k}}) \right) \tag{5.34}$$

$$\mathbf{P}^{\mathbf{k+1|k+1}} = \mathbf{P}^{\mathbf{k+1|k}} - \mathbf{K} \cdot \mathbf{J} \cdot \mathbf{P}^{\mathbf{k+1|k}} \tag{5.35}$$

It can be noticed that when $\|\mathbf{\Sigma_p}\| \ll \|\mathbf{P}\|$, the Kalman gain becomes:

$$\begin{aligned} \mathbf{K} &\approx \mathbf{P}^{\mathbf{k+1|k}} \cdot \mathbf{J}^{\mathbf{T}} \left(\mathbf{J} \cdot \mathbf{P}^{\mathbf{k+1|k}} \cdot \mathbf{J}^{\mathbf{T}} \right)^{-1} \\ &= \mathbf{P}^{\mathbf{k+1|k}} \cdot \mathbf{J}^{\mathbf{T}} \cdot \mathbf{J}^{\mathbf{T}^{\dagger}} \cdot \mathbf{P}^{\mathbf{k+1|k}^{-1}} \cdot \mathbf{J}^{\dagger} \\ &= \mathbf{J}^{\dagger}; \quad \text{with } \|\mathbf{\Sigma_p}\| \ll \|\mathbf{P}\| \end{aligned} \tag{5.36}$$

and the limit for Equation 5.34 is then: $\mathbf{s}^{\mathbf{k+1|k+1}} \approx \mathbf{J}^{\dagger} \cdot \left(\widetilde{\mathbf{\Phi}}^{\mathbf{k+1}} - \mathbf{\Phi}^{\mathbf{k+1|k}} \right)$, which is the same of Equation 5.4, or one step of the Gauss-Newton algorithm.

To conclude, the EKF can be employed to update the tracked sensor pose directly from the field measurements and, at the same time, include a law of linear motion. It is assumed that the previous sensor position and orientation are known with a level of accuracy that allows one to consider the flux model to be quasi-linear between subsequent sensor poses.

5.4 Dynamic test

A dynamic EMT test was performed to measure the speed, stability, and accuracy of the methods introduced in this chapter.

Two sensors, Y and Z-oriented, were moved at a constant speed of $2\,^{cm}/_{s}$ along two pre-defined planar trajectories at a high of 15 cm, covering an area of 18 cm^2 and 28 cm^2, respectively. The 2D actuator introduced in Section 3.4 was used for this scope.

The paths are shown in Figure 5.2 and were designed to move at constant velocity both on shorter and longer straight lines, to include

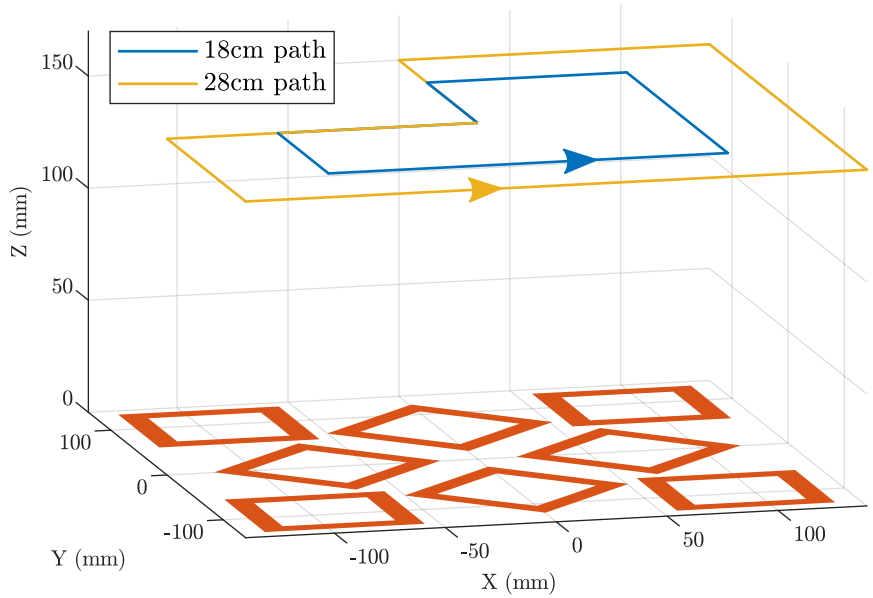


Figure 5.2: Dynamic tracking test. Two sensors, horizontally (Y) and vertically (Z) oriented, were tracked using a high update rate of 100 Hz. The experiment was repeated for two path lengths.

sudden changes in the motion direction with angles at 90 degrees, as well as to pass through points at the centre and at the edge of the tracking volume.

In both cases, a fast update rate of 100 Hz was used, resulting in a total number of 3843 poses tracked for the shorter trajectory, and 5911 for the longer one.

The parameters of the EMAs and the KFs were selected to give similar performance, as a trade-off between noise suppression and fast dynamics.

5.4.1 Results

The EMT pose given by the fast algorithm introduced in Section 5.1.1 was compared to the results obtained with the Trust-region algorithm of the *lsqnonlin* function, introduced in Section 3.2.4. At every sampled point, the error was calculated between the EMT solutions of the Trust-region algorithm compared to the novel algorithm. The position error was expressed as the Euclidean distance, and the orientation error as the angular displacement between the two solutions.

Table 5.1: Speed of different tracking algorithms and filtering techniques.

Solver	Trust-region		Fast algorithm		Double EMA		Kalman filter	
	Y	Z	Y	Z	Y	Z	Y	Z
	Path of 18 cm, *average values for 3843 points*							
Speed (ms)	3.1	4.9	0.22	0.22	0.22	0.27	0.25	0.26
	Path of 28 cm, *average values for 5911 points*							
Speed (ms)	3.6	5.1	0.22	0.22	0.22	0.24	0.26	0.26

For the path of 18 cm, the average error values calculated for the 3843 points are 0.33 µm and 1.30×10^{-4} degrees for the sensor oriented along Y, and 1.79 µm and 2.09×10^{-3} degrees for the sensor oriented along Z.

For the path of 28 cm, the average error values calculated for the 5911 points are 0.68 µm and 4.30×10^{-4} degrees for the sensor oriented along Y, and 1.96 µm and 2.08×10^{-3} degrees for the sensor oriented along Z.

Such small differences in the tracking results demonstrate that the two algorithms converged to approximately the same solution but with substantially different speeds, as reported in the first two columns of Table 5.1.

The larger errors obtained with the Z-oriented sensor can be explained by the larger magnetic fields and spatial variation in the Z direction, due to the planar configuration of the field generator. For this reason, the same positional displacement causes a larger difference in the magnetic fluxes measured if the sensor is Z-oriented rather than Y-oriented, and therefore the algorithms require more iterations to converge to the optimal point. This also explains why the Trust-region algorithm is, on average, slower when the sensor is vertically oriented, as seen in Table 5.1.

The low-pass digital filters presented in Sections 5.2 and 5.3 were applied in conjunction with the fast algorithm and the total speed was measured. As expected, the filters did not introduce a relevant delay, and they are therefore compatible with real-time tracking at a high update rate and low latency. The average running times are reported in Table 5.1 for the double EMA and the Kalman filter.

The profile of the tracked y coordinate of the Y-oriented sensor is visualised in Figure 5.3a for the smaller and larger trajectories to demonstrate the filtering results in terms of jitter reduction and latency increment. The other position and angular coordinates of the pose vector, and the results for the Z-oriented sensor, demonstrated similar outcomes and are, therefore, omitted.

Two portions of the tracked trajectories were selected to highlight some characteristics of the filters. The moving average over the last ten windows and the EKF are not visualised because they gave results almost coincident with the EMA with $\lambda = 0.2$ and the KF, respectively. As stated, the raw solutions obtained from the Trust-region and the one-step Gauss-Newton methods are indistinguishable, with differences in the order of micrometres and micro-degrees.

Figure 5.3b shows the sensor moving at a constant speed and suddenly stopping. In the first part, the delay of 50 ms caused by the exponential smoothing is visible, whereas the double EMA and the KF do not manifest evident latency.

When the sensor stops, the double EMA and the KF show some inertia, making the pose estimate shift towards the previous velocity direction. Both solutions take approximately 20 points, i.e. 200 ms, to re-establish correct tracking.

In the last part of the trajectory, mechanical oscillations are attenuated after filtering. In this case, the sensor velocity changes periodically, and all the filters considered follow the motion with some delay.

In Figure 5.3c, the y coordinate is constant, and the jitter of the raw solution is evident. The unfiltered points span a range of ± 0.5 mm, and the noise is reduced by a factor of five after filtering.

In this example, the simple and the double EMA show almost the same outcomes because the velocity is null. The KF demonstrates a slightly better smoothing effect but overall similar performance.

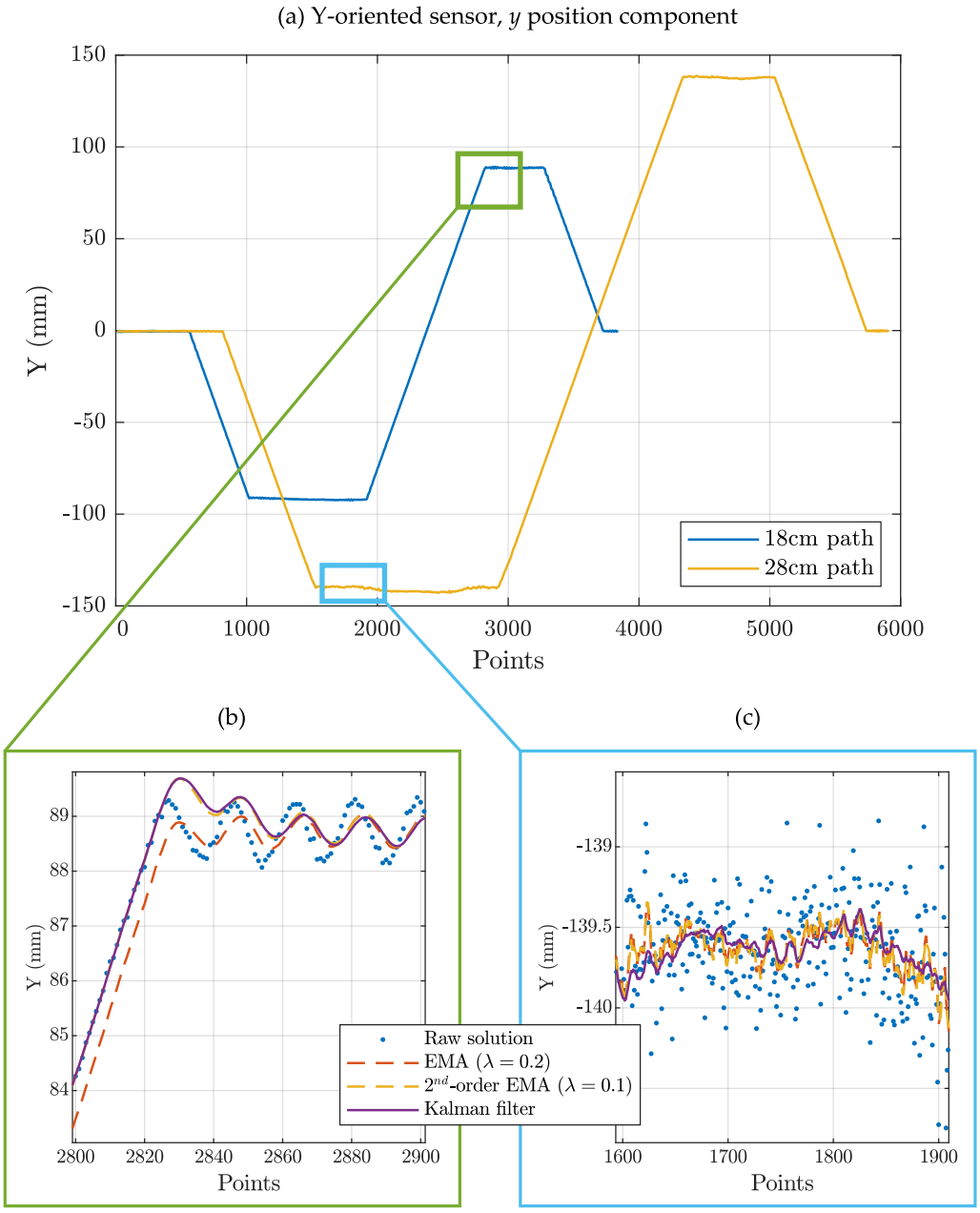


Figure 5.3: (a) Profile of the tracked y coordinate of the Y-oriented sensor. Two sections were selected to better visualise the performance of the filters (b) at constant velocity and with a sudden change in the motion direction, and (c) when the y coordinate is constant and the jitter noise is more evident.

5.5 Conclusions

The tracking algorithm previously employed by the ANSER EMT system allowed convergence to the optimal pose in approximately 5 ms per sensor and did not include filtering techniques, causing excessive jitter for acquisition times below 50 ms.

This imposed limits to the maximum update rate and latency effectively reachable, with typical values of 20 Hz for the update rate, and 25 ms, plus 5 ms per sensor, for the latency, to guarantee smooth tracking.

Using the novel algorithm and magnetic model interpolation presented in Section 5.1.1, multiple sensors can be tracked with less than 0.5 ms latency. Moreover, low-pass filters were introduced in Sections 5.2 and 5.3, which reduced the random noise and compensation for the latency by estimation of the velocity. In this way, a refresh rate of 100 Hz with reduced jitter and a global latency of 10 ms were achieved in the dynamic tracking experiment presented in Section 5.4, when the sensor moved at a constant speed.

A second advantage of the filters proposed in this chapter is the automatic rejection of sporadic incorrect solutions due to short-term (on the scale of filtering) inaccurate measurements, magnetic distortions, or local-minima convergence, because the effect is averaged with the previous and the following solutions.

The simplest filters considered were a moving average on the last ten acquisitions or, similarly, an exponential smoothing with $\lambda = 0.2$. Although they showed effective noise suppression, they caused a latency increase of about 50 ms.

A second-order exponential moving average and a Kalman filter were used to compensate for the latency introduced. They both produced the effects expected, with the Kalman filter being slightly superior in noise reduction, as seen in Figure 5.3c.

All filters are subject to delay when there is a change in the linear or angular velocity, due to the inability to measure the acceleration with the current hardware setup.

On a final note, it is recommended to keep the signal acquisition window as small as allowed by the hardware setup and use a sliding DFT or moving average technique, such as those presented in this chapter. In this way, with no change in computational cost, it is possible to achieve higher update rates and get better insight into the signal measured. This may be used, for example, to recognise and reject interference that takes the form of short impulses or to calculate the sample standard deviation.

References

[1] MathWorks, *Solve systems of linear equations $Ax = B$*. [Online]. Available: https://uk.mathworks.com/help/matlab/ref/mrdivide.html (visited on 09/14/2022).

[2] J. Nocedal and S. J. Wright, *Numerical Optimization*. Springer, 1999.

[3] MathWorks, *Gridded data interpolation*. [Online]. Available: https://uk.mathworks.com/help/matlab/ref/griddedinterpolant.html (visited on 09/13/2022).

[4] Bruno Luong, *Multiple same-size linear solver*, 2022. [Online]. Available: https://uk.mathworks.com/matlabcentral/fileexchange/24260-multiple-same-size-linear-solver (visited on 11/14/2022).

[5] R. J. Hyndman and G. Athanasopoulos, "Exponential smoothing," in *Forecasting: Principles and Practice*, 2nd edition, Lexington, Ky.: Otexts, online, open-access textbook, 2018, ISBN: 978-0-9875071-1-2. [Online]. Available: https://otexts.com/fpp2/expsmooth.html.

[6] B. D. O. Anderson and J. B. Moore, *Optimal Filtering* (Dover Books on Engineering), Dover ed., unabridged republ. Mineola, NY: Dover Publ, 2005, ISBN: 978-0-486-43938-9.

[7] R. E. Kalman, "A new approach to linear filtering and prediction problems," 1960, ISSN: 0021-9223.

[8] G. Welch and G. Bishop, "An Introduction to the Kalman Filter," p. 16, 2006.

[9] S. J. Julier and J. K. Uhlmann, "New extension of the Kalman filter to nonlinear systems," in *Signal Processing, Sensor Fusion, and Target Recognition VI*, vol. 3068, SPIE, 1997, pp. 182–193. DOI: 10.1117/12.280797.

[10] E. Wan and R. Van Der Merwe, "The unscented Kalman filter for nonlinear estimation," in *Proceedings of the IEEE 2000 Adaptive Systems for Signal Processing, Communications, and Control Symposium (Cat. No.00EX373)*, Lake Louise, Alta., Canada: IEEE, 2000, pp. 153–158, ISBN: 978-0-7803-5800-3. DOI: 10.1109/ASSPCC.2000.882463.

[11] M. S. Grewal and A. P. Andrews, *Kalman Filtering: Theory and Practice Using MATLAB*, Fourth edition. Hoboken, New Jersey: John Wiley & Sons Inc, 2015, ISBN: 978-1-118-85121-0.

[12] S. J. Russell, P. Norvig, and E. Davis, *Artificial Intelligence: A Modern Approach* (Prentice Hall Series in Artificial Intelligence), 3rd ed. Upper Saddle River: Prentice Hall, 2010, ISBN: 978-0-13-604259-4.

[13] A. Vaccarella, E. De Momi, A. Enquobahrie, and G. Ferrigno, "Unscented Kalman Filter Based Sensor Fusion for Robust Optical and Electromagnetic Tracking in Surgical Navigation," *IEEE Transactions on Instrumentation and Measurement*, vol. 62, no. 7, pp. 2067–2081, 2013, ISSN: 0018-9456. DOI: 10.1109/TIM.2013.2248304.

[14] A. Sabatini, "Quaternion-based extended Kalman filter for determining orientation by inertial and magnetic sensing," *IEEE Transactions on Biomedical Engineering*, vol. 53, no. 7, pp. 1346–1356, 2006, ISSN: 1558-2531. DOI: 10.1109/TBME.2006.875664.

[15] H. Ren, D. Rank, M. Merdes, J. Stallkamp, and P. Kazanzides, "Multisensor Data Fusion in an Integrated Tracking System for Endoscopic Surgery," *IEEE Transactions on Information Technology in Biomedicine*, vol. 16, no. 1, pp. 106–111, 2012, ISSN: 1089-7771, 1558-0032. DOI: 10.1109/TITB.2011.2164088.

[16] Y. Zhang, K. Wang, J. Jiang, and Q. Tan, "Research on Intraoperative Organ Motion Tracking Method Based on Fusion of Inertial and Electromagnetic Navigation," *IEEE Access*, vol. 9, pp. 49 069–49 081, 2021, ISSN: 2169-3536. DOI: 10.1109/ACCESS.2021.3068741.

[17] H. Sadjadi, K. Hashtrudi-Zaad, and G. Fichtinger, "Fusion of Electromagnetic Trackers to Improve Needle Deflection Estimation: Simulation Study," *IEEE Transactions on Biomedical Engineering*, vol. 60, no. 10, pp. 2706–2715, 2013, ISSN: 1558-2531. DOI: 10.1109/TBME.2013.2262658.

[18] H. Sadjadi, K. Hashtrudi-Zaad, and G. Fichtinger, "Needle deflection estimation: Prostate brachytherapy phantom experiments," *International Journal of Computer Assisted Radiology and Surgery*, vol. 9, no. 6, pp. 921–929, 2014, ISSN: 1861-6429. DOI: 10.1007/s11548-014-0985-0.

[19] M. Li, C. Hansen, and G. Rose, "A simulator for advanced analysis of a 5-DOF EM tracking systems in use for image-guided surgery," *International Journal of Computer Assisted Radiology and Surgery*, vol. 12, no. 12, pp. 2217–2229, 2017, ISSN: 1861-6429. DOI: 10.1007/s11548-017-1662-x.

[20] G. De Angelis, A. De Angelis, A. Moschitta, and P. Carbone, "Comparison of Measurement Models for 3D Magnetic Localization and Tracking," *Sensors*, vol. 17, no. 11, p. 2527, 2017. DOI: 10.3390/s17112527.

[21] R. Jin and B. Jung, "Magnetic Tracking System for Heart Surgery," *IEEE Transactions on Biomedical Circuits and Systems*, vol. 16, no. 2, pp. 275–286, 2022, ISSN: 1940-9990. DOI: 10.1109/TBCAS.2022.3163172.

[22] H. C. Gilbert, A. Saglembeni, M. Rakijas, and K. K. Kohnen, "Linear perturbation method for Kalman filter tracking of magnetic field sources," US6292758B1, 2001. [Online]. Available: https://patents.google.com/patent/US6292758B1/en (visited on 02/26/2020).

[23] M. Birsan, *Non-Linear Kalman Filters for Tracking a Magnetic Dipole*. Defence Research & Development Canada, Defence R & D Canada-Atlantic, 2003.

[24] D. Roetenberg, P. Slycke, A. Ventevogel, and P. H. Veltink, "A portable magnetic position and orientation tracker," *Sensors and Actuators A: Physical*, vol. 135, no. 2, pp. 426–432, 2007, ISSN: 0924-4247. DOI: 10.1016/j.sna.2006.08.020.

[25] MathWorks, *Solve systems of linear equations xA = B*. [Online]. Available: https://uk.mathworks.com/help/matlab/ref/mrdivide.html (visited on 09/14/2022).

[26] NumPy, *Numpy.linalg.solve — NumPy v1.23 Manual*. [Online]. Available: https://numpy.org/doc/stable/reference/generated/numpy.linalg.solve.html (visited on 09/29/2022).

[27] M. I. Ribeiro, "Kalman and Extended Kalman Filters: Concept, Derivation and Properties," p. 44, 2004.

[28] S. Thrun, W. Burgard, and D. Fox, *Probabilistic Robotics* (Intelligent Robotics and Autonomous Agents). Cambridge, Mass: MIT Press, 2005, ISBN: 978-0-262-20162-9.

Chapter 6

Magnetic models for elongated sensors

This chapter introduces an alternative formulation for the magnetic field model of elongated sensors used in EMT. The model shows improvements in terms of speed and storage requirements and can inherently take into account the length of elongated inductive sensor coils used in endoscopy applications.

The method is based on a magnetic *scalar potential* formulation. It is the counterpart of the method presented in Chapter 7, where the finite dimension of large-area planar sensor coils is resolved using a magnetic *vector potential* expression to reduce tracking errors.

The chapter is structured as follows. Section 6.1 introduces the problem, and Sections 6.2 and 6.3, following some theoretical background, present the derivation of an analytical model for the magnetic scalar potential of filament-based spiral coils, such as those used in the ANSER EMT system. The experiments performed in this work are introduced in Section 6.4. In particular, storage requirements and interpolation performance are compared for the existing field model and the novel formulation. Then, the speed and accuracy of the two models are evaluated through simulated and experimental tracking tests. Finally, a tracking method is proposed

This chapter is based on M. Cavaliere and P. Cantillon-Murphy, "Electromagnetic Tracking of Elongated Sensors for Endoscopic Navigation," *Magnetism*, vol. 2, no. 3, pp. 271–287, 2022 [1].

to localise flexible sensor coils of several centimetres in length. The experimental results are outlined in Section 6.5, and the main findings are commented in Section 6.6.

6.1 Introduction

As seen in Section 2.3, in the most common EMT architecture for computer-assisted interventions, an external field generator comprising multiple emitter coils generates a signal, and a small magnetic sensor attached to the tracked instrument is used as a target. Knowledge of the magnetic field in the volume of interest allows for finding the position and orientation of every sensor based on the received signal [2, 3].

Magnetic sensors used in endoscopy applications are generally inductive pick-up coils, which are passive and therefore reduce the risk to the patient in the event of a malfunctioning medical device, compared to active devices. Such coils can be manufactured to miniature sizes of less than 0.3 mm in diameter [4], and they provide high sensitivities in the presence of AC excitation magnetic fields [5, 6].

However, to guarantee human safety [7], EMT systems used in clinical settings have limited magnetic field amplitudes. In order to meet the sensitivity requirements, the sensor coils must be designed with an elongated shape and are typically several millimetres in length. This geometry can potentially introduce positioning errors if the coil's length cannot be ignored compared to the spatial variation of the magnetic field.

6.2 Magnetic models

Inductive magnetic sensors have an output proportional to the time derivative of the magnetic flux enclosed by the sensor coil, as was shown in Section 3.1.1.2.

We consider a sensor coil of length L, comprising N turns, and with constant turn density, $n = N/L$, and cross-sectional area, A_c. We identify the coil end-points as P_A and P_B. The coil is considered *long* relative to the spatial variation of the magnetic flux density, $\mathbf{B}$, if this cannot be assumed

constant or linearly varying across the sensor length. In this case, the induced voltage must be calculated by the line integral of $\mathbf{B}$ along the coil:

$$\Phi = A_c \int_{P_A}^{P_B} \mathbf{B} \cdot \mathbf{n}\, n(l)\, dl = A_c \frac{N}{L} \int_{P_A}^{P_B} \mathbf{B} \cdot \mathbf{n}\, dl = A_c N \langle \mathbf{B} \rangle \cdot \mathbf{n} \tag{6.1}$$

where $\langle \mathbf{B} \rangle$ is the average magnetic flux density along the coil, and the unit vector $\mathbf{n}$ identifies the orientation and is constant for a rigid sensor.

The magnetic field equations in the magnetoquasistatic approximation are [8]:

$$\nabla \cdot \mathbf{B} = 0 \tag{6.2}$$

$$\nabla \times \mathbf{H} = \mathbf{J} \tag{6.3}$$

with $\mathbf{B} = \mu \mathbf{H}$, where μ is the magnetic permeability of the medium, $\mathbf{H}$ is the magnetic field intensity and $\mathbf{J}$ is the current density.

Equation 6.3 is also known as Ampere's law and, in current-free volumes where $\mathbf{J} = 0$, the magnetic field is curl-free: $\nabla \times \mathbf{H} = 0$. Therefore, in regions of the space with no electric current, the magnetic field vector can be expressed as the gradient of a magnetic scalar potential, ψ:

$$\mathbf{H} = -\nabla \psi \tag{6.4}$$

Because, for the frequencies used in EMT, biological tissues have effectively the magnetic permeability of free space, μ_0, the integral of Equation 6.1 can be expanded using Equation 6.4:

$$\begin{aligned} \int_{P_A}^{P_B} \mathbf{B} \cdot \mathbf{n}\, dl &= -\mu_0 \int_{P_A}^{P_B} \nabla \psi \cdot \mathbf{n}\, dl = -\mu_0 \int_{P_A}^{P_B} \frac{\partial \psi}{\partial l}\, dl = -\mu_0 \int_{\psi_A}^{\psi_B} d\psi \\ &= \mu_0 (\psi_A - \psi_B) \end{aligned} \tag{6.5}$$

When elongated sensors are tracked, Equation 6.1 is usually resolved by evaluating $\mathbf{B}$ at the sensor midpoint. If this introduces unacceptable position errors, $\langle \mathbf{B} \rangle$ may be approximated using an n-point quadrature rule [9, 10] at the cost of speed. Therefore, it may be computationally more convenient to calculate the magnetic flux from Equation 6.6 obtained after

substituting Equation 6.5 in Equation 6.1:

$$\Phi = \frac{\mu_0 A_c N}{L}(\psi_A - \psi_B) \tag{6.6}$$

Equation 6.1 and Equation 6.6 will be the basis for the two analytical magnetic flux models used in this chapter.

6.2.1 Magnetic field of the ANSER EMT field generator

An analytical model for the planar ANSER EMT field generator was obtained in Section 3.2.3. The model is based on Biot-Savart's law to calculate the magnetic field vector at the desired location of the space, and a dot product multiplication is performed between the field vector and the sensor orientation unit vector to find the magnetic flux enclosed by the coil:

$$\Phi(\mathbf{r}, \mathbf{n}) = \mu_0 A_c N \, \mathbf{H}(\mathbf{r}) \cdot \mathbf{n} \, [\mathrm{V}] \tag{6.7}$$

where the magnetic field $\mathbf{H}(\mathbf{r})$ is calculated as per Equation 3.8.

According to this model, the magnetic sensor is approximated as a single point located at $\mathbf{r}$, as shown in Figure 6.1a, and the variation of the magnetic flux density along the coil is not considered. In the remainder of this chapter, Equation 6.7 is referred to as the *single-point* model of the mutual coupling between the sensor and the field generator.

6.2.2 Scalar potential formulation

In this section, a scalar potential formulation is obtained for the magnetic field of the ANSER EMT system.

As can be verified, the magnetic field calculated from Biot-Savart's law satisfies Ampere's law, given in Equation 6.3, only if the divergence of the current density, $\nabla \cdot \mathbf{J}$, is zero everywhere in the space, as is the case for steady currents in *closed* loops [11].

A finite segment of wire has a *source* of current at one end of the wire and a *sink* of current at the other. Therefore the current is not divergence-free, and $\mathbf{H_i}(\mathbf{r})$ of Equation 3.7 does not satisfy Ampere's law. In particular, the magnetic field due to each individual straight conductor composing

the emitter coils is not curl-free, even at points where there is no current, and it cannot be formulated using a scalar potential.

For this reason, it is not possible to express the scalar potential of $\mathbf{H}(\mathbf{r})$ as a sum of contributions due to individual wire segments, as is done in Equation 3.8, instead the closed current path of the emitter coil must be considered in full.

A scalar potential for the field generated by the current I flowing in the closed loop Γ is then given by Equation 6.8:

$$\psi(\mathbf{r}) = -\frac{I}{4\pi}\Omega \tag{6.8}$$

where Ω is the solid angle subtended at point $\mathbf{r}$ by the area enclosed by the loop Γ [12]. Once more, it is clear that the loop Γ must be *closed* because it is defined as the boundary of a surface.

The solid angle bounded by a rectangular spiral, such as the current path formed by the emitter coils considered in this work, can be calculated as detailed in Section 6.3. Alternatively, it is possible to approximate the spiral as a set of concentric squares, as shown in Figure 6.1b, and calculate the total solid angle enclosed by each emitter coil as the sum of the solid angles enclosed by rectangular plates [13].

The magnetic field model of Section 6.2.1 and the correspondent scalar potential formulation introduced in this section are visualised in Figure 6.2 for the emitter coil number 4, highlighted in Figure 6.3a. It can be seen that the contour lines of ψ are always perpendicular to the field lines, as expected, considering that the $\mathbf{H}$ field was defined as $-\nabla\psi$.

Finally, for a tracking sensor at position $\mathbf{r}$ and oriented along $\mathbf{n}$, the magnetic flux crossing the sensor winding is obtained by substituting Equation 6.8 in Equation 6.6:

$$\Phi(\mathbf{r},\mathbf{n}) = \frac{\mu_0 A_c N}{L}\left(\psi\left(\mathbf{r}-\mathbf{n}\frac{L}{2}\right)-\psi\left(\mathbf{r}+\mathbf{n}\frac{L}{2}\right)\right) \tag{6.9}$$

which has to be calculated for every emitter coil in the field generator.

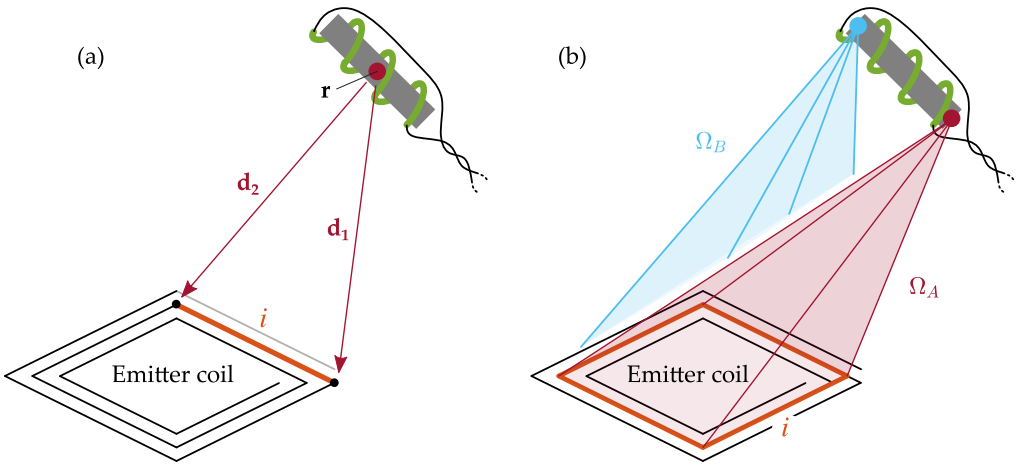


Figure 6.1: Calculation of the magnetic flux crossing an elongated inductive sensor (a) from the sum of the contributions due to the individual filaments forming the emitter coil, where the sensor is approximated as a single point. (b) The full sensor length is considered by calculating the flux as the finite difference of the magnetic scalar potential, which depends on the solid angles, Ω_A and Ω_B, subtended by the emitter coil current path at the sensor end-points.

This model accounts for the total length of the magnetic sensor. In the remainder of this chapter, Equation 6.9 is referred to as the *full-length* model of the mutual coupling between the sensor and the field generator.

6.3 Solid angle subtended by a planar spiral

The solid angle subtended by the surface Σ at a point $\mathbf{r}$ is given by:

$$\Omega = \iint_{\Sigma} \frac{\mathbf{r} \cdot \mathbf{n}}{R^3} d\Sigma \tag{6.10}$$

where $\mathbf{n}$ is the unit vector normal to $d\Sigma$ and $R = |\mathbf{r}|$.

If $\mathbf{r} = [x, y, z]$, it can be verified that:

$$\nabla \cdot \frac{\mathbf{r}}{R^3} = \nabla \cdot \frac{[x, y, z]}{(x^2 + y^2 + z^2)^{3/2}} = 0; \quad (\text{for } \mathbf{r} \neq [0, 0, 0]) \tag{6.11}$$

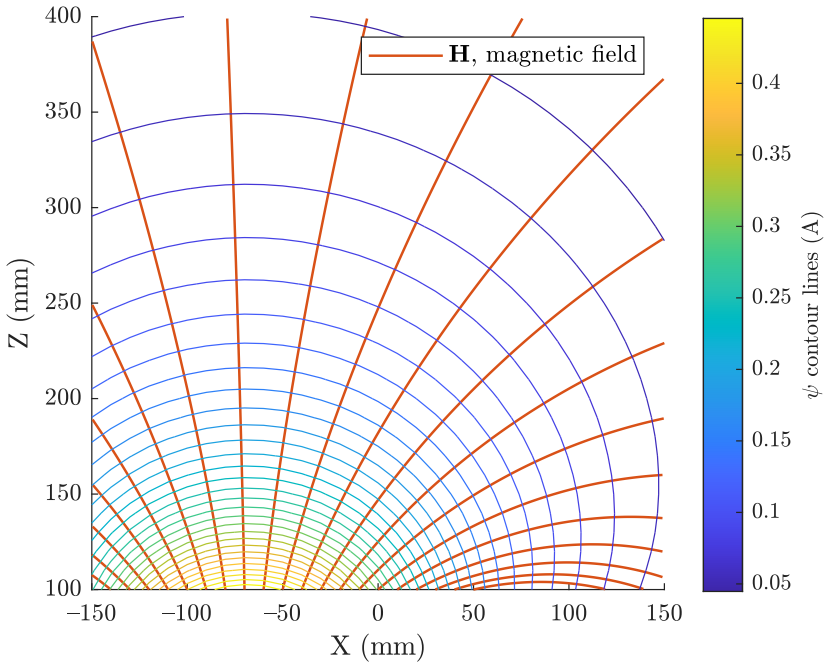


Figure 6.2: Magnetic field and associated scalar potential of the 4^{th} emitter coil of the field generator, evaluated on an XZ plane at $Y = 0$.

As $\mathbf{r}/R^3$ is divergence-free, it is possible to express it as the curl of a new vector, $\mathbf{G}$, and Equation 6.10 can be rephrased using Stokes' theorem:

$$\Omega = \iint_{\Sigma} (\nabla \times \mathbf{G}) \cdot \mathbf{n}\, d\Sigma = \oint_{\Gamma} \mathbf{G} \cdot \mathbf{t}\, d\Gamma \tag{6.12}$$

where Γ is the boundary of the area Σ and $\mathbf{t}$ is the unit vector tangent to $d\Gamma$. It has to be noticed that since Γ is the boundary of Σ, it must be a closed integral path.

One possible solution for $\mathbf{G}$ is:

$$\mathbf{G} = \left(-\frac{yz}{(x^2+z^2)\sqrt{x^2+y^2+z^2}}, 0, \frac{xy}{(x^2+z^2)\sqrt{x^2+y^2+z^2}} \right) \tag{6.13}$$

This solution is particularly convenient because the square planar emitter coils considered in this work are composed of horizontal straight filaments on an XY plane and, therefore, $\mathbf{t}$ is alternately equal to $[1,0,0]$ or $[0,1,0]$.

Because $\mathbf{G} = [G_1, 0, G_3]$, Equation 6.12 vanishes for the conductors in the Y direction and the contribution of every conductor in the X direction

is given by Equation 6.14:

$$\begin{aligned}\Omega_i &= \int_{P_1}^{P_2} -\frac{yz}{(x^2+z^2)\sqrt{x^2+y^2+z^2}}dx \\ &= -\tan^{-1}\left(\frac{xy}{z\sqrt{x^2+y^2+z^2}}\right)\Bigg|_{[x_1,y_1,z_1]}^{[x_2,y_2=y_1,z_2=z_1]}\end{aligned} \tag{6.14}$$

where the only variable quantity is x, while y and z are fixed for each X-oriented straight filament, and P_1 and P_2 are the i^{th} wire end-points.

It is worth noting that if the planar emitter coil is printed on multiple layers of a PCB or, in general, if the spiral path is not planar, vertical current filaments may be considered at some points in order to close the path Γ. Alternatively, Γ may be split into multiple closed paths belonging to different layers.

Following the steps presented above, the contribution given by a conductor in the Z direction is calculated as follows:

$$\Omega_i = \tan^{-1}\left(\frac{yz}{x\sqrt{x^2+y^2+z^2}}\right)\Bigg|_{[x_1,y_1,z_1]}^{[x_2=x_1,y_2=y_1,z_2]} \tag{6.15}$$

Finally, Ω is given by the sum of all the contributions Ω_i calculated as per Equations 6.14 and 6.15. The same result could have been obtained by defining $\mathbf{G} = [0, G_2, G_3]$ and integrating along the Y direction.

6.4 Materials and methods

The *full-length* model introduced in this chapter and based on the magnetic scalar potential formulation was evaluated in terms of speed and accuracy and compared with the *single-point* model currently used by the ANSER EMT system. In the two cases, interpolation performance is tested for different grid densities, and a criterion to select the optimal grid spacing is presented. All models were tested through simulated and real EMT experiments. Finally, methods for the tracking of a long flexible sensor are simulated.

6.4.1 Performance metrics

In this study, the following metrics were used to compare the different magnetic field predictions of the models analysed and the corresponding error in the position tracking of the electromagnetic sensor.

We define $\mathbf{\Phi} \in \mathbb{R}^{8\times P}$ and $\widetilde{\mathbf{\Phi}} \in \mathbb{R}^{8\times P}$ as the vectors comprising the magnetic flux values according to the reference model and a model under test, respectively, for the eight emitter coils and P observation points.

The average field error was defined as the normalised mean absolute error (NMAE), where the range of the observations was used as the normalisation parameter:

$$\mathrm{NMAE}(\widetilde{\mathbf{\Phi}}, \mathbf{\Phi}) = \frac{1}{8P} \sum_{i=1}^{8P} \left| \widetilde{\Phi}_i - \Phi_i \right| / \left(\max_i \mathbf{\Phi} - \min_i \mathbf{\Phi} \right). \tag{6.16}$$

It can be noticed that since the eight emitter coils are equal, the corresponding magnetic models only differ by a roto-translation, and averaging between all the test positions is effectively equivalent to considering eight times P random points for a singular emitter coil.

The difference between the two magnetic field models was quantified in terms of EMT error. The pose error $\Delta\mathbf{p} = (\widetilde{\mathbf{p}} - \mathbf{p})$ was estimated from the field difference $\Delta\mathbf{\Phi} = (\widetilde{\mathbf{\Phi}} - \mathbf{\Phi})$ as explained in Section 3.5.2, where $\mathbf{p} = [x, y, z, \theta, \varphi]$ is the reference *pose* vector and $\widetilde{\mathbf{p}}$ is the pose associated to $\widetilde{\mathbf{\Phi}}$. In other words, $\widetilde{\mathbf{p}}$ is the solution to which the tracking algorithm would converge when measuring $\widetilde{\mathbf{\Phi}}$ and using the EMT model $\mathbf{\Phi}$.

The error metrics presented in Section 3.6.1 were used. Specifically, the root mean square error (RMSE), the mean error (ME), the median or 50^{th} percentile (PRC50), and the 95^{th} percentile (PRC95).

6.4.2 Model interpolation

The magnetic model can be pre-evaluated at grid points within the region of interest (ROI) to speed up the tracking algorithm of the EMT system. The values at any point of the volume are given by interpolation between the tabulated values stored in a look-up table (LUT).

The interpolation error was evaluated for the magnetic scalar potential and the magnetic field vector. In the first case, only one scalar value is stored, while in the second case, the three field components are saved separately. However, the magnetic field is obtained from the scalar potential after the gradient operation, which decreases the order of the interpolation polynomial by one degree. Therefore, even if the storage intake is one-third as large, it may be required to decrease the spacing between grid points to obtain the same level of accuracy, which increases the number of stored values following a cubic power law.

The interpolation performance was evaluated for different grid densities within a $30 \times 30 \times 30\,\mathrm{cm}^3$ cubic volume placed 10 cm above the field generator. Regular interpolation grids were considered, and the same grid spacing was used in all three dimensions. The LUTs were generated by evaluating and storing the scalar potential or the three field components, respectively, at the grid points for the eight emitter coils of the field generator.

The interpolation error was estimated by randomly sampling 10 000 positions inside the ROI. The interpolated values were predicted using a tri-cubic spline interpolation with *not-a-knot* end conditions [14]. At every point, a random orientation was used to calculate the magnetic fluxes for the two models as per Equation 6.7 and Equation 6.9, respectively.

For each tabulated model, the interpolation error was calculated relative to the correspondent analytical model reference, as described in Section 6.4.1. The size of each LUT was obtained using the *whos* function in MATLAB [15].

6.4.3 Simulated tracking test

For the *full-length* and the *single-point* magnetic flux formulations compared in this chapter, two LUTs were selected to give approximately the same interpolation error and require similar storage space, as will be justified in Section 6.5.1.

For convenience, in the remainder of the chapter, the table storing the magnetic scalar potential is referred to as *LUT FL*, and the table of the three magnetic field components is called *LUT SP*.

The four models, two analytical and two LUTs, were compared, and the differences were quantified using synthetic data. In this way, it was possible to decouple the sources of error: (1) the physical approximation of the sensor as a single point, which was compared to the new formulation that takes into account the full sensor length, and (2) the numerical approximation due to the cubic spline interpolation.

The same cubic volume of $30 \times 30 \times 30\,\text{cm}^3$ used in Section 6.4.2 was considered. Within this region, 100 000 random positions and orientations were selected for an elongated sensor of 10 mm, chosen as a reference length for inductive coils used in endoscopic tracking [16].

The magnetic fluxes NMAE and the tracking position errors were calculated as described in Section 6.4.1. The error introduced by the *single-point* approximation was calculated relative to the *full-length* model. In contrast, the error of each LUT was compared to the respective analytical model.

The speed of the four models was computed as an average on the 100 000 flux evaluations, using the *tic* function in MATLAB [17], running on a Windows 10 laptop with i5-11th Gen. Intel Core Processor.

6.4.4 Experimental tracking test

An experimental EMT test was performed where the four models introduced in Section 6.4.3 were used to resolve the position and orientation of a miniature clinical sensor (610158, Northern Digital Inc., Waterloo, Canada [16]). The elongated inductive coil is 0.45 mm in diameter and 8.2 mm in length, as shown in Figure 6.3c.

Tool T introduced in Section 3.3 was used for the experiment, with the two sensor coils oriented along the Y and Z axes of the field generator, as defined in Figure 6.3a. The sensors are glued on the 3D-printed support, which is also used to host the passive spheres of the Polaris Vega optical system (Northern Digital Inc., Waterloo, Canada) for position and

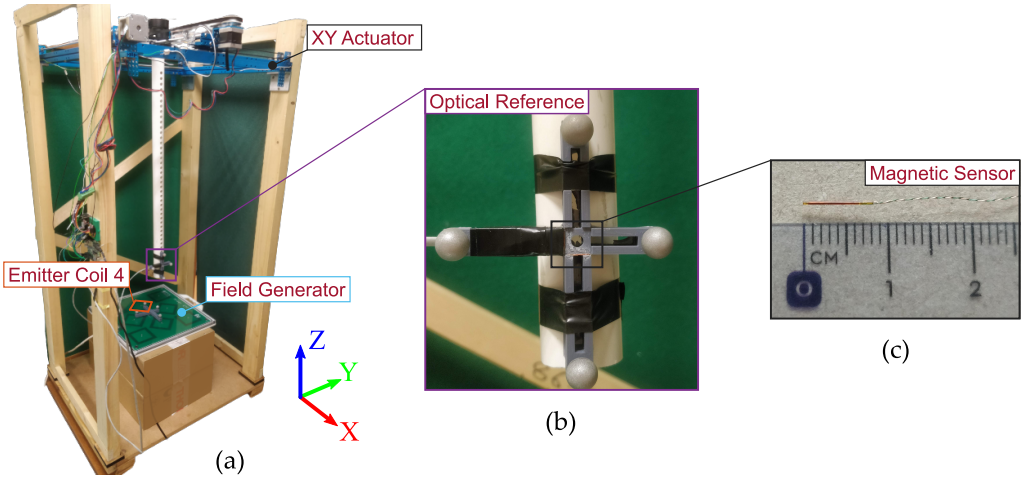


Figure 6.3: (a) The motorised actuator introduced in Section 3.4 was used to move the EMT sensors on an XY plane. Optical tracking provided accurate pose reference. One of the eight emitter coils of the field generator is highlighted in orange. (b) Two sensors were embedded in the dynamic reference frame to collect data in different directions. (c) A miniature sensor coil was used in the experiments [16].

orientation reference. The frame with the magnetic sensors and the optical markers is shown in Figure 6.3b.

The automated motorised system presented in Section 3.4 was used to move the two magnetic sensors. A grid of 26×26 points was sampled within a $25 \times 25\,\mathrm{cm}^2$ XY plane, placed approximately 15 cm above the field generator, as shown in Figure 6.3a.

For every field measurement, the sensors were kept steadily at the test position, and 40 values were collected. The noise level was estimated both from the standard deviation of the 40 measured signal values and from a frequency domain analysis, as explained in Section 3.2.2, resulting in a signal-to-noise ratio (SNR) of 68 dB in the first case and of 67 dB using the second approach. In this experiment, the random error due to the jitter noise was removed by averaging the 40 measured values to isolate the systematic error of the EMT system caused by inaccurate magnetic modelling or introduced by the acquisition hardware [18].

The experimental magnetic measurements were used to find the sensor pose by minimising the difference in a least-squares sense between the eight flux measurements and the values predicted by the model at the

estimated position and orientation. EMT errors were calculated using optical tracking as a ground truth.

6.4.5 Long flexible inductive sensors

A possible application of the new formulation presented in this chapter is tracking a long inductive coil, which can be wound around a flexible surgical instrument, such as a guidewire or a catheter. The benefits of such a sensor would be the higher sensitivity due to the longer length and larger cross-sectional area, and the improved linearity due to the absence of a ferrite core [5].

Localising a long inductive sensor in real time is challenging because the model of the sensed field must be calculated from the line-integral of the magnetic flux density along the coil axis, as per Equation 6.1. The integral may be evaluated numerically, leading to inaccurate results and slowing computation. It is worth mentioning that the integral of Equation 6.1 can be calculated without knowing the shape of the coil axis because the magnetic field is curl-free in the region considered. Therefore, any integration path connecting the two end-points is equivalent. The straight line defined by the two end-points might be used for simplicity.

Alternatively, the scalar potential formulation expressed in Equation 6.6 directly gives the exact analytical integral, which is then compared to the measured magnetic flux to find the position of the coil end-points. The sensor shape remains unknown because it cannot be deduced from the electromagnetic measurement, which depends only on the end-points position. However, in endoscopic procedures where the sensor moves through narrow passages, the instrument's shape can be inferred by considering anatomic constraints or sequentially tracked end-point positions.

In this preliminary experiment, a flexible sensor shape was arbitrarily defined as:

$$\begin{bmatrix} x \\ y \\ z \end{bmatrix} = \begin{bmatrix} 25\cos\left(3\pi/2\, t\right) \\ 25\sin\left(3\pi/2\, t\right) \\ 100 + 50\, t \end{bmatrix} \text{ mm}; \quad \text{with } 0 \leq t \leq 1 \tag{6.17}$$

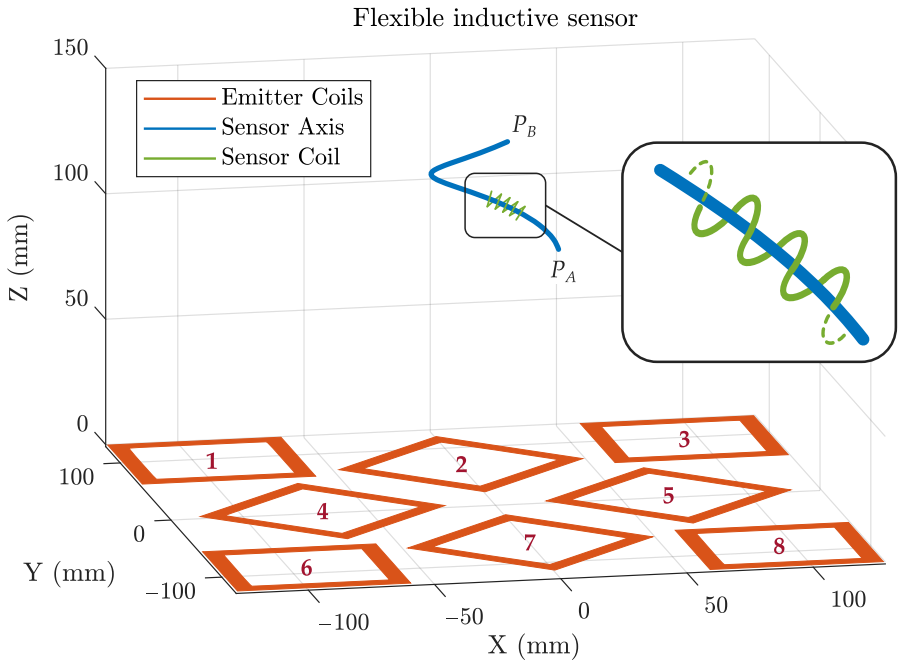


Figure 6.4: A simulated EMT test was performed on a 128 mm-long flexible sensor wrapped in a loop of radius 25 mm, ranging from 100 to 150 mm above the field generator. The inset shows an enlarged image of the inductive coil, which is wound around the sensor axis, coloured in blue.

The sensor axis consisted of a loop of radius 25 mm, ranging from 100 to 150 mm above the field generator, as drawn in Figure 6.4. The total length of the sensor can be calculated as follows:

$$\begin{aligned} L &= \int_0^1 \sqrt{\left(-25\frac{3\pi}{2}\sin\theta\right)^2 + \left(25\frac{3\pi}{2}\cos\theta\right)^2 + 50^2}\, dt \\ &= \sqrt{\left(25\frac{3\pi}{2}\right)^2 + 50^2} \approx 128\,\text{mm} \end{aligned} \tag{6.18}$$

The eight simulated flux measurements were calculated using the *full-length* magnetic model presented in this chapter. The values were confirmed by integrating the *single-point* model along the sensor axis. The MATLAB *integral* function [19], which makes use of adaptive quadrature methods, was used to this end.

The robustness of the proposed tracking algorithm was evaluated by adding Gaussian noise to the simulated flux measurements and studying how the noise affected the position solutions. The noise level was selected to be 63 dB below the magnitude of the simulated signal, in accordance with the approximate signal-to-noise ratio measured during the real experiment of Section 6.4.4.

6.5 Results

This section presents the results of the experimental method described in Section 6.4. The study of the interpolation performance allowed us to choose a table of the magnetic scalar potential and a table of the three field components that are approximately equivalent in terms of position accuracy and table size. Then, the results of the simulated and real EMT tests are reported. Finally, the stability of the proposed tracking algorithm for long, flexible coils is shown using position error confidence regions.

6.5.1 Model interpolation

The interpolation and position errors of the two tabulated models introduced in Section 6.4.2 are plotted in Figure 6.5 for the varying grid sizes.

The interpolation error was expected to be proportional to the distance between the data points to the power $n + 1$, where n is the degree of the interpolation polynomial [20]. The power-law dependence is confirmed in Figure 6.5a, where the best-fit exponents resulted in $k = 3.5$ and $k = 4.4$ for the two interpolated models, respectively.

In fact, a quadratic spline interpolates the magnetic fluxes obtained from the magnetic scalar potential because they are calculated from the gradient operation, which involves first derivatives and makes the order of the polynomial one degree lower. Conversely, the cubic spline is maintained for the magnetic fluxes obtained from the magnetic field component-wise interpolation.

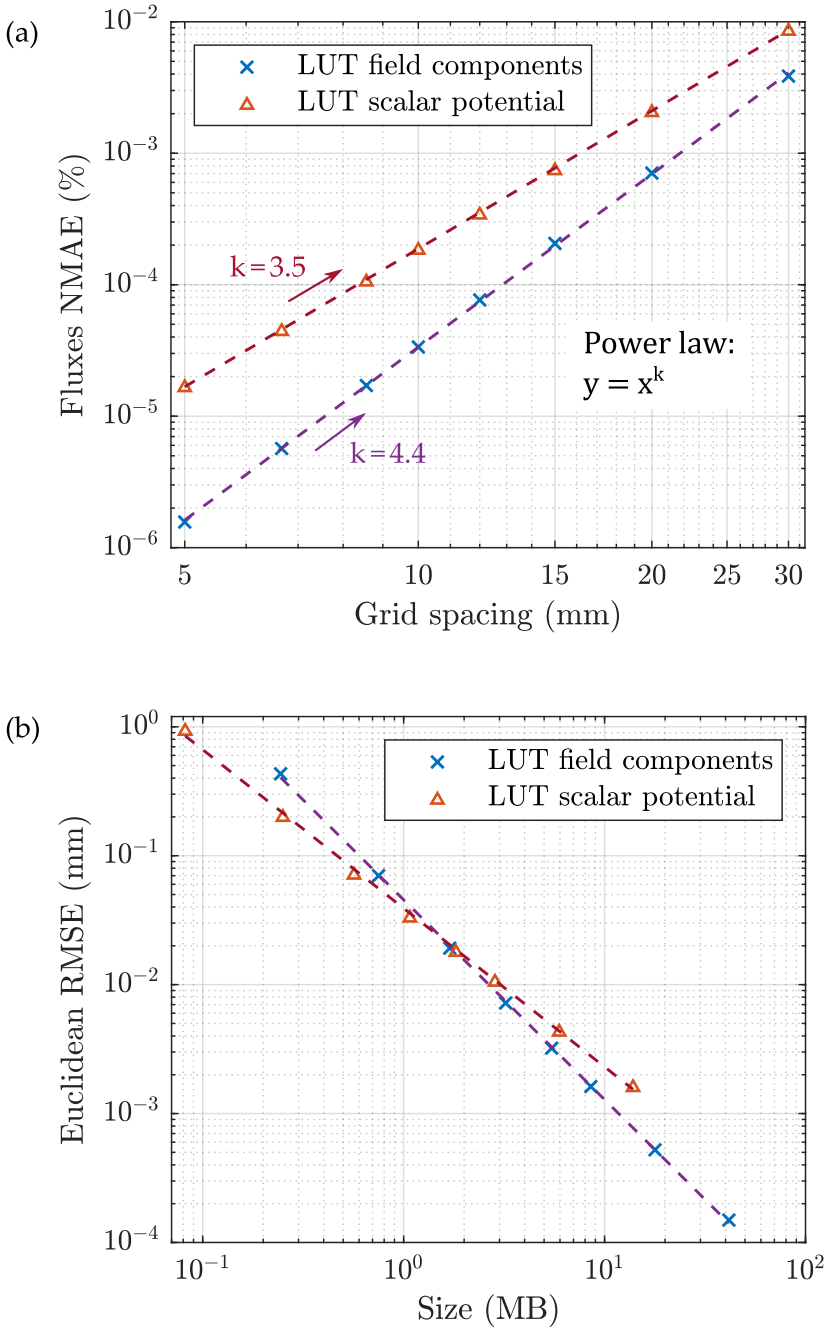


Figure 6.5: (a) Interpolation error and (b) correspondent position tracking error as a function of the table size for the two tabulated models compared. Blue crosses: the three magnetic field components are stored independently, and the fluxes are obtained from Equation 6.1. Red triangles: the magnetic scalar potential is saved at grid points, and the fluxes are calculated from Equation 6.6. The interpolation error follows a power law with exponents of $k = 3.5$ and $k = 4.4$, respectively.

The average position error is shown in Figure 6.5b for the two tabulated models as a function of the table size. The two curves intersect approximately at 20 µm, where the storage requirement is around 2 MB, which corresponds to a grid spacing of 1 cm ($31 \times 31 \times 31$ grid-points) for the scalar potential table and a grid spacing of 1.5 cm ($21 \times 21 \times 21$ grid-points) for the field components table. The two associated LUTs were selected for the models *LUT FL (full-length)* and *LUT SP (single-point)* used in the simulated and experimental tracking tests presented in Section 6.4 of this chapter.

6.5.2 Simulated tracking test

The results of the simulated tracking test described in Section 6.4.3 are reported in Table 6.1, comparing the *full-length* and *single-point* models, and the associated interpolated models *LUT FL* and *LUT SP*.

As explained in Section 6.5.1, the two LUTs were chosen to be approximately equivalent in terms of position RMSE and table size, and the results demonstrate similar performance, with a 95^{th} percentile (PRC95) of the position error of approximately 0.03 mm in either case.

The effect of the *single-point* approximation is evaluated relative to the *full-length* model. The position error PRC95 of the 100 000 test locations is below 0.2 mm, demonstrating a minimal difference between the two models.

The two analytical models were computationally more expensive than the corresponding tabulated models. In either case, the average evaluation time was approximately halved when using a LUT. The analytical *full-length* model, based on the calculation of the magnetic scalar potential, was 1.7 times faster than the *single-point* model, based on the calculation of the three components of the magnetic field vector.

Table 6.1: Model comparison, based on a simulation of a 10 mm-long sensor placed at 100 000 random positions and orientations within the tracking region. The normalised mean absolute error (NMAE) of the magnetic field, **H**, is averaged across the eight equal emitter coils, and the associated position error, P, is reported. The error introduced by the *single-point* approximation is calculated relative to the *full-length* model. Each LUT is evaluated against the correspondent analytical model.

Model	**Full length**	**Single point**	**LUT FL**	**LUT SP**
Time (µs)	44.3	74.8	22.8	33.7
H, NMAE (‰)	N/A	0.0169	0.0015	0.0019
P, RMSE (mm)	N/A	0.098	0.018	0.018
P, PRC95 (mm)	N/A	0.161	0.025	0.031
Size (MB)	N/A	N/A	1.8193	1.6965

6.5.3 Experimental tracking test

As demonstrated by the results of Section 6.5.2 above, for sensors of 10 mm in length and the spatial variation of the magnetic field in the region considered, the *full-length* and the *single-point* models are almost equivalent in terms of accuracy, although the *full-length* model is faster on average.

The position error is compared for the two analytical models and the two sensor orientations in Figure 6.6, showing the cumulative distribution function (CDF) of the position error. The two tabulated models are not shown because they produce almost precisely the same results as the associated analytical model, as indicated in the error statistics reported in Table 6.2.

Although a slight difference can be observed in Figure 6.6 when using the two alternative magnetic model formulations, this is entirely irrelevant compared to the CDF error curve. In clinical applications of EMT, other sources of error are dominant, such as thermal noise, metallic distortion, patient movements, and systematic errors in the system.

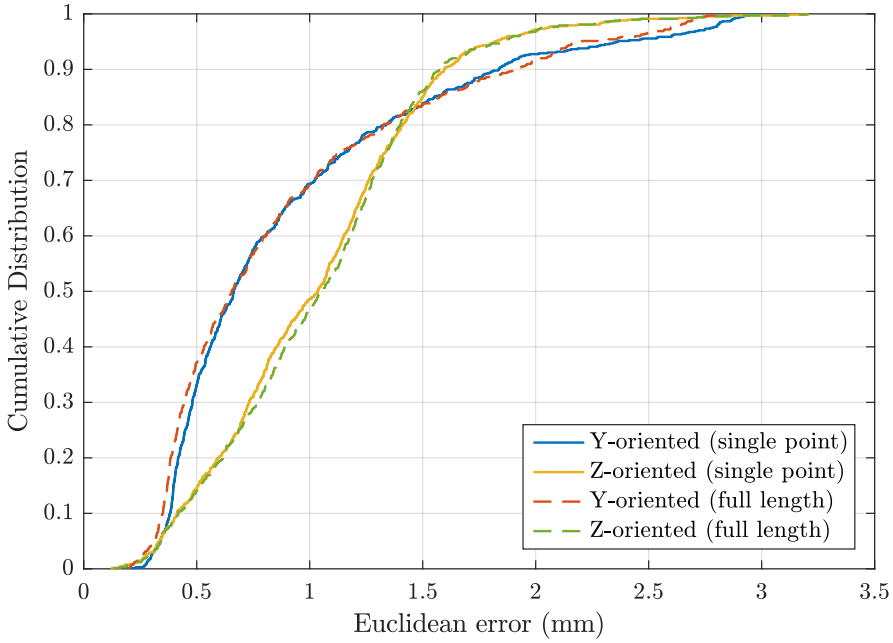


Figure 6.6: Cumulative distribution function of the position error obtained using the *full-length* and the *single-point* magnetic models. The associated error metrics are reported in Table 6.2.

Table 6.2: Position and orientation errors, comparing the *full-length* and the *single-point* analytical and tabulated magnetic models.

	Full length	Single point	LUT FL	LUT SP
Y-oriented sensor				
RMSE (mm / deg)	1.08 / 0.70	1.10 / 0.70	1.08 / 0.70	1.10 / 0.70
ME (mm / deg)	0.88 / 0.49	0.90 / 0.49	0.88 / 0.49	0.90 / 0.49
PRC50 (mm / deg)	0.65 / 0.30	0.66 / 0.30	0.65 / 0.30	0.67 / 0.30
PRC95 (mm / deg)	2.20 / 1.64	2.36 / 1.69	2.20 / 1.64	2.35 / 1.69
Z-oriented sensor				
RMSE (mm / deg)	1.15 / 0.87	1.14 / 0.87	1.15 / 0.87	1.14 / 0.87
ME (mm / deg)	1.05 / 0.78	1.03 / 0.77	1.05 / 0.78	1.03 / 0.77
PRC50 (mm / deg)	1.05 / 0.80	1.04 / 0.80	1.05 / 0.80	1.03 / 0.80
PRC95 (mm / deg)	1.86 / 1.44	1.82 / 1.45	1.86 / 1.45	1.82 / 1.45

6.5.4 Long flexible inductive sensors

The noise resilience of the proposed tracking method of a long coil is evaluated by propagating the errors from the simulated flux to the sensor end-points.

The Gaussian noise was assumed to be uncorrelated for the eight field frequencies, resulting in a diagonal 8×8 covariance matrix, $\Sigma_{\mathbf{\Phi}}$. The positions of the end-points include six degrees of freedom (6 DOF), which constitute the vector $\mathbf{s} \in \mathbb{R}^{6\times 1}$:

$$\mathbf{s} = [x_A \, y_A \, z_A \, x_B \, y_B \, z_B] \tag{6.19}$$

where (x_A, y_A, z_A) and (x_B, y_B, z_B) are the Cartesian coordinates of the two end-points, defined in Figure 6.4.

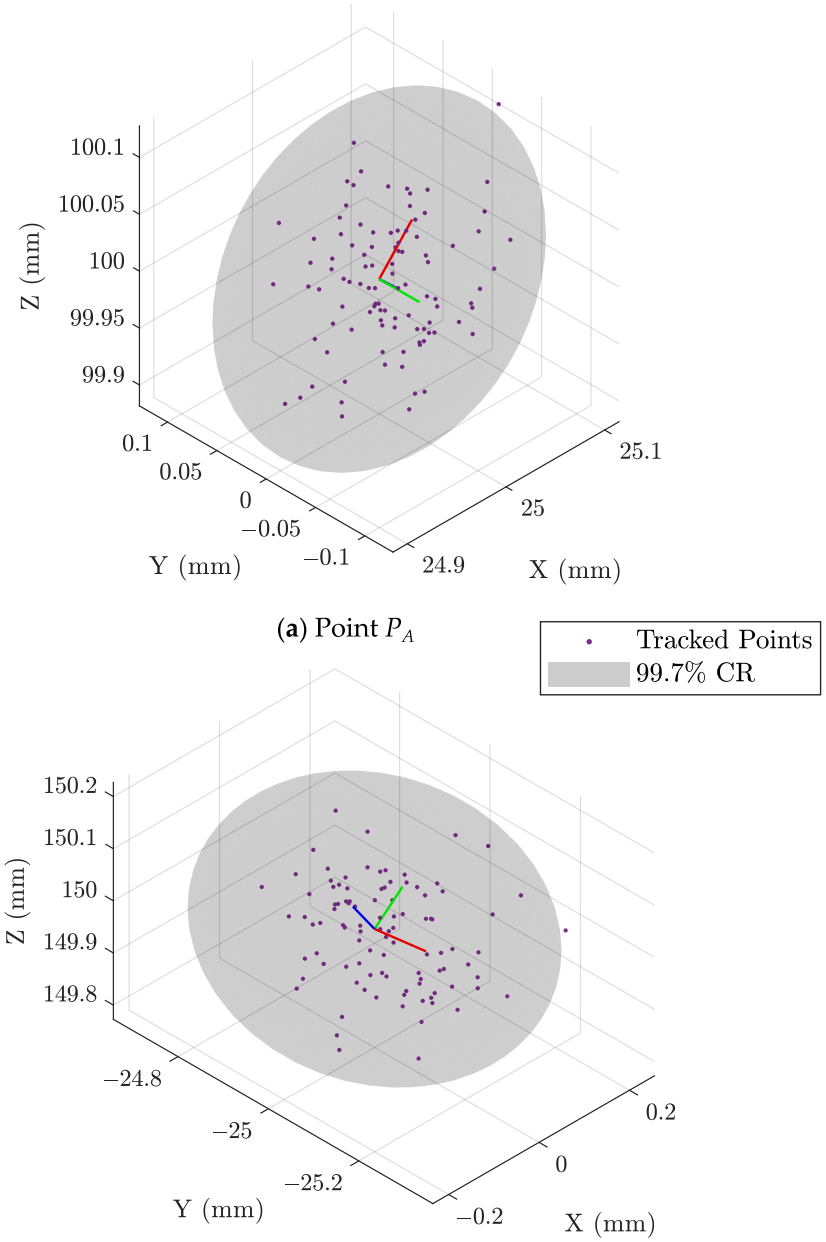
The position covariance matrix, $\Sigma_{\mathbf{p}}$, was obtained by the propagation of uncertainty theory, as given by Equation 6.20:

$$\Sigma_{\mathbf{s}} = \mathbf{J}_{\mathbf{s}}^{\dagger} \cdot \Sigma_{\mathbf{\Phi}} \cdot \mathbf{J}_{\mathbf{s}}^{\dagger T} \tag{6.20}$$

where $\mathbf{J}_{\mathbf{s}}^{\dagger}$ is the Moore–Penrose inverse of the Jacobian matrix for the flux values calculated in $\mathbf{s}$.

One hundred solution vectors $\widetilde{\mathbf{s}}$ were sampled from the multivariate Gaussian distribution with covariance matrix $\Sigma_{\mathbf{s}}$, and they are visualised separately in Figure 6.7, for the end-points P_A and P_B.

Two independent trivariate Gaussian distributions can quantify the total variation in the EMT positions of the two end-points. They are visualised through the associated ellipsoidal confidence regions to make the worst position error directions immediately clear. Values of 0.049 mm and 0.12 mm were obtained for the position standard deviation in the direction of the longest semi-axes of the ellipsoids for the solutions at points P_A and P_B, respectively.



(**a**) Point P_A

(**b**) Point P_B

Figure 6.7: Simulated position error where the signal was perturbed with white Gaussian noise at −63 dB. The tracked positions are visualised in (a) and (b) for end-points P_A and P_B of the 128 mm flexible sensor depicted in Figure 6.4. The position noise of P_A is highly correlated to P_B and is modelled by a 6×6 covariance matrix. The two corresponding uncorrelated trivariate Gaussian distributions are visualised through the 99.7% confidence regions (CR), which are ellipsoids with the main axes indicated by the RGB triplets.

6.6 Discussion

In this section, the principal results and findings obtained in this chapter are commented on, and their implications and future research directions are highlighted.

6.6.1 Model interpolation

A method was presented to evaluate the model interpolation error in terms of EMT accuracy. It was applied to the ANSER EMT field generator to compare the existing model based on the magnetic field vector with the new scalar potential formulation presented in this chapter.

The analysis demonstrated that the two models are equivalent in terms of storage requirements when the position error due to the interpolation approximation is approximately 20 μm. If higher accuracy is required, the table of the three field components takes less storage space when the same interpolation performance is maintained. However, considering typical EMT accuracy between 0.1 mm and 1 mm, the table of the magnetic scalar potential has a smaller size.

The choice of the model formulation and interpolation grid size must be evaluated specifically for the field generator to be modelled, the maximum interpolation error desired, the storage and memory availability, and the time requirements. The methodology presented in this chapter can be followed to find the optimal solution for the specific application.

Further optimisations could reduce the look-up table size while maintaining the same interpolation performance. For example, using different grid-points for each emitter coil, possibly with cylindrical coordinates around the coil axis and adaptive spacing in the Z direction, or considering different sub-regions where the grid spacing is selected based on the spatial variation in the local magnetic field. Such optimisations would benefit the implementation of the tracking algorithm in embedded systems with limited memory. However, they are not critical when the software runs on a computer machine, for which the tables analysed in this chapter can be fully loaded into RAM.

6.6.2 Simulated and experimental tracking tests

The simulated and the experimental tracking tests demonstrated similar results for the magnetic field model formulations compared.

The tabulated models proved to be approximately two times faster than the corresponding analytical model, although both the analytical and the tabulated models met the speed requirements for real-time tracking.

The experiments demonstrated that for an inductive sensor of 10 mm in length, the *single-point* approximation is in practice equivalent to the *full-length* model within the tracking volume considered. This result shows that the spatial variation of the magnetic field of the ANSER EMT field generator is approximately linear within the space covered by the sensor length for the test points considered in the experiments.

The *single-point* approximation introduces errors that increase with the sensor length, the non-linear spatial variation of the magnetic flux density, and the proximity to the field generator. In such cases, the novel *full-length* model introduced in this chapter should be preferred.

6.6.3 Long flexible inductive sensors

A method for tracking a 128 mm-long inductive sensor was presented. The method can find the position of the sensor end-points while the sensor shape remains unknown. The shape may usually be inferred from the passage constraints or precedent end-point positions. More advanced shape reconstruction techniques include using mathematical models [21, 22], fluoroscopic images, or shape sensing based on fiber Bragg gratings [23]. Future work could include sensor manufacturing, tracking validation, and the development of a shape detection algorithm.

A robustness test was carried out, where a realistic noise level was added to simulated magnetic measurements, and the effect on the tracking results was shown. The test was used to predict the expected jitter noise of the EMT positions of the flexible sensor due to random errors in the magnetic flux measurements and shows the noise resilience of the proposed tracking method and algorithm.

6.7 Conclusions

In this chapter, a magnetic scalar potential formulation was studied for application in EMT systems. The formulation resolves the non-zero length ambiguity of elongated tracking sensors and demonstrates a higher speed and lower storage requirements.

Based on the magnetic scalar potential formulation, a novel theoretical model was introduced for the ANSER EMT field generator, and experiments were carried out to compare the new and the existing models.

The new model remains accurate even when the assumption of a single-point sensor is invalid, e.g. if long sensors are tracked near the field generator or if high-gradient fields are used to improve the tracking resolution.

The method might enable the use of longer EMT sensor coils, which can achieve higher sensitivities, possibly without the requirement for a magnetic core, with advantages in terms of linearity, larger dynamic range, lower production costs, and increased flexibility.

References

[1] M. Cavaliere and P. Cantillon-Murphy, "Electromagnetic Tracking of Elongated Sensors for Endoscopic Navigation," *Magnetism*, vol. 2, no. 3, pp. 271–287, 2022, ISSN: 2673-8724. DOI: 10.3390/magnetism2030020.

[2] H. P. Kalmus, "A New Guiding and Tracking System," *IRE Transactions on Aerospace and Navigational Electronics*, vol. ANE-9, no. 1, pp. 7–10, 1962, ISSN: 2331-0812. DOI: 10.1109/TANE3.1962.4201833.

[3] F. H. Raab, E. B. Blood, T. O. Steiner, and H. R. Jones, "Magnetic Position and Orientation Tracking System," *IEEE Transactions on Aerospace and Electronic Systems*, vol. AES-15, no. 5, pp. 709–718, 1979, ISSN: 2371-9877. DOI: 10.1109/TAES.1979.308860.

[4] *Aurora Sensors - NDI*. [Online]. Available: https://www.ndigital.com/products/aurora/aurora-sensors/ (visited on 04/22/2022).

[5] M. Cavaliere, O. McVeigh, H. A. Jaeger, S. Hinds, K. O'Donoghue, and P. Cantillon-Murphy, "Inductive Sensor Design for Electromagnetic Tracking in Image Guided Interventions," *IEEE Sensors Journal*, vol. 20, no. 15, pp. 8623–8630, 2020, ISSN: 1558-1748. DOI: 10.1109/JSEN.2020.2984323.

[6] H. Jaeger, K. O'Donoghue, and P. Cantillon-Murphy, "Induction sensor characterisation for electromagnetic tracking systems," in *IEEE I2MTC 16-19 May 2022*, Ottawa, ON, Canada, 2022.

[7] IEEE, "IEEE Standard for Safety Levels with Respect to Human Exposure to Electric, Magnetic, and Electromagnetic Fields, 0 Hz to 300 GHz," *IEEE Std C95.1-2019 (Revision of IEEE Std C95.1-2005/ Incorporates IEEE Std C95.1-2019/Cor 1-2019)*, pp. 1–312, 2019. DOI: 10.1109/IEEESTD.2019.8859679.

[8] J. D. Jackson, *Classical Electrodynamics*, 3rd ed. New York: Wiley, 1999, pp. 174–236, ISBN: 978-0-471-30932-1.

[9] M. Abramowitz and I. A. Stegun, Eds., *Handbook of Mathematical Functions: With Formulas, Graphs, and Mathematical Tables* (Dover Books on Mathematics), 9. Dover print. New York, NY: Dover Publ, 2013, ISBN: 978-0-486-61272-0.

[10] W. H. Press, S. A. Teukolsky, W. T. Vetterling, and B. P. Flannery, *Numerical Recipes: The Art of Scientific Computing*. Cambridge [Cambridgeshire] ; New York: Cambridge University Press, 1986, ISBN: 978-0-521-30811-3.

[11] D. J. Griffiths, *Introduction to Electrodynamics*. Englewood Cliffs, N.J: Prentice-Hall, 1981, ISBN: 978-0-13-481374-5.

[12] J. Vanderlinde, *Classical Electromagnetic Theory* (Fundamental Theories of Physics v. 145), 2nd ed. Dordrecht Boston: Kluwer Academic Publishers, 2004, pp. 26–28, ISBN: 978-1-4020-2700-0.

[13] R. J. Mathar, "Solid angle of a rectangular plate," *Max-Planck Institute of Astronomy, Heidelberg, Germany*, pp. 1–9, 2015. [Online]. Available: https://vixra.org/abs/2001.0603 (visited on 02/08/2022).

[14] MathWorks, *Gridded data interpolation*. [Online]. Available: https://uk.mathworks.com/help/matlab/ref/griddedinterpolant.html (visited on 09/13/2022).

[15] MathWorks, *List variables in workspace, with sizes and types*. [Online]. Available: https://uk.mathworks.com/help/matlab/ref/whos.html (visited on 09/14/2022).

[16] Northern Digital Inc., *Aurora Sensors*. [Online]. Available: https://www.ndigital.com/electromagnetic-tracking-technology/aurora/aurora-sensors/ (visited on 09/13/2022).

[17] MathWorks, *Start stopwatch timer*. [Online]. Available: https://uk.mathworks.com/help/matlab/ref/tic.html (visited on 09/13/2022).

[18] H. A. Jaeger *et al.*, "Anser EMT: The first open-source electromagnetic tracking platform for image-guided interventions," *International Journal of Computer Assisted Radiology and Surgery*, vol. 12, pp. 1059–1067, 2017. DOI: 10.1007/s11548-017-1568-7.

[19] MathWorks, *Numerical integration*. [Online]. Available: https://uk.mathworks.com/help/matlab/ref/integral.html (visited on 09/13/2022).

[20] A. Quarteroni, R. Sacco, and F. Saleri, *Numerical Mathematics*. Heidelberg, Germany: Springer Science & Business Media, 2010, vol. 37, ISBN: 3-540-49809-5.

[21] C. Shi *et al.*, "Shape Sensing Techniques for Continuum Robots in Minimally Invasive Surgery: A Survey," *IEEE Transactions on Biomedical Engineering*, vol. 64, no. 8, pp. 1665–1678, 2017, ISSN: 1558-2531. DOI: 10.1109/TBME.2016.2622361.

[22] S. Song, C. Zhang, J. Wang, H. Ren, and M. Q. H. Meng, "Real-time shape estimation of curvilinear flexible surgical robots: Methods, experiments and analysis," *International Journal of Robotics and Automation*, vol. 33, no. 5, pp. 559–568, 2018, ISSN: 08268185. DOI: 10.2316/Journal.206.2018.5.206-5329.

[23] X. T. Ha *et al.*, "Robust Catheter Tracking by Fusing Electromagnetic Tracking, Fiber Bragg Grating and Sparse Fluoroscopic Images," *IEEE Sensors Journal*, vol. 21, no. 20, pp. 23 422–23 434, 2021, ISSN: 1558-1748. DOI: 10.1109/JSEN.2021.3107036.

Chapter 7

Magnetic models for planar sensors

This chapter focuses on the modelling and tracking of planar inductive sensors on the centimetre scale.

Large planar coils integrated into patches and applied on the body of the patient can improve the robustness of EMT for image-guided interventions. A set of sensors placed around the operative region can be used to track and compensate for respiratory and cardiac movements [2] or enable real-time compensation of field distortion by dynamically evaluating the field at multiple locations, as discussed in Section 4.5.

Another possible application involves tracking the planar transmitter coils of one or more field generators [3, 4]. ANSER EMT field generator, presented in Section 3.1, comprises a set of eight coils, each composed of straight filaments and embedded in a printed circuit board. Identical coils can also be used as pick-up coils to measure magnetic fields, and the five degrees of freedom of the transmitter coils can be derived using traditional EMT methods. In this way, the reciprocal position between two boards can be determined by tracking the position of the coils of one board relative to the other. Therefore, two boards can be placed next to each other to enlarge the tracking region, or flexible boards can be designed where the position of the emitter coils is automatically determined [4].

This chapter is based on M. Cavaliere *et al.*, "Planar Body-Mounted Sensors for Electromagnetic Tracking," *Sensors*, vol. 21, no. 8, p. 2822, 2021 [1].

Moreover, in a rigid field generator where the emitter coils are at fixed positions, the change in the reciprocal mutual inductance can be used as a distortion detection method [5].

This chapter presents new general formulas to calculate the mutual inductance between a filamentary-based large-area sensor and the transmitter coils of the ANSER EMT field generator. The model is then compared to the single-point approximation in terms of speed and accuracy.

This work demonstrates the first EMT method based on the mutual coupling between straight filaments and is suited to large-area sensor coils.

7.1 Introduction

As introduced in Section 2.2, EMT systems allow inferring the position and orientation information based on the coupling between magnetic field sources and sensors.

Inductive sensors measure the variation of the magnetic flux across the sensor area. While small-diameter sensors can be approximated with a single point without accuracy loss [6], large-diameter sensors require the evaluation of the field at more points within the sensor area [7] in order to numerically integrate the magnetic flux measured by the sensor. The more accuracy is required, the more points may be considered, resulting in a slower tracking algorithm.

In Section 7.2, a novel method is proposed which makes the flux calculation faster by using magnetic vector potential integration along the perimeter of the sensor coil.

7.2 Mutual inductance between large-area planar coils

The mutual inductance, M_{TxRx}, between two coils is defined by the magnetic flux generated by one coil (which can be considered the transmitter

coil Tx) that is linked to the loop of the second coil (or receiver coil Rx) per unit current I_{Tx}.

Calculating the magnetic flux across a closed loop Γ_{Rx} can be performed in two ways, as per Equations 7.1 and 7.2. In the first case, the magnetic field vector, $\mathbf{B_{Tx}}$, is integrated over the surface Σ_{Rx} enclosed by Γ_{Rx}. In the second case, the line integral of the magnetic vector potential $\mathbf{A_{Tx}}$ along Γ_{Rx} is performed.

$$M_{TxRx} = \frac{1}{I_{Tx}} \int_{\Sigma_{Rx}} \mathbf{B_{Tx}}(\mathbf{r}) \cdot \mathbf{n_{Rx}} \, d\Sigma_{Rx} \tag{7.1}$$

$$= \frac{1}{I_{Tx}} \int_{\Gamma_{Rx}} \mathbf{A_{Tx}}(\mathbf{r}) \cdot \mathbf{t_{Rx}} \, d\Gamma_{Rx} \tag{7.2}$$

where $\mathbf{n_{Rx}}$ and $\mathbf{t_{Rx}}$ are the unit vectors perpendicular to $d\Sigma_{Rx}$ and tangential to Γ_{Rx}, respectively, and $\mathbf{r}$ is the position vector where $\mathbf{B_{Tx}}$ or $\mathbf{A_{Tx}}$ are evaluated. The two approaches are illustrated in Figure 7.1. For particular shapes of Tx and Rx, the integrals admit analytical solutions, while in general, numerical integration can be performed by approximation as the sum of finite-size elements.

In a linear and homogeneous medium like air, the magnetic field $\mathbf{B_{Tx}}(\mathbf{r})$ generated by the current I_{Tx} along the path Γ_{Tx}, is given by the Biot-Savart law, as reported in Equation 7.3:

$$\mathbf{B_{Tx}}(\mathbf{r}) = \frac{\mu_0 I_{Tx}}{4\pi} \int_{\Gamma_{Tx}} \frac{\mathbf{t_{Tx}} \times \mathbf{r}}{|\mathbf{r}|^3} \, d\Gamma_{Tx} \tag{7.3}$$

where μ_0 is the magnetic permeability of air.

If the coil Tx is composed of straight wires, such as the transmitter coils of the ANSER EMT field generator, the integral of Equation 7.3 can be decomposed to a sum of integrals over straight lines. Calculating the magnetic flux from Equation 7.1 reduces to the integral across the receiving surface Σ_{Rx} of the magnetic field generated by each transmitting filament.

Magnetic sensors used in EMT systems are often around one millimetre in diameter [8], which allows approximating Σ_{Rx} as a single point, considering the field to be constant throughout the sensor volume due to

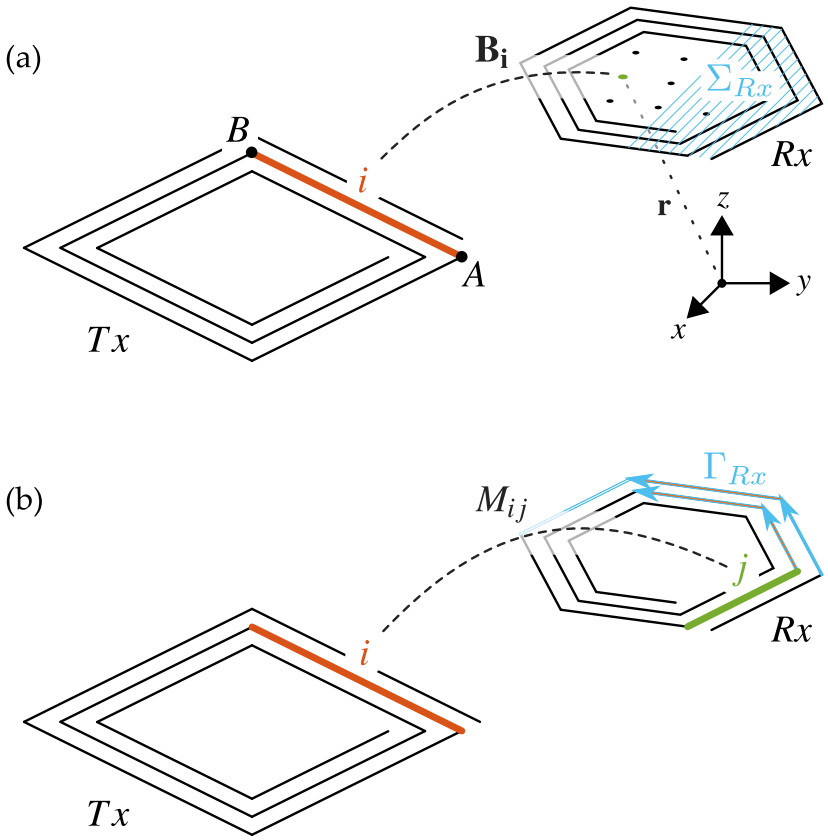


Figure 7.1: The mutual inductance between coil Tx and coil Rx can be calculated in two ways: (a) from Equation 7.1 and numerically approximated by evaluation of the magnetic field generated by Tx across the area of Rx; (b) from Equation 7.2 as the sum of the partial mutual inductances between the straight filaments of the two coils.

its small dimensions relative to the field spatial variation. From the mean value theorem, the positional error introduced by this simplified magnetic model is smaller than the sensor radius.

For large-area inductive sensors, such as those studied in this work, Equation 7.3 may be evaluated at multiple points within the cross-sectional area of the sensor coil in order to perform numerical integration, as depicted in Figure 7.1a. The number of evaluation points needed to achieve a given accuracy scales quadratically with the diameter of the receiving coil. In this case, it becomes numerically more convenient to use Equation 7.2, where the integral is performed along the loop of the sensor coil, and the

number of segments that approximate the perimeter increases linearly with the diameter, as depicted in Figure 7.1b.

Biot-Savart's law can be expressed in terms of magnetic vector potential [9, 10]:

$$\mathbf{A_{Tx}}(\mathbf{r}) = \frac{\mu_0 I_{Tx}}{4\pi} \int_{\Gamma_{Tx}} \frac{\mathbf{t_{Tx}}}{|\mathbf{r}|}\, d\Gamma_{Tx} \tag{7.4}$$

Considering Equation 7.4, Equation 7.2 becomes:

$$\begin{aligned} M_{TxRx} &= \int_{\Gamma_{Rx}} \left[\frac{\mu_0}{4\pi} \int_{\Gamma_{Tx}} \frac{\mathbf{t_{Tx}}}{|\mathbf{r}|}\, d\Gamma_{Tx} \right] \cdot \mathbf{t_{Rx}}\, d\Gamma_{Rx} \\ &= \frac{\mu_0}{4\pi} \int_{\Gamma_{Tx}} \int_{\Gamma_{Rx}} \frac{\mathbf{t_{Tx}} \cdot \mathbf{t_{Rx}}}{|\mathbf{r}|}\, d\Gamma_{Rx} d\Gamma_{Tx} \end{aligned} \tag{7.5}$$

which is referred as the *Neumann integral* [11, 12]. Equation 7.5 shows that the coupling between two loops is a geometric quantity dependent on the loops' shape and reciprocal position. Interchanging the order of integration demonstrates that the mutual inductance is also equal to the flux generated by Rx and linked to Tx, so that $M_{RxTx} = M_{TxRx}$.

If both Tx and Rx are composed of straight filaments, the double integral of Equation 7.5 becomes the summation of the contributions given by all filaments pairs:

$$M_{TxRx} = \sum_{i \in Tx} \sum_{j \in Rx} M_{ij} \tag{7.6}$$

where M_{ij} is defined as the partial mutual inductance between filament i of coil Tx and filament j of coil Rx, as shown in Figure 7.1b, and will be analytically evaluated in Section 7.2.1.

Equation 7.6 can also be used to compute the self-inductance of any circuit made of straight filaments, in which case filaments i and j are part of the same circuit.

7.2.1 Partial mutual inductance between straight wires

The Neumann integral of Equation 7.5 performed between two straight filaments provides the partial mutual inductance between the filaments and can be solved analytically [13–15]. The analytical solution presented

in this chapter represents an improvement in accuracy and speed over previous works which used numerical integration [16, 17].

According to Figure 7.2, the following notation is defined. Points A and B are the 3-dimensional vectors of the start and end points of the transmitting filament AB, respectively. It will be clear from Section 7.2.2 that A and B could be $3 \times N$ matrices of N transmitting vectors, such as the filaments composing a coil or a set of coils, allowing for fast vectorial implementation. Analogously, the receiving filament is defined by points a and b. The distances between the end-points of segments AB and ab are R_1, R_2, R_3, R_4, as indicated in Figure 7.2a.

Two direction vectors are found:

$$\vec{D} = B - A; \qquad \vec{d} = b - a \tag{7.7}$$

The lengths of the two filaments are $l = \|\vec{D}\|$ and $m = \|\vec{d}\|$

For any two straight lines in space, two planes exist which are parallel and contain these lines. The distance between the planes, s, corresponds to the minimum distance between the straight lines. The position of minimal distance is identified by point P. When projecting the filaments on the same parallel plane, the angle between the projections is θ. The quantities α and β are the lengths of the prolongations to the intersection point of minimal distance P, as indicated in Figure 7.2b.

Equation 7.8 gives the mutual inductance between two filamentary wires at any angle and not on the same plane [14][15]:

$$\begin{aligned} M_{ij} = \frac{\mu_0}{2\pi}\cos(\theta)\Bigg[&(\beta+m)\tanh^{-1}\left(\frac{l}{R_1+R_4}\right)+ \\ &-\beta\tanh^{-1}\left(\frac{l}{R_2+R_3}\right)+ \\ &+(\alpha+l)\tanh^{-1}\left(\frac{m}{R_1+R_2}\right)+ \\ &-\alpha\tanh^{-1}\left(\frac{m}{R_4+R_3}\right)-\frac{\Omega s}{2\sin(\theta)}\Bigg] \end{aligned} \tag{7.8}$$

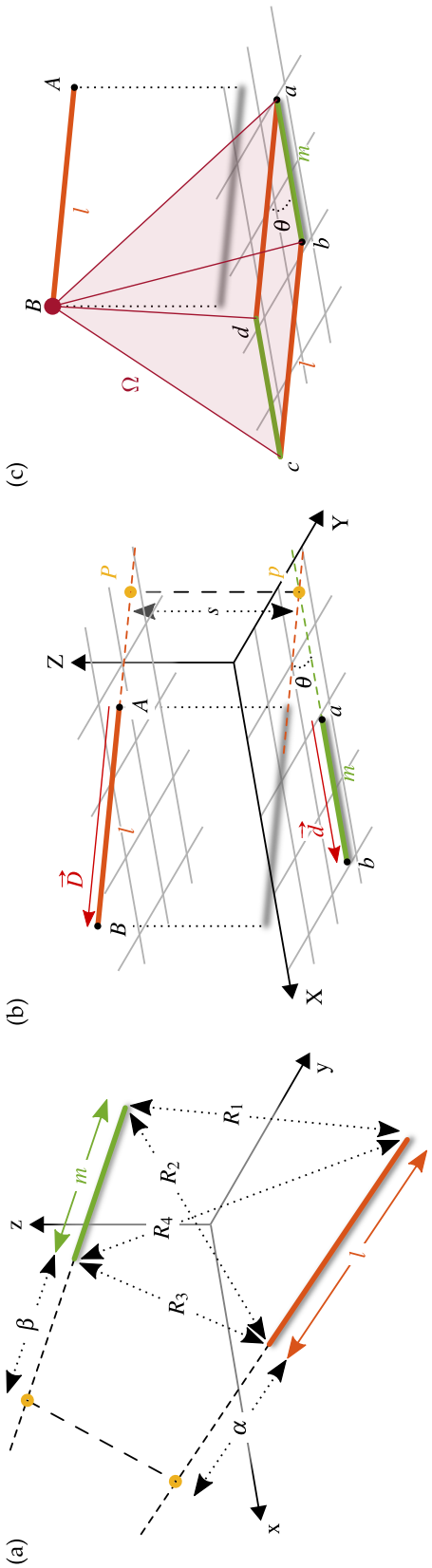


Figure 7.2: (a) Two straight filaments at any angle. For convenience, l is considered the transmitting filament, which generates a magnetic field, and m is the receiving filament, where the variable field induces a voltage.
(b) A change of coordinates is performed to calculate the mutual inductance between the two wires.
(c) Solid angle, Ω, subtended from point B by the parallelogram constructed on ab with bc parallel and equal to AB.

in which Ω is the positive solid angle, defined in Figure 7.2c and given by:

$$\begin{aligned}\Omega = &\tan^{-1}\left(\frac{s^2\cos\theta + (\alpha+l)(\beta+m)\sin^2\theta}{sR_1\sin\theta}\right) + \\ &- \tan^{-1}\left(\frac{s^2\cos\theta + (\alpha+l)\beta\sin^2\theta}{sR_2\sin\theta}\right) + \\ &+ \tan^{-1}\left(\frac{s^2\cos\theta + \alpha\beta\sin^2\theta}{sR_3\sin\theta}\right) + \\ &- \tan^{-1}\left(\frac{s^2\cos\theta + \alpha(\beta+m)\sin^2\theta}{sR_4\sin\theta}\right)\end{aligned} \tag{7.9}$$

Equation 7.8 can be generalised by defining α and β with a positive sign if the prolongation towards point P is directed as the filament, negative otherwise [18].

7.2.2 Novel implementation of the formula

This section presents a new implementation of the formula in Equation 7.8 starting from the Cartesian coordinates of the end-points of the filaments. The procedure is well suited to vectorial input for the simultaneous calculation of the partial mutual inductances between one filament and many others.

As depicted in Figure 7.2, a change of coordinates is performed, to a reference system where the quantities required by Equations 7.8 and 7.9 can be easily computed. The new X-axis is defined to be aligned along the receiving filament. The unit direction vector is identified by $\vec{d}$, following normalisation:

$$\mathbf{u_X} = \vec{d}/\|\vec{d}\| = \vec{d}/m \tag{7.10}$$

Axis Z is chosen perpendicular to both filaments, i.e. perpendicular to the uniquely identified parallel planes containing the filaments, and axis Y is consequently found to complete the triplet:

$$\mathbf{u_Z} = \vec{D}\times\vec{d}/\|\vec{D}\times\vec{d}\|; \quad \mathbf{u_Y} = \mathbf{u_Z}\times\mathbf{u_X} \tag{7.11}$$

It should be noted that $\mathbf{u_Z}$ and $\mathbf{u_Y}$ change for each transmitting filament and become $3 \times N$ matrices, $\mathbf{U_Z}$ and $\mathbf{U_Y}$ respectively, if N transmitting filaments AB are considered at the same time. Vectorisation is still possible for Equation 7.11 if the three vector components are computed by separate equations:

$$\begin{aligned} \mathbf{U_{Y}}_x &= \mathrm{u_{X}}_z \, \mathbf{U_Z}_y - \mathrm{u_{X}}_y \, \mathbf{U_Z}_z \\ \mathbf{U_{Y}}_y &= \mathrm{u_{X}}_x \, \mathbf{U_Z}_z - \mathrm{u_{X}}_z \, \mathbf{U_Z}_x \\ \mathbf{U_{Y}}_z &= \mathrm{u_{X}}_y \, \mathbf{U_Z}_x - \mathrm{u_{X}}_x \, \mathbf{U_Z}_y \end{aligned} \tag{7.12}$$

The change of coordinates of the quantities of Figure 7.2 is performed by the dot product with the new directions. For example, point $\mathbf{A} = [A_x \; A_y \; A_z]$ becomes:

$$\begin{aligned} A_X &= \mathrm{u_X}_x \, A_x + \mathrm{u_X}_y \, A_y + \mathrm{u_X}_z \, A_z \\ A_Y &= \mathrm{u_Y}_x \, A_x + \mathrm{u_Y}_y \, A_y + \mathrm{u_Y}_z \, A_z \\ A_Z &= \mathrm{u_Z}_x \, A_x + \mathrm{u_Z}_y \, A_y + \mathrm{u_Z}_z \, A_z \end{aligned} \tag{7.13}$$

In the new reference system XYZ, the distance between the straight lines is given by the Z-components:

$$s = |A_Z - a_Z| \tag{7.14}$$

and the sine and cosine of the angle θ are:

$$\sin\theta = \frac{D_Y}{l}; \qquad \cos\theta = \frac{D_X}{l} \tag{7.15}$$

Considering X and Y components only, the straight lines lay on the same plane and point P is their intersection:

$$\begin{aligned} P_X &= \frac{D_X}{D_Y}(a_Y - A_Y) + A_X \\ P_Y &= a_Y \end{aligned} \tag{7.16}$$

Finally, α and β, defined with sign as in [18], are:

$$\begin{aligned} \alpha &= \frac{1}{l}\left[\left(A_X - P_X\right) D_X + \left(A_Y - P_Y\right) D_Y\right] \\ \beta &= a_X - P_X \end{aligned} \tag{7.17}$$

Applying Equation 7.8 is impossible when two filaments are parallel. In practice, Equation 7.16 fails to find the point of intersection P, which is at an infinite distance. In this case, the simplified formula for the mutual partial inductance between parallel wires must be used [19].

7.3 Sensor manufacturing

Planar coils were manufactured on PCB to experimentally validate the formula proposed in Section 7.2. This section details the sensor coil design optimisation and the resulting sensor parameters.

7.3.1 Planar sensor coil design

The procedure presented in this section applies to planar coils of any shape and will be used in Section 7.3.2 to compare hexagonal, circular, and rectangular sensors. However, the formulas are reported for spirals with a hexagonal footprint because this shape was selected for manufacturing, as will be justified in Section 7.3.3.

Two parameters are of primary importance for a coil used as an inductive sensor: the sensitivity, or sensor gain, and the signal-to-noise ratio (SNR) [20]. Another relevant parameter is the resonance frequency, related to the parasitic capacitance between the winding turns [21].

The sensitivity is proportional to the total area enclosed by each turn of the coil. The main sources of noise are the thermal noise and the noise introduced by the signal amplifier. In particular, the thermal noise is a function of the coil resistance, which is linear with the winding length.

The coil's total length and area are calculated as follows for a hexagonal planar coil. Similar formulas apply to other planar shapes. The winding is approximated by concentric hexagons, as shown in Figure 7.3.

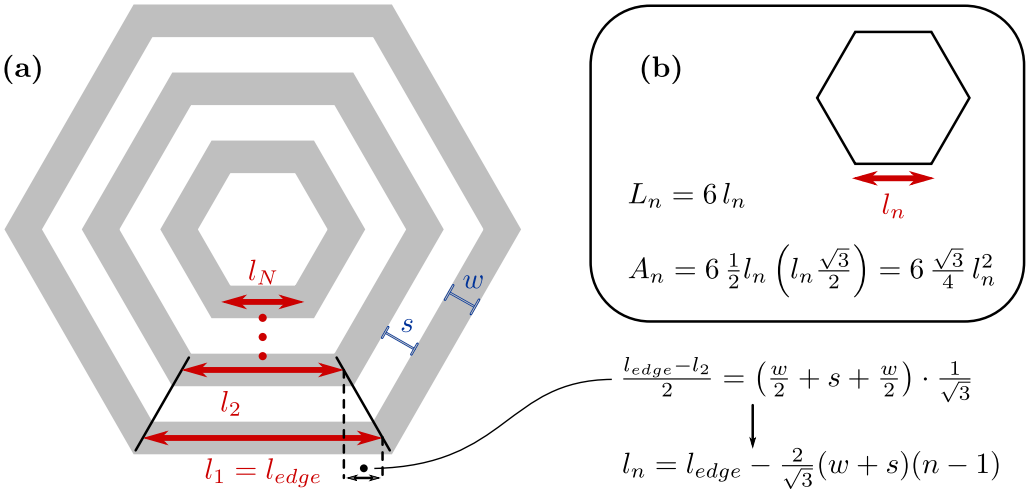


Figure 7.3: The spiral of a hexagonal planar coil is approximated as a set of concentric hexagons to calculate the coil's cross-sectional area and total length. (a) The edge length, l_n, of the n^{th} inner turn depends on the external edge, l_{edge}, and the trace width, w, and spacing, s.
(b) Formulas for the equilateral hexagon perimeter L_n and area A_n.

If l_{edge} is the edge length of the external turn and w and s are the trace width and spacing, respectively, the edge length of the n^{th} inner turn is computed as:

$$l_n = l_{edge} - \frac{2}{\sqrt{3}}(w+s)(n-1) \tag{7.18}$$

where n starts from $n = 1$ for the external turn.

The total winding length L_c and area A_c are:

$$\begin{aligned} L_c &= N_{layers} \cdot \sum_{n=1}^{N_{turns}} 6 \left[l_{edge} - \frac{2}{\sqrt{3}}(w+s)(n-1) \right] \\ &= N_{layers} \cdot 6 N_{turns} \left[l_{edge} - \frac{1}{\sqrt{3}}(N_{turns}-1)(w+s) \right] \end{aligned} \tag{7.19}$$

and

$$A_c = N_{layers} \cdot \sum_{n=1}^{N_{turns}} 6\frac{\sqrt{3}}{4}\left[l_{edge} - \frac{2}{\sqrt{3}}(w+s)(n-1)\right]^2$$
$$= N_{layers} \cdot 6\frac{\sqrt{3}}{4} N_{turns}\left[l_{edge}^2 - \frac{2}{\sqrt{3}}(N_{turns}-1)l_{edge}(w+s) + \right. \tag{7.20}$$
$$\left. + \frac{2}{9}(N_{turns}-1)(2N_{turns}-1)(w+s)^2\right]$$

where N_{turns} is the total number of turns, and N_{layers} is the number of PCB layers, assuming that the same coil design is used for all layers.

In Equations 7.19 and 7.20, the series sums are derived from the following identities:

$$\sum_{n=1}^{N} n = \frac{N(N+1)}{2}; \quad \sum_{n=1}^{N} n^2 = \frac{N(N+1)(2N+1)}{6} \tag{7.21}$$

A copper coil is considered, with a resistivity of $\rho_{Cu} = 1.74_{\times 10^{-8}}\ \Omega$m and a trace thickness $t = 34.79\ \mu$m, corresponding to 1 oz per square foot, as this is a standard PCB manufacturing specification. The coil ohmic resistance is:

$$R_c = \rho_{Cu}\frac{L_c}{wt} \tag{7.22}$$

where L_c is the total winding length with constant trace width, w.

The thermal noise RMS density is given by Equation 7.23:

$$U_{nt} = \sqrt{4K_B T R_c}\left[\frac{\text{nV}}{\sqrt{\text{Hz}}}\right] \tag{7.23}$$

where $K_B = 1.38_{\times 10^{-23}}$ J/K is the Boltzmann constant and $T = 300$ K is the ambient temperature.

The inductive sensor signal requires amplification before sampling. A low-noise instrumentation amplifier INA163 (Texas Instruments, Dallas, Texas) is used in the ANSER EMT system [6]. The INA163 introduces an input stage noise of $U_{nin} = 1\,\text{nV}/\sqrt{\text{Hz}}$ and an output stage noise of $U_{nout} = 60\,\text{nV}/\sqrt{\text{Hz}}$. In addition, an input noise current density of

$0.8\,\mathrm{pA}/\sqrt{\mathrm{Hz}}$ is reported, which was multiplied by the coil impedance, given by Equation 7.22, to determine the voltage noise density associated, U_{ni}. The amplifier was configured with a gain of $G_{amp} = 500$.

The total noise magnitude depends on the signal bandwidth, Δf. The system uses frequency division multiplexing (FDM) to demodulate the eight magnetic field measurements from the eight transmitter coils. The measured voltage was sampled at $F_s = 100\,\mathrm{kHz}$, and 1000 samples were used for the frequency analysis [6]. For each of the eight frequencies, the target signal frequency is contained in a bin width of $\Delta f = {}^{F_s}/_{1000} = 100\,\mathrm{Hz}$, which is the bandwidth of the noise added to the signal of interest.

Noise contributions sum quadratically, and the total noise is then computed as:

$$\begin{aligned} U_n = &\sqrt{\Delta f} \cdot \Big[(G_{amp} \cdot U_{nt})^2 + \\ &+ (G_{amp} \cdot U_{nin})^2 + (G_{amp} \cdot U_{ni})^2 + U_{nout}^2 \Big]^{\frac{1}{2}} \ [\mathrm{V}] \end{aligned} \tag{7.24}$$

The voltage induced on the sensor equals the time derivative of the magnetic flux enclosed by the sensor coil. Assuming the magnetic field to be constant across the sensor area, A_c, the magnitude of the signal measured is given by Equation 7.25, after amplification:

$$U_s = G_{amp} \cdot 2\pi f A_c B_n \ [\mathrm{V}] \tag{7.25}$$

where f is the signal frequency, and B_n is the magnetic flux density normal component.

In the system configuration used in the following experiments, the eight sinusoidal fields have frequencies around $f = 20\,\mathrm{kHz}$, and the average magnitude of the normal component of the magnetic flux density exceeds $B_n = 0.1\,\mu\mathrm{T}$. As the field frequencies can be configured in a range between 2 and 50 kHz [6], and the signal magnitude depends on the sensor position and orientation, the values considered for f and B_n are simply a reference used for the coil geometry optimisation and design process.

Finally, the SNR is calculated from Equations 7.24 and 7.25:

$$\mathrm{SNR} = 20 \log_{10} \frac{U_s}{U_n} \; [\mathrm{dB}] \tag{7.26}$$

Equation 7.26 shows that the coil area, A_c, only appears in the numerator, and the winding length, L_c, is only present in the denominator. As the ratio A_c/L_c increases with the coil dimension, it follows that larger coils always provide larger SNR and signal U_s. The spatial constraints of the final application limit the coil dimension.

7.3.2 Coil design optimisation

In the optimisation process, the sensor coils' external dimension, D_{out}, was fixed to 3 cm, and the SNR was optimised for the number of turns, N_{turns}, trace width, w, and spacing, s. The parameters w and s were constrained to a minimum value of $t = 0.127$ mm, corresponding to 5 mil, as this is a common PCB limit for standard production. The maximum N_{turns} was limited by what is physically manufacturable on a planar spiral of $D_{out} = 3$ cm, for a given w and s.

The MATLAB function *fmincon* was used to solve the constrained optimisation problem [22]. The highest gain and SNR are obtained for these constraints when trace width and spacing are minimised within manufacturable constraints, $w = s = 0.127$ mm, and the number of turns is maximised.

It should be noted that this is not always the case. For larger coil dimensions, the inner turns could contribute more to noise than signal. Therefore, selecting a wider trace width and not filling all the space available would be more convenient. In this way, the coil resistance and thermal noise are reduced. In particular, when the signal is so large that the amplifier noise can be neglected, the thermal noise would dominate in the coil design for SNR optimisation.

Three planar coil shapes were compared: hexagonal, circular, and square. The three coils were designed to give the same footprint area as the hexagonal coil, which had a 3 cm diagonal. The SNR calculated from Equation 7.26 is plotted in Figure 7.4 with increasing turn count.

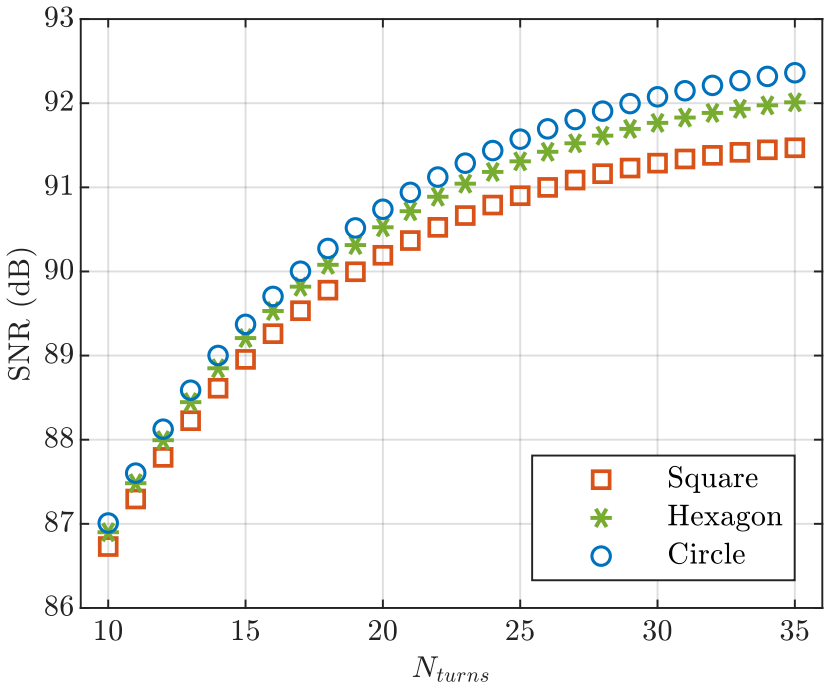


Figure 7.4: SNR predicted from Equation 7.26 with variation in turn count. Circular, hexagonal, and square planar coil shapes are compared. The three planar coils have the same footprint area of a hexagon with a diagonal of 3 cm ($A_c = 5.85\,\text{cm}^2$).

The circular shape provides slightly higher SNR for two reasons: 1) when more turns are added, the cross-sectional area increases more for a circular winding than for a hexagonal or square winding, yielding a higher signal magnitude, and 2) a circular coil has the maximum enclosed area for a given winding length, minimising the resistance and the thermal noise.

The parasitic capacitance of planar coils is mainly due to the electrical coupling between overlapping traces of different layers [23, 24]. Parasitic capacitances were minimised by designing the footprints of subsequent layers with shifted traces, as illustrated in Figure 7.5. In this way, the self-resonance frequency of the coil is maximised.

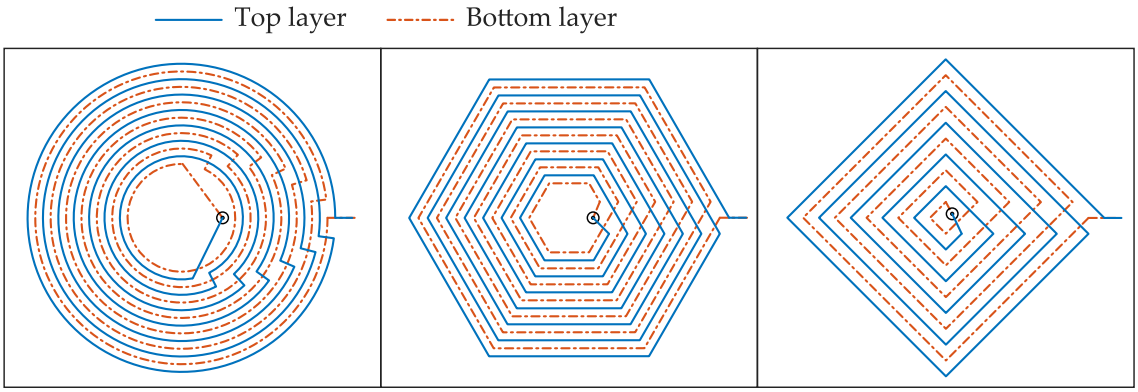


Figure 7.5: The footprints of subsequent layers are shifted so that the traces do not overlap. In this way, the parasitic capacitance of the winding is minimised, and the self-resonance frequency is maximised.

7.3.3 Coil measured parameters

The hexagonal planar coil of Figure 7.6a was manufactured on PCB to experimentally validate Equation 7.8, which applies to coils composed of straight filaments. A hexagonal shape provides higher SNR than a square coil, as demonstrated in Figure 7.4, and can be entirely modelled by six filaments per turn. The coil parameters are $w = s = 0.127\,\text{mm}$, $N_{turns} = 30$, $D_{out} = 3\,\text{cm}$, $N_{layers} = 4$.

Two other coils were used for comparison, the first having a smaller number of turns, $N_{turns} = 15$, and the second with a smaller diagonal dimension, $D_{out} = 2\,\text{cm}$. They are shown in Figures 7.6b and 7.6c, respectively. The three coils (a, b, and c) were otherwise identical.

The coil resistance was calculated from Equation 7.22. For the three coils of Figure 7.6, the predicted ohmic resistance is:

$$R_a = 30.47\,\Omega; \quad R_b = 18.36\,\Omega; \quad R_c = 16.30\,\Omega \tag{7.27}$$

The self-inductance can be estimated by Equation 7.6 if the transmitting and receiving filaments are part of the same coil:

$$L_a = 304.2\,\mu\text{H}; \quad L_b = 133.3\,\mu\text{H}; \quad L_c = 111.2\,\mu\text{H} \tag{7.28}$$

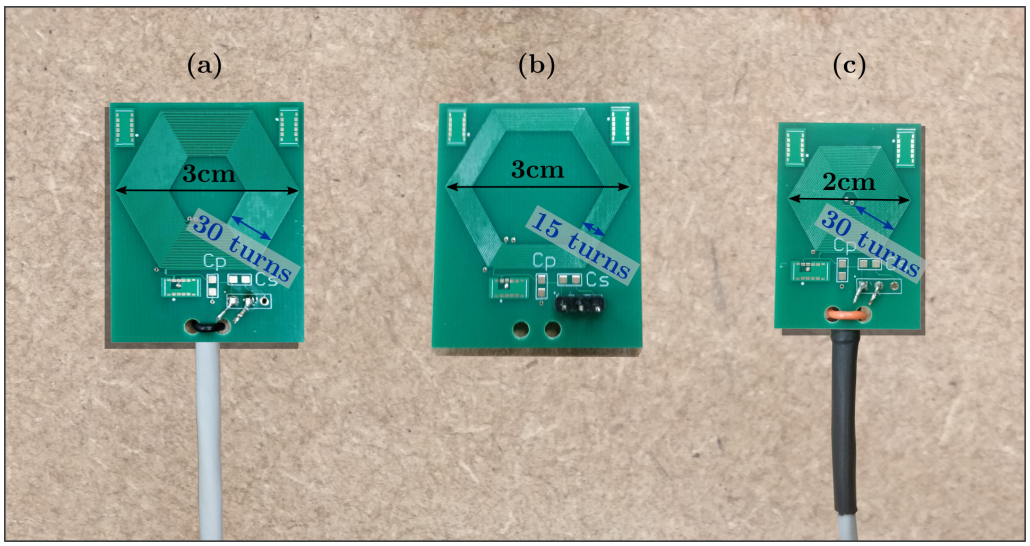


Figure 7.6: Three hexagonal sensors were manufactured on a four-layer PCB. (a) The reference coil has a diagonal, D_{out}, of 3 cm and 30 turns per layer. (b) Another version with 15 turns, and (c) a smaller coil with $D_{out} = 2$ cm, were realised to validate the formulas used in the coil design procedure.

For the three coils of Figure 7.6, the values of the coil resistance and self-inductance measured at 1 kHz are:

$$\begin{aligned} R_a &= 37.0\,\Omega; \quad R_b = 22.8\,\Omega; \quad R_c = 18.6\,\Omega; \\ L_a &= 289.4\,\mu\text{H}; \quad L_b = 121.2\,\mu\text{H}; \quad L_c = 98.2\,\mu\text{H} \end{aligned} \tag{7.29}$$

which should be compared with Equations 7.27 and 7.28.

The inductive sensor sensitivity to a sinusoidal magnetic field is theoretically given by [7]:

$$k_s = 2\pi A_c \left[\frac{\text{V}}{\text{THz}}\right] \tag{7.30}$$

where the coil area is calculated as per Equation 7.20.

The sensitivities of the three sensors under analysis were measured and compared to the values calculated as per Equation 7.30, and the results are summarised in Table 7.1. For reference, commercial sensors' typical sensitivity is on the order of 0.1 $\text{V}\,\text{T}^{-1}\,\text{Hz}^{-1}$ [25].

Table 7.1: Coil resistance and self inductance predicted and measured at 1 kHz, for the three coils of Figure 7.6. Sensitivity predicted by Equation 7.30 and experimentally measured. The sensitivity variation between the three coil designs is also reported.

	Coil *a*	Coil *b*	Coil *c*
Outer diameter [cm]	3	3	2
Turn count	30	15	30
Resistance (Equation 7.27) [Ω]	30.47	18.36	16.3
Resistance meas. [Ω]	37	22.8	18.6
Inductance (Equation 7.8) [μH]	304.2	133.3	111.2
Inductance meas. [μH]	289.4	121.2	98.2
Sensitivity (Equation 7.30) $\left[\frac{\mathrm{V}}{\mathrm{THz}}\right]$	0.239	0.166	0.077
Sensitivity meas. $\left[\frac{\mathrm{V}}{\mathrm{THz}}\right]$	0.223	0.157	0.071
Sensitivity increment [%]	—	69.4%	32.4%
Sensitivity increment meas. [%]	—	70.3%	31.8%

Coil *a* of Table 7.1, shown in Figure 7.6a, was selected as the preferred sensor model for the other experiments presented in the following sections of this chapter.

7.4 System simulation

The mutual inductance model provides the mutual inductance between transmitter and receiver coils based on their relative position and orientation. The EMT algorithm aims to solve the inverse problem of finding the sensor pose given the set of mutual inductances measured between the eight transmitter coils of the field generator and the sensor coil.

As described in Section 3.2.4, the problem can be solved by minimising, in a least-squares sense, the difference between the mutual inductance values measured and calculated according to the model.

7.4.1 Simplified magnetic models

The ANSER EMT transmitter board, introduced in Section 3.1, comprises eight square planar coils of 25 turns, for a total of $8 \times 4 \times 25 = 800$

filaments. The receiving sensor is a hexagonal planar coil of 30 turns, composed of $6 \times 30 = 180$ filaments, as shown in Figure 7.6a. The *full* magnetic model accounts for the mutual magnetic coupling between all the pairs of transmitting and receiving filaments, which is given by Equation 7.8. Vectorisation is critical for speed because a total of $800 \times 180 = 144\,000$ filament couples are considered.

The EMT algorithm was implemented on MATLAB, running on an HP EliteBook 840 G3 (HP Inc., Palo Alto, CA, USA) with a Core i7-6500U 2.5 GHz processor and 8 Gb of RAM. An average solution time on the order of seconds was obtained using this setup. Therefore, the *full* model is unsuitable for real-time tracking applications, which require update rates at least on the order of tens of Hertzs [26].

Two simplified, faster models are proposed and analysed. The first model considers only one turn for the receiving coil, or *six filaments*. A further simplification does not take into account the receiving coil area and evaluates the magnetic field at a *single point* at the centre. In both cases, the transmitter coils are not simplified, and all 800 filaments are considered.

7.4.2 Dependence on distance

The simplified *6-filaments* and *single-point* models were tested for the mutual inductance calculation between two coils, with variation in the distance. The *full model* was used as a ground-truth reference.

Two hexagonal planar coils of 3 cm diagonal were considered. The mutual inductance was calculated at increasing distances for different reciprocal orientations, as shown in Figure 7.7a. The yellow dot indicates the position of the evaluation point for the *single-point* model, and the green hexagon highlights the single turn considered in the *6-filaments* model.

The mutual inductances calculated using the *full*, *6-filaments*, and *single-point* models are plotted in Figure 7.7b on a normalised distance relative to the hexagonal coil diagonal, D_{out}. Figure 7.7c shows the relative percentage error of the two simplified models against the exact model reference.

As expected, the relative error decreases with the distance between the coils as model approximations become less relevant. The error depends on the coil orientation, but some general observations are valid for all three orientation cases considered.

For the *single-point* model, the relative error becomes smaller than 1% at a distance of approximately five times the coil diagonal, corresponding to 15 cm for the 3 cm coil *a* under analysis.

For the *6-filaments* model, the relative error maintains almost constantly five times smaller than the *single-point* error, becoming less than 1% when the distance is less than two times D_{out}.

7.4.3 Static tracking simulation

Virtual tracking simulations can be used to validate magnetic models for EMT [27]. The sensor is virtually positioned at many locations within the tracking region, where an accurate field simulation gives the magnetic field. The magnetic model being tested is used to infer the sensor pose, starting from the simulated magnetic measurement.

The signal measurement, $\widetilde{\mathbf{\Phi}}$, was simulated using the *full* model described in Section 7.4.1, while $\mathbf{\Phi}$ is the signal predicted by the magnetic model being tested.

Two virtual static tracking accuracy tests were performed to compare the *6-filaments* and the *single-point* models. In the first test, the position errors due to model approximations were studied. The magnetic sensor was virtually placed at 512 random positions between 1 and 11 cm from the transmitter board.

In the second test, random white noise was added to the simulated signal to analyse the robustness of the two models. The sensor was placed at 512 random locations in a cube of $30 \times 30 \times 30$ cm. The simulated noise magnitude was considered fixed and independent of the signal, representing an external noise source. Therefore, the SNR is not constant and depends on the signal magnitude. Test points further from the field generator have a smaller signal and, thus, present a smaller SNR.

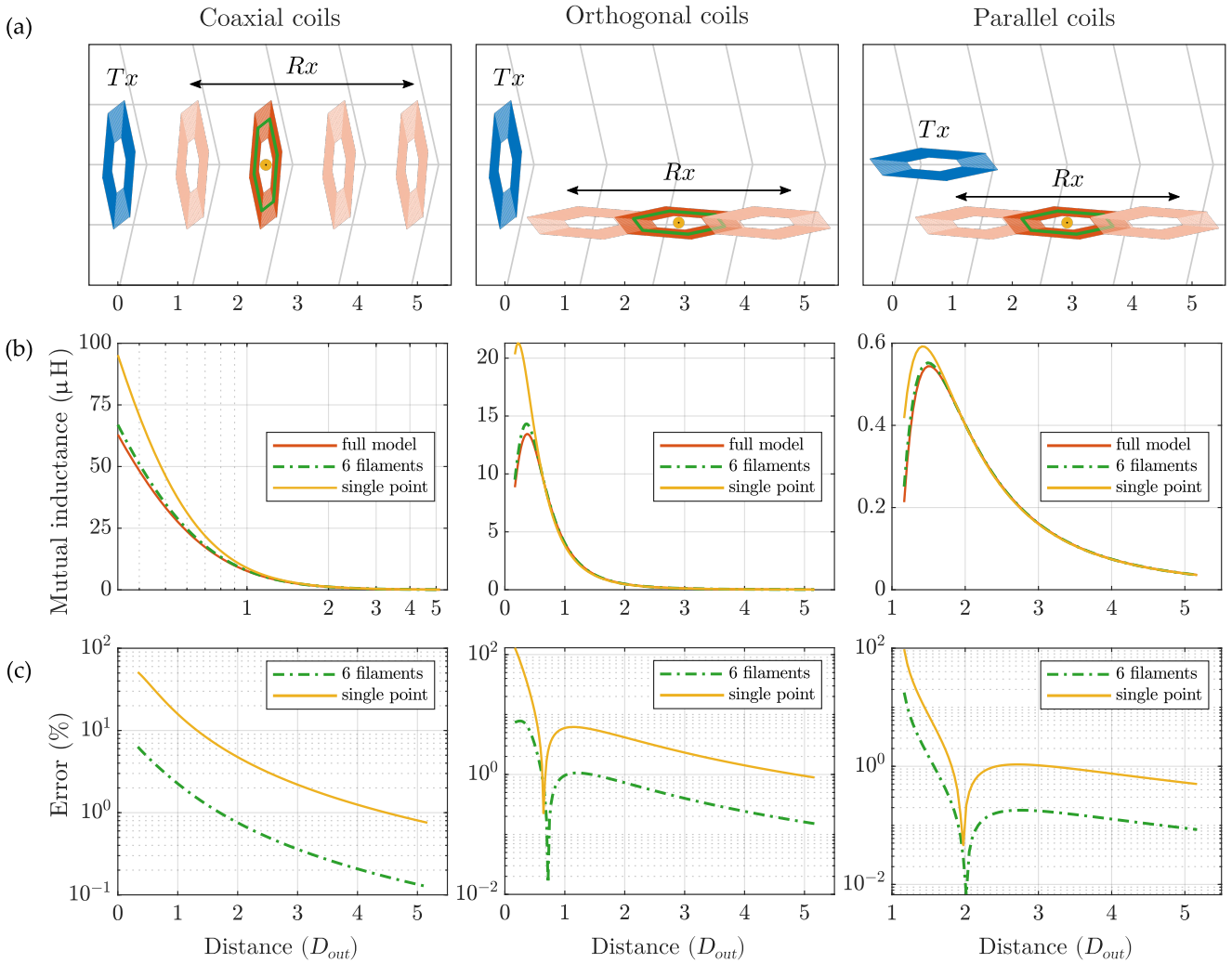


Figure 7.7: (a) A transmitter coil, Tx, and a receiver coil, Rx, at increasing distances for three orientation configurations. Distance is normalised relative to the hexagonal coil diagonal, D_{out}. (b) The mutual inductance was calculated with the *full* model, *6-filaments*, and *single-point* approximations. (c) The relative error falls below 1% at a distance larger than 2 p.u. and 5 p.u. for the *6-filaments* and *single-point* models, respectively, for all the three orientations considered.

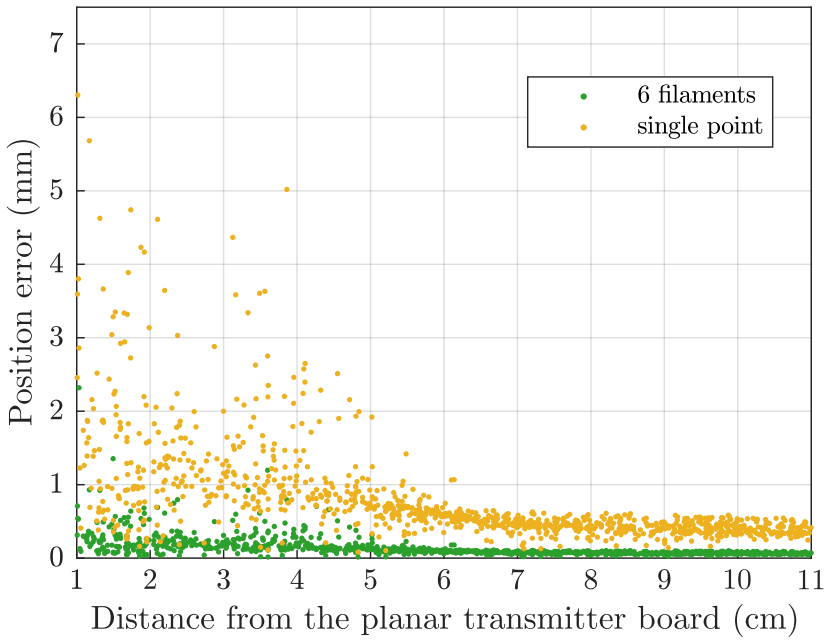


Figure 7.8: Static accuracy test simulation with no added noise. The position errors are due to model approximations. The two simplified models presented in Section 7.4.1 are compared.

The test was repeated using two different Gaussian noise magnitudes to evaluate the influence of noise on the tracking error. The average SNR values over all the test points are 65 dB and 50 dB for the two cases, respectively.

The position error was calculated as the Euclidean distance between the test position $\mathbf{x} = [x\, y\, z]^T$ used to simulate the magnetic measurement, and the position solved by the tracking algorithm, $\widetilde{\mathbf{x}}$.

Figure 7.8 shows the scatter plot of the position error. It can be noticed that the *single-point* approximation is not accurate in the proximity of the field generator. Nevertheless, this model demonstrates sub-millimetre errors for the large-area coils under analysis at distances exceeding 6 cm. For more accurate tracking near the field generator, the *6-filaments* model may be used at the cost of a higher computation time.

The computation time was calculated as the average time for solving each of the 512 test points. The average solution time, the root-mean-square error (RMSE), and the mean error (ME) are detailed in Table 7.2 for the two models described.

Table 7.2: Speed and accuracy of the *6-filaments* and the *single-point* models used in a simulated electromagnetic tracking experiment. A scatter plot of the error is shown in Figure 7.8. The computation time is calculated as the average solution time for 512 random test points.

Model	Time (s)	Distance (cm)	RMSE (mm)	ME (mm)
6-filaments	0.052	1–6	0.2615	0.1903
		6–11	0.0754	0.0733
single-point	0.007	1–6	1.4083	1.1024
		6–11	0.4485	0.4357

Figure 7.9 shows the results when Gaussian noise was added to the simulated signal, $\widetilde{\mathbf{\Phi}}$. Compared to the noiseless simulation of Figure 7.8, the average tracking error increases as the noisy measured signal deviates from the magnetic model.

The scatter plot of Figure 7.9a shows that the EMT points far from the transmitter board, where the signal and SNR are lower, have higher position errors for both models under test. In this case, the error is mainly due to the externally added noise. In contrast, different noise levels have less influence at positions near the field generator, where the inaccuracies due to the simplified *6-filaments* and the *single-point* models become dominant.

The cumulative distribution function of the error is plotted in Figure 7.9b. Using an average SNR of 65 dB, almost all the points obtained with the *6-filaments* model and approximately 90 % of the points for the *single-point* model exhibit sub-millimetre errors. If the average SNR is reduced to 50 dB, the percentage of points with sub-millimetre errors decreases to approximately 70 % and 60 %, respectively.

7.5 Experimental tests

This section presents the experimental tests performed to assess the accuracy of the magnetic model proposed in this chapter.

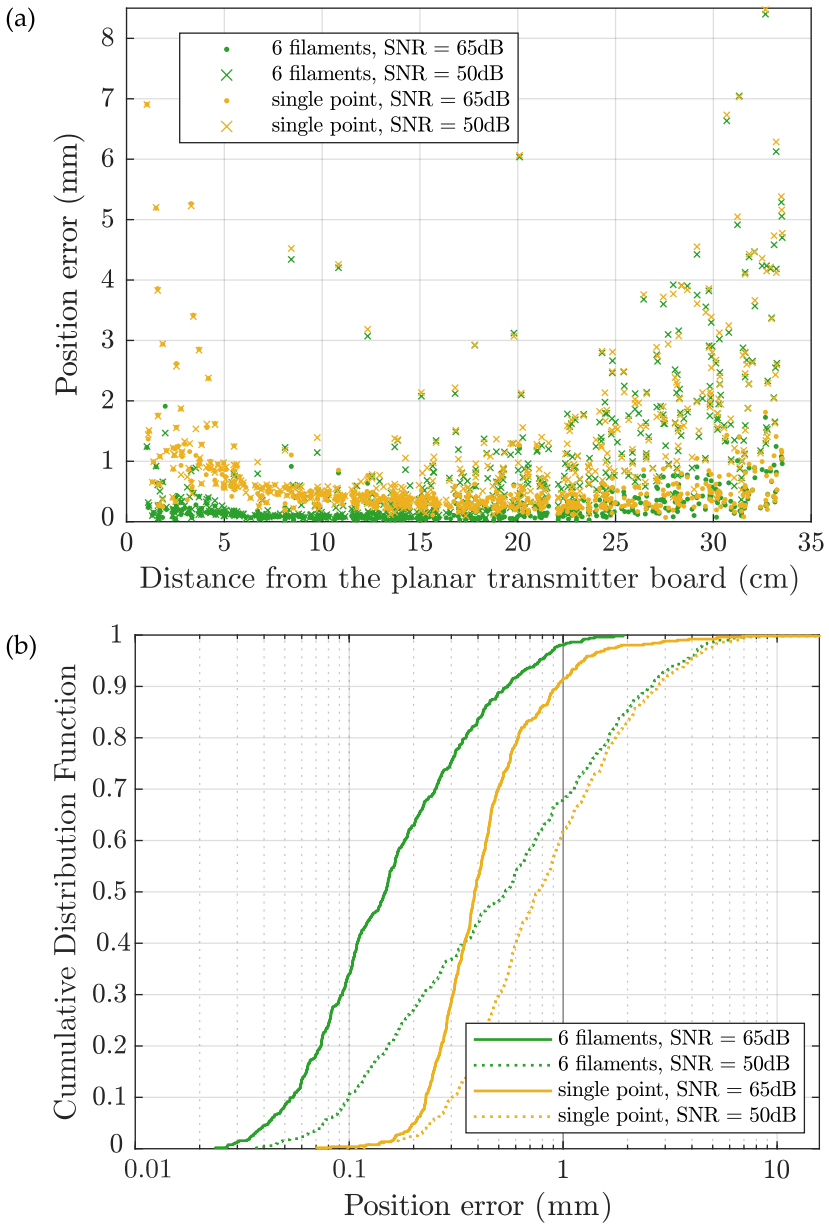


Figure 7.9: (a) Static accuracy test simulation for two noise levels compared. Position errors depend on model approximations and noise magnitude. (b) Cumulative distribution function of the position error for the two magnetic models considered and average noise levels of -50 and -65 dB.

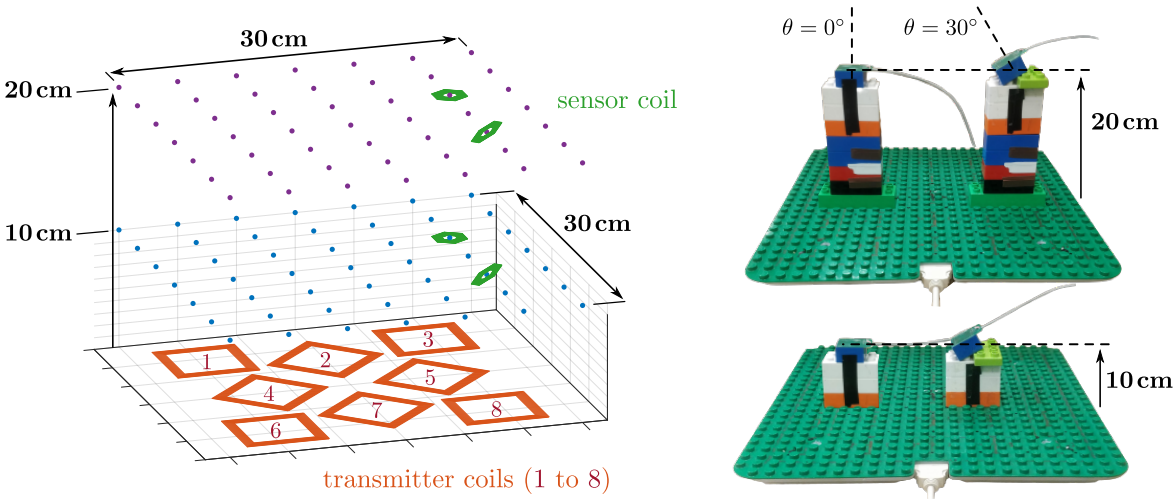


Figure 7.10: (a,b) The mutual inductance was measured on a grid of 7×7 points at 10 cm and 20 cm from the planar field generator, for two sensor orientations: pitch angles $\theta = 0°$ and $\theta = 30°$. At every test point, the eight mutual inductances between the sensor coil and the eight transmitter coils are considered, leading to a total of $49 \times 4 \times 8 = 1568$ mutual inductances experimentally evaluated.

7.5.1 Mutual inductance measurement

A set of mutual inductances was measured between coil a and the eight transmitter coils of the field generator.

The receiving coil was positioned on a grid of 7×7 test points on a horizontal plane. The experiment was repeated for two distances from the planar transmitter board, 10 cm and 20 cm, and for two sensor orientations, vertically oriented and with an angle of 30° from the vertical axis, as shown in Figure 7.10a.

Duplo blocks (The Lego Company, Billund, Denmark) were used to precisely locate the sensor in known positions (Figure 7.10b). The dimension of Duplo bricks can be measured to be around 31.8 mm to allow some tolerance for imperfections in the plastic and to facilitate the fit with neighbouring bricks. An effective grid spacing of 32 mm was considered.

At every test position, 100 measurements were collected, and the average was considered to reduce random error. For each sensor position and orientation, the eight mutual inductances between the sensor and

Table 7.3: Each test includes 392 mutual inductance values, with average M_{avg}. RMSE and MAXE are calculated between the measured values and the predictions of the theoretical model proposed in Section 7.2.

Test	M_{avg} (nH)	RMSE (nH)	MAXE (nH)
Z = 10 cm, theta = 0°	85.808	1.354	6.585
Z = 10 cm, theta = 30°	78.061	0.979	4.343
Z = 20 cm, theta = 0°	30.428	0.174	0.549
Z = 20 cm, theta = 30°	26.990	0.144	0.490

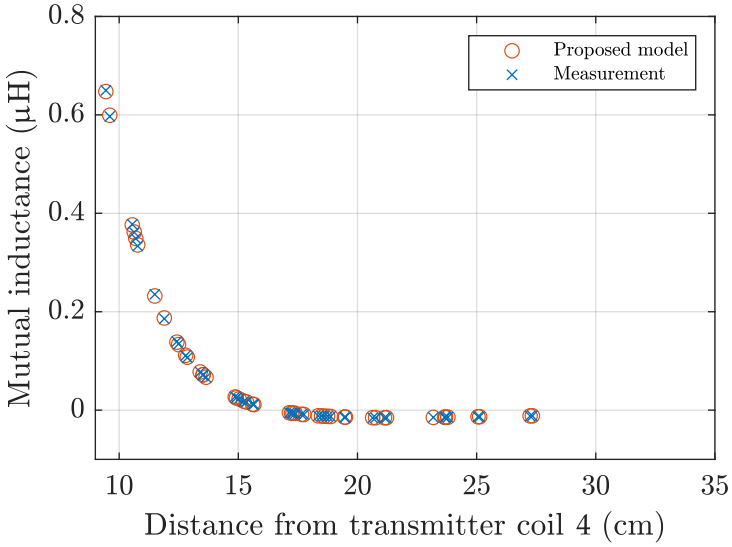
the transmitter coils of the field generator were measured, leading to a total of 1568 mutual inductance values experimentally collected for the 98 different positions and two sensor orientations.

The mutual inductances at test points were simulated with the analytical model proposed in Section 7.2, in which PCB traces of the transmitting and the receiving planar coils were approximated as zero-radius straight filaments. Previous work demonstrated that this assumption is valid almost everywhere apart from the proximity to the conductor, approximately less than five times the trace width, which is 0.635 mm in this case [28, 29].

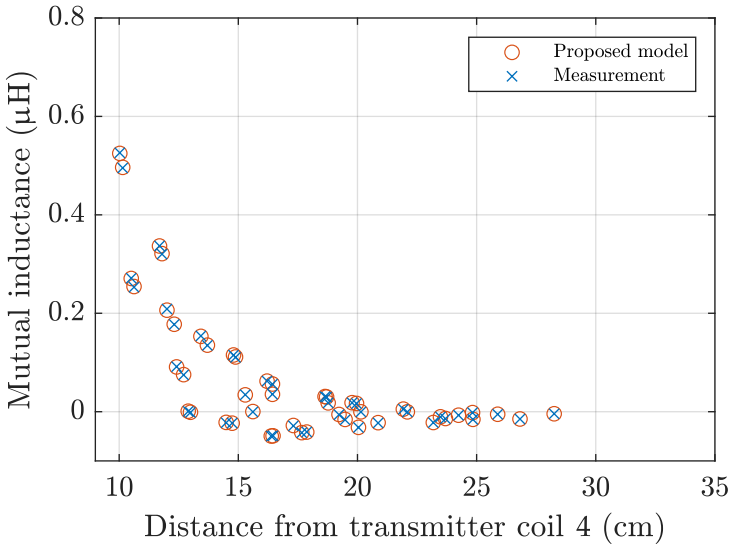
The model considers all the filaments composing the hexagonal sensor coil and the square emitter coil to compute the mutual inductance between the two coils as the sum of the contributions given by every pair of filaments.

Figure 7.11 shows the mutual inductance between the sensor coil a and the transmitter coil 4, as defined in Figure 7.10a, for the grid of points at $Z = 10$ cm and the two sensor orientations. The values experimentally measured are compared to those predicted by the theoretical formula.

The results of the four tests are summarised in Table 7.3. Each of the four cases includes $49 \times 8 = 392$ inductance values. The average measured mutual inductance, M_{avg}, the root-mean-square error (RMSE) and the maximum error (MAXE) between the measurement and the model are reported.



(a) Z = 10 cm, $\theta = 0°$



(b) Z = 10 cm, $\theta = 30°$

Figure 7.11: Mutual inductance between coil *a* of Figure 7.6a, and transmitter coil 4 of the field generator, as defined in Figure 7.10a. Experimental values are compared to those predicted by the analytical model of Section 7.2. (a) Test points at 10 cm from the planar field generator, for a pitch angle $\theta = 0°$. (b) Test points at 10 cm from the planar field generator, for a pitch angle $\theta = 30°$.

Table 7.4: Speed and accuracy of the *6-filaments* and the *single-point* models used in a real EMT experiment. A scatter plot of the error is shown in Figure 7.12. The computation time is calculated as the average solution time for the 49 test points.

Test	Model	Time (s)	RMSE (mm)	ME (mm)
$Z = 10\,\text{cm}, \theta = 0°$	6-filaments	0.1420	0.54	0.49
	single-point	0.0091	1.54	1.31
$Z = 10\,\text{cm}, \theta = 30°$	6-filaments	0.1483	0.63	0.52
	single-point	0.0094	1.92	1.57
$Z = 20\,\text{cm}, \theta = 0°$	6-filaments	0.1541	0.58	0.52
	single-point	0.0098	2.47	2.23
$Z = 20\,\text{cm}, \theta = 30°$	6-filaments	0.1488	0.57	0.48
	single-point	0.0097	2.29	2.07

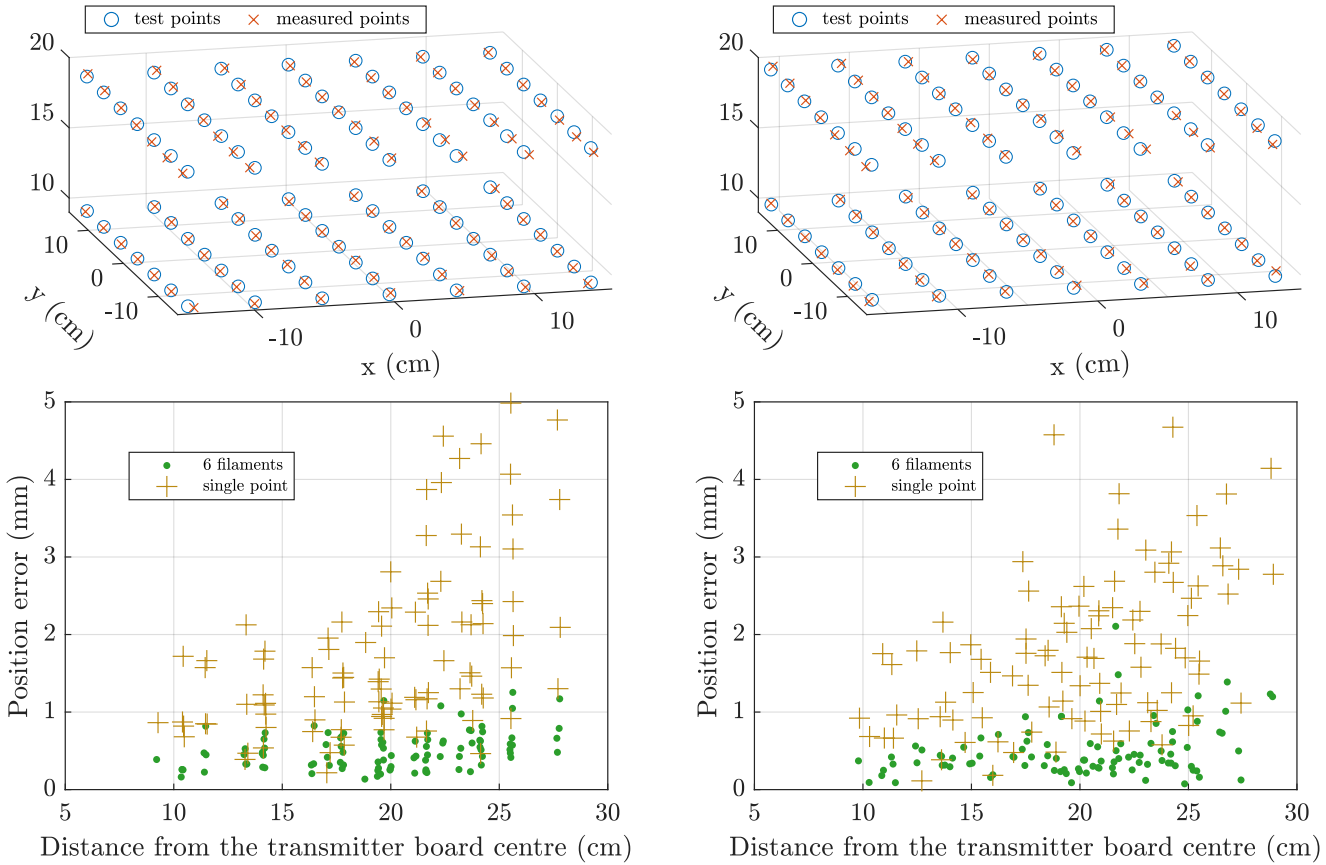
7.5.2 Static tracking accuracy

The four test cases described in Section 7.5.1 and visualised in Figure 7.10 were repeated, where in this case, the real field measurements, $\widetilde{\mathbf{\Phi}}$, were used to estimate the position of the sensor. The *6-filaments* and the *single-point* magnetic models previously presented are compared in terms of tracking accuracy and speed.

EMT results are presented separately in Figure 7.12 for the two sensor orientation cases, $\theta = 0°$ and $\theta = 30°$. The first row of Figure 7.12 shows the two grids of 49 points at $Z = 10\,\text{cm}$ and $Z = 20\,\text{cm}$ above the field generator, together with the positions estimated by the *single-point* model.

The second row of Figure 7.12 shows the scatter plot of the total position error as a function of the distance from the centre of the field generator. The *6-filaments* model demonstrates higher accuracy than the *single-point* model, with errors below 1 mm for almost all the test points. In comparison, the EMT errors obtained with the *single-point* model are as large as 5 mm. On average, positions further from the centre of the field generator show more significant errors due to signal attenuation and decreased SNR.

The average solution time, root-mean-square error (RMSE) and mean error (ME) are detailed in Table 7.4 for the four test cases and the two magnetic models described.



(a) $z = 10\,\text{cm} - 20\,\text{cm}, \theta = 0°$ (b) $z = 10\,\text{cm} - 20\,\text{cm}, \theta = 30°$

Figure 7.12: Static accuracy tests with real data. First row: test points and EMT positions solved using the *single-point* model. Second row: scatter plot of the position error for the *6-filaments* and *single-point* models. Columns (a,b): results for different sensor orientations, $\theta = 0°$ and $\theta = 30°$, respectively.

7.6 Discussion

The mutual inductance between coils composed of straight filaments was calculated using a novel formulation for the partial mutual inductance between arbitrarily oriented straight filaments.

Coil design demonstrated that planar coils on the centimetre scale are optimised when the minimum trace width and spacing are chosen, and the number of turns is maximised. The circular shape is optimal for SNR optimisation, as seen in Figure 7.4, but a hexagonal coil shape was selected because it can be entirely modelled by straight filaments. In Table 7.1, the measured coil resistance, inductance, and sensitivity are compared with the values predicted in the design stage.

A hexagonal planar coil with a diameter of 3 cm was PCB manufactured. A set of mutual inductances was measured between the sensor coil and the eight transmitter coils of the field generator. Experimental values validated the model proposed in Section 7.2. A selection of the results is plotted in Figure 7.11, and the average error is reported in Table 7.3.

The tracking algorithm was implemented in MATLAB with an average solution time on the order of seconds when all the pairs of transmitting and receiving filaments were considered. Two simplified models were introduced for real-time EMT. The sensor coil was approximated by *six filaments* or by a *single point*, respectively.

The virtual tracking error is plotted in Figure 7.8. The *single-point* model provides sub-millimetre positioning errors at distances larger than 6 cm from the transmitter board. In contrast, the *6-filaments* model reaches the same level of accuracy even for more close positions.

Four EMT static tests were performed, varying the sensor orientation and distance from the field generator. As reported in Table 7.4, using the *6-filaments* model, the position error is three to four times smaller than using the *single-point* model. However, the average solution time is approximately 0.15 s, compared to 0.01 s for the *single-point* model. This time is still suitable for real-time tracking but at lower update rates.

7.7 Conclusions

This chapter analysed the tracking performance of planar coils on the centimetre scale. An accurate magnetic model was proposed and experimentally validated.

The model computes the inductive coupling between all the straight filaments comprising the transmitter and the receiver coils. While this model was too slow for effective real-time EMT, it proved helpful in performing sensor design and calibration and running tracking simulations. The introduction of model simplifications increased the calculation speed, and the real-time tracking of large-area planar sensors was demonstrated with sub-millimetre positioning errors.

It is worth noting that the model introduced in this chapter is used to directly compute the mutual inductance between spatially extended coils. The sensor orientation cannot be decoupled from the model by expressing the result as the dot product between the transmitted field vector and the orientation axis of the receiving coil. Therefore, speeding up the model by pre-characterising the field values as was done in Sections 5.1.2 and 6.4.2 is impossible in this case.

References

[1] M. Cavaliere, H. A. Jaeger, K. O'Donoghue, and P. Cantillon-Murphy, "Planar Body-Mounted Sensors for Electromagnetic Tracking," *Sensors*, vol. 21, no. 8, p. 2822, 2021. DOI: 10.3390/s21082822.

[2] G. Ahmad *et al.*, "Impact of Fluoroscopy Unit on the Accuracy of a Magnet-Based Electroanatomic Mapping and Navigation System: An In Vitro and In Vivo Validation Study," *Pacing and Clinical Electrophysiology*, vol. 37, no. 2, pp. 157–163, 2014, ISSN: 1540-8159. DOI: 10.1111/pace.12231.

[3] H. A. Jaeger and P. Cantillon-Murphy, "Electromagnetic Tracking Using Modular, Tiled Field Generators," *IEEE Transactions on Instrumentation and Measurement*, vol. 68, no. 12, pp. 4845–4852, 2019, ISSN: 1557-9662. DOI: 10.1109/TIM.2019.2900884.

[4] L. Koyrakh, S. Morgan, and A. Brown, "Modular reconfigurable magnetic navigation system and method," US20220037085A1, 2022. [Online]. Available: https://patents.google.com/patent/US20220037085A1/en (visited on 12/20/2022).

[5] H. A. Jaeger and P. Cantillon-Murphy, "Distorter Characterisation Using Mutual Inductance in Electromagnetic Tracking," *Sensors*, vol. 18, no. 9, p. 3059, 2018. DOI: 10.3390/s18093059.

[6] H. A. Jaeger *et al.*, "Anser EMT: The first open-source electromagnetic tracking platform for image-guided interventions," *International Journal of Computer Assisted Radiology and Surgery*, vol. 12, pp. 1059–1067, 2017. DOI: 10.1007/s11548-017-1568-7.

[7] M. Cavaliere, O. McVeigh, H. A. Jaeger, S. Hinds, K. O'Donoghue, and P. Cantillon-Murphy, "Inductive Sensor Design for Electromagnetic Tracking in Image Guided Interventions," *IEEE Sensors Journal*, vol. 20, no. 15, pp. 8623–8630, 2020, ISSN: 1558-1748. DOI: 10.1109/JSEN.2020.2984323.

[8] *Aurora Sensors - NDI*. [Online]. Available: https://www.ndigital.com/products/aurora/aurora-sensors/ (visited on 04/22/2022).

[9] C. T. A. Johnk, "Engineering electromagnetic fields and waves," *New York, John Wiley and Sons, Inc., 1975. 667 p.*, 1975.

[10] C. R. Paul and S. A. Nasar, *Introduction to Electromagnetic Fields*. New York, NY, USA: McGraw-Hill, 1987, ISBN: 0-07-045908-8.

[11] F. E. Neumann, "Allgemeine Gesetze der inducirten elektrischen Ströme," *Annalen der Physik und Chemie*, vol. 143, no. 1, pp. 31–44, 1846, ISSN: 00033804, 15213889. DOI: 10.1002/andp.18461430103.

[12] H. L. Chan, K. W. E. Cheng, and D. Sutanto, "A simplified Neumann's formula for calculation of inductance of spiral coil," in *8th International Conference on Power Electronics and Variable Speed Drives*, 2000, pp. 69–73. DOI: 10.1049/cp:20000222.

[13] E. B. Rosa, "The self and mutual-inductances of linear conductors," *Bulletin of the Bureau of Standards*, vol. 4, no. 2, p. 301, 1908, ISSN: 0096-8579. DOI: 10.6028/bulletin.088.

[14] G. A. Campbell, "Mutual Inductances of Circuits Composed of Straight Wires," *Physical Review*, vol. 5, no. 6, pp. 452–458, 1915. DOI: 10.1103/PhysRev.5.452.

[15] F. W. Grover, *Inductance Calculations: Working Formulas and Tables*. Albuquerque, NM, USA: Instrument Society of America, 1946, ISBN: 978-0-87664-557-4.

[16] P. T. Anderson, "A source of accurately calculable quasi-static magnetic fields," Ph.D. dissertation, The University of Vermont, Burlington,VT,USA, 2001.

[17] C. L. W. Sonntag, E. A. Lomonova, and J. L. Duarte, "Implementation of the Neumann formula for calculating the mutual inductance between planar PCB inductors," in *2008 18th International Conference on Electrical Machines*, 2008, pp. 1–6. DOI: 10.1109/ICELMACH.2008.4799978.

[18] Y. Cheng and Y. Shu, "Mutual inductance calculation between arbitrarily positioned rectangular filaments," *International Journal of Applied Electromagnetics and Mechanics*, vol. 46, no. 1, pp. 287–298, 2014, ISSN: 1383-5416. DOI: 10.3233/JAE-141779.

[19] C. R. Paul, *Inductance*. Hoboken, NJ, USA: John Wiley & Sons, Inc., 2009, ISBN: 978-0-470-56123-2. DOI: 10.1002/9780470561232.

[20] M. Ulvr, "Design of PCB search coils for AC magnetic flux density measurement," *AIP Advances*, vol. 8, no. 4, p. 047 505, 2017. DOI: 10.1063/1.4991643.

[21] A. Islam, S. Islam, and F. Tulip, "Design and Optimization of Printed Circuit Board Inductors for Wireless Power Transfer System," *Faculty Publications and Other Works – EECS*, 2013. [Online]. Available: https://trace.tennessee.edu/utk_elecpubs/21.

[22] MathWorks, *Find minimum of constrained nonlinear multivariable function*. [Online]. Available: https://uk.mathworks.com/help/optim/ug/fmincon.html (visited on 09/12/2022).

[23] C. Yue and S. Wong, "Physical modeling of spiral inductors on silicon," *IEEE Transactions on Electron Devices*, vol. 47, no. 3, pp. 560–568, 2000, ISSN: 00189383. DOI: 10.1109/16.824729.

[24] A. Zolfaghari, A. Chan, and B. Razavi, "Stacked inductors and 1-to-2 transformers in CMOS technology," in *Proceedings of the IEEE 2000 Custom Integrated Circuits Conference (Cat. No.00CH37044)*, vol. 36, IEEE, 2000, pp. 345–348, ISBN: 0-7803-5809-0. DOI: 10.1109/CICC.2000.852681.

[25] K. O'Donoghue *et al.*, "Catheter Position Tracking System Using Planar Magnetics and Closed Loop Current Control," *IEEE Transactions on Magnetics*, vol. 50, no. 7, pp. 1–9, 2014, ISSN: 0018-9464. DOI: 10.1109/tmag.2014.2304271.

[26] Z. Yaniv, E. Wilson, D. Lindisch, and K. Cleary, "Electromagnetic tracking in the clinical environment," *Medical Physics*, vol. 36, no. 3, pp. 876–892, 2009, ISSN: 00942405. DOI: 10.1118/1.3075829.

[27] G. De Angelis, A. De Angelis, A. Moschitta, and P. Carbone, "Comparison of Measurement Models for 3D Magnetic Localization and Tracking," *Sensors*, vol. 17, no. 11, p. 2527, 2017. DOI: 10.3390/s17112527.

[28] C. L. W. Sonntag, M. Sprée, E. A. Lomonova, J. L. Duarte, and A. J. A. Vandenput, "Accurate Magnetic Field Intensity Calculations for Contactless Energy Transfer Coils," in *Proceedings of the 16th International Conference on the Computation of Electromagnetic Fields, Achen, Germany*, 2007, pp. 1–4.

[29] Y. Cheng and Y. Shu, "A New Analytical Calculation of the Mutual Inductance of the Coaxial Spiral Rectangular Coils," *IEEE Transactions on Magnetics*, vol. 50, no. 4, pp. 1–6, 2014, ISSN: 1941-0069. DOI: 10.1109/TMAG.2013.2290972.

Chapter 8

Summary and future work

The thesis presented a comprehensive study on electromagnetic tracking (EMT), focusing on developing methods and techniques to reduce and compensate for distortions in the magnetic field through improved modelling and real-time correction methods.

This chapter summarises and discusses the main findings of the study, concluding with suggestions for future research directions.

8.1 Thesis summary

The thesis began with a literature review of EMT systems, methods, and techniques used to reduce and compensate for distortions in the magnetic field, in Chapter 2. The survey gave a background context to the specific open-source EMT platform used in the following work, ANSER EMT.

Chapter 3 presented and evaluated the ANSER EMT system, with a focus on testing the existing limits of the system [1]. The design and implementation of a 2D actuator for field sampling were presented, and methods for EMT sensor calibration and registration to an optical system reference were proposed. Novel methods for error evaluation and noise analysis were also introduced.

These introductory studies set the stage for the novel work presented in Chapter 4 aimed to enhance EMT accuracy, either without introducing further magnetic distortion or in the presence of metallic materials. To this end, a method for modelling magnetic fields was developed and used

to improve the ANSER EMT magnetic model by correcting for systematic errors and including magnetic shielding [2].

The focus shifted towards testing for distortions introduced by medical equipment. Novel techniques for distortion detection were employed in this experiment. Real-time compensation for dynamic distortion was proposed using external reference sensors. Two approaches were tested, the first involved an updated magnetic field model using a virtual distribution of magnetic dipole sources [3], while the second aimed to localise the source of distortion and interpolate between static field maps [4].

The narrative continued by presenting further improvements to the ANSER EMT system in Chapter 5, this time targeting dynamic tracking. The EMT model and algorithm were optimised to achieve faster update rates and reduce noise and latency. As a result of this study, Kalman filtering was incorporated into the tracking algorithm.

In Chapter 6, the effectiveness of the ANSER EMT system for developing novel EMT applications was demonstrated by introducing an alternative tracking technique based on the magnetic *scalar potential* formulation [5]. The novel model showed increased speed and lower storage requirements relative to the implementation through the traditional magnetic field vector approach. The new technique is particularly suited for tracking the elongated sensor coils used in medical applications.

As discussed in Chapter 4, external reference sensors can help detect and minimise the effect of magnetic distortions. A cost-effective solution to manufacture such sensors with high precision and repeatability is printing planar coils on flexible PCB. In this way, the sensors might be embedded in adhesive patches on the patient for future clinical applications.

In the final part of the thesis, Chapter 7 explored EMT using large-area planar sensors. These coils demonstrated high sensitivity even without a magnetic core [6]. A novel accurate model accounting for the coil extension was proposed based on the magnetic *vector potential* formulation [7]. Experimental tests demonstrated the effectiveness of the new model for designing planar coils and performing EMT simulations to evaluate the accuracy of simplified models.

In summary, the thesis discussed the following research topics.

1. Extensive literature review of EMT methods, topologies, medical applications, commercial systems, and distortion compensation (Chapter 2).

2. Detailed presentation of the ANSER EMT system and experimental performance evaluation (Chapter 3).

3. Novel methods to convert the measurement error directly into the corresponding EMT error, study random noise propagation, and analyse the tracking resolution of an EMT system (Section 3.5).

4. Customised tools to host EMT sensors, with methods for calibration and registration to the optical system reference (Section 3.3).

5. Design and programming of a robotic actuator to automatise volume characterisation tasks and perform accuracy evaluation tests (Section 3.4).

6. Novel magnetic modelling technique based on virtual magnetic dipole sources (Section 4.1).

7. Evaluation of different shielding materials and methods to model the shielded field generator (Section 4.3).

8. Novel metallic distortion detection techniques to raise a warning when the EMT accuracy is reduced (Section 4.4).

9. Characterisation of distortion in different clinical environments (Sections 4.3.2 and 4.4.4).

10. Novel technique to compensate for distortions in real time using the interpolation of pre-trained magnetic maps (Section 4.5.2).

11. Novel tracking algorithm with increased speed and minimal computation requirements (Section 5.1.1).

12. Speed improvements for the magnetic model of ANSER EMT (Section 5.1.2).

13. Enhanced update-rate using filtering techniques to lower the jitter noise and increase the precision (Section 5.3).

14. Novel magnetic model for elongated sensors, with improvements in accuracy, speed, and storage requirements (Chapter 6).

15. Novel approach to calculate the solid angle subtended by the surface enclosed by a 3D boundary (Section 6.3).

16. More accurate magnetic model for planar sensors composed of straight filaments (Chapter 7).

17. Planar coil design on PCB with optimised SNR (Section 7.3).

8.2 Thesis contributions

A significant portion of the research contributed to introducing novel features to the ANSER EMT system developed in University College Cork and available for free to any research group aiming to investigate new methods for EMT. The other part of the work involved using the ANSER EMT platform to develop novel techniques that can be applied to any EMT system where modifications are enabled. The principal contributions of this thesis are listed as follows.

Performance of the open-source ANSER EMT *system.* Materials and methods for EMT error measurement and evaluation were developed, the update-rate was increased using Kalman filtering, and the speed and memory requirements were improved using a modular C++ environment [1, 6].

Data-driven magnetic modelling technique. The technique of magnetic modelling using virtual magnetic dipole sources can be employed as a novel method for EMT calibration to correct systematic errors and model static field distortions, such as those introduced by magnetic shielding materials or medical equipment [2].

Methods for distortion detection and compensation. Novel techniques were proposed for EMT system calibration, metallic distortion detection, and magnetic distortion compensation. These methods have the potential for online error correction during clinical procedures [3, 4].

Accurate magnetic model for elongated sensor coils. A new approach to model the mutual inductance between transmitting coils and elongated sensor coils was introduced. The model included a novel method to calculate the solid angle subtended by a spiral path [5].

Accurate magnetic model for planar sensor coils. Formulas for the partial mutual inductance between straight wires were applied to calculate an accurate EMT model for planar sensor coils. Additionally, methods for planar coil design for sensing applications were presented [7].

8.3 Perspectives for future work

This thesis suggests numerous possibilities for further research in EMT. This section proposes recommendations for future investigations that build upon the topics explored in this work.

8.3.1 Radiation exposure reduction in a clinical study

As discussed in Chapter 4, compensation of magnetic distortion in EMT is divided into two distinct problems. Static distortion can be characterised in advance and corrected by updating the magnetic model used for tracking. Dynamic distortion, on the other hand, poses a more significant challenge because EMT errors change in magnitude and direction in a way that depends on the distorted environment.

In Section 4.5, the dynamic distortion introduced by a C-arm machine was considered, and two possible solutions were proposed. The first methodology was enabled by the novel magnetic modelling technique introduced in Section 4.1 and involves fitting a compensated model to the

measurements of reference sensors at known positions. The second approach considers multiple static distortion scenarios, using interpolation of pre-recorded data to recognise unseen configurations and adopt the correct characterisation map.

The proposed techniques potentially apply to any procedures that combine EMT with intraoperative fluoroscopy. However, their implementation requires increasing the complexity of both the hardware and software components of the EMT system because additional sensors must be introduced and their measurements acquired and analysed in real time. Therefore, the necessity of employing these techniques should be considered together with the concrete benefits that can be obtained. Tracking accuracy requirements depend on the specific application case. As seen in Chapter 4, even the most critical distortion is typically below 5 cm. If such EMT errors are deemed acceptable, compensation would not be essential.

This study primarily emphasised the technical and engineering aspects, aiming to advance the theory and introduce novel concepts. Future research directions may explore real clinical applications by analysing the benefits in existing minimally-invasive operations and identifying the new procedures that distortion-free EMT might enable. Once a specific application is selected, the work should investigate ways to optimise the methodologies and integrate them into the clinical workflow. Finally, a pre-clinical study should be conducted to assess the effective level of radiation reduction achieved using the more accurate, undistorted EMT methods proposed.

8.3.2 Self-shielded field generator

Section 4.3 analysed the use of conductive and high-permeability metal plates to shield the planar field generator from distortions under it.

As explained in Section 4.3, the working principle of the aluminium conductive shield is based on the surface eddy currents that oppose the field variation. The same current distribution can be reproduced by a planar coil specifically designed to generate a field that nullifies the normal component of the magnetic flux density crossing the shielding plane.

In this way, the transmitting and shielding coils could be combined to create a field generator that is *self-shielded* and does not rely on external shielding materials. This configuration offers several benefits, such as the option to activate or deactivate the shield as required, high stability and reproducibility, higher compatibility with X-ray imaging systems, and the possibility to model the magnetic field without relying on finite-element simulations or data measurements.

As a proof of concept, Figure 8.1a shows the surface current density that shields one of the emitter coils of the ANSER EMT field generator. The current distribution that nullifies the magnetic field at 1 cm below the emitter coil was obtained using the stream function method implemented by the *bfieldtools* Python library [8, 9].

The magnitude map of the combined magnetic fields is shown Figure 8.1b. The field magnitude is higher in the region above the emitter coil compared to the region below it, thus demonstrating the shielding effect.

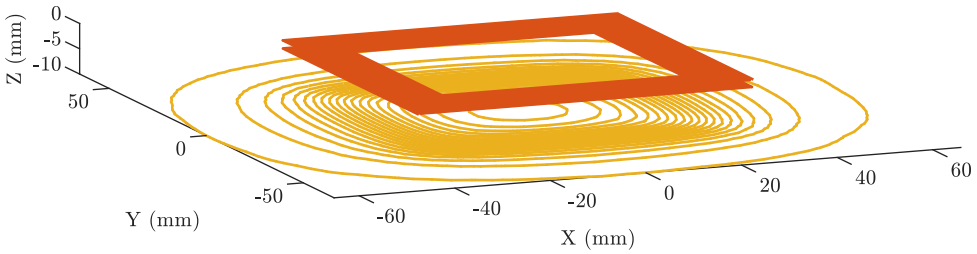
It should be noted that the proposed coil configuration is not power efficient because it involves generating magnetic fields that cancel out each other. As a result, most of the magnetic energy is deposited within the volume between the emitter and the shielding coils and is not used for the EMT signal. Nevertheless, the active shield may be turned on only when required, such as if a distortion is detected as described in Section 4.4 or to periodically re-calibrate the non-shielded EMT solution.

8.3.3 Fusion with complementary imaging systems

As extensively discussed in this thesis, magnetic distortion is one of the main challenges to EMT technology. Chapter 2 reported multiple solutions proposed in the literature to mitigate this problem. Chapter 4 introduced novel techniques for distortion detection and compensation.

These studies and experimental analyses indicate that the state-of-the-art may have reached the limit of what is realistically achievable in terms of accuracy and robustness using only EMT methods. Additional advancements may be possible through the strategic integration of EMT

(a) Transmitting and shielding coils



(b) Field magnitude normalised to the maximum value

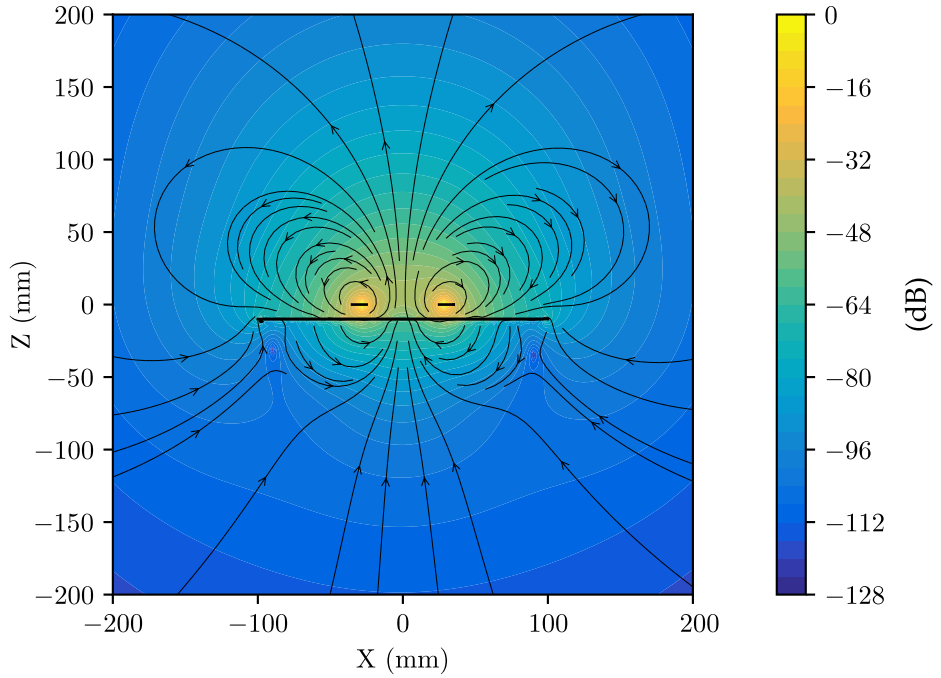


Figure 8.1: (a) Current distribution for an active shield located at 1 cm below the transmitting coil. (b) Magnetic field magnitude map of the self-shielded coil configuration.

technology with complementary systems to improve minimally invasive procedures.

The initial stage would be integrating EMT field generators into various medical equipment, including surgical beds, C-arm gantries, probes, and other tools used in the medical field. As demonstrated in Section 4.3.1, systematic distortion can be factory calibrated through pre-characterisation. Therefore, most issues caused by metallic objects moving within the operative space would be automatically solved by fixing the field generator to these components.

Further work may investigate the use of fluoroscopy for intraoperative recalibration of the EMT system. To this end, image recognition might be used to localise the marker position in an X-ray snapshot to create an EMT error map or update the magnetic model. Additionally, the same technique might be applied to find the position of redundant sensors placed around the region of interest and compensate for metallic distortion using the method described in Section 4.5.1. The PCB planar sensors studied in Chapter 7 could be used in this instance.

Finally, in the future artificial intelligence (AI) might be employed in EMT analogously to how it is used in self-driving cars. The AI algorithm may be trained on multiple real or simulated medical procedures, learning to recognise the context and identifying common patterns between operations. In this scenario, the EMT system could provide an approximate position, with more accurate information obtained through the use of endoscopic cameras, low-dose X-ray, ultrasound, or a combination of these methods.

8.3.4 Reversed magnetic model

This thesis explored several magnetic models for EMT. Some models were based on theoretical considerations, as explained in Section 3.2.3 and Chapters 6 and 7, and others were derived from real measurements, such as those introduced in Chapter 4.

In all these cases, solving for the EMT pose is the inverse problem where the measured signal is used to calculate the sensor pose most likely

to give the same magnetic measurements. The tracking algorithm presented in Section 3.2.4 estimates the solution using iterative methods. The faster EMT algorithm introduced in Section 5.1.1 is based on a local linearisation of the magnetic model but requires knowledge of the previous sensor pose and assumes that the target moves sufficiently slowly.

Advanced machine learning techniques should be investigated to invert the field map and obtain a *reversed* magnetic model that can directly output the sensor pose given a set of field measurements as an input. It is not necessary for this process to be interpretable, where the EMT model and algorithm might be combined in a single artificial neural network (ANN) that estimates the correct EMT pose as a black box.

Calculating the ANN output involves basic operations like additions and multiplications. However, these models are typically defined by many parameters and require significant storage capacity. One possible solution is implementing the ANN in hardware using a field-programmable gate array (FPGA) to increase speed and reduce memory requirements. In this case, a simple low-power microcontroller might be enough to handle signal acquisition and interfacing with the FPGA.

References

[1] M. Cavaliere, C. Walsh, H. A. Jaeger, K. O'Donoghue, and P. Cantillon-Murphy, "Magnetic tracking using a modular C++ environment for image-guided interventions," *Computer Methods in Biomechanics and Biomedical Engineering: Imaging & Visualization*, vol. 10, no. 4, pp. 383–389, 2021, ISSN: 2168-1163. DOI: 10.1080/21681163.2021.1998926.

[2] M. Cavaliere, D. Crowley, H. A. Jaeger, K. O'Donoghue, and P. Cantillon-Murphy, "Magnetic Model Calibration and Distortion Compensation for Electromagnetic Tracking in a Clinical Environment," *IEEE Transactions on Magnetics*, vol. 59, no. 7, pp. 1–12, 2023, ISSN: 1941-0069. DOI: 10.1109/TMAG.2023.3275297.

[3] M. Cavaliere and P. Cantillon-Murphy, "Intraoperative compensation of magnetic field distortions for fluoroscopic and electromagnetic hybrid navigation," *International Journal of Computer Assisted Radiology and Surgery*,

vol. 17, pp. 1717–1721, 2022, ISSN: 1861-6429. DOI: 10.1007/s11548-022-02663-7.

[4] M. Cavaliere and P. Cantillon-Murphy, "Enhancing electromagnetic tracking accuracy in medical applications using pre-trained witness sensor distortion models," *International Journal of Computer Assisted Radiology and Surgery*, 2023, ISSN: 1861-6429. DOI: 10.1007/s11548-023-02994-z.

[5] M. Cavaliere and P. Cantillon-Murphy, "Electromagnetic Tracking of Elongated Sensors for Endoscopic Navigation," *Magnetism*, vol. 2, no. 3, pp. 271–287, 2022, ISSN: 2673-8724. DOI: 10.3390/magnetism2030020.

[6] M. Cavaliere, O. McVeigh, H. A. Jaeger, S. Hinds, K. O'Donoghue, and P. Cantillon-Murphy, "Inductive Sensor Design for Electromagnetic Tracking in Image Guided Interventions," *IEEE Sensors Journal*, vol. 20, no. 15, pp. 8623–8630, 2020, ISSN: 1558-1748. DOI: 10.1109/JSEN.2020.2984323.

[7] M. Cavaliere, H. A. Jaeger, K. O'Donoghue, and P. Cantillon-Murphy, "Planar Body-Mounted Sensors for Electromagnetic Tracking," *Sensors*, vol. 21, no. 8, p. 2822, 2021. DOI: 10.3390/s21082822.

[8] A. J. Mäkinen, R. Zetter, J. Iivanainen, K. C. J. Zevenhoven, L. Parkkonen, and R. J. Ilmoniemi, "Magnetic-field modeling with surface currents. Part I. Physical and computational principles of bfieldtools," *Journal of Applied Physics*, vol. 128, no. 6, p. 063 906, 2020, ISSN: 0021-8979. DOI: 10.1063/5.0016090.

[9] R. Zetter, A. J. Mäkinen, J. Iivanainen, K. C. J. Zevenhoven, R. J. Ilmoniemi, and L. Parkkonen, "Magnetic field modeling with surface currents. Part II. Implementation and usage of bfieldtools," *Journal of Applied Physics*, vol. 128, no. 6, p. 063 905, 2020, ISSN: 0021-8979. DOI: 10.1063/5.0016087.